January 2015

Structure and Dynamics of a Reacting Jet Injected into a Vitiated Crossflow in a Staged Combustion System

Pratikash Prakash Panda
Purdue University

Graduate School Form 30
Updated 1/15/2015

PURDUE UNIVERSITY
GRADUATE SCHOOL
Thesis/Dissertation Acceptance

This is to certify that the thesis/dissertation prepared

By Pratikash Prakash Panda

Entitled

STRUCTURE AND DYNAMICS OF A REACTING INJECTED INTO A VITIATED CROSSFLOW IN A STAGED COMBUSTION SYSTEM

For the degree of Doctor of Philosophy

Is approved by the final examining committee:

ROBERT P. LUCHT
Chair

GREGORY M. SHAVER

HUKAM C. MONGIA

STEPHEN D. HEISTER

WILLIAM ANDERSON

To the best of my knowledge and as understood by the student in the Thesis/Dissertation Agreement, Publication Delay, and Certification Disclaimer (Graduate School Form 32), this thesis/dissertation adheres to the provisions of Purdue University's "Policy of Integrity in Research" and the use of copyright material.

Approved by Major Professor(s): ROBERT P. LUCHT

Approved by: JAY P. GORE 9/28/2015

Head of the Departmental Graduate Program Date

STRUCTURE AND DYNAMICS OF A REACTING JET INJECTED INTO A VITIATED CROSSFLOW IN A STAGED COMBUSTION SYSTEM

A Dissertation

Submitted to the Faculty

of

Purdue University

by

Pratikash Prakash Panda

In Partial Fulfillment of the

Requirements for the Degree

of

Doctor of Philosophy

December 2015

Purdue University

West Lafayette, Indiana

To my mother, *Pratima,* father, *Prakash* and my wife *Susmita*

ACKNOWLEDGEMENTS

The following dissertation although is an individual work, it could not have been plausible without the help, guidance and support of a lot people.

Firstly, I would like to express my gratitude to my advisor and mentor Prof. Robert Lucht for giving an opportunity to work in his research group and having the belief in me. This research would not have been possible without Prof. Lucht's continuous encouragement and guidance. I have learnt a lot from him, and will seek to incorporate them as I move ahead. I am thankful to my committee members, Prof. Steve Heister, Prof. Bill Anderson, Prof. Greg Shaver and Prof. Hukam Mongia for their useful inputs. I would like to express my gratitude to Prof. Mongia's continuous guidance and advice during the course of my graduate studies.

I would like to thank Scott Meyer for his continuous support, and extremely useful inputs in the development, integration, and operation of the staged combustion test rig. The help and inputs of Rob McGuire in hardware modification, running the experiments and pulling me out of any hardware related issues are also greatly appreciated. I would like to recognize the quick response and turn overs of Jerry, Jeff and Verlin from RMS. I would also like to convey my appreciation to Joan, Edie, Charlotte and Michelle for their immense help in hardware purchasing and procurement process.

I would like to extend my gratitude towards the wonderful faculty members in the School of Mechanical Engineering. I would like a special mention of Prof. John Abraham's course on Combustion; the course not only improved my understanding of Combustion physics but also motivated me to pursue my research in this area. I thoroughly enjoyed Prof. Merkle's course on Air-Breathing Propulsion. His vast experience and expertise alongwith his real life stories aptly explaining the concepts of propulsion, made the learning very interesting. One of the most stimulating courses during my graduate studies was Prof. Heister's Advanced Rocket Propulsion. I enjoyed his unique way of teaching, especially the homework and exam problems related to real propulsion devices made the course very interesting.

I would like to further thank Dr. Mario Roa for guiding me through the unique experimental research at the HPL, Zucrow Labs. I would also like to thank Yashowardhan Wagh and Oluwatobi Busari for their immense contributions in the experiments. Special thanks to all my colleague at Zucrow Labs and Applied Spectroscopy Lab, Dr. Carson Slabaugh, Dr. Christopher Fugger, Dr. Aman Satija, Rohan Gejji, Andrew Pratt, Bob Zhang, Michael Bedard, Brandan Kan, Heather Wiest, Dong Han. The friendly environment in the research group, and insightful discussions provided a positive ambience for research work.

I thank my friends, Nikhil, Prabhakar, Niranjan, Kamesh, Kedaresh, Raviraj, Nitin, Suchi, Aarti, Neha, Prasoon, Romila, Gaurav and others who made my entire stay at Purdue so memorable. Lastly, I would like to thank my family for their love and support. My parents have always set a great example for me to follow, and they have given me every opportunity to succeed in life. I cannot thank them enough for that. My father has always

been my source of inspiration and motivated me to pursue my dreams; he has taught me the value of hard work and discipline. No word could do the justice to explain the continuous support and sacrifice of my mother. She has been the pillar of strength and perseverance in my life. I could not have achieved what I have because of her. I am extremely thankful to my in-laws for their support and blessings. Most importantly, I would like to thank my wife Susmita. She has been a constant and never ending source of love, support, encouragement and inspiration throughout my time at Purdue University. I cannot imagine completing this dissertation without her. The journey of graduate school is one of most memorable part of my life and I feel lucky to experience it with her.

TABLE OF CONTENTS

Page

LIST OF TABLES

Table Page

LIST OF FIGURES

Figure Page

Figure Page

Figure Page

Figure Page

Figure Page

Figure Page

Figure Page

Figure Page

Appendix Figure

LIST OF SYMBOLS

D: Injector outer wall diameter.

E (k): Turbulent Kinetic Energy

J: Jet to Crossflow Momemtum Flux Ratio

H_2: Hydrogen

Ma: Mach Number

MW: Megawatt

N_2: Nitrogen

NG: Natural Gas

Re: Reynolds Number

S: Jet to Crossflow Density Ratio

St_{wake}: Wake Strouhal Number

T: Temperature

U': Fluctuating component of Velocity

V_x: X-Component of Velocity

V_x: X-Component of Velocity

V_y: Y-Component of Velocity

|V|: Velocity Magnitude

X: x-coordinate

X': Coordinate transformed x-coordinate

Y: y-coordinate

Y': Coordinate transformed y-coordinate

Z: z-coordinate

a: Temporal coefficient of POD mode

d: Injector exit diameter

f: Peak Frequency

k: Wavenumber

ms: Milli-second

p': Fluctuating component of pressure

r: Separation Distance in Velocity-Field

Subscript

CF: Crossflow

i: x, y

j: Jet

main: Main Combustion Zone

L: Longitudinal

T: Transverse

Greek Symbols

Δ**:** Gradient

Λ: Integral Length Scale

κ: Flame Stretch Rate

μs: Micro-second

ω_Z: Out-of-plane Vorticity

Φ: Equivalence Ratio

φ: POD Mode

ρ: Density

Acronym

ACSCS: Accelerating Crossflow Staged Combustion System

BBB: Bluff-Body Burner

CO_2: Carbon dioxide

CVP: Counter-rotating Vortex Pair

HRR: High-Repetition-Rate

JICF : Jet in Crossflow

LBO: Lean Blow-Out

LSB: Low Swirl Burner

LSL: Lower Shear Layer

MCZ: Main Combustion Zone

NO_x: Nitrous Oxide

NR: Non-Reacting

OH-PLIF: OH Planar Laser Induced Flourescence

PIV: Particle Image Velocimetry

POD: Proper Orthogonal Decomposition

R: Reacting

RR: Recirculation Region

RJICF: Reacting Jet in Crossflow

SCS: Staged Combustion System

SCZ: Secondary Combustion Zone

SLV: Shear Layer Vortices

TIT: Turbine Inlet Temperature

USL: Upper Shear Layer

WV: Wake Vortices

ABSTRACT

Panda, Pratikash P. Ph.D., Purdue University, December 2015. Structure and Dynamics of a Reacting Jet Injected into a Vitiated Crossflow in a Staged Combustion System.
Major Professor: Robert P. Lucht, School of Mechanical Engineering

Secondary injection of the fuel, also referred to as staged combustion, is being studied by gas turbine manufacturers as a means of increasing the power output of the gas turbine systems with minimal contribution to NO_x emission. A reacting jet issuing into a high pressure vitiated cross flow operating at gas turbine relevant conditions was investigated as a means of secondary injection. In this application rapid mixing and chemical reaction in the near field of jet injection is desirable. In this work, advanced diagnostic measurements were performed on an experimental representation of such a system, with a transverse jet injection into a swirling vitiated crossflow. High repetition rate simultaneous particle image velocimetry (PIV) and OH planar laser-induced fluorescence (PLIF) were performed at five measurement planes perpendicular to the jet axis. Transverse jets composed of premixed natural gas and H_2 diluted with N_2 were injected through a tube protruding into the crossflow. The influence of the nature of vitiated crossflow, swirling or uniform, on to the reacting jets and its corresponding influence on flame stabilization mechanism was investigated. The vitiated crossflow is produced by a low swirl burner (LSB) that imparted a swirling component to the crossflow and a bluff-body burner produced a uniform vitiated crossflow. The crossflow exhibits considerable

swirl at the location of the transverse jet injection. The PIV measurements clearly demonstrate the influence of a swirling/ uniform crossflow on the jet. The jet-to-crossflow momentum flux ratio was varied to study the corresponding effect on the flow field. Two momentum flux ratios, J=3 and J=8 were employed to study the effect of momentum flux ratio on the stabilization of reaction fronts. The time averaged flow field shows a steady wake vortex very similar to that seen in the wake of a cylindrical bluff body which helps to stabilize the reaction zone within the wake of the jet. Jet with J = 8 had a deeper penetration into the crossflow as compared to J = 3 jet. Velocity field for a reacting/non-reacting jet in swirling crossflow exhibits higher in-plane velocity gradients as compared to jets in uniform crossflow. The vorticity field is also found to be weaker in case of jets in uniform crossflow as a result there is delay in the formation of the wake vortex structure. The HRR data acquisition also provided temporally resolved information on the transient structure of the wake flow associated with the reacting jet in crossflow. The wake Strouhal number calculation provides a better physical insight into the influence of jet velocity profile and nature of crossflow. A decrease in wake Strouhal number is noticed with an increase in nozzle separation distance. The effect of near-field heat release is also apparent from the wake Strouhal number. It is higher for a reacting jet as compared to that of a non-reacting jet owing to increase in rate of dilatation due to heat release. Based on the experimental data, it can be stated that wake vortices play a significant role in stabilizing a steady reaction zone within the near-wake region of the jet. The time averaged OH-PLIF images show a broad region of OH distribution in the wake of the jet. The measurements provided qualitative as well as quantitative information on the evolution of complex flow structures and transient events such as re-ignition, local extinction and vortex-flame

interactions in the turbulent reacting flow. There is a noticeable difference in the flame structure of a H_2/N_2 flame as compared to a premixed natural gas flame. A thin flame front in the windward side of the jet is apparent for a H_2/N_2 flame. Due to the higher propensity of strain rate induced extinctions and lower flame speeds of a natural gas flame, a stable reaction zone is seen only in the jet wake. Thus, such high-data-rate measurements provide significantly improved understanding of the complex flow-field and flame stabilization mechanisms in a turbulent reacting flow. Such data-sets are critical for the development of high fidelity turbulence-chemistry interaction models.

CHAPTER 1. INTRODUCTION

1.1 Motivation

The Intergovernmental Panel on Climate Change (IPCC) in its fifth assessment report has included multiple lines of evidence for climate change. The first tier evidences are based on careful analysis of observational records of the atmosphere, land, ocean and cryosphere systems [1]. There is incontrovertible evidence that the atmospheric concentration of greenhouse gases such as CO_2, CH_4, N_2O and H_2O have increased significantly over the last 100 years. Observations from satellites and in-situ measurements suggest reductions in glaciers, Arctic sea ice and ice sheets. The radiative heat budget, as shown in Figure 1.1, suggest a small imbalance. There are many indicators of climate change, which includes physical responses such as changes in surface temperature, changes in atmospheric water vapor, changes in precipitation, changes in severe events, changes in glaciers, changes in ocean and land ice and changes in sea level. Key indicators of global climate change also include the changing concentrations of the radiatively important greenhouse gases that are important drivers of this change [2] [3]. Figure 1.2, show the recent globally and annually averaged observed concentrations for the gases for most concern, CO_2 and these measurements are compared with the projections from the previous IPCC assessments.

The range of projections from the FAR (IPCC, 1990) [4] for CO_2 concentrations tend to be in the middle of the scenarios used for the projection.

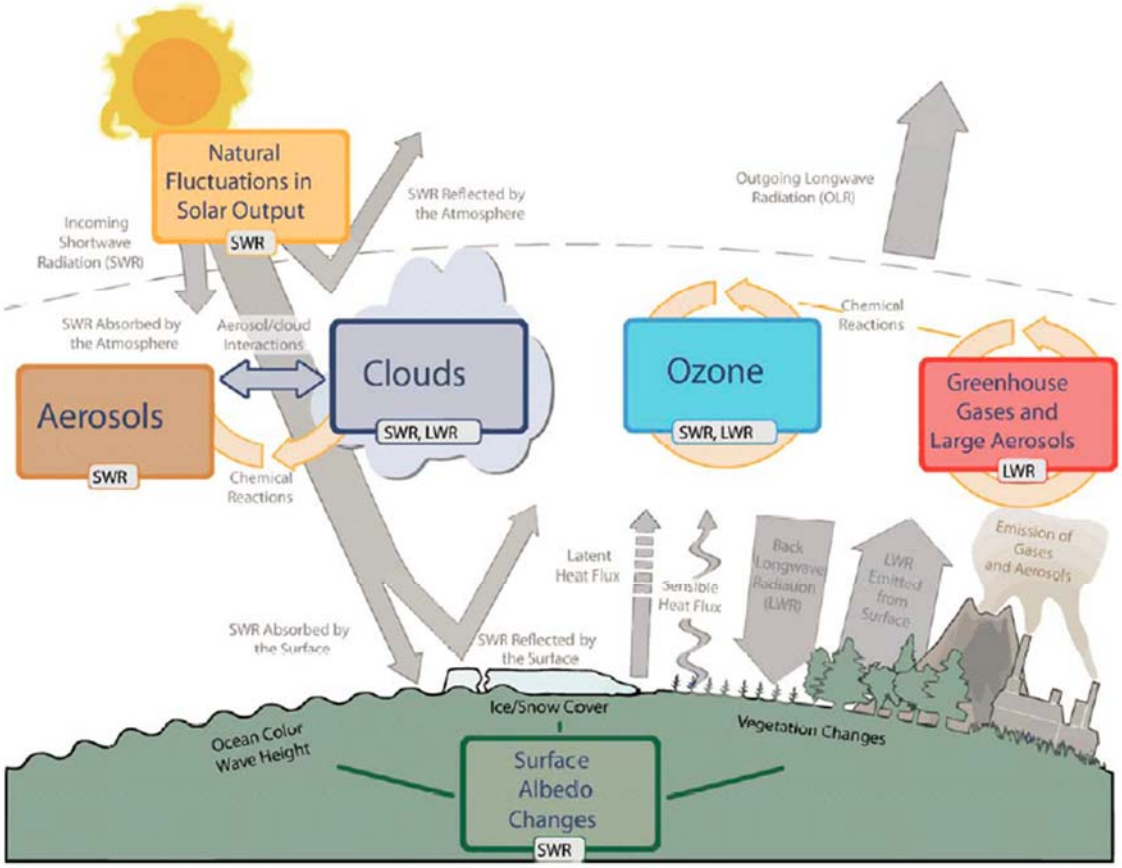

Figure 1.1. Main drivers for climate change. The radiative balance between incoming solar shortwave radiation (SWR) and outgoing longwave radiation (LWR) is influenced by global climate [1].

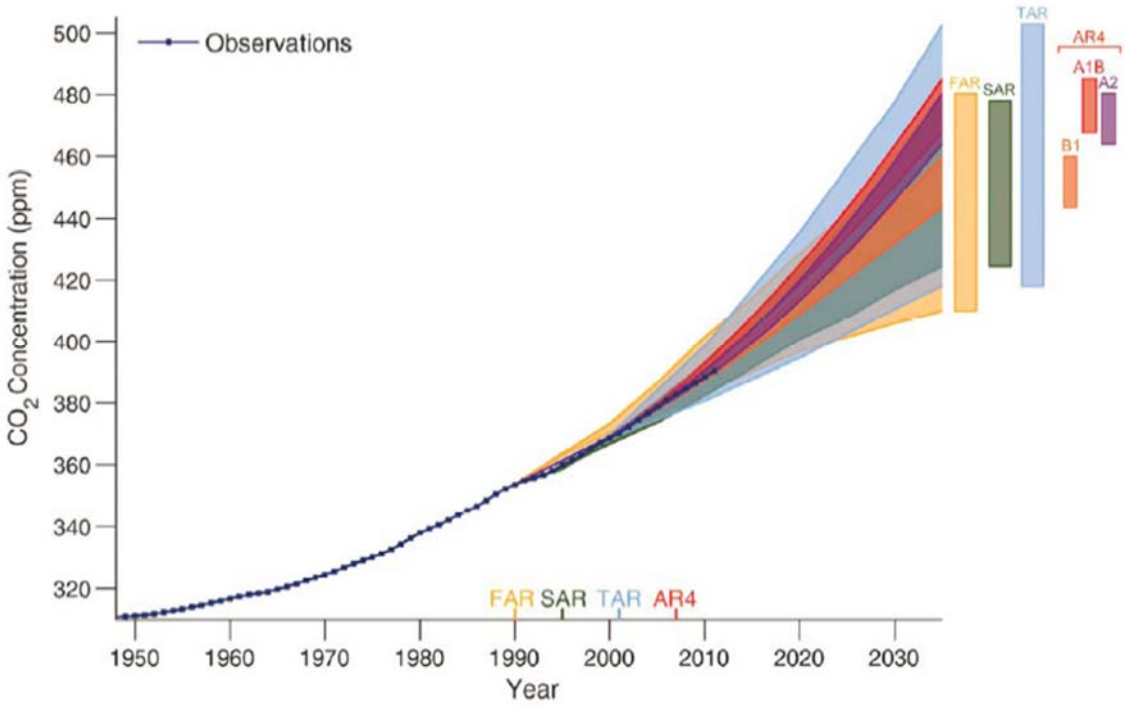

Figure 1.2. Observed globally and annually averaged CO_2 concentrations in parts per million (ppm) since 1950 compared with projections from the previous IPCC assessments [1].

Combustion of fossil fuel is still one of the major sources of producing energy. Its contribution towards increase in the atmospheric concentration of green-house gases is constantly under scrutiny. A widespread concern over reduction in the atmospheric carbon emission level has initiated extensive efforts towards use of low carbon content fuel (eg, Natural Gas), coal gasification and expansion in hydrogen combustion capabilities [5] . In recent years significant progress has been made in the development of market application for hydrogen fuel use in gas turbines [6]. These applications include integrated gasification combined cycle (IGCC) and other types of process/power plants. In the recent past natural gas fueled combined-cycle power plants have become the preferred technology for electric power generation because of the low capital costs and short construction times compared

to coal or nuclear power [5]. A combined-cycle power plant typically uses the waste heat from a gas turbine to generate steam for a steam turbine [7]. New electric power plants using these combined-cycle systems can attain total efficiencies of 60% or more [8][9]. Two of the recent advanced gas turbine engines in the H-class of engines (firing temperature between 2600 F - 2900 F) by GE and Siemens are shown in Figure 1.3. The combined-cycle efficiency of GE 9HA.01 and Siemens SGT5-8000H is reported to be 61.4% and 60.75%, respectively [10] [11]. Both the engines meet the required emission norms with NO_x emissions less than 25 ppm and that for CO less than 9 ppm.

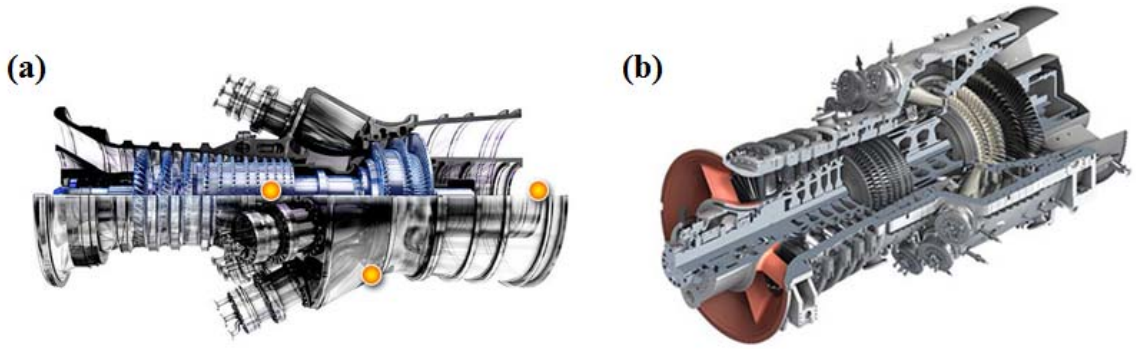

Figure 1.3. Recent advanced power generation type gas turbine engine by (a) GE 9HA.01 [10] and (b) Siemens SGT5-8000H [11] with combined cycle efficiency above 60 %.

Natural gas fueled combined-cycle power plants also have the capability of cycling electricity production to dynamically meet changes in demand. In the near future, the share of energy from natural gas will increase for a low-carbon (CO_2) future [5]. Emissions from natural-gas-fueled power generation gas turbines are regulated by environmental legislation, which places increasingly stringent limits on the emission of nitrogen oxides (NO_x) [12]. One means to achieve low NO_x emissions is to reduce peak flame temperatures, which can be attained by the premixed, lean burn approach: premixing the air and the fuel

prior to combustion and burning the globally lean mixture, downstream, in the combustor [13]. Thus, the new generation low-emission gas turbine combustors operate in fuel lean conditions to meet the increasingly stringent emission regulations. However, lean combustion is often accompanied by instability, wherein, resulting pressure pulsations can lead to catastrophic mechanical damage.

Secondary injection of the fuel, also referred to as staged combustion, has been identified as a means of increasing the power output of the gas turbine systems with minimal contribution to NO_x emission and also as a means of controlling combustion instabilities. Recent progress in the field of turbine blade materials has enabled gas turbine manufacturers to raise the turbine inlet temperatures leading to an increase in thermal efficiency of the engine [13]. One of the main motivations behind staged combustion or secondary injection of fuel is to increase the turbine inlet temperature with minimal contribution in NO_x emissions and also as a means of controlling combustion instabilities.

The work herein investigates the role of a reacting jet in crossflow as a means of secondary fuel injection. The remainder of the chapter reviews some of the most relevant literature of reacting jets in crossflow building a foundation to the rest of this dissertation. Section 1.2.1 gives a brief overview of staged combustion system technologies and their performances and emissions. Section 1.2.2 highlights the influence of key parameters such as jet momentum flux ratio, fuel reactivity, jet inlet velocity profile, etc., on the structure and dynamics of the reacting jet. Finally, stating the key objectives of this research in section 1.3.

1.2 Background

1.2.1 Staged Combustion System in Gas Turbine Applications

Staged combustion strategies were explored in NASA's Experimental Clean Combustor Program (ECCP) of the 1970s [14] [15]. During the ECCP program the low NOx potential of staged combustion systems were demonstrated in rig level research efforts on modified versions of Pratt & Whitney's JT8D and JT9D [16]. However, production engines featuring staged combustion systems were not deployed until the advent and implementation of the Full Authority Digital Electronic Control (FADEC) system. Currently, staging is widely used in modern combustors, and many different arrangements are found in practice [17]. Figure 1.4 shows two examples of staged combustors: the General Electric (GE) LM2500 [18] and the International Aero Engines V2500 [19]. Alstom's GT24/GT26 stationary gas turbine employs a reheat cycle [20], also referred to as sequential combustion, which is a form of combustion staging. In sequential combustion, an additional combustion system is placed between the high pressure and low pressure turbine [13][21]. These arrangements can delivery higher specific work and thermal efficiency at lower TIT than a conventional gas turbine combustion system [22].

In axial staging, the main combustion zone (or stage) is used on engine starting and provides the temperature rise needed to reach engine idle conditions. As the engine power increases, the function of the main combustion zone is to act as a pilot providing the heat needed to initiate rapid combustion of the fuel supplied to the second stage [23]. The vitiated pilot gases also ensure high combustion efficiency (low CO and UHC) even at low overall equivalence ratios. In conventional combustors, the flame temperature exceeds the TIT which results in additional NOx formation without an increase in efficiency [8]. The

axial staged arrangement allows for the combustion temperature, and NOx formation, to remain low for most of the combustor. The additional fuel in the secondary zone rapidly raises the combustion gas temperature to the desired TIT: increasing the thermal efficiency while minimizing NOx formation. The reductions in NOx can be attributed to the overall decrease in the residence time at high temperature and a reduction in oxygen content [23]. Staging can also improve turn-down and combustion dynamics of the gas turbine. Stationary gas turbines, being connected to a synchronous generator, are required to run at a constant rotational speed at all loads and thus the airflow must remain constant. In conventional combustion systems, reducing the fuel flow necessarily reduces the equivalence ratio, which can lead to unstable operation

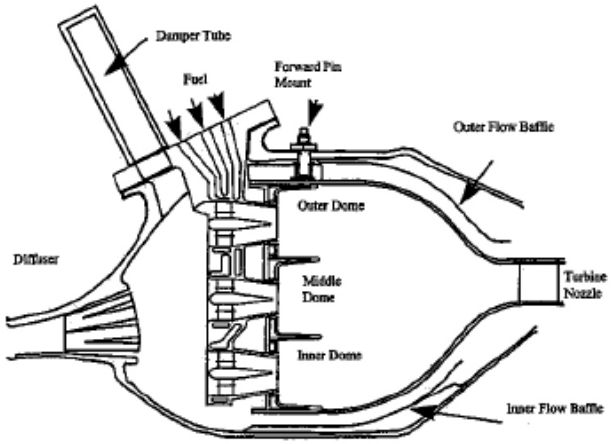

(a) GE LM2500

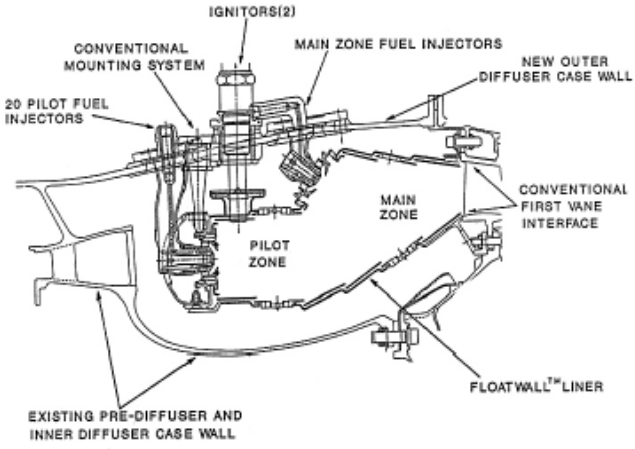

(b) IAE V2500

Figure 1.4. Cross sections of staged combustors [18][19].

and reduces the lean blow-out margin. Staging allows the secondary fuel flow to vary independently of the main or pilot stage which can operate at a stable and efficient equivalence ratio. Staging can also passively disrupt the Rayleigh mechanism of combustion instability by moving the heat release zone to a different spatial location [24]

1.2.2 Reacting Jet in Crossflow (RJICF)

Reacting jets in cross-flow is identified as an important configuration due to its widespread application, in energy and propulsion systems [25][26][27]. The flow-field associated with jet in cross-flow has superior mixing characteristics in its near field region and entrain the ambient fluid at a much faster rate as compared to jets in co-flow. It is due to this superior mixing characteristics and an interesting dynamics, jet flames in cross-flow has attracted the interest of several researchers leading to a number of practical application, viz, gas turbine combustor, industrial furnaces, flares, etc [28]. A Reacting Jet in Cross-Flow (RJICF) features a fuel jet (premixed/non-premixed) injected transversely into a vitiated/non-vitiated sub-sonic cross-flow

Non-reacting jets in cross-flow has been extensively studied experimentally [29][30][31] and computationally [32][33][34][35]. The important flow structures identified in jets in cross-flow are:

i) Counter-rotating vortex pair (CVP).

ii) Shear layer loop vortices (SLV).

iii) Horse shoe vortices.

iv) Wake vortices (WV).

The flow structure seen in the flow field of a jet in crossflow (JICF) is schematically shown in Figure 1.5. The counter-rotating vortex pair (CVP) is the dominant flow structure. It has been established that the vorticity distortion within the evolving jet shear layer and the pressure difference between the windward and leeward sides of the jet lead to an accumulation of vorticity sufficient to form the CVP downstream of the jet injection

[36][37][38][39]. The presence of this flow structure is responsible for imparting enhanced mixing in the far-field of the jet. In addition to the CVP, flow structures associated with JICF include horseshoe vortices, shear layer loop vortices and upright wake vortices. The jet momentum flux ratio is defined in Equation (1.1),

$$J = \frac{\rho_j U_j}{\rho_{CF} U_{CF}} \tag{1.1}$$

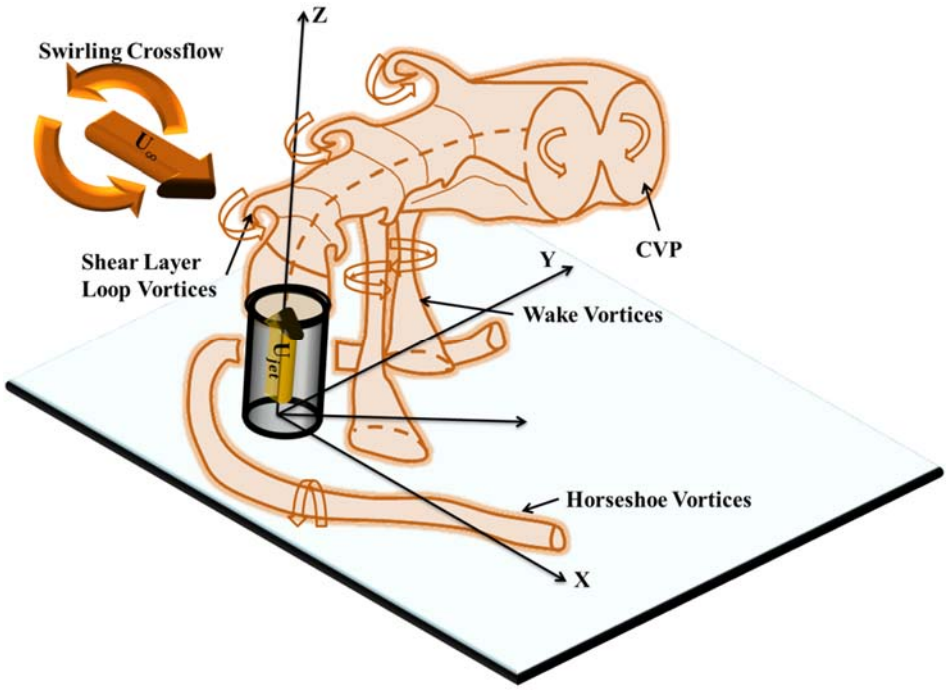

Figure 1.5. Schematic of a transverse jet, injected into a swirling crossflow through an extended injector. Crossflow velocity, U_{CF} is in the positive x-direction, the swirling motion is in the Y-Z plane and the jet velocity, U_j is in positive Z-direction [40].

Fric et al. [41][42], demonstrated the characteristics of the wake vortices by smoke visualization technique. The wake vortices appear similar to the Karman vortex street found in wake field of a cylindrical bluff body [43]. However, the source of vorticity for the wake of the JICF is fundamentally different than for a cylindrical bluff body. The

source of wake vorticity is found to be the vorticity originating from the boundary layer of the nozzle walls [44]. This vorticity is convected into the wake of the jet. In the case of the reacting jet in crossflow (RJICF), the flow encounters sharp density gradients, due to heat release. The heat release causes local volumetric expansion that leads to the generation of vorticity along the shear layer between the jet and the crossflow fluid. This vorticity is then convected into the wake of the jet. There is an additional source of vorticity generation due to sharp density gradients and dynamic pressure gradients, which is termed as baroclinic torque. Thus, the near wake region of an RJICF features three sources of vorticity, namely, vorticity originating from the boundary layer of the nozzle, vorticity originating at the shear layer due volumetric expansion, and vorticity due to baroclinic torque. It has been reported that the wake Strouhal number varies between 0.07 – 0.15 (shown in Figure 1.6), indicating similarity between the dynamics of the wake field of the transverse jet and a solid cylinder (St_{wake} = 0.2 for 2000 < Re < 100000). However, the source of vorticity in the case of the wake of the JICF is fundamentally different than for the cylindrical bluff body. The vorticity within the wake region of a transverse jet depends on several important factors. The vortex tube that is generated within the walls of the extended nozzle is tilted and stretched by the crossflow towards the lee side of the jet resulting in the formation of the upright wake vortices. In addition to this, vorticity generated at the shear layer of the crossflow and jet fluid rolls up into periodically shed vortices. These two vortex sources mainly contribute towards the vorticity within the wake region of the jet. For reacting jets in crossflow, the flow field encounters sharp temperature gradients due to the heat release as a result of fuel-air combustion. This leads to local volumetric expansion in the flow field which causes vorticity generation in these regions

of volumetric expansion. There is additional vorticity generation due to the density and dynamic pressure gradients encountered in these regions of heat release which is termed as baroclinic torque.

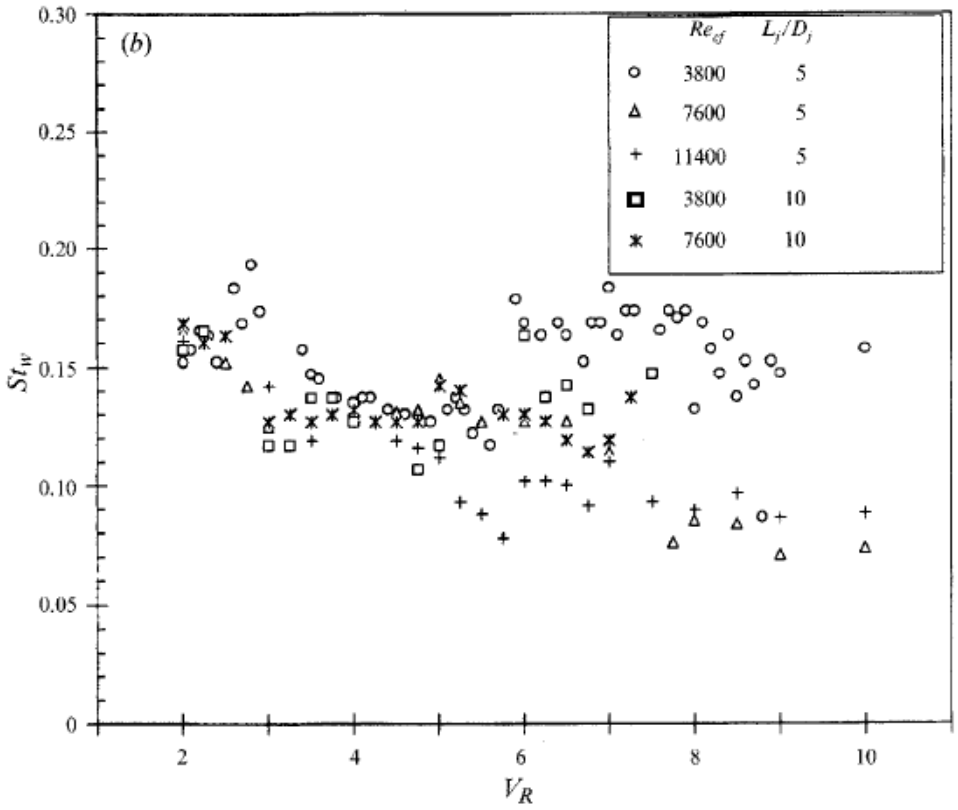

Figure 1.6. Wake Strouhal number at $Z/d_j = 0.5$ for a range of crossflow Reynolds number [41].

New et al., [45], experimentally studied the influence of jet exit velocity profile on the formation of shear layer loop vortices and flow structure in the leeward side of the jet. The authors considered a top-hat and a parabolic velocity profile. It was reported that a thicker shear layer in case of parabolic profile JICF delays the formation of shear layer vortices. Figure 1.7, shows an instantaneous snapshot of Mie scattering images comparing a parabolic and a top-hat JICF. The top-hat profile JICF is more susceptible to the

instability as a result the rate of entrainment of crossflow fluid into the wake of the jet is significantly higher in case of top-hat velocity profile JICF.

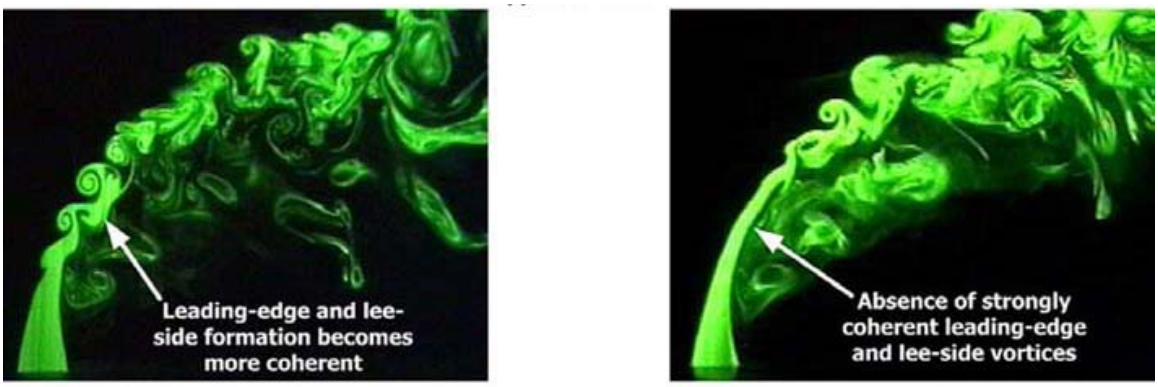

Figure 1.7. Streamwise laser cross-sections along the symmetry plane of a) top-hat and b) parabolic jets exhausting transversely into a cross-flow at J =2.3–5.8. Note that parabolic JICF display a higher resilience against initiation of large-scale leading-edge and leeside vortices along the jet shear layers than the corresponding top-hat JICF [45].

The flow-field associated with JICF has superior mixing characteristics. The JICF entrains the ambient fluid at a much faster rate than a jet in co-flow. Many early studies on RJICF focused on developing empirical models for the jet trajectory (Gollahalli and Nanjundappa 1995; Huang and Chang 1994; Bandaru and Turns 2000; [46][47][48][49][50][51]. Hasselbrink and Mungal [52][53], show the impact of jet momentum ratio in establishing a lifted/attached flame. Measurements indicate that the RJICF are shorter than the equivalent jet flames in co-flow [51]. This excellent mixing characteristic of JICF is attributed to the presence of dual mode of entrainment. Figure 1.8 indicates that in RJICF, after a critical momentum ratio the flame length reaches an asymptotic value with further increase in jet momentum ratio, [50].

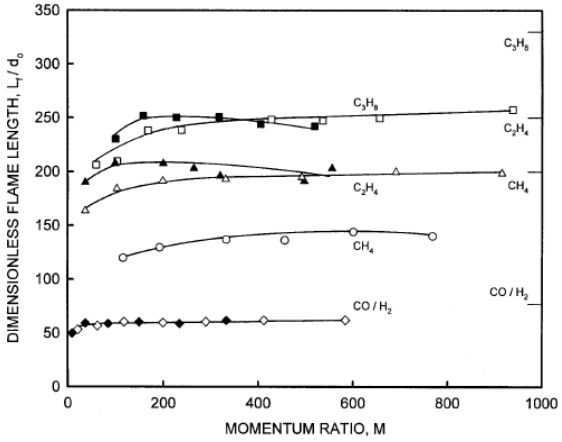

Figure 1.8. Downstream flame length as a function of momentum ratio for different fuels [50].

The jet centerline trajectory and trajectory of the mean temperature field can be predicted with some degree of accuracy from the famous Holdeman's correlations shown in Equation (1.2) and Equation (1.3) [52].

$$\frac{z}{d\sqrt{J}} = A\left(\frac{x}{d\sqrt{J}}\right)^{B} \tag{1.2}$$

$$\frac{z}{d\sqrt{J}} = 0.76(J^{0.155})\left(\frac{\rho_J}{\rho_m}\right)^{0.15}\left(\frac{x}{d\sqrt{J}}\right)^{0.27} \tag{1.3}$$

It has been shown that flame stabilization of RJICF depends on local vorticity and strain rate, jet injector geometry, cross-flow chemical composition (air or combustion gas), cross-flow temperature and fuel composition (pertaining to laminar flame speed and auto-ignition characteristics). Huang et al.,[49], have shown in an experimental study the effect of protruded tube versus flush mounted injection on flow centerline trajectory and species trajectory was studied. It is shown that, elevated injectors exit into the relatively undisturbed cross-flow and, therefore, jet penetration does not increase proportionally to

protrusion distance, due to the greater momentum present in the free stream as opposed to the boundary layer. The cross-flow boundary layer thickness influences the jet trajectory because low momentum fluid near the wall effectively increases the jet momentum flux ratio, with a corresponding increase in jet penetration. Similar, behavior is observed in case of species concentration as well. RJICF emanating from a protruded tube has been broadly classified into two fundamental types of flames: lifted and non-lifted [49]. Lifted flames occur when the momentum flux ratio is sufficiently high that the flame is lifted-off and stabilized away from injector mouth. In two different experimental studies [52], [46], results indicate that when the flame was ignited below some critical cross-flow velocity, and then increasing the jet velocity would result in flame lift-off. However, in the case where J is sufficiently low to have a non-lifted/attached flame five different characteristic flow modes for the flame is observed. Depending on the momentum flux ratio, J: a) a mode in which the flame experiences down-wash downstream of the pipe, for $J < 0.1$, b) a mode in which the cross-flow dominates flame behavior, flashing ($0.1 < J < 1.6$), c) a transitional regime, developing ($1.6 < J < 3.0$), d) a jet-dominated regime, e) dual ($3.0 < J < 10$),and f) a strong jet regime, flickering ($J > 10$) .The streamlines, vorticity distributions, and flame appearance all vary significantly in these different modes.

A recent DNS study of an auto-igniting hydrogen jet injected into a high temperature crossflow shows that the mean velocity field preserves the most dominant flow feature of JICF, the counter rotating vortex pair (CVP) [54]. In another DNS-based study of a reacting JICF configuration, it was found that the flame stabilizes in a low velocity region between the large vortices of the CVP, where the mixture is near stoichiometric [55][56]. Kolla et al, [55] in a DNS study discussed flame stabilization mechanism for an

preheated (420 K) hydrogen-nitrogen jet issuing from a square flush mounted injector into an 750 K cross-flow with J = 11.5. A top-hat jet velocity profile was assumed for the simulation. It was seen that despite pre-heating the transverse jet flame stabilizes in a lifted region on the leeward side of the jet approximately 4d from the wall. The lack of flame stabilization in the windward side of the jet shows that the local strain rates induced by the shear layer vortices exceed the critical limit. This region with flame stabilization corresponded to a lower velocity recirculation zone with relatively low scalar dissipation rate and a point where the mixture was near stoichiometric as shown in Figure 1.9.

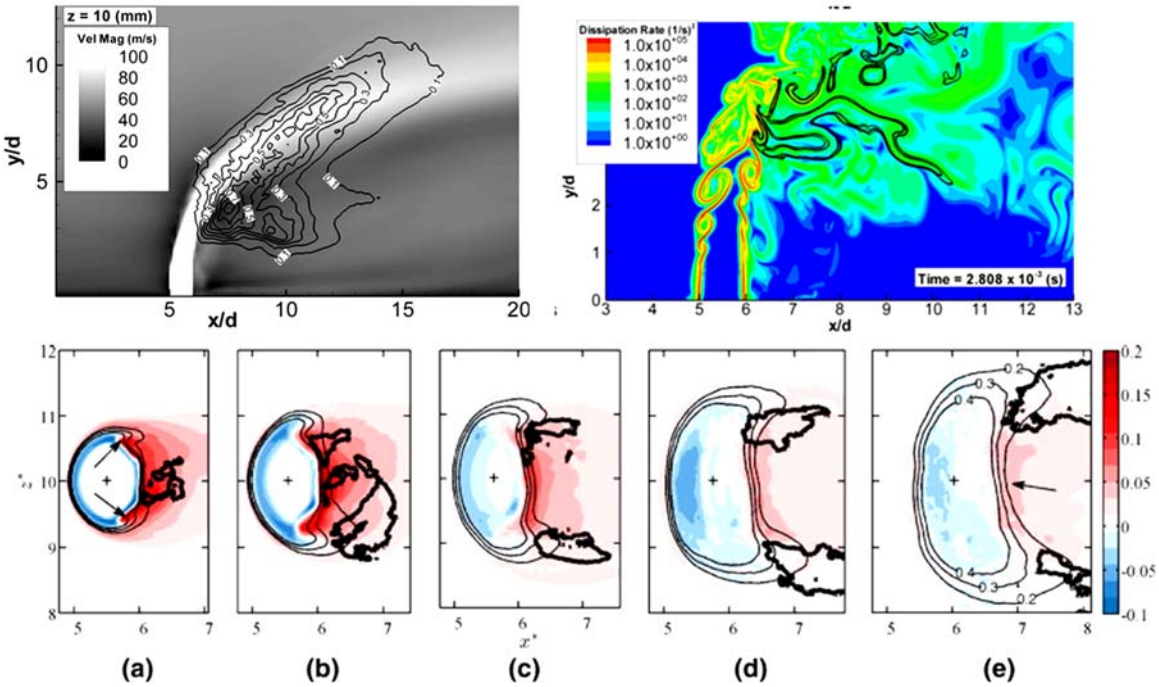

Figure 1.9. RANS averaged velocity field and normalized heat released rate (left) and instantaneous scalar dissipation rate and heat release rate (right) [55].

Furthermore Grout et al. [44] showed intermittent appearance of flamelets in the highly strained shear layer regions of the jet. It was suggested that the shear layer loop vortices play the role of intense fuel/air mixing, whereas the wake vortices modulate the

heat release rate. Distributed pockets of heat release were observed which is attributed to chemical reactions as soon as the magnitude of velocity drops. The only region where reaction occurred along the windward side of the jet was far downstream location where the jet has already assumed the direction of the crossflow. In an LES based numerical study on a swirling jet injected into an isothermal crossflow the swirl number is seen to influence the CVP, in turn affecting the local vorticity and mean strain rate [57]. It is observed that for higher swirl numbers, the CVP is inclined with respect to the mean crossflow streamlines, indicating a strong influence of the swirling motion. Because of the enhanced mixing efficiency that the CVP provides to a JICF, most of these studies have focused on the role of CVP in flame stabilization in the far downstream.

In the past decade PIV has evolved as one of the preeminent techniques to measure velocities in complex fluid systems, viz., high Mach number flow, boundary layer flow, reacting flow, etc., and has helped researchers develop a deeper insight into turbulence and fluid dynamics [58][59][60]. With the commercial advent of high-repetition-rate (HRR) laser systems, it is now possible to perform non-intrusive temporally and spatially resolved measurements in reacting flows [61][62][63][64]. Boxx et al., [65], were one of the first to implement high repetition rate advanced laser diagnostics techniques to study a high pressure combustor. The ability of these techniques to track extremely transient events occurring in turbulent flames has contributed significantly to enhancing our understanding the underlying physics of flow-flame interaction [66][67]. In an experimental study PIV measurements performed on a RJICF indicates that the flame centerline penetrate slightly further into the cross-flow as compared to an isothermal jet [53]. It is also observed that although heat release rate alters the instantaneous velocity field, the reacting jet trajectory

followed the trajectory of a non-reacting jet rather closely. Instantaneous snapshots of showing the jet flame structure and the seeded flow field is shown in Figure 1.10

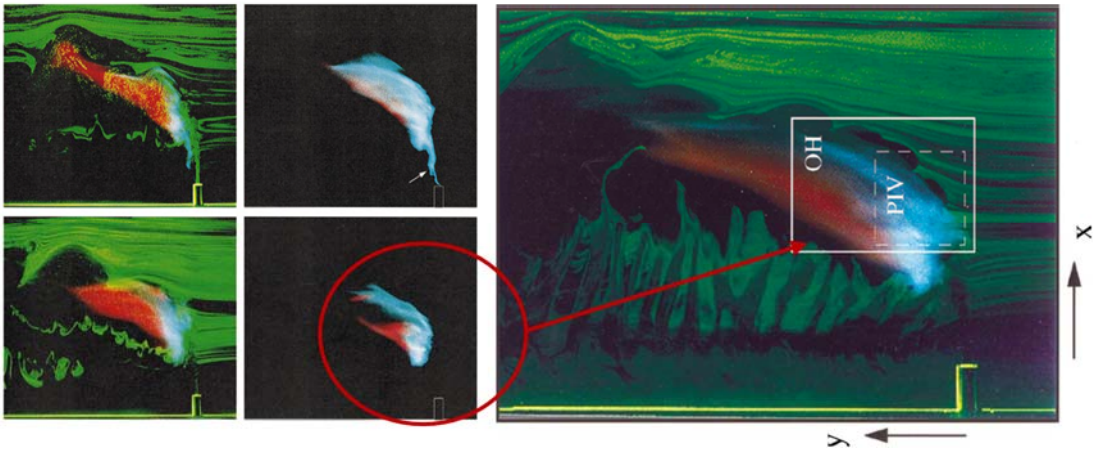

Figure 1.10. i) Showing the side view of the flow and flame patterns in the plane of symmetry for non-lifted/attached flames, ii) side view of the flow and flame patterns in the plane of symmetry as observed for lifted flames [53].

More recently, reacting jets in high temperature/ vitiated crossflow have been investigated as a means of understanding the flow physics for its potential application in a staged combustion system. Some of these recent experimental studies on RJICF reported in the literature have focused on understanding the associated flow field, flame structure and emission characteristics [68][69][70][71].

Micka et.al.,[72] in their experimental study have demonstrated the role of auto-ignition in flame stabilization in a reacting jet in high temperature and high velocity crossflow. They proposed three-region flame structure where region is dominated by auto-ignition. It is proposed that the initial flame kernel appears as a result of auto-ignition that supports a secondary region of the flame which is characterized as a premixed flame. The remainder of the fuel is burnt in a non-premixed mode of combustion. They suggest a wake dominated heat release for low J values.

Sullivan et.al., [71] studied the reacting jet behavior and emissions from a high pressure staged combustion system. They operating pressure was 6 atm and the vitiated crossflow was at 1775 K. They observed that depending on the ignition time the reaction can occur uniformly or can originate only in the wake of the jet and then propagate along the windward side far downstream. This behavior of flame stabilization could be changed by increase in H2 to the secondary fuel. A 100 % H2 case was fully attached to the nozzle injector with flame stabilized both along the windward as well as leeward side of the jet.

Lamont et al., [73], was one of the first to report optical diagnostics and emissions measurements in a reacting jet in high pressure (5.5 atm) vitiated crossflow. The jet fluid in this study comprised of natural gas premixed with high temperature air. The research findings indicated that beneficial conditions pertaining to NO_x emissions is possible for J values in the range of 1 – 5 and for jet equivalence ration between 0.4 – 1.1. It was also seen that for J values between 5 – 20 and jet equivalence ratio between, 4 – 20 provide a temperature rise of approximately 100 K across the SCZ with a moderate in increase in NO_x levels (25 ppm). It was suggested that the NO_x levels could be further reduced to single digit levels by post treatment of exhaust gases. Dual-pump CARS techniques was implemented in this study to perform temperature and species measurements along the center plane of the reacting jet. In a follow up research by Roa et al., [74] it was discovered that for an extended injector configuration, with the injector tip protruding approximately 1.5 jet diameter into the crossflow, a high temperature region was established in the leeward side and wake of the jet. The highest standard deviation in temperature was seen in the windward and leeward side reactive shear layer, particularly around the core of the jet. Furthermore, in this research for the first time high-repetition-rate OH-PLIF and PIV

techniques were demonstrated in a high pressure staged combustion system.

During the similar time frame, Wilde et al., [75], demonstrated simultaneous stereo-PIV/OH-PLIF measurements at a repetition rate of 10 kHz in a reacting jet in an unsteady vitiated crossflow operating at atmospheric conditions. The reacting jet comprised of a mixture of H_2 diluted with N_2 and He to attain a range of jet density. The study showed the detailed flame stabilization mechanism along the jet shear layers for a wide range of J values. The measurements were made in the center plane of the reacting jet trajectory. It was found that the near field heat release depends on the momentum flux ratio (J) and the density ratio (S). For lower J values ($J < 5$) the leeward side of the jet featured a broad, diffused reaction zone and the windward side showed a thin non-premixed flame front attached to the injector. This was different for higher J values (> 20). Although there were similarities in the flame structure in the wake of the jet between lower and higher J values, the windward side of the jet showed intermittent flame lift-off for higher J values. It was also reported that the response of lower J jets to an unsteady vitiated crossflow was more significant than higher J cases. There were significant amount of jet flapping observed for lower J cases leading to higher velocity fluctuations.

Concurrently, in another study by Fugger et al., [76], similar diagnostic techniques (simultaneous PIV/OH-PLIF at 10 kHz) were implemented to study the response of a reacting jet to an unsteady crossflow operating at high pressure (9.5 atm), high temperature conditions (725 K). Two types of crossflow forcing were investigated on a H_2/N_2 reacting jet. For one of the configurations the jet was injected at a pressure node and in the second configuration jet was injected at velocity node. Pressure fluctuations, as high as 20% of the mean pressure, could be generated in the test rig. It was discovered that the jet coupled

with the crossflow oscillation leading to instantaneous variation in the momentum flux ratio and hence the jet penetration depth. It was also observed that for higher pressure oscillations (p'> 5%) the hydrodynamic instabilities leading to the characteristic flow structures were suppressed.

These studies reveal that fuel jets injected into a high temperature, high pressure vitiated crossflow auto-ignites and a stable flame front can be established at regions much closer to the injector. For a stable reaction front a region with desirable flow velocity and continuous supply of reactants is needed. Based on these studies the near wake region in the leeward side of the jet provides the most favorable condition to establish a stable reaction zone. Thus, it is of utmost importance to understand the flame stabilization dynamics in the wake of the jet at engine relevant conditions. Thus, the relevance of the current research is to understand the structure and dynamics of the flow-field and the flame stabilization mechanism in the near wake region of the jet and the variation in flame structure with fuel of different reactivity. Furthermore, in a practical combustor a flush mounted injector is not a desirable configuration, in order to, avoid any reaction zone closer to the combustor wall. Thus, the main focus of this study will be investigation of flow-flame interaction in the wake of a reacting jet with an extended injector configuration.

1.3 Objectives

The primary objective of the current dissertation is to investigate the structure and dynamics of the flow-field and the flame stabilization mechanism in the near wake region of a reacting jet into a subsonic vitiated crossflow at engine relevant conditions. Following are the specific objectives of this work:

1. To investigate the structure and dynamics of the flow-field of non-reacting/reacting JICF into a swirling vitiated crossflow. High-data-rate particle image velocimetry (PIV) is used to characterize the wake of the reacting jets.
2. To investigate the structure and dynamics of the flow-field of non-reacting/reacting JICF into a uniform vitiated crossflow. High-data-rate particle image velocimetry (PIV) is used to characterize the flow-field. Also to compare and contrast the reacting jet response to the nature of crossflow (swirling/uniform) conditions.
3. Investigation of flame stabilization mechanism in the wake of the reaction jet and to understand the flow-flame interaction. High-repetition-rate simultaneous PIV/ OH-PLIF measurements are used to understand the flame stabilization mechanism.
4. Design and development of an accelerating crossflow staged combustion system to study the dynamics of reacting jets injected at higher flow Ma number.

Thus, it is intended to study the response of a reacting jet to three types of crossflow conditions, as shown in Figure 1.11, i) Swirling vitiated crossflow, ii) Uniform vitiated crossflow and iii) accelerating vitiated crossflow.

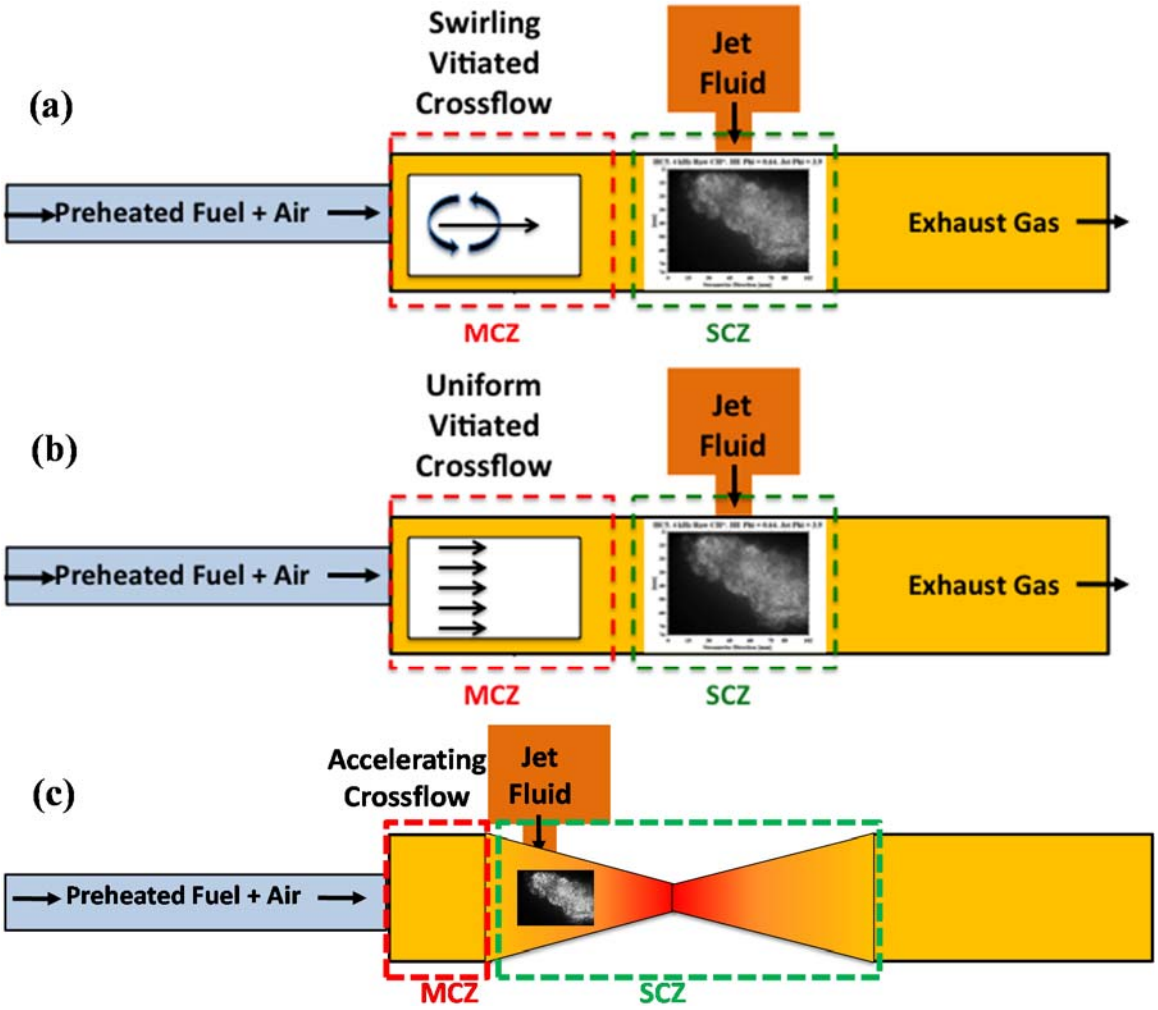

Figure 1.11. Configurations to study the influence of reacting jets to a (a) swirling vitiated crossflow, (b) uniform vitiated crossflow and (c) accelerating vitiated crossflow.

1.4 Scope of the Dissertation

The scope of this dissertation is organized around the objectives defined in section 1.3. In Chapter 2 the details of the experimental test system and associated facility will be discussed. A brief discussion on experimental operating conditions and data acquisition system will be presented. Finally, the details of the advanced laser diagnostic techniques employed in this study will be discussed.

The focus of Chapter 3 will be high-repetition-rate PIV measurements to characterize the velocity field of swirling crossflow and non-reacting/reacting jets in swirling crossflow. Multi-plane velocity measurements showing the three-dimensional structure of the flow-field will be discussed. The difference in the velocity field of a premixed NG reacting and that of a H_2/N_2 jet will be shown. Considerations on the turbulence and flow dynamics of the reacting jets will also be presented. Finally, the chapter will conclude showing the influence of jet velocity profile (parabolic and top-hat) on the flow dynamics.

The structure of Chapter 4 is along the similar lines as Chapter 3. Here, the influence of a uniform crossflow on a non-reacting/ reacting JICF will be discussed. It will be shown that there is a delay in the formation of wake vortex structures in reacting jets in uniform crossflow. The out of plane vorticity field is also significantly lower as compared to the jets in swirling crossflow.

In Chapter 5 details of flame stabilization mechanism in the wake of the reacting jets will be discussed. Simultaneous PIV/OH-PLIF measurements are performed to study the flow-flame interaction in the wake of the jet. The difference in the flame structure of a premixed NG jet and that of a non-premixed H_2 jet will be also be discussed.

Chapter 6 concludes summarizing the key findings from the current research and proposing recommendations for future work. A brief discussion on the design details of the new accelerating crossflow staged combustion test rig will be presented

CHAPTER 2. EXPERIMENTAL SYSTEM AND LASER DIAGNOSTICS

2.1 Experimental Test Hardware

The experimental facility was designed for high temperature and high pressure combustion based experimental studies. The design of the facility is modular as a result; it can be adopted suitably for different types of industrial gas turbine burners. For the current study the experimental text facility was adopted to include a staged combustion system. The design and development of the test facility was done previously [73]. The experimental test rig features a main combustion zone (MCZ) and a secondary combustion zone (SCZ). The schematic of the staged combustion test rig is shown in Figure 2.1. The experimental test rig is a scaled down version of an industrial staged combustion system, simulating the pressure, temperature and vitiated gas composition. The design residence times for the MCZ and SCZ are 7.5 ms and 5.0 ms, respectively. Comparatively, the typical residence time for a 150 MW gas turbine can combustor is around 20 ms [21]. The actual residence time realized for any given test is a function of the mass flow rate, combustion temperature and pressure.

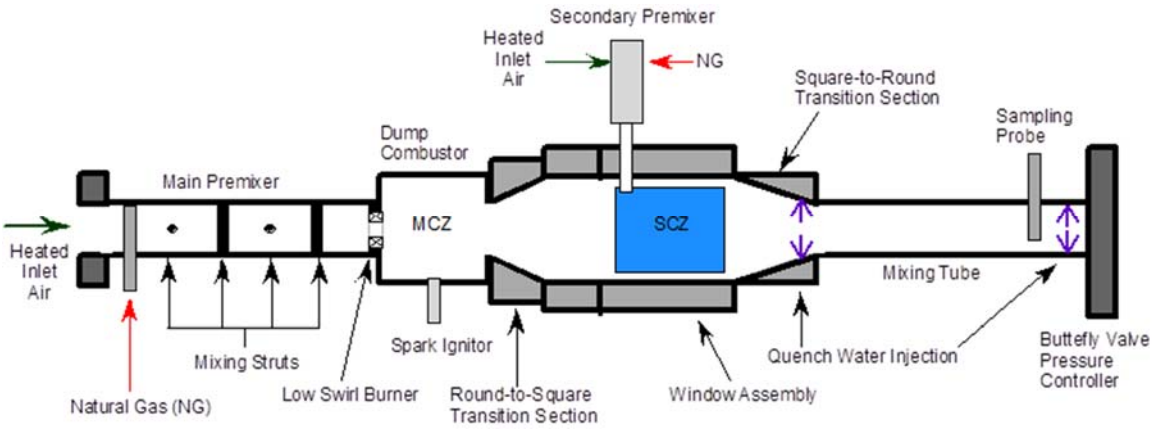

Figure 2.1. Schematic diagram of the staged combustion system test rig indicating the MCZ and optically accessible SCZ.

The experimental test rig is shown in more detail in Figure 2.2 and Figure 2.3. The section upstream to the MCZ is the premixing section. Heated air at 725 K enters the section where it is premixed with the main fuel (NG gas). The fuel is injected into the premixing section through a fuel peg, as shown in Figure 2.4. A series of bluff bodies installed in the premixing section generated sufficient amount of turbulence to enhance fuel-air premixing. The MCZ features a low-swirl burner (LSB) fueled with premixed natural gas and air. The low-swirl burner, as shown in Figure 2.5, is similar to that reported in the literature [77]. The MCZ was operated at a pressure of 5.5 bar, an air inlet temperature of 725 K, an equivalence ratio of 0.5, and mass flow rate of 0.39 kg/s. There is a round-to-square cross section transition downstream of the MCZ. The SCZ is contained in a square-cross section assembly with optical access, as shown schematically in Figure 2.6. The fuel jet is injected transversely into the SCZ, mixes with the in-coming crossflow and auto-ignites. The fuel is injected from a straight nozzle with an D of 15.3 mm and d_{JET} of 10 mm. The nozzle extends 15 mm into the vitiated flow stream, as shown in Figure 2.6. The SCZ window assembly provides optical access from three sides; one window port

is used for the fuel injection into the SCZ. Each window port features a two-window configuration, a thin inner window to contain the flame gases and a thick outer window to contain the pressure. The pressure is controlled within the test section with a butterfly valve at the exit of the test rig. The cavity between the inner and outer window is pressurized by extracting a fraction of the inlet air from upstream of the main fuel injection and redirecting it into the cavity. This is done to try to match the 5.5 bar combustion pressure within the window combustor, but because of the pressure drop in the premixing section the pressure in the cavity is slightly higher than that in the combustor. The inner windows provide an optical viewing area of 98 mm x 73 mm. The window assembly has a square cross-section with dimensions of 107 mm x 107 mm. The reacting jet fluid in our study was composed of two types of fuel, i) H_2 diluted with N_2 and ii) premixed natural gas. The two fluids were mixed together in a plenum before being introduced into the combustor.

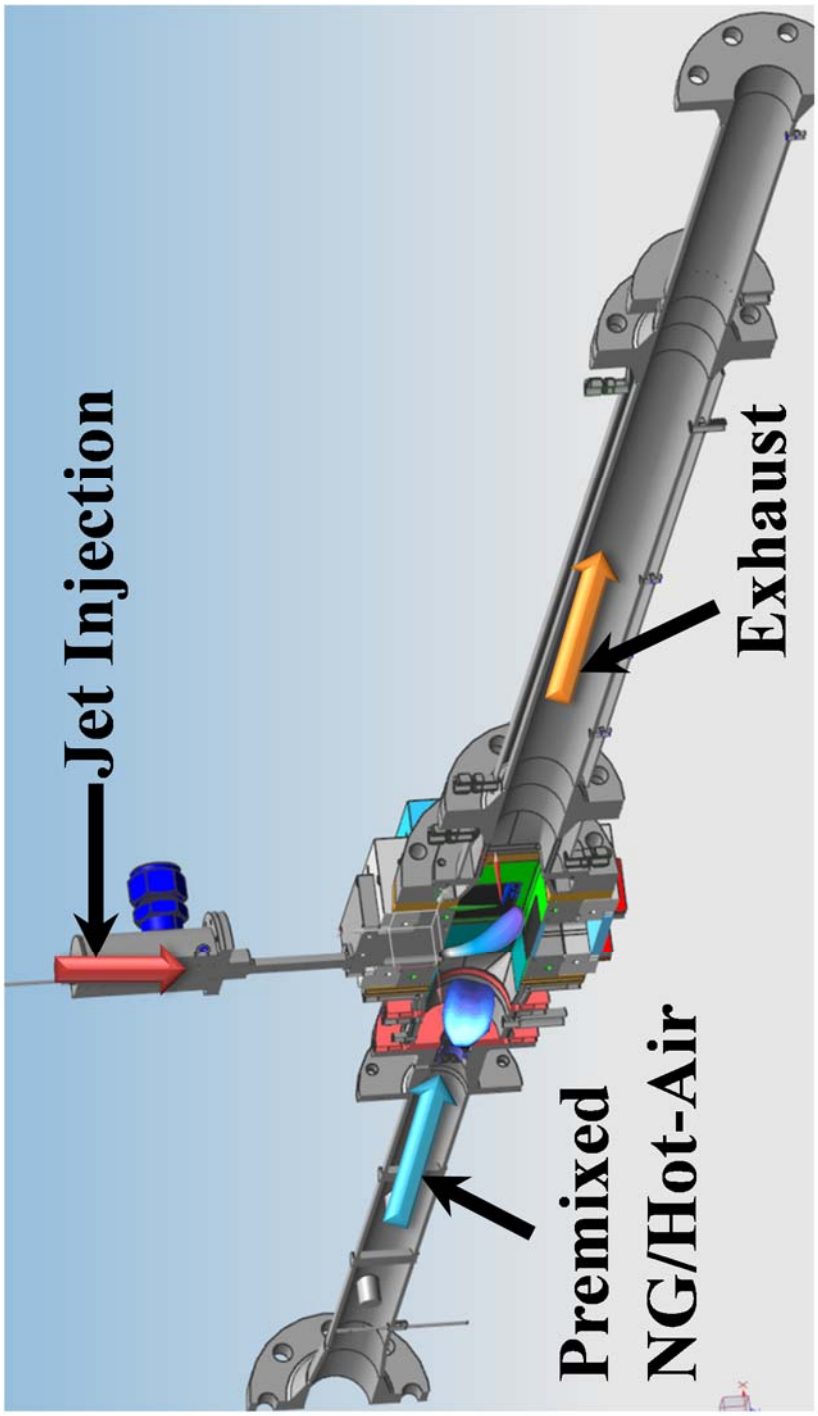

Figure 2.2. CAD representation of the staged combustion test rig.

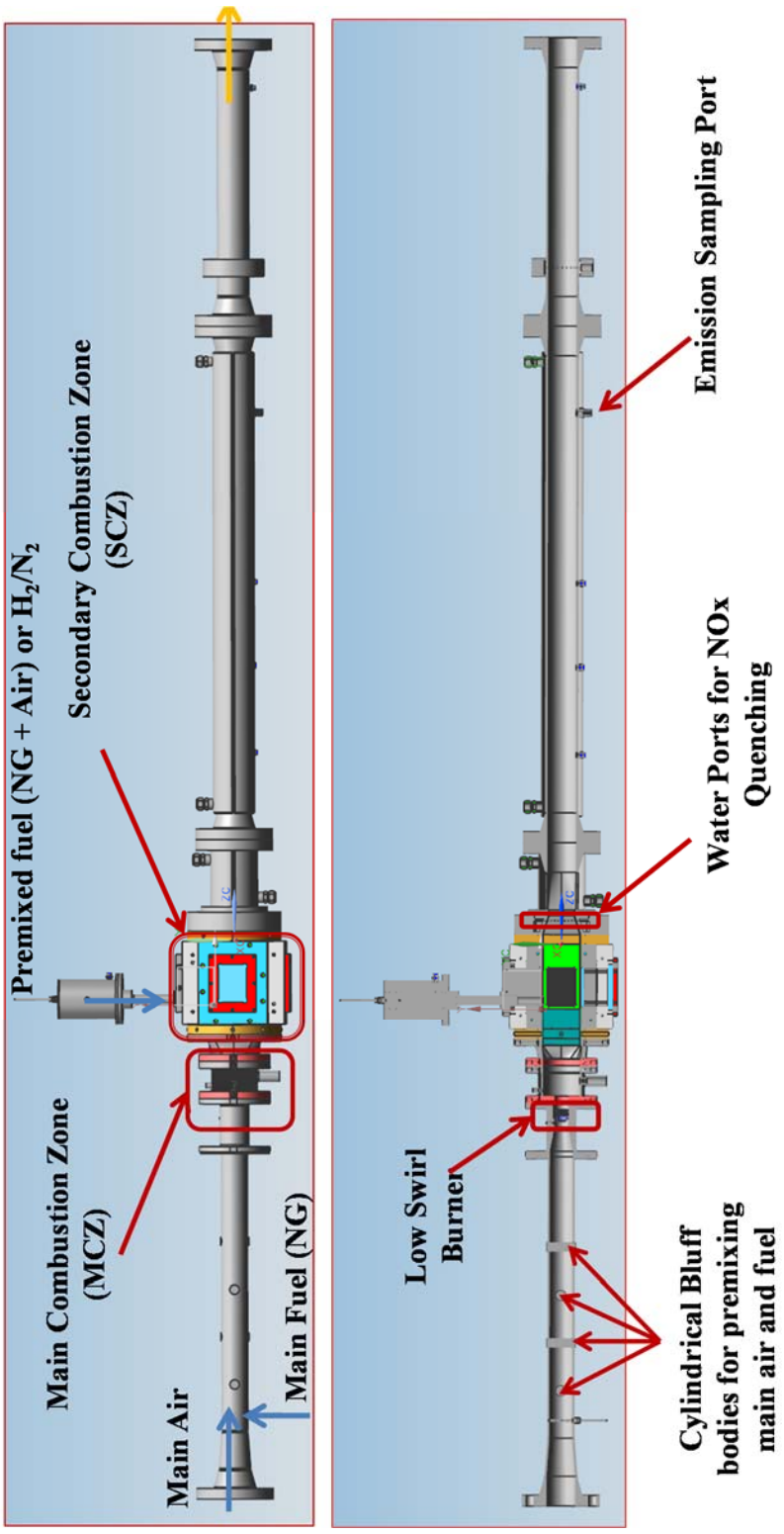

Figure 2.3. Staged combustion system test rig indicating key sections of the MCZ .and optically accessible SCZ.

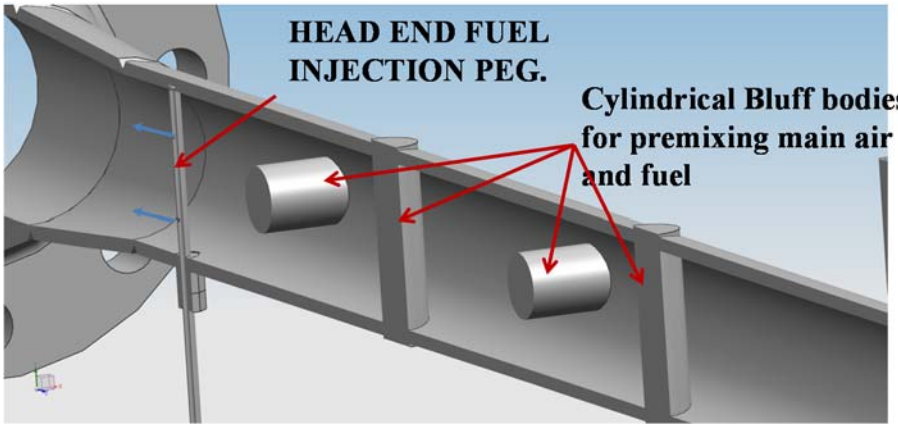

Figure 2.4. Schematic of the premixer showing main fuel injection system and the cylindrical bluff bodies for premixing main air and fuel.

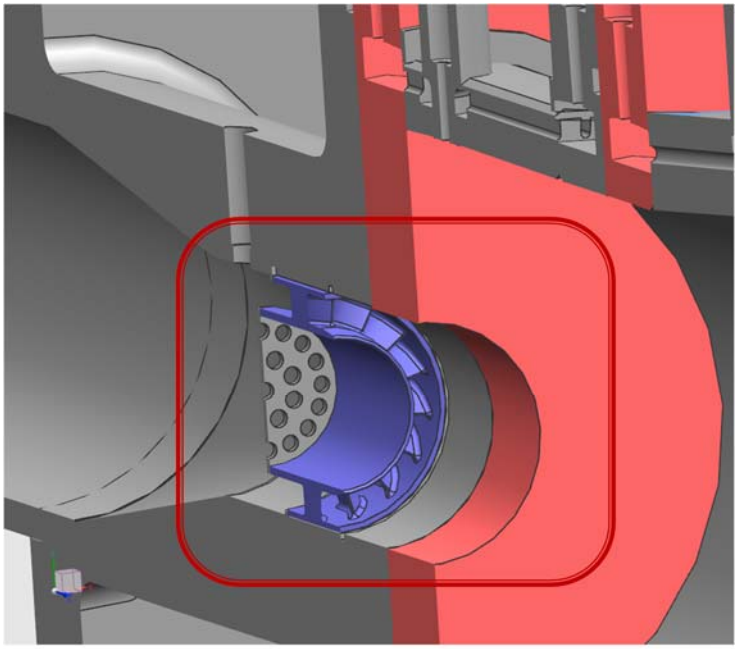

Figure 2.5. Schematic of the Low-Swirl Burner (LSB) vitiator.

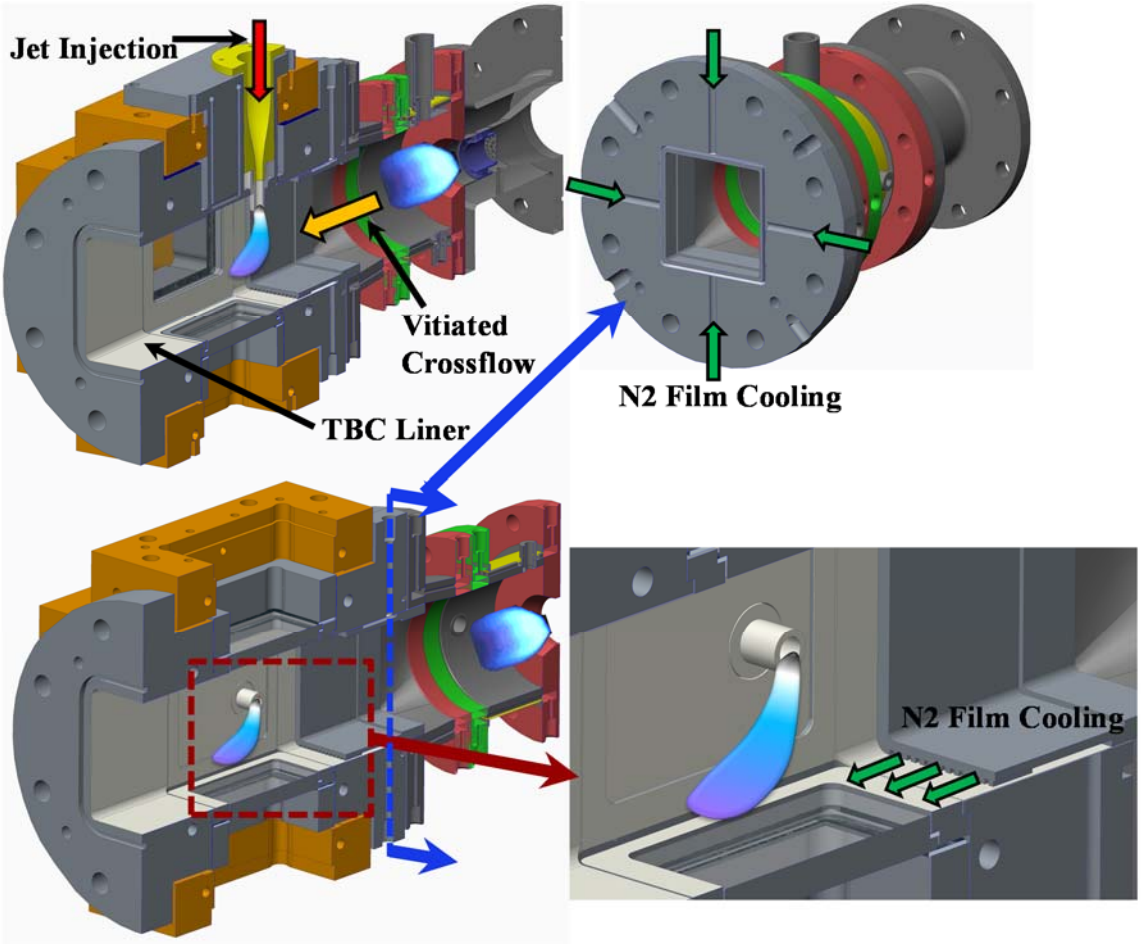

Figure 2.6. Schematic of the MCZ and SCZ showing the N_2 film cooling manifold.

2.1.1 Bluff-Body Burner

The current study includes investigation of reacting jet response to swirling vitiated crossflow and uniform vitiated crossflow. So, for the uniform vitiated crossflow conditions MCZ features a bluff-body burner (BBB) fueled with premixed natural gas and air. The bluff-body burner is designed to provide a radial velocity component into the dump plane to create a recirculation region. Figure 2.7, shows the staged combustion system test rig featuring the bluff-body burner in the MCZ. Two-dimensional axisymmetric CFD simulations are carried out varying the angle of the bluff-body. Figure 2.8, shows, the x-

component of velocity field showing the length of the recirculation region for bluff-body angles of 45, 35 and 30 degrees. The simulations show that the recirculation region for bluff-body with 35 degrees inclination has a recirculation region fully within the dump combustor. The lean blow-out (LBO) limit for the MCZ with bluff-body burner was typically between the equivalence ratios of 0.5 and 0.51. Thus, the MCZ was operated at an equivalence ratio that was slightly above this limit and that allowed for stable operation ($\phi \sim 0{:}53$). At this equivalence ratio, the adiabatic flame temperature is 1844 K.

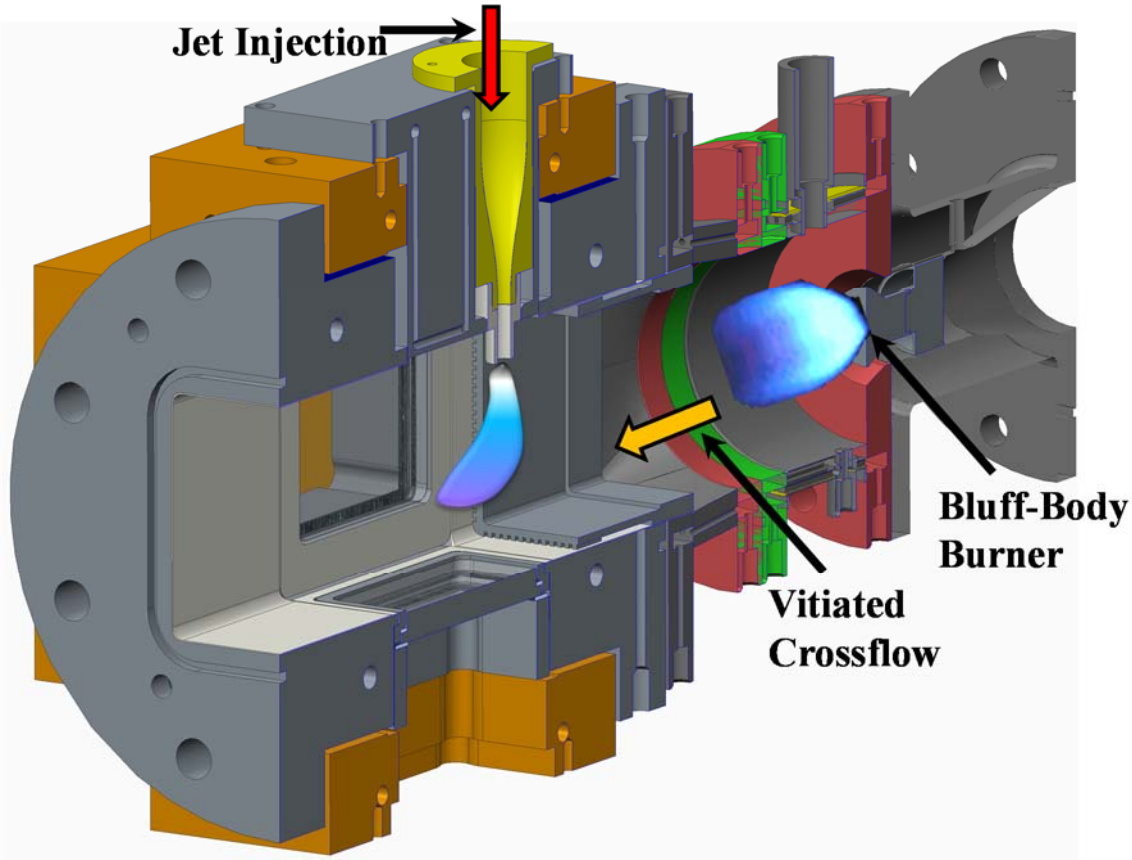

Figure 2.7. Schematic of the MCZ and SCZ showing the bluff-body burner for a uniform vitiated crossflow.

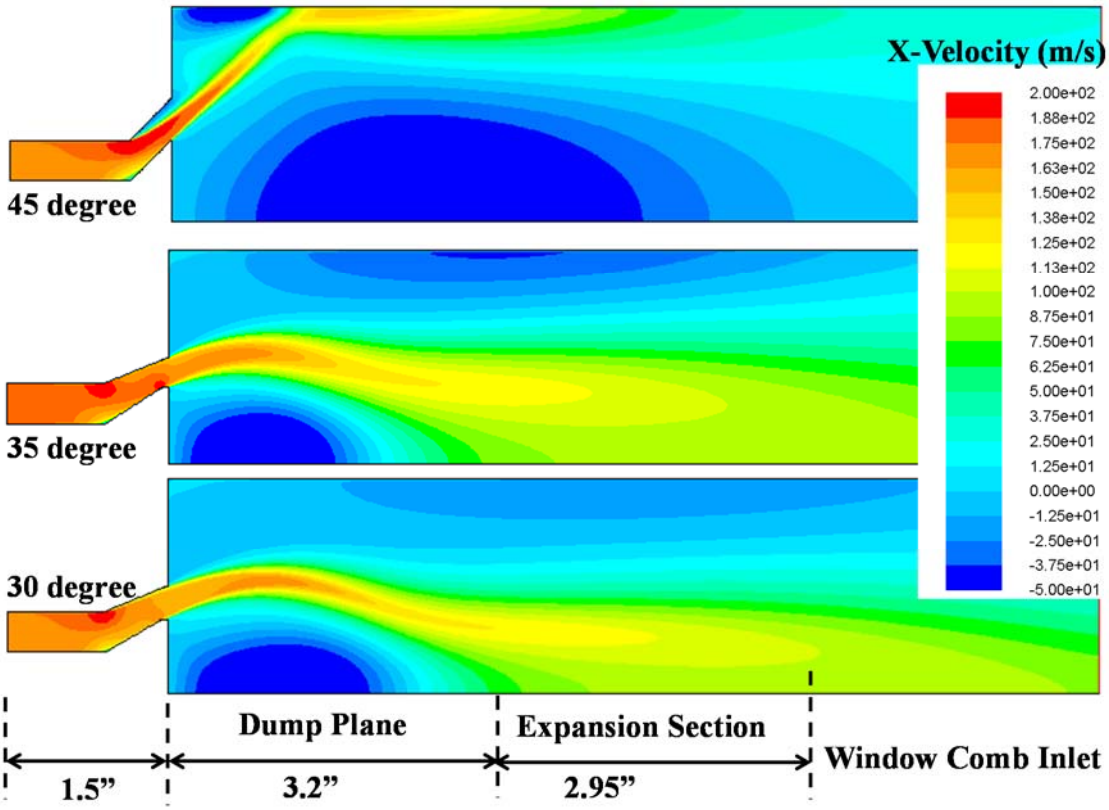

Figure 2.8. Non-reacting CFD solutions for the bluff body angle of 30, 35 and 45 degrees, showing the extent of the recirculation region. The dimensions indicate the axial length of the MCZ, the transition section and the SCZ.

2.2 Instrumentation and Control

Significant potential energy is contained within an experiment operating at high pressures. All testing operations are contained in an isolated test cell and controlled from a remote location. A National Instruments (NI) LabView Virtual Instrument (.vi) was developed for live control of the experiment and data acquisition (this system runs at 100 Hz). The LabView program also serves as a live redline monitoring system, with automatic abort operations programmed for emergencies such as a drop in cooling water flow rate or a spike in the temperature upstream of the burner (indicating a flashback). Experiment set-points, such as equivalence ratio, are calculated in real time for live tuning of experimental

conditions. All data and control channels are connected through a shared architecture for the test cell. Analog input channels are patched through a series of NI SCXI chassis with signal conditioning modules for each respective channel type: i.e. amplified pressure transducers and thermocouples. An NI PCI-6052e analog to digital converter is used to read and store data through the .vi. Ninety-six channels of digital control are available through a series of NI PCI-6534 digital IO boards connected to a Grayhill solid-state relay backplanes. A series of NI PCI-6733 cards patched through NI TBX-68 connection blocks provide thirty-six channels of variable set-point control for system components such as pressure regulators and electronic valve actuators.

Sonic nozzles and cavitating venturis are used throughout the system to control and meter fluid mass flow rates. This configuration permits very accurate control of mass flow rate by controlling the upstream pressure set-point with a closed-loop feedback controlled electronic regulator (Tescom ER-3000). System pressures are measured using high-level output amplified pressure transducers (GE -Sensing UNIK). System and experiment temperatures are measured using shielded Type-K thermocouples. A snapshot of the LabView front panel is shown in Figure 2.9.

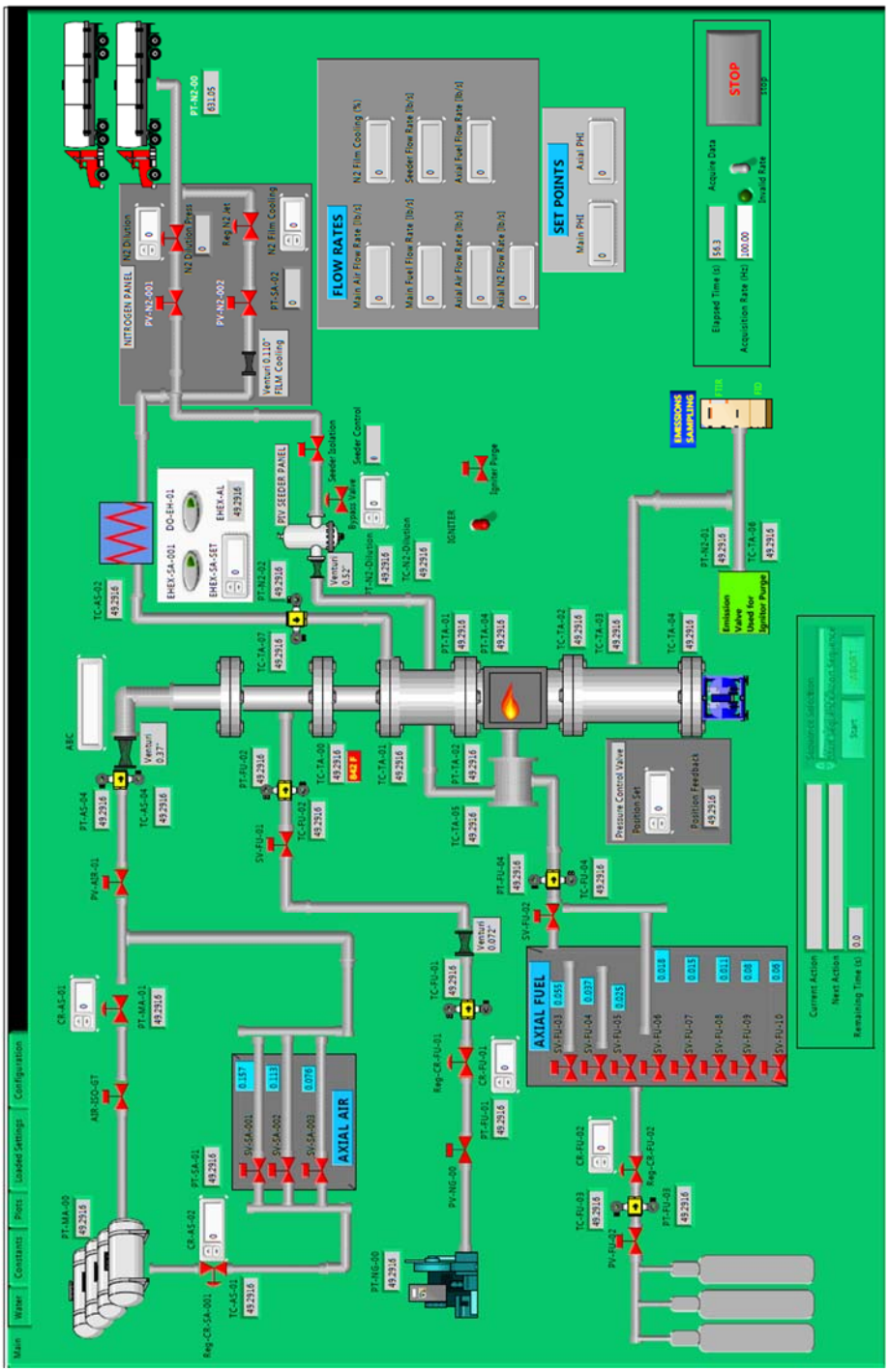

Figure 2.9. The front panel of the LabView interface used to run the experiment.

2.3 Uncertainty Analysis

The experimental uncertainty in the reported values was calculated using the second-power equation for the estimation of uncertainty given in Kline and McClintock [78]. Instrument bias error is included in addition to precision errors arising from multiple measurements and random variations [79]. Measurement uncertainties for all reported measurements are calculated for each run condition. Data was taken on steady state conditions at a repetition rate of 100 Hz. With over 10000 samples on a single condition, the precision component of total measurement uncertainty was found to be small. The nominal values of the calculated uncertainty in the temperature and pressure measurements were 0.2% and 0.04%, respectively. These contribute to an uncertainty in the measured main air mass flow rate of 1.1%. The uncertainty in the measured fuel mass flow rates are nominally 2.3%, leading to an uncertainty in the total equivalence ratio of 2.65%. The uncertainty measured in the cooling water flow rate is 4.3%.

2.4 Experimental Operating Conditions

In previous work a detailed parametric study on the staged combustion system (SCS) [73] was conducted to show the effect of jet-to-crossflow momentum flux ratio (J), nozzle exit diameter (d_{JET}) and jet equivalence ratio (ϕ_{jet}) on pollutant emissions like NO_x and CO etc. In the present study, high-repetition-rate laser diagnostic techniques are employed to compare and contrast the effects of two momentum flux ratios, J =3 and J=8, on the structure and dynamics of the reacting jet flame. With J =3 the fuel reacts closer to the nozzle exit with the reaction zone stabilized within the wake of the jet, while with J=8 the jet carrying fuel penetrates deeper into the crossflow and has a higher degree of mixing.

The fuel jets provide a calculated net rise in temperature of ΔT across the SCZ. The MCZ operating condition is shown in Table 2.1 for all the experimental study.

Table 2.1. Test operating condition of the MCZ.

Cross Flow Operating Condition	
Operating Pressure (atm)	5.5
Operating Temperature (K)	723/760
MCZ Air Flow Rate (kg/s)	0.39
MCZ Equivalence Ratio, ϕ_{main}	0.5/0.53
Main Flow Reynolds Number(NR), Re_{main}	105000
Main Flow Reynolds Number(R), Re_{main}	61000

2.5 Advanced Laser Diagnostics

Laser-based measurement techniques provide the only non-intrusive means of collecting quantitative data in a turbulent reacting flow-field. For obvious reasons, the application of these techniques is quite challenging under the flame conditions seen in most modern combustors. The first requirement, maintaining optical access, requires extensive design efforts to ensure that the windows will withstand the extremely high temperatures and pressures, which can be greater than 2000 K and 50 bar, respectively. Only a select few research groups in the world have achieved these testing capabilities and the availability of the data produced remains quite limited. This is due to the high cost associated with large-scale experiments in addition to the physical challenges of performing useful measurements in such environments [80][81][82][83][84].

Particle Image Velocimetry (PIV) is a very powerful technique in which successive images of elastically scattered laser light from seed particles in a flow are used to measure the velocity field. Enclosed test sections (with windows) present challenges for this technique due to reactions and scattered light from internal surfaces. Being at the same

wavelength as the signal, it is not possible to optically filter these noise sources from the particle field. Seeding the flow in high pressure experiments is also a challenge due to geometric constraints and window contamination concerns. Field of view restrictions also limit the application of more advanced techniques such as stereoscopic PIV. In flames with high thermal power density, seeding can be very challenging as the flow will have regions of very strong local acceleration across the flame front where local heat release rate is high and the gas density changes rapidly [85].

Planar Laser Induced Fluorescence (PLIF) is a commonly applied technique used to measure the spatial distribution of a targeted species within a measurement plane. Absorption of temporally, spatially, and spectrally controlled light pumps molecules of the targeted species to an excited energy state through an allowed transition. Collisional transfer of energy broadens the structure of the excited energy state to populate neighboring levels not originally pumped by the laser light. The fluorescence signal is generated by the spontaneous decay from the excited state manifold back to a similar manifold in the ground energy state [86]. Strong intermolecular collisions can cause molecules to decay from the excited energy level back to the ground state without emission of a photon through the process of quenching. In the linear regime (see Equation (2.1)), the fluorescence signal is linearly proportional to the number density of the targeted species in the ground state (n_0^1), the rate of stimulated absorption (W_{12}), and the ratio of the rate of spontaneous emission from the excited state manifold to the ground state manifold ($A_{v'v''}$) to the total rate population decay from the excited state ($A_{v'v''} + Q_{quench}$) [87]:

$$S_f \propto n_1^0 W_{12} \left(\frac{A_{v'v''}}{A_{v'v''} + Q_{quench}} \right) \tag{2.1}$$

In high pressure flames, there are several effects that can lead to great difficulty in performing useful PLIF measurements. In theory, the number densities of the targeted species will be greater in high pressure flames, leading to increased signal levels. In practice, high number densities of absorbing particles in the flame can also lead to significant absorption and attenuation of the excitation laser sheet as it propagates through the medium [20, 56,58]. Re-absorption of the fluorescence signal as it propagates from the probe volume, through the flame, to the detection system is a well-known effect that can be more pronounced under high pressure conditions [86] [88]. Increased occurrences of collisional processes act as damping effects which broaden the frequency width of the resonance susceptibility, reducing the peak strength of the coupling between the transition and the incident laser field. This effect is captured in the W_{12} term of Equation (2.1) and causes lower signal strength [89]. It is noted that the reduced coupling strength could be beneficial in experiments where the laser sheet attenuation is strong; by pumping a weaker transition, the spatial variation in signal-to-noise ratio (SNR) in the direction of sheet propagation could be reduced.

2.5.1 OH-PLIF System

The OH PLIF system has a high repetition rate (HRR) diode-pumped, Q-switched Nd:YAG slab laser (Edgewave – IS8IIDZ) that pumps a dye laser (Sirah Credo); the frequency-doubled output of the dye laser is tuned to the strong $Q_1(8)$ transition (at 283.2 nm) of the OH $A^2\Sigma^+$ $(v' = 1)\leftarrow X^2\Pi$ $v'' = 0$ band. The pump laser provided an output of 9 mJ/pulse for 10 kHz operation. Using Rhodamine 590 Perchlorate dye (dissolved in ethanol), the 566.4-nm fundamental wavelength was frequency doubled to 283.2 nm to

excite the Q1(8) line. The average laser pulse energy at 283.2 nm was 0.6 mJ/pulse for 10 kHz operation (6 W average power). A reference leg was integrated to continuously monitor the dye laser power output and tune the wavelength as needed. The first surface reflection from an uncoated fused silica window directed a small amount of the total beam energy through a Bunsen flame. The resulting LIF signal was collected with a photomultiplier tube and the average signal monitored with a Stanford Research Systems boxcar integrator and an oscilloscope. For measurements in the test rig, the laser beam is collimated and focused using a 1000-mm focal length spherical lens, a cylindrical lens of -25.4 mm focal length and finally by a 300 mm focal length cylindrical lens. This lens system is used to form a laser sheet that is 35 mm wide and less than 1 mm thick. A three-dimensional schematic of the simultaneous PIV/PLIF system shows the orientation of both the 532 nm and 283 nm laser sheets as they are directed into the windowed combustor. The OH-PLIF signal is focused onto a high-speed image intensifier (LaVision IRO) using a 100-mm focal length, f/2.8 ultraviolet (UV) camera lens (Soden Cerco Type-2178). An optical band-pass filter (Semrock 320/40) was fitted to the lens to transmit the fluorescence from $A^2\Sigma^+$ $(v' = 1) \rightarrow X^2\Pi$ $v'' = 1$ and $A^2\Sigma^+$ $(v' = 0) \rightarrow X^2\Pi$ $v'' = 0$ bands occurring over the 305–320 nm range of wavelengths. The effective filter width was sufficient to block the entire wavelength range of the intensifier photocathode sensitivity, removing elastic scattering of the laser beam from the seed particles and further reducing background flame luminosity. The filter had a transmission efficiency of >98 % over the selected bandwidth and an ultra-steep transmission cutoff (<1 nm). Though of course OH* chemiluminescence can be suppressed only through intensifier gating. The intensified

signal is detected using a high-speed camera (Phantom v7.4). The intensifier time gate is set to 100 ns to suppress background luminosity from OH*.

2.5.2 PIV System

The PIV laser is a HRR, dual-cavity, diode-pumped solid-state Nd:YAG laser (Quantronix Dual Hawk 80-M). Each of the laser cavities produces a 532 nm beam with a pulse energy of 3.5 mJ at 10 kHz. The time delay between the two PIV laser pulses is optimized to 10 μs in order to optimize the measurement dynamic range. The PIV laser sheet was formed using a 1000 mm focal length spherical lens, a cylindrical lens of -50 mm focal length and a 250 mm cylindrical lens, as shown in Figure 2.10. The resulting laser sheet is 35 mm wide and less than 1 mm thick. A fluidized bed was used to seed the flow field with TiO_2 particles (nominal diameter of 250 nm) with the jet fluid. The scattered light from the particles was collected using a second high-speed CMOS camera (Photron SA-5) and a 105 mm focal length Nikon f/2.8 lens. A custom ultra-steep band-pass filter (3 nm FWHM centered on 532 nm) was used to suppress the background luminosity.

Application of PIV in high-temperature and high-pressure flows with optical windows also faces additional challenges. Due to the presence of non-uniform temperature and density gradients in turbulent flames, PIV measurements are affected by non-uniform seeding density. As a result the peak correlation values are lower as compared to an isothermal flow field. In addition, at high temperature, the quartz windows soften, causing seed particle fouling and, consequently, increased background measurement noise. Indeed,

accumulation of seed on the windows limits the total measurement duration, before windows must be replaced.

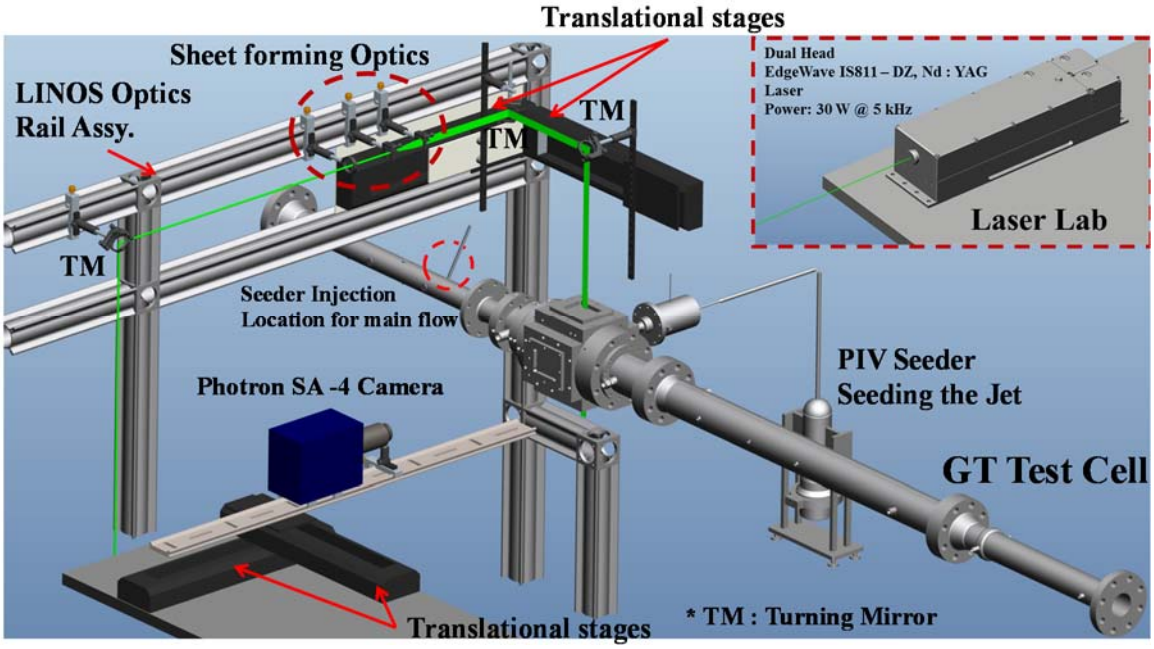

Figure 2.10. Schematic diagram showing the high-repetition-rate (HRR) two-component PIV experimental test system.

2.5.3 Laser-Camera Synchronization

The temporal synchronization of the two lasers and the imaging systems was accomplished with an external timing box (Quantum Composer 9520 Digital Delay Pulse Generator) that provided the input signals at necessary time delays. The OH-PLIF laser pulse was delayed from the first PIV pulse by $\frac{\Delta t}{2}$ (5 μs). Laser pulse timings were continuously monitored by photomultiplier tubes connected to an oscilloscope. A dichroic beam-splitter, with high transmissivity at 532 nm and high reflectivity at 283 nm, was used for the spatial overlap of the two laser sheets. Alignment and overlap of the lasers sheets was confirmed both in the near- and far field of the combustor. Calibration of the images

was accomplished (just before the start of each experiment) with a dual-plane dot target (LaVision Type 05). The two camera systems as shown in Figure 2.11 (OH-PLIF and PIV camera systems) were installed perpendicular to each other with a second dichroic mirror to separate the signals. Figure 2.12, shows a picture of the experimental test system during operation.

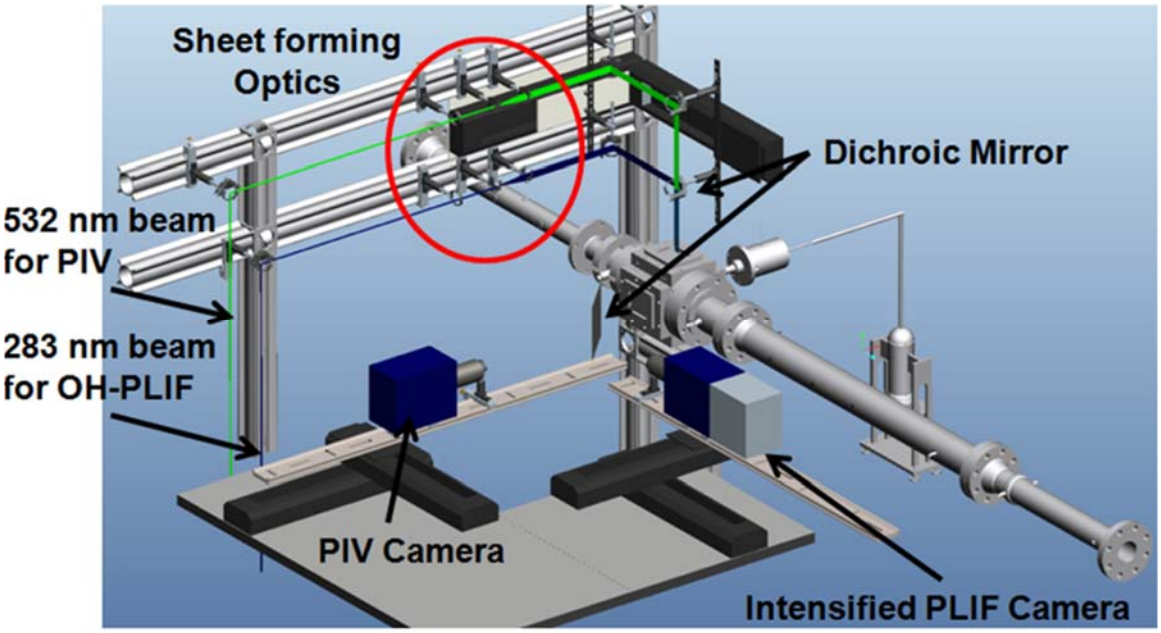

Figure 2.11. Schematic diagram of the HRR simultaneous PIV/OH-PLIF experimental setup.

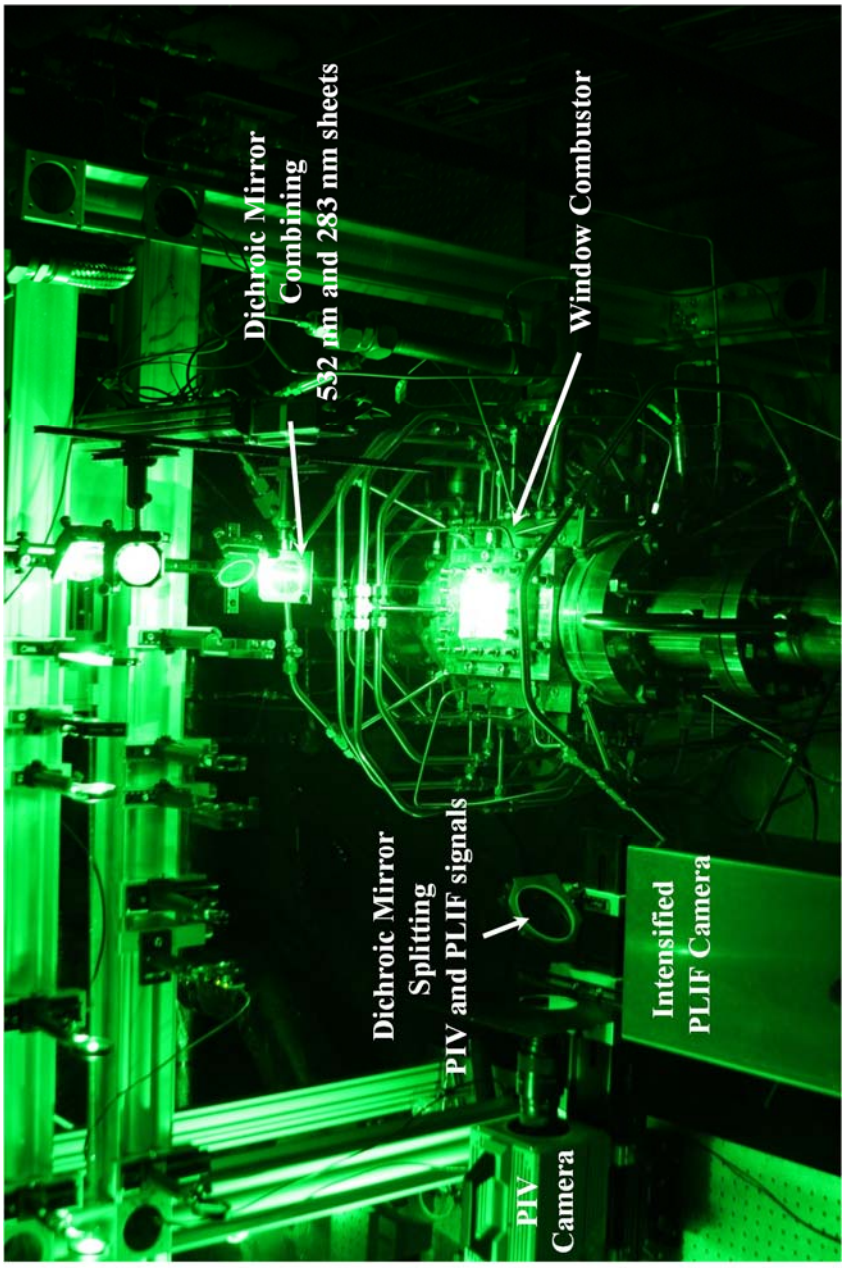

Figure 2.12. Picture of the HRR simultaneous PIV/OH-PLIF experimental setup.

CHAPTER 3. STRUCTURE AND DYNAMICS OF THE WAKE OF A REACTING JET INJECTED INTO A SWIRLING VITIATED CROSSFLOW

3.1 Introduction

The emissions from natural gas-fueled stationary gas turbines, like those used in combined-cycle power plants, are regulated by environmental legislation. Legislation places increasingly stringent limits on nitrogen oxides (NO_x) [12]. Most manufacturers achieve the desired levels of low NO_x emissions by reducing the flame temperatures, which is attained by premixed, lean-burn approach: premixing the air and the fuel prior to combustion and burning lean in the combustor [13]. However, burning lean does introduce problems with maintaining stable combustion, and the resulting pressure pulsations and combustion noise can lead to catastrophic mechanical damage. Secondary injection of the fuel, also referred to as staged combustion, is being studied by gas turbine manufacturers as a means of increasing the power output of the gas turbine systems with minimal contribution to NO_x emission. By introducing staged combustion, combustion instabilities introduced due to the lean burning can be minimized by controlling the fuel flow rate through the primary and secondary combustion zones.

In this work, high repetition rate (HRR) PIV measurements are discussed. The measurements are used to characterize the wake flow field of an auto-igniting jet carrying fuel issuing into a swirling, vitiated crossflow at gas turbine relevant conditions. In the

case of secondary injection of fuel in a gas turbine combustor, rapid mixing and chemical reaction in the near field of jet injection is desirable. Therefore, the main objective here is to characterize the velocity field of the wake of the jet in a swirling crossflow the impact of the wake vortices in stabilizing a steady reaction front within the near wake region of the jet.

3.2 Experimental Test Matrix

In the present study HRR laser diagnostic techniques are employed to characterize the structure and dynamics of the transverse jet interacting with a swirling and vitiated crossflow. A detailed test matrix for the PIV studies is shown in Table 3.1. The current study focuses on two momentum flux ratios, J=3 and J=8. The J =3 case corresponds to a lower momentum flux ratio where the premixed fuel reacts closer to the nozzle exit, with the reaction zone stabilized within the wake of the jet. The J=8 case allows the jet fluid to penetrate deeper into the crossflow with a higher degree of mixing. The jet equivalence ratios of ϕ_{jet} = 0.9 and 3 are chosen for the premixed natural gas cases, in order to study leaner and richer jet flame cases that provide different changes in temperature across the SCZ. A fuel mixture of 40%H_2/60% N_2 and 50%H_2/50% N_2 are chosen for the non-remixed H_2 jet flames. The non-reacting cases were involved isothermal crossflow and jet fluid, thus the density ratio for the JICFs was S = 1. The premixed NG cases features NG premixed with heated air. The net temperature of the mixture of cold fuel, heated air and cold PIV seed carrying air was 400 K. Thus, the mixture provides a density ratio of S = 2.5. The mixture temperature of H_2/N_2 reacting jet cases was 280 K. leading to a jet to crossflow density ratio of 4.25. Velocity measurements were performed at 5 planes along

the cross-section of the jet, as shown in Figure 3.1a, Z = -5 mm, 2 mm, 5 mm, 10 mm and 15 mm away from nozzle exit plane. Here Z represents the distance from the nozzle exit plane. The nozzle exit plane is considered as the origin for this geometry as shown by the coordinate axes in Figure 3.1a and b. The horizontal green lines indicate the locations of laser sheet and the view shown in the schematic is defined as the side view of the jet in the X-Z plane. The red dotted lines represent the reacting jet edges in the wake region of the jet are shown in Figure 3.1b. The PIV measurements were made along X-Y plane which is perpendicular to the jet axis, the span of laser sheet is shown in Figure 3.1b. Henceforth, the X-Z planes will be referred as the planes parallel to the jet trajectory and the X-Y plane will be referred as jet cross-section planes. The jet injector exit diameter, d_{JET} = 10 mm and the outer wall diameter of the injector is D = 15 mm. The secondary fuel injector protrudes 1.5 jet diameter into the crossflow. The extended injector configuration is in particular relevance to practical combustors, as it would ensure flame stabilization away for the combustor wall.

Note that PIV measurements were not successful on planes parallel to the jet trajectory due to high scattering when the laser sheet impinges on the TBC-coated combustor wall, saturating the camera pixels. In order to isolate the effect of heat release on the flow field, non-reacting flow PIV measurements were performed. Multi plane velocity measurements on non-reacting jets were performed for 4 different J values, J = 3, 6 and 8. In these measurements both the crossflow and the jet comprised of hot air and the incoming temperature of both the fluid streams were kept at 450 K. The reason behind keeping the air temperature below the operating condition was to match the temperature of the jet and the crossflow. In the PIV experiments the jet air comprises of two different

fluid streams, i) heated air and ii) cold air with the PIV seed particles. When the two streams of fluid mix within the mixing plenum the final mixture temperature drops and a maximum mixture temperature that could be maintained during the course of experiment was 450 K.

Table 3.1. Crossflow and jet operating conditions.

Cross Flow Operating Condition					
Operating Pressure (atm)			5.5		
Operating Temperature (K)			723		
MCZ Air Flow Rate (kg/s)			0.39		
MCZ Equivalence Ratio, ϕ_{main}			0.5		
Main Flow Reynolds Number(NR), Re_{main}			105000		
Main Flow Reynolds Number(R), Re_{main}			61000		
Non-Reacting JICF Conditions					
High Temperature Air Jet	Momentum Flux Ratio, J	Density Ratio, S	Jet Reynolds Number, Re_{jet}		
	3	1	16900		
	6	1	24200		
	8	1	27600		
Reacting JICF Conditions					
FUEL JET	Momentum Flux Ratio, J	Density Ratio, S	Jet Reynolds Number, Re_{jet}	ϕ_{jet} =0.9	ϕ_{jet} = 3.0
Premixed Natural Gas	3	2.5	27500	ΔT = 36 K	ΔT = 145 K
	8	2.5	45000	ΔT = 52 K	ΔT = 212 K
				40%/60%	50%/50%
H2/N2	3	4.25	72,000	ΔT = 28 K	ΔT = 96 K
	8	4.25	118,000	ΔT = 44 K	ΔT = 147 K

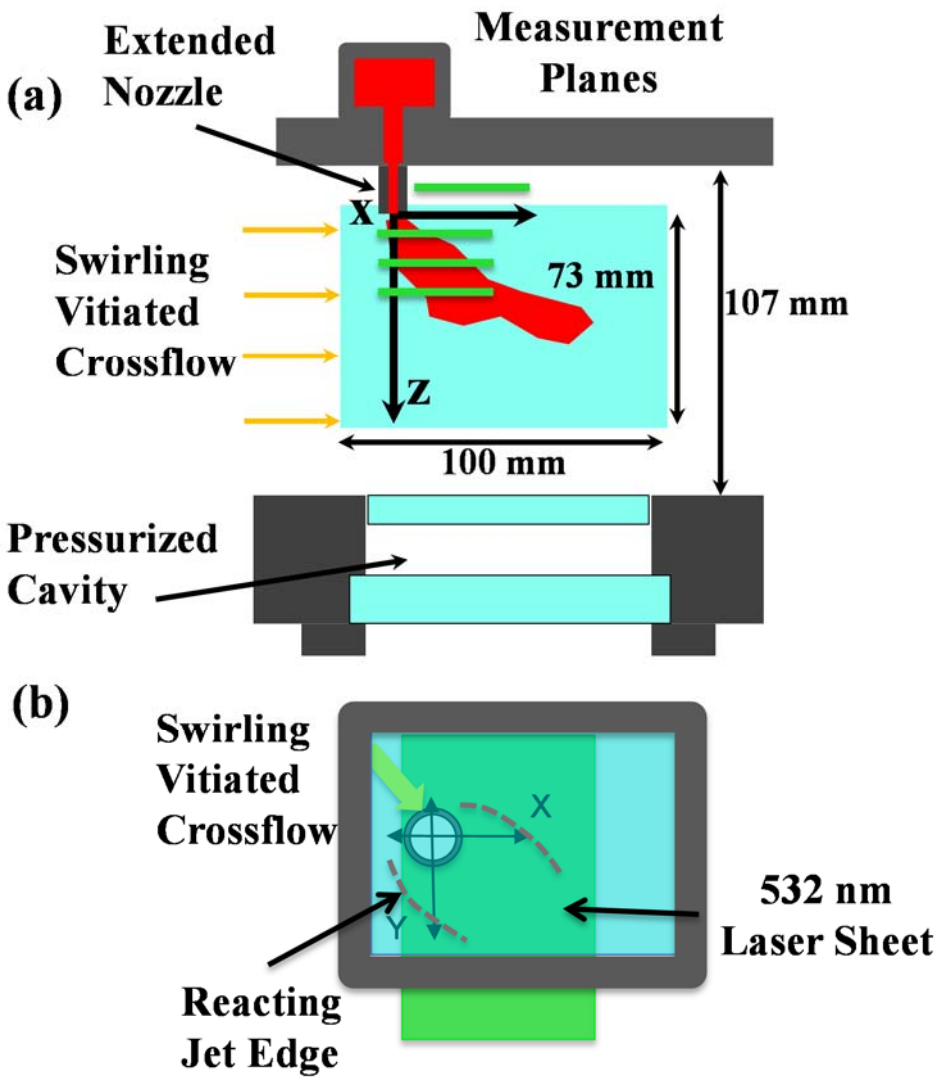

Figure 3.1. (a) Schematic diagram of the window assembly portion of the test rig with the extended nozzle showing the side view of the RJICF. The green horizontal lines indicate the PIV measurement planes. (b) The flow streamlines indicating the near field wake region of the RJICF along one of the x-y measurement planes.

3.3 PIV Vector Processing

The PIV images were pre-processed before vector computation. Similar to the OH-PLIF image correction, the PIV images were spatially calibrated and then corrected for the average background (from each of the image pairs). The particle image intensity was then

normalized to correct for the non-uniformity in the particle intensity field due to laser sheet intensity variations. The vector field was computed using LaVision software, version 8.2.0. A detailed analysis based on the particle density, the time delay between the two laser pulses, and the cross-correlation technique, was performed to balance the cross-correlation strength and resolution. A multi-pass cross correlation technique featuring an auto-adaptive interrogation window with a first pass window size of 64x64 pixels to a window size of 16x16 pixels with 50% overlap between the image pairs was used for computing the vector field. A sequence of instantaneous Mie scattering images of reacting JICF, J = 8, ϕ_{JET} = 0.9 at Z = 5 mm, is shown in Figure 3.2. Since, the flow field is seeded through the jet fluid only, a masking function was used to mask out the regions without the particles. The masking function included a geometric mask that allowed the cross-correlation algorithm to compute vectors within a rectangular region bounded between, X = -5 mm – 27.5 mm and Y = -30 mm – 15 mm, within the white rectangular region shown in the Mie scattering images. In order to avoid vector computation from the regions without any particles a threshold function was used that ensured vector computation only from the particles scattering the laser. The field of view utilized to perform the cross correlation was 35 mm x 55 mm, with a vector resolution of 0.8 mm. Based on these parameters, the total number of rejected vectors varied between 15 and 25 % and the vector quality factor (Q-factor) was always maintained greater than 1.5, where the Q-factor is defined as the ratio between the two highest correlation peak In order to capture the turbulent statistics, a total of 10,000 image pairs were acquired for each measurement, which corresponds to a data acquisition time of 1.0 s at a rate of 10 kHz.

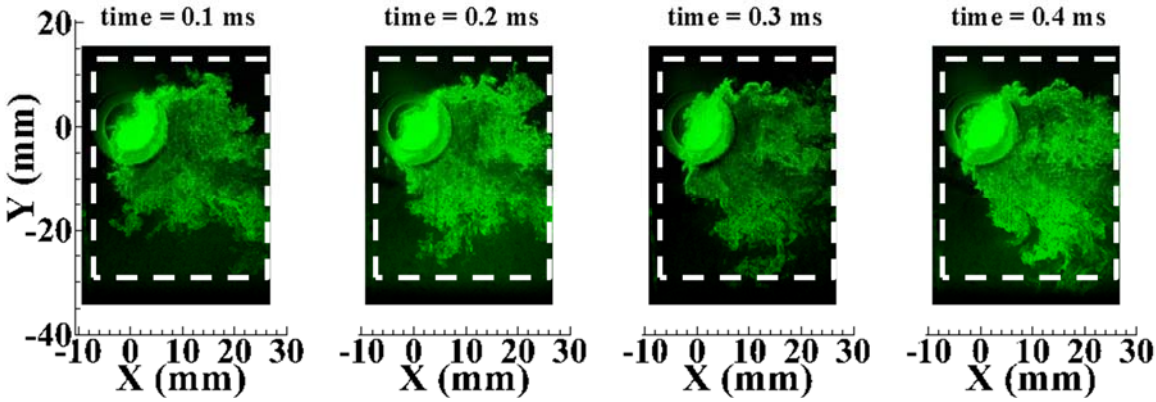

Figure 3.2. Instantaneous Mie scattering images acquired at Z= 5 mm from the nozzle exit plane, for the reacting jet case of J = 8 and ϕ = 0.9.

Figure 3.3, shows the distribution of number of vectors computed at every spatial locations for the reacting jet case of J = 8, 40% H_2/60% N_2, measured at Z =5 mm. For a reliable computation of the time averaged vector field, velocity vectors at any spatial location appearing less than 1000 times out of the 10000 snapshots (or 10% of the number of snapshots) were rejected, thus, ensuring vector computation from locations with continuous seeding. It is evident from Figure 3.3 that except for region above Y = 12.5 mm and below Y = -35 mm number velocity vectors computed at every spatial location exceeds 8000 vectors. This indicates that the instantaneous vector fields are computed reliably for most of the spatial locations. Furthermore, velocity fields were extracted from three time slices of 0.2 s, i.e., 0 – 0.2 s, 0.4 – 0.6 s and 0.8 – 1.0 s, and time-averaged velocity field was computed for each of these time slices. Figure 3.4 shows the time averaged velocity vectors computed from all the ten thousand vectors and compares with the time averaged velocity field computed from velocity fields extracted from each of the time slices of 0.2 s. The time averaged velocity fields computed from the time slices of 0.2 s are then subtracted from the time average of velocity vectors computed from 0 – 1 s

to identify the regions with variation in the velocity magnitude. Figure 3.5 shows that out of the 1620 vectors computed more than 90% of the spatial locations have a velocity magnitude difference less than 2 m/s. The velocity magnitude differences are as high as 10 m/s within the recirculation region and about 20 m/s for all the three time slices above the injector and region below Y = -30 mm.

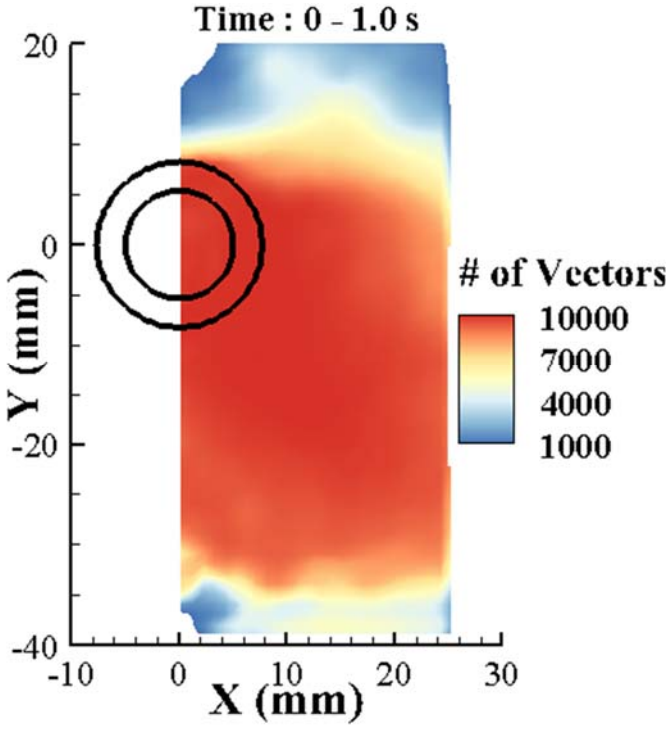

Figure 3.3. Distribution of number of vectors computed at each of the spatial location in a measurement plane 5 mm from the nozzle exit plane, for the reacting jet case of J=8 and 40%H_2/60%N_2.

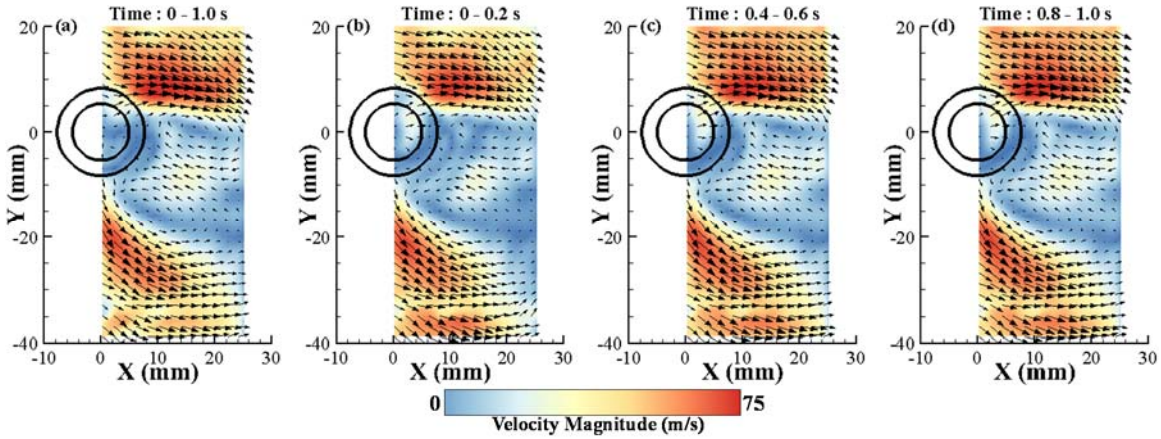

Figure 3.4. The time averaged velocity vectors overlaid on velocity magnitude averaged over (a) 0 -1 s, (b) 0 – 0.2 s, (b) 0.4 – 0.6 s and (c) 0.8 – 1.0 s for J = 8; 40%H_2/60%N_2 case measured at Z = 5 mm away from the nozzle exit.

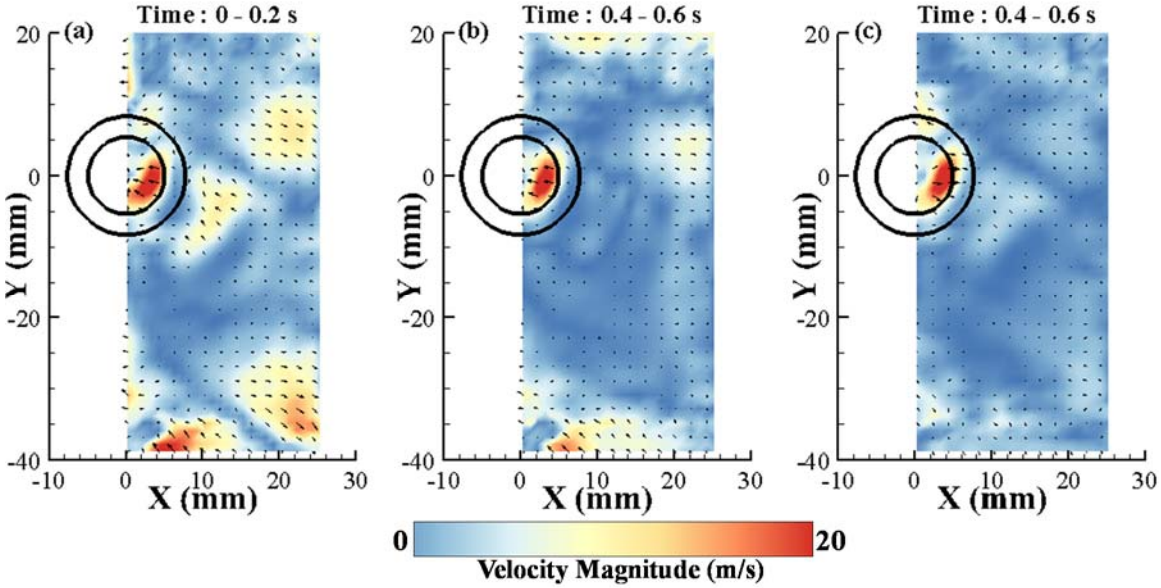

Figure 3.5. The difference velocity field by subtracting the time averaged velocity field of (a) 0 -0.2 s, (b) 0.4– 0.6 s, and (c) 0.8 – 1.0 s from the time averaged velocity field of 0 – 1 s, for J = 8; 40%H_2/60%N_2 case measured at Z = 5 mm away from the nozzle exit.

3.4 Time Averaged Velocity Field

In this section time-averaged velocity field of the non-reacting JICF and the reacting JICF has been discussed. Velocity data were collected for duration of 0.5 s at a repetition

rate of 10 kHz, providing enough sampling time to extract accurate time-averaged fields and flow statistics. We performed PIV measurements (i) to characterize the velocity of the vitiated crossflow fluid stream without the jet, (ii) characterize the velocity field of the non-reacting jets, and (iii) the reacting jets. Multi plane measurements along the X-Y planes were made to fully characterize the three dimensional nature of the complex flow-field of the JICF. The time averaged velocity fields obtained from these studies are discussed in the sections 3.4.1 – 3.4.2.

3.4.1 PIV Measurements of the Crossflow

In order to understand the influence of a swirling crossflow on a non-reacting and reacting JICF, the vitiator (MCZ) in these experiments was a low-swirl-burner (LSB) that imparted a swirling component to the crossflow. The vane angle of the swirler was 45 degree with a swirl number of 0.5. PIV measurements were made to characterize the flow-field of the vitiated crossflow. Specifically, for these measurements the jet injector was replaced with a planar metallic blank. Multi-plane PIV measurements were performed at measurement planes Z = 5, 10, 15, 35, 45 and 50 mm away from the jet exit plane. It is important to note that these distances are with respect to the jet exit plane with the injector protruding 15 mm into the crossflow. However, physically there was no injector during the measurements. The actual measurement planes were 20, 25, 30, 50, 60 and 65 mm away from the wall. The time-averaged velocity field of the vitiated crossflow computed at all the measurement planes are shown in Figure 3.6. The velocity vectors are overlaid on top of a false color map of velocity magnitude. The directions of the velocity vectors in the planes Z = 5, 10 and 15 mm are towards the bottom corner of the image and that in the planes Z = 45 and 50 mm are towards the top corner of the image, which shows the

direction of swirling motion of the crossflow. At the center of the combustor the velocity vectors are nearly parallel to the X-axis. The velocity magnitude is found to be varying between 35 – 40 m/s across all the measurement planes, however, at the center of the combustor (Z = 35 mm), the velocity magnitude is roughly 25 m/s. This is probably due to the velocity deficit at the center of the LSB [77]. Thus, in addition to the swirling motion there is a velocity gradient across the combustor due to the LSB. The spanwise variation of the mean and standard deviation of X- and Y-components of the velocity field at X/d_{JET} = 0.5, is shown in Figure 3.7. The X-component of velocity is seen to be higher than the mean magnitude of velocity between Y = -15 and -5 mm in the planes Z = 45 mm and 50 mm. The Y-component of velocity is negative for the planes Z = 5, 10 and 15 mm, positive for the planes Z = 45 and 50 mm and is approximately zero for Z = 35 mm plane, as shown in Figure 3.7b. The y-velocity trend clearly shows the behavior of the swirling crossflow. The standard deviations in the measured values of X and Y components of velocity lie in the range of 7 – 15 m/s across all the planes, as shown in Figure 3.7c and d.

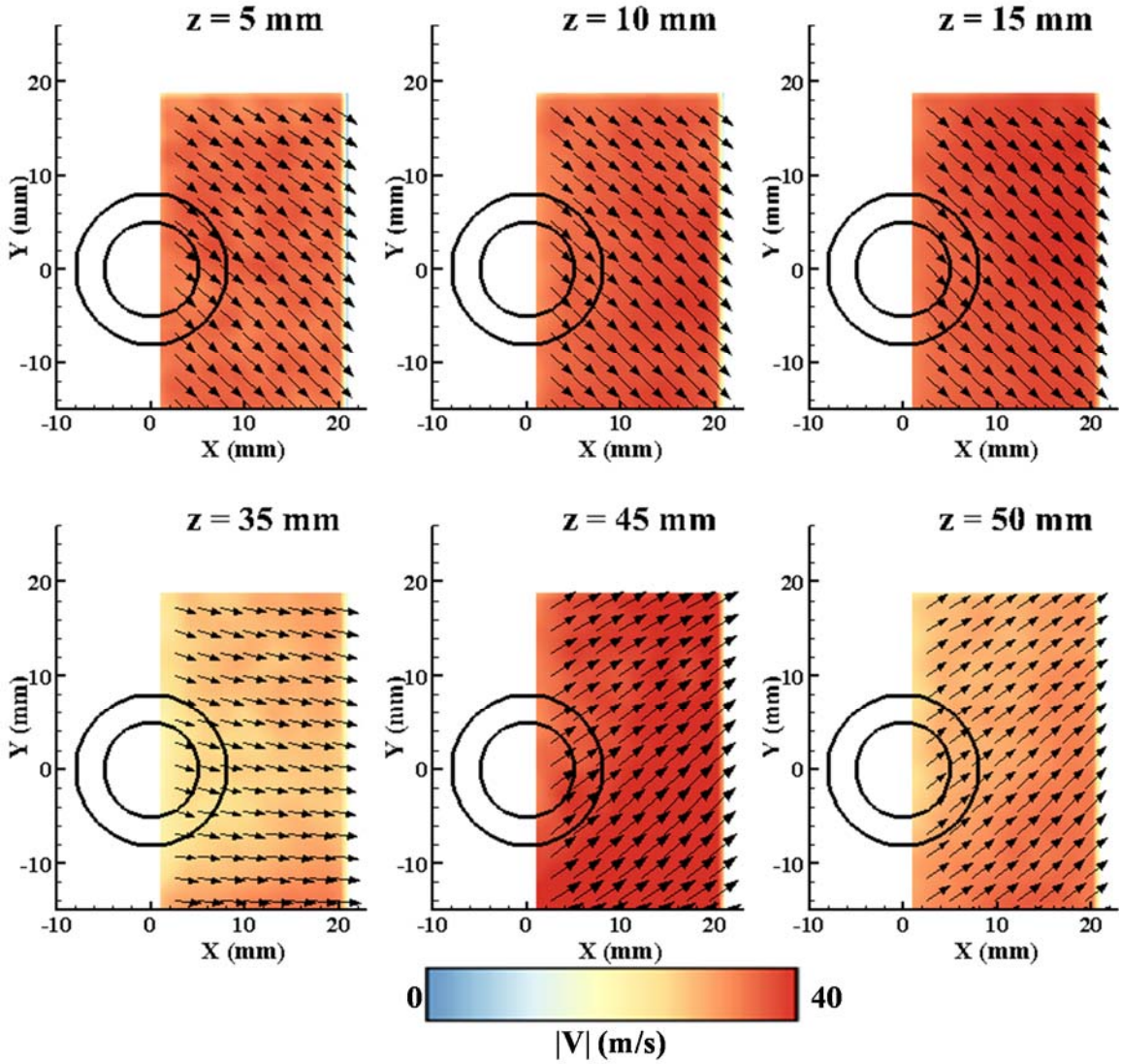

Figure 3.6. Comparing the crossflow velocity field measured at planes Z = 5 mm, 10 mm, 15 mm, 35 mm, 45 mm and 50 mm. The velocity vectors are overlaid on top of velocity magnitude |V| (0 – 40 m/s). The direction of the velocity vectors observed the measurement planes shown confirms the strong swirling motion present in the crossflow.

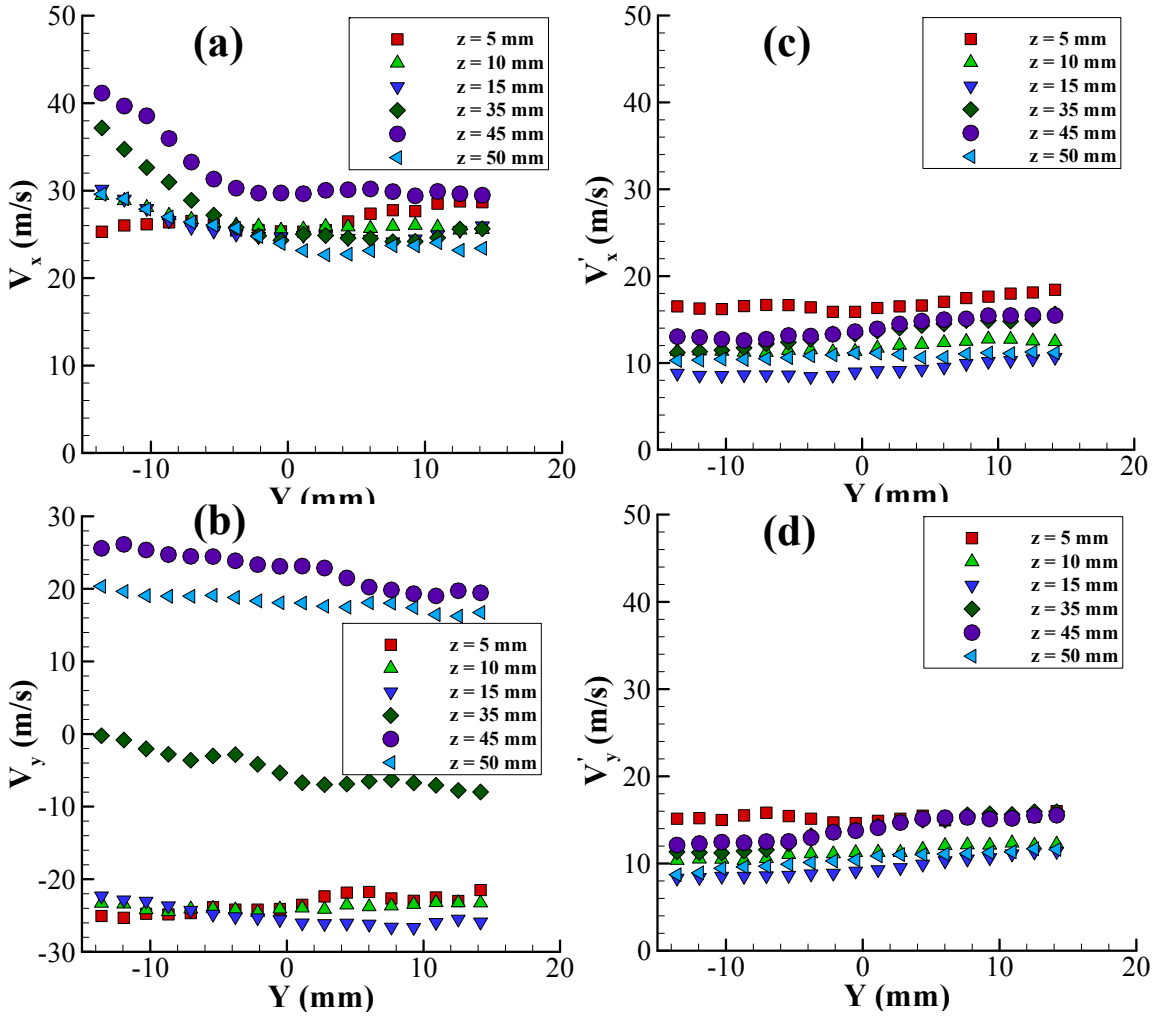

Figure 3.7. Variation of the x- and y- components of velocity of the crossflow measured at planes Z = 5 mm, 10 mm, 15 mm, 35 mm, 45 mm and 50 mm, plotted at x/d = 0.5 from the physical location of the center of the injector.(a) time averaged x-component of velocity, (b) time averaged y-component of velocity, (c) standard deviation of the x-component of velocity and (d) standard deviation of the y-component of velocity.

3.4.2 Non-Reacting Flow Field of JICF

Non-reacting flows provide baseline information on the flow-field dynamics and the prevalent dominant flow structures. PIV measurements were performed along the cross-section (X-Y plane) of the non-reacting JICF for J = 3, 6 and 8, at planes Z = 2, 5, 10 and 15 mm. In these measurements both the crossflow and the jet comprised of hot air and the

incoming temperature of both the fluid streams were maintained at 450 K. Figure 3.8a shows the time-averaged velocity vectors overlaid on top of velocity magnitude contour map calculated at measurement planes, Z = 2 mm, 5 mm, 10 mm and 15 mm. The velocity vectors are inclined at approximately at 45 degrees (aligned in the direction of the mean crossflow). The nozzle exit, represented by the concentric circles centered at x = 0 mm, y = 0 mm, has been included to indicate the vector direction with respect to the nozzle location. The jet fluid interacts with the incoming crossflow by forming the shear layer that surrounds the wake of the jet. Figure 3.8b, shows the time-averaged velocity vectors overlaid on out of plane vorticity magnitude. A counter-rotating pair of wake structure with vorticity magnitude greater than $\pm 5000\ s^{-1}$ is evident at all the measurement planes. The wake structures are symmetric along the mean flow direction. It is evident that the wake structure moves downstream along the mean flow direction with an increase in nozzle separation distance. Also the vorticity magnitude decreases with an increase in nozzle separation distance in the Z-direction.

A coordinate transformation was performed on the velocity field by rotating it by 45 degrees in a counterclockwise direction (this corresponds to the mean velocity angle calculated from the mean crossflow velocity field [40] at the planes Z = 2, 5, 10 and 15 mm), with the new coordinates X' (aligned with the mean flow) and Y'(normal to the mean flow). Velocity and vorticity profiles are extracted at various streamwise locations to further understand the effect of momentum flux ratio on the flow field. The time-averaged velocity and vorticity profiles for the non-reacting jet case of J= 8 are shown in Figure 3.8, Figure 3.9 and Figure 3.10. The profiles are extracted from four streamwise locations (X'/d_{JET} = 1.0, 1.5, 2.0, 2.). The streamwise variation of x-component of velocity shows a

dip in the velocity magnitude within the near wake region of the jet, between x = -10 mm – 10 mm. The velocity deficit is highest at Z = 2 mm. It is noticeable that the velocity gradient across all the streamwise location reduces with increase in nozzle separation distance. Negative x-velocity is evident at X'/d_{JET} = 1.0. This indicates presence of a recirculation region within the near wake region of the jet. The time-averaged contour plot of y-velocity magnitude of J = 8 measured at Z = 5 mm and its streamwise variation, is shown in Figure 3.9. The contour map of y-component of velocity indicates that due to the interaction of crossflow fluid and jet fluid near the nozzle exit the flow turns away from each other around the jet. This is due to the fact the jet fluid provides a blockage to the incoming crossflow fluid as a result the fluid elements at the interface of crossflow and jet tend to accelerate around core of the jet leading to a positive y-velocity above the injector and a negative y-velocity below the injector. By X'/d_{JET} = 1.5 the accelerating fluid turns back towards the center, due to the low pressure wake region of the jet. As a result there is change in flow direction and negative and positive y-velocity is evident above and below the injector, respectively. The y-velocity profiles show the same behavior observed in the contour map. The spanwise variation of y-velocity at X'/d_{JET} = 1.0 is opposite to the rest of the velocity profiles. The time-averaged vorticity profiles show a decrease in vorticity magnitude with increase in the streamwise distance indicating the extent of the wake of the jet in the streamwise direction. Also there is a drop in the vorticity magnitude with an increase in nozzle separation distance which gives a qualitative implication of the extent of the wake region in the Z-direction of the flow. The time-averaged flow fields for the non-reacting jet cases (Figure 3.10) show that an increase in jet momentum flux ratio results in an increase in the out-of-plane vorticity magnitude, (ω_z). The vorticity magnitude

is extracted at X/d_{JET} = 1.0 and 1.5from the velocity field computed at Z = 5 mm. The vorticity profiles indicate that for a higher momentum flux ratio, the rate of mixing of the jet fluid with the crossflow fluid will be higher because of high vorticity magnitudes.

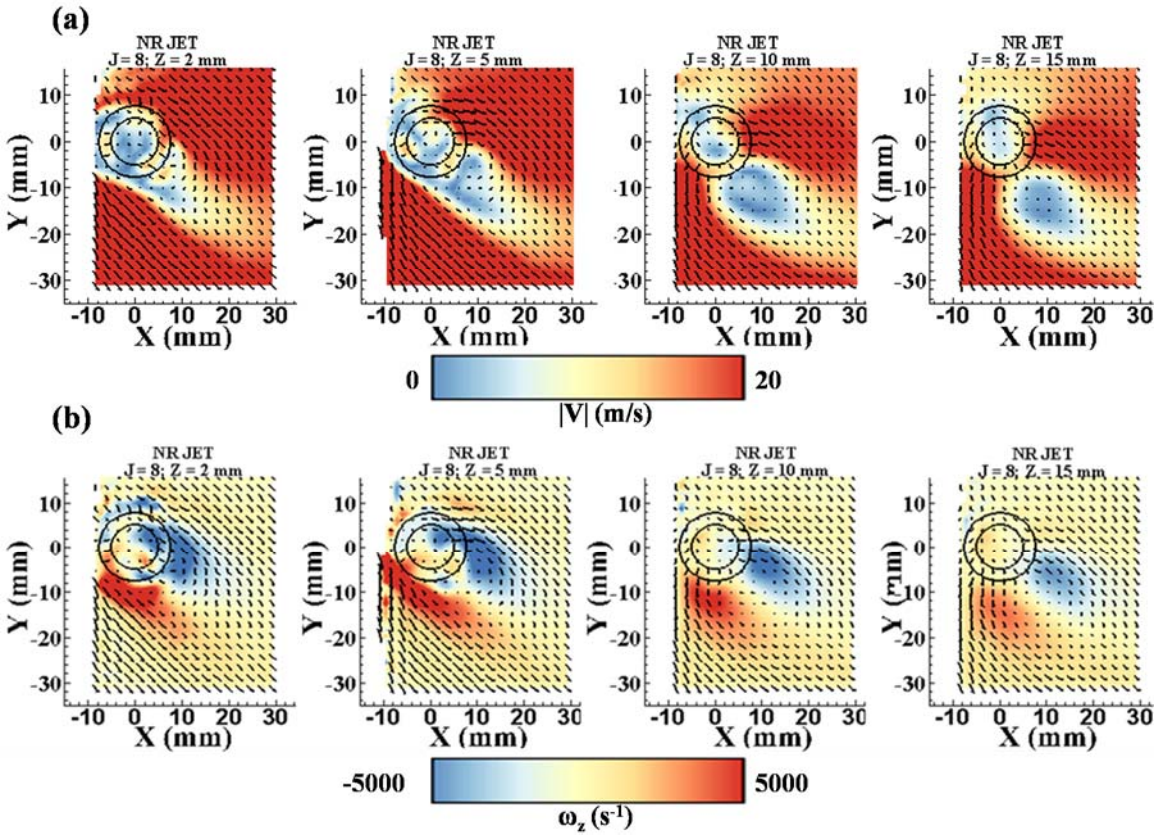

Figure 3.8. Computed velocity vectors overlaid on top of a) velocity magnitude, |V| (0 – 20 m/s) and b) z-vorticity, ω_z (-5000 – 5000 s^{-1}) J = 8, measured at Z = 2mm, 5 mm, 10 mm and 15 mm.

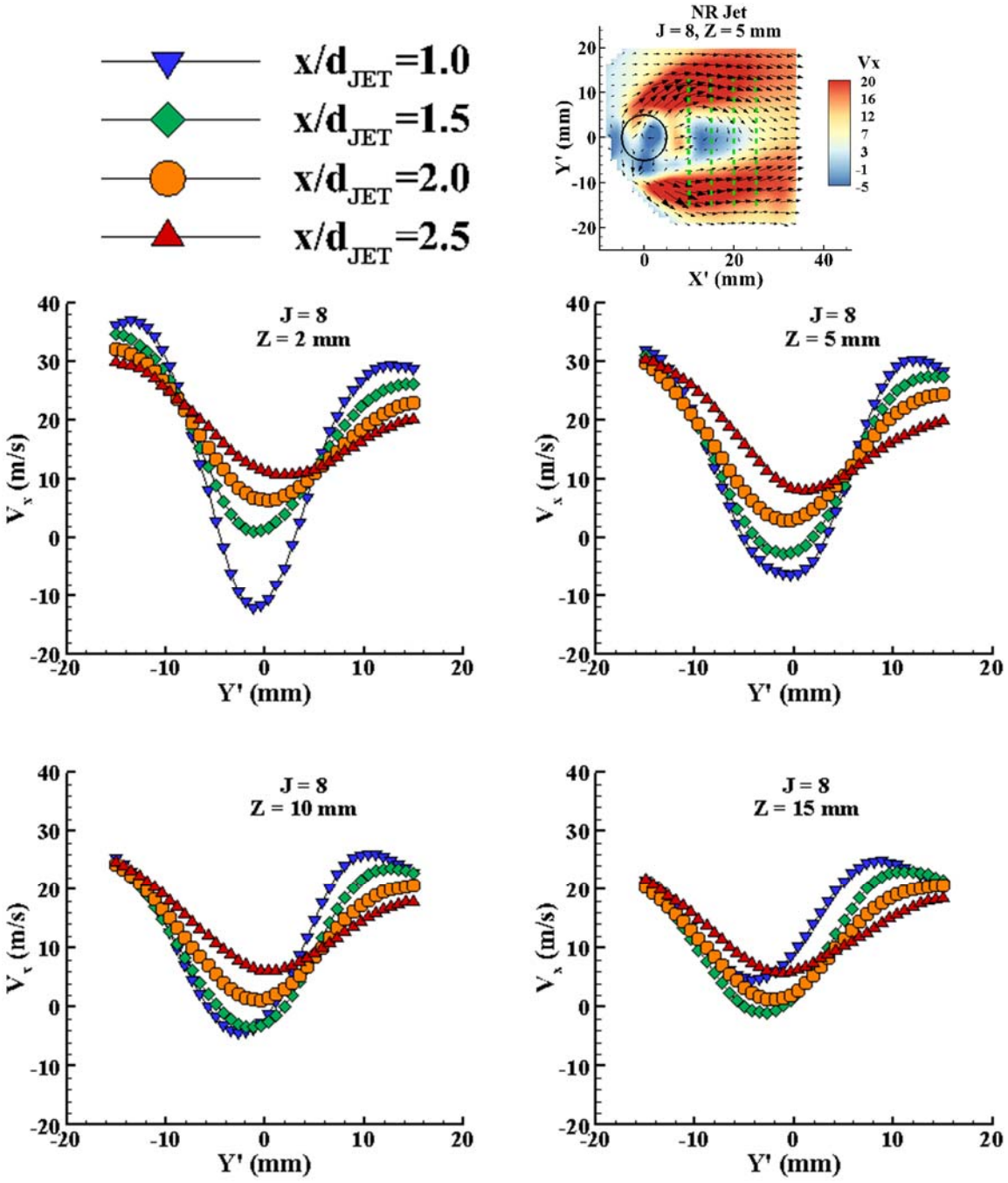

Figure 3.9. Variation of V_x along the streamwise direction indicating the variation in the flow field across different measurement planes for J = 8 case. The velocity profiles are extracted from the green dotted lines shown on the time-averaged x-component of velocity field.

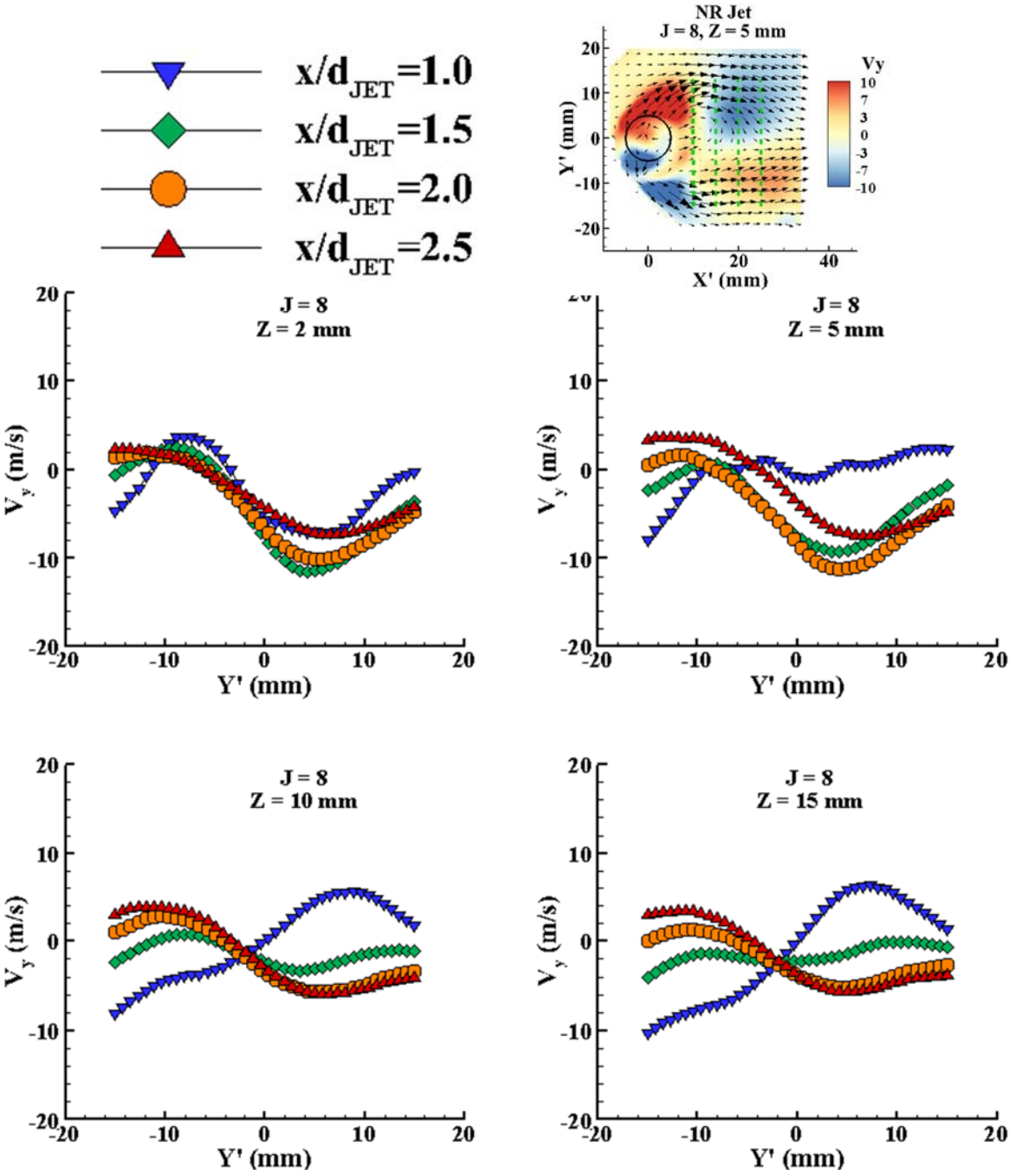

Figure 3.10. Variation of V_y along the streamwise direction indicating the variation in the flow field across different measurement planes for J = 8 case. The velocity profiles are extracted from the green dotted lines shown on the time-averaged y-component of velocity field.

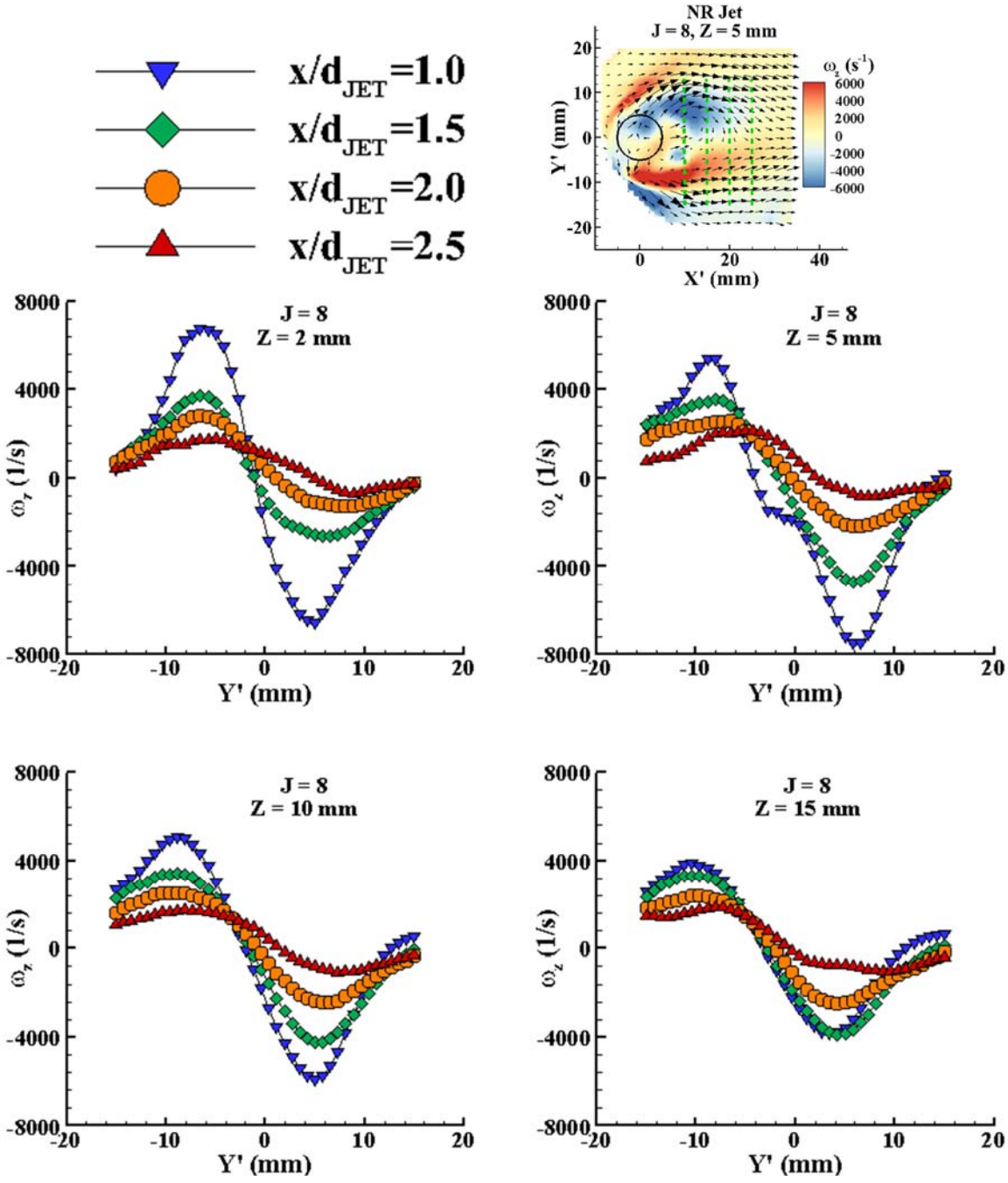

Figure 3.11. Variation of ω_z along the streamwise direction indicating the variation in the flow field across different measurement planes for J = 8 case. The vorticity profiles are extracted from the green dotted lines shown on the time-averaged z-component of vorticity field.

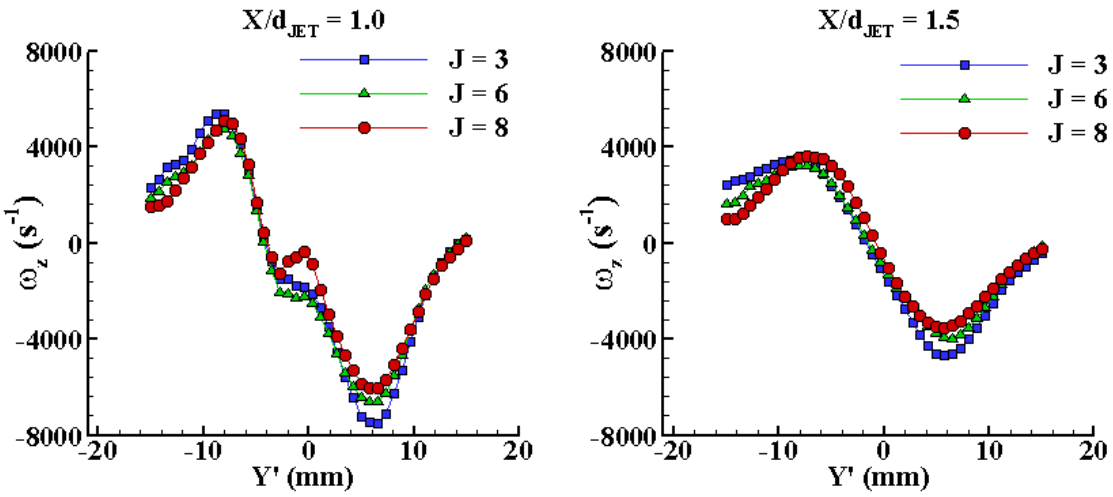

Figure 3.12. Variation of ω_z along the stream-wise direction indicating the effect of the momentum flux ratio on the magnitude of mean z-component of vorticity at Z=5mm for all the non-reacting jet cases.

3.4.3 Reacting Flow Field of RJICF

The time-averaged velocity field of the reacting jet case of J = 3 and ϕ_{jet}= 0.9 and J = 8 and ϕ_{jet}= 0.9 at measurement planes Z = -5 mm, 5 mm, 10 mm and 15 mm are shown in Figure 3.13 and Figure 3.14, respectively. The velocity field measurement at Z = -5 mm corresponds to a plane below the injection plane of the jet fluid. The PIV measurements at Z = -5 mm shows a continuous entrainment of particle seed into this plane. However, the flow physics in this plane is more closely related to a cylinder in a crossflow than to JICF. Further comparison of the flow dynamics at plane Z = -5 mm and other measurement planes will be discussed in detail in subsequent sections. Figure 3.13a shows the mean velocity vectors are overlaid on a false color map of the x-component of velocity contour at all the measurement planes. The velocity field calculated at Z = -5 mm shows the velocity field in the wake of the injector. The velocity vectors are in inclined at approximately 45 degrees. The velocity field has two high speed regions along the shear

layers and a low velocity wake region enveloped between the two shear layers. The source of vorticity in this plane is completely different than in planes above the jet injection plane. The vorticity is generated by fluid and injector wall interaction. The seeded and unseeded regions are clearly demarcated by the high vorticity magnitude forming a boundary to the velocity field. It is difficult to clearly identify the jet fluid and the crossflow fluid at this location. Figure 3.14a shows the velocity field of reacting jet case J = 8 and ϕ_{jet}= 0.9, and at Z = -5 mm the velocity and vorticity magnitudes are higher than J = 3.

The velocity field above the jet injection point has a different structure and dynamics. Figure 3.13a shows the mean velocity vectors are overlaid on a false color map of the x-component of velocity contour at all the measurement planes. The velocity vectors calculated at Z = 5 mm are inclined at approximately 45 degrees and aligned with the direction of mean swirling crossflow. The jet fluid interacts with the incoming crossflow by forming the shear layer that surrounds the wake of the jet. Within the two shear layers there are two distinct high speed regions. A strong recirculation region is evident between the two high speed flow regions at Z = 5 mm. The recirculation region is a characteristic feature of the wake of the jet. The wake vorticity entrains the jet fluid and the crossflow fluid within the wake of the jet, leading to chemical reactions and stabilization of a reaction zone. Figure 3.13b shows the same vector field overlaid on a false color map of the y-component of velocity. The contour map of y-component of velocity indicates that due to the interaction of crossflow fluid and jet fluid near the nozzle exit the flow turns away from each other around the jet. This is due to the fact the jet fluid provides a blockage to the incoming crossflow fluid as a result the fluid elements at the interface of crossflow and jet tend to accelerate around core of the jet leading to a positive y-velocity above the injector

and a negative y-velocity below the injector. The recirculating region of the flow field has a positive y-velocity. Figure 3.13c shows the velocity vectors overlaid on a false color map of the z-component of vorticity (ω_z). A steady counter-rotating wake structure aligned in the direction of the mean velocity vectors is clearly evident at z = 5 mm. The direction of the velocity vector at Z = 10 mm is approximately at 45 degree with respect to x-direction. However, the size of the recirculation region is smaller than that in Z = 5 mm and has shifted along the streamwise direction by half a jet diameter. The vorticity magnitude is also smaller than that at Z = 5 mm. The trend continues with an increase in nozzle separation distance and at Z = 15 mm the vorticity magnitude reduced to $\pm 2500\ s^{-1}$. The wake structure and the recirculation region are no longer seen at this plane. This implies that measurement plane Z = 15 mm is no longer within the wake of the jet. The time averaged flow streamlines shown in Figure 3.13d provide a different visualization of the wake vortical structure at Z = 5 mm and 10 mm. The wake structure is surrounded by the two high speed shear layers. The velocity field of reacting jet case J = 8 and ϕ_{jet}= 0.9 at Z = 5 mm and 10 mm are similar to that of J = 3. However, the wake structure is seen at Z = 5 mm, 10 mm and 15 mm indicating deeper penetration of the jet into the crossflow with an increase in J and thus, a larger wake region along Z-direction.

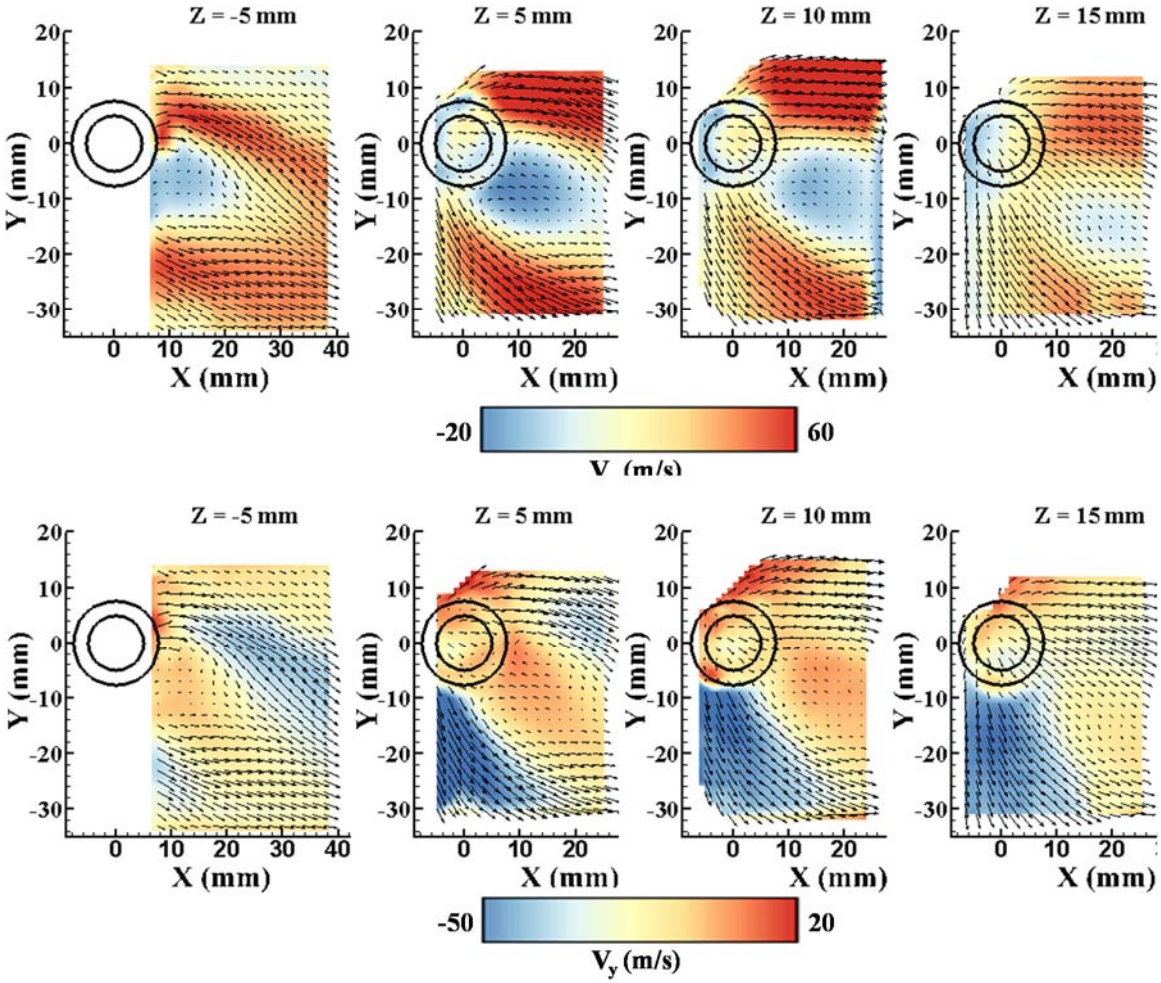

Figure 3.13. Computed velocity vectors overlaid on top of x- velocity (row 1), V_x (-20 – 60 m/s),y- velocity (row 2), V_y (-50 – 20 m/s), c) z-vorticity (row 3), ω_z (-10000 – 10000 s^{-1}) and d) flow streamlines (row 4) colored by the velocity magnitude, |V| (0 – 70 m/s) for J = 3 and ϕ_{jet} = 0.9, measured at Z = -5 mm, 5 mm, 10 mm and 15 mm.

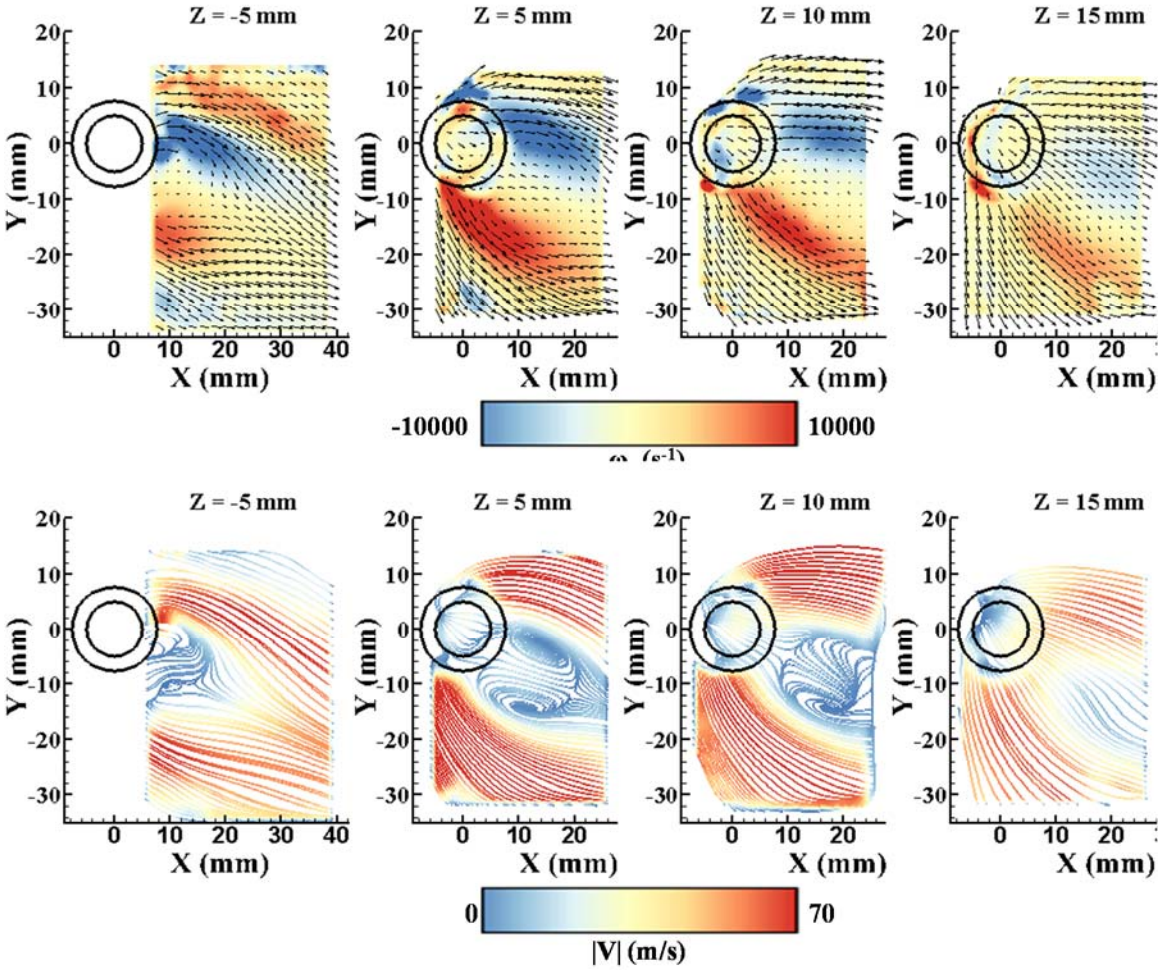

Figure 3.13. (Continued)

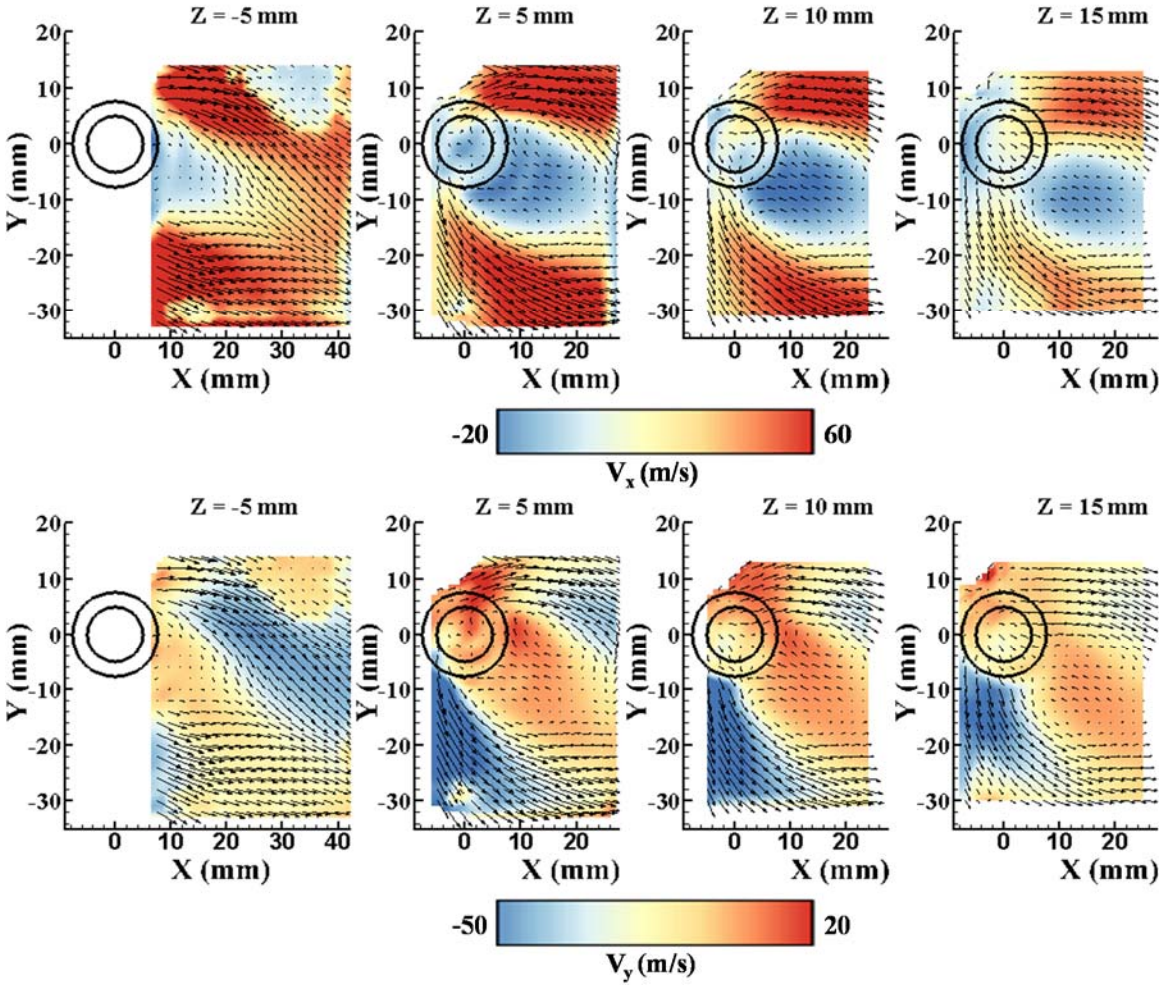

Figure 3.14. Computed velocity vectors overlaid on top of x- velocity (row 1), V_x (-20 – 60 m/s),y- velocity (row 2), V_y (-50 – 20 m/s), c) z-vorticity (row 3), ω_z (-10000 – 10000 s^{-1}) and d) flow streamlines (row 4) colored by the velocity magnitude, |V| (0 – 70 m/s) for J = 3 and ϕ_{jet} = 0.9, measured at Z = -5 mm, 5 mm, 10 mm and 15 mm.

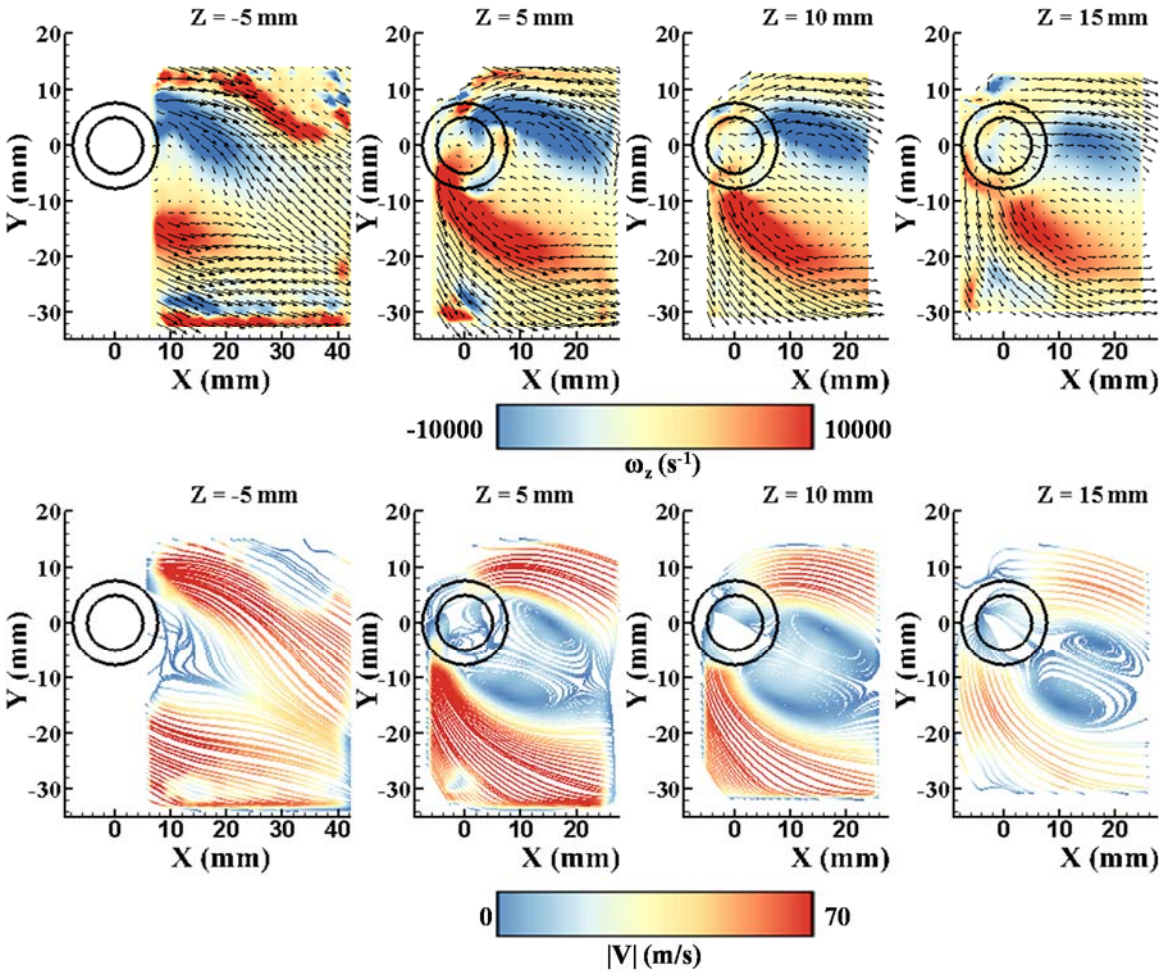

Figure 3.14. (Continued)

The time-averaged velocity vectors, overlaid on a z-vorticity contour map for the reacting jet case of J = 8 and J = 3, 40% H_2/ 60 % N_2, are shown in Figure 3.15 and Figure 3.16, respectively. The measurement locations correspond to the Z = 5 mm, 10 mm and 15 mm planes. Similar to the velocity field of NG jets a pair of counter-rotating wake vortex structure is evident at Z = 5 mm for the H_2 jets too. In the contour map of z-vorticity, red represents a counter-clockwise rotation and blue represents a clockwise rotation. A strong recirculation region is evident between the two flows at Z = 5 mm. The wake vorticity entrains the jet fluid and the crossflow fluid within the wake of the jet, leading to chemical

reactions and stabilization of a reaction zone. The magnitude of vorticity decreases as the distance from the nozzle exit plane increases, which suggests that the vortex structure is a characteristic flow structure of the wake of the jet. The zone of influence of the wake structure is smaller for the J=3 case, as compared to the J=8 case, which is an expected result because the higher J jet has deeper penetration into the crossflow. Thus, multi-plane measurements provide an insight into the zone of influence of the wake of the jet. It is important to note that the time-averaged velocity fields were combined to generate a time-averaged, three-dimensional wake structure for the J = 8 case, as shown in Figure 3.17. The structure shown in Fig is a vorticity iso-surface of z-vorticity of magnitude ± 5000 s^{-1}. The location of the nozzle is included in the figure, and the nozzle exit is at Z = 0 mm. The three-dimensional perspective view of the wake structure shows its spatial evolution with respect to the jet axis.

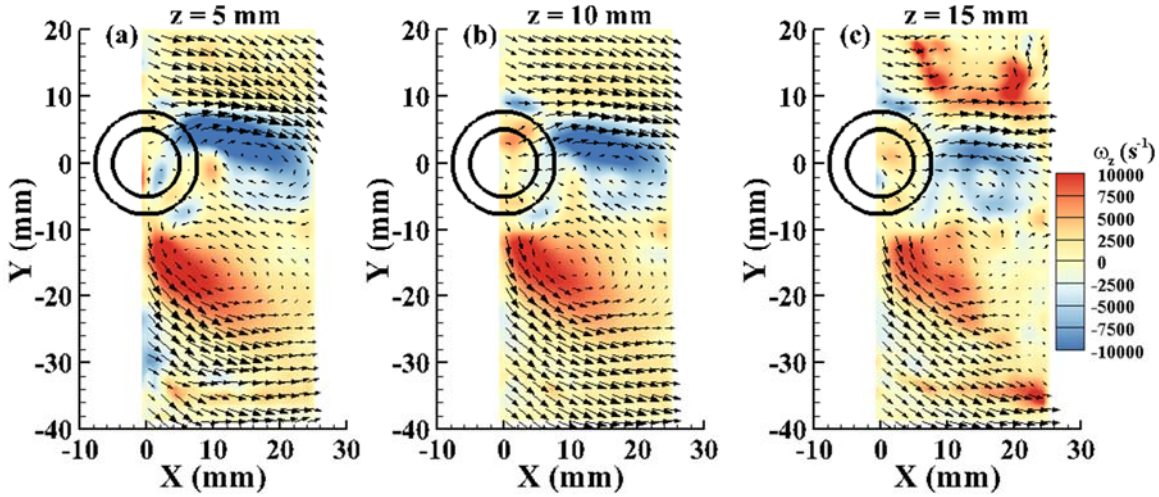

Figure 3.15. The time-averaged velocity vectors overlaid on top of z-vorticity contour map for J = 8; 40%H_2/60%N_2 case measured at a) Z = 5 mm, b) Z = 10 mm and c) Z = 15 mm away from the nozzle exit.

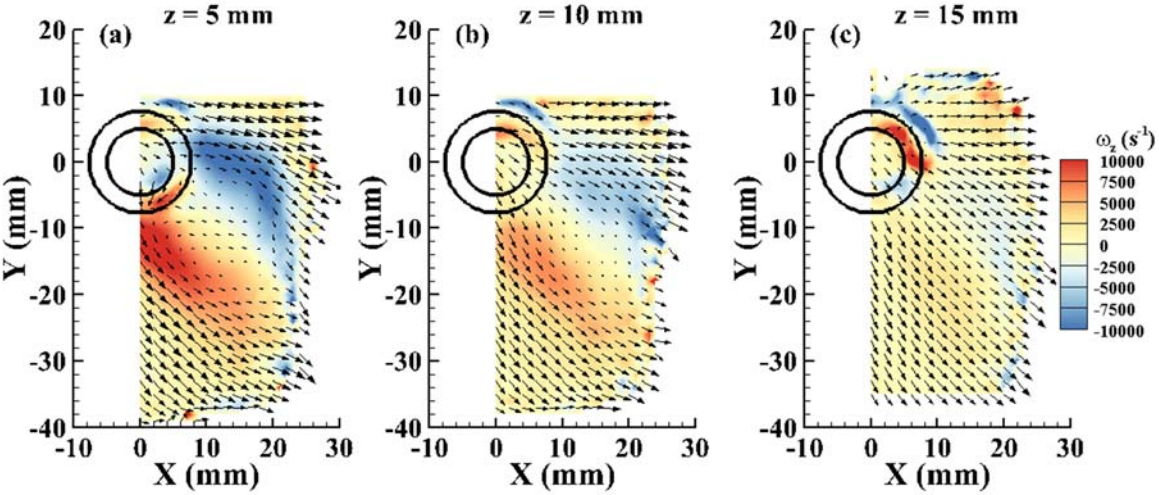

Figure 3.16. The time-averaged velocity vectors overlaid on top of z-vorticity contour map for J = 3; 40%H_2/60%N_2 case measured at a) Z = 5 mm, b) Z = 10 mm and c) Z = 15 mm away from the nozzle exit.

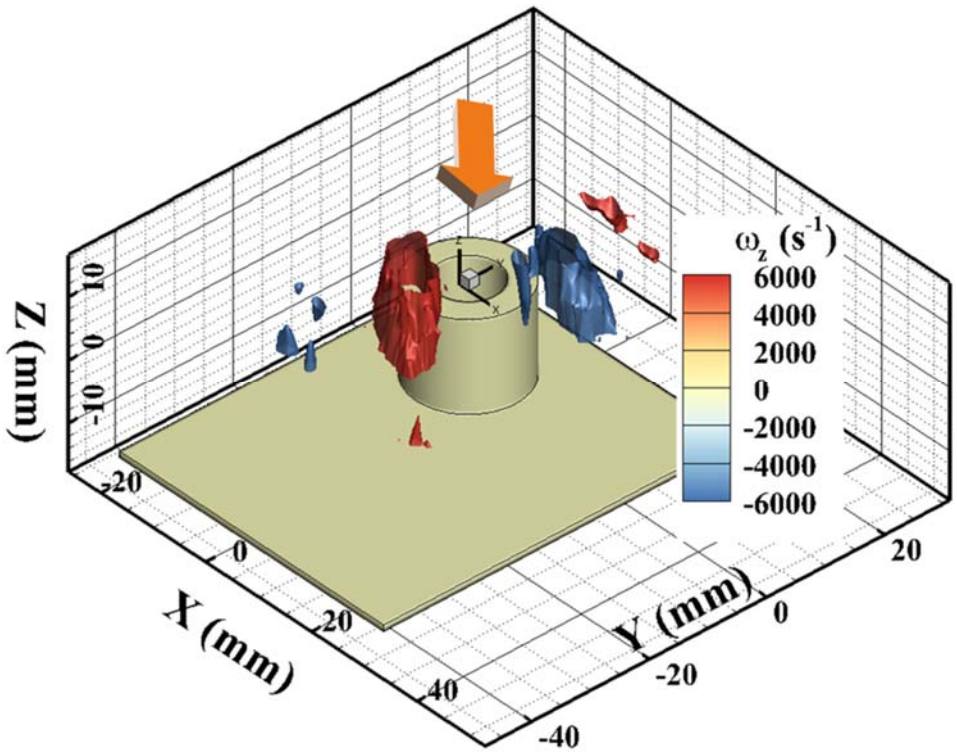

Figure 3.17. Iso-surface of time-averaged out of plane vorticity (ω_z) for J = 8; 40%H_2/60%N_2 case indicating the evolution of the wake vortex structure. The orange arrow indicates the direction of the crossflow. The wake structure is a vorticity iso-surface of $\pm$5000 s^{-1}.

The flow field for the PIV measurements discussed in this study was seeded through the jet. Seeding the flow field by injecting the particles through the jet leads to some bias in the magnitude of the velocity field measured. Injecting the PIV seed particles into the crossflow was challenging due to two main reasons. Firstly, due to the swirling motion, seeding the crossflow resulted in much faster coating of the windows as compared to seeding only the jet. To maximize the amount of data collected on a single test day, seeding the jet was preferred over seeding the crossflow. Secondly, the crossflow seeded experiments could not capture the wake structure due to the lack of particles entrained in the wake region, which is an important flow structure for the current study. In order to quantify this bias some PIV measurements were performed by seeding the crossflow.

Figure 3.18 shows the streamwise variation of the velocity difference, given by Equation (3.1) between the flow field obtained by seeding the crossflow and seeding the jet for reacting jet case of J = 3 and ϕ_{jet} = 0.9 at Z = 5 mm.

$$\nabla V_i = V_{i,CF} - V_{i,JET} (i = x, y) \tag{3.1}$$

Here, the velocity field is extracted from a region X = 0 mm – 15 mm and Y = -10 mm - -25 mm. It is observed that the x-component of velocity is approximately 10 – 15 m/s higher for the crossflow seeded case. At X = 10 mm and 15 mm the y-component of velocity is higher for the jet seeded case and this is mainly due to the lack of particles within the wake of the jet for the crossflow seeded case. Due to this reason the wake structure and the recirculation region could not be captured by seeding the crossflow. Thus, these observations confirm that there is a bias in the velocity magnitude when seeding the jet versus the crossflow and the velocity data needs to be carefully interpreted. However, as the focus of the current study is characterizing the structure and dynamics of the wake vorticity, henceforth, all the discussions are based on the velocity fields obtained by seeding the jet.

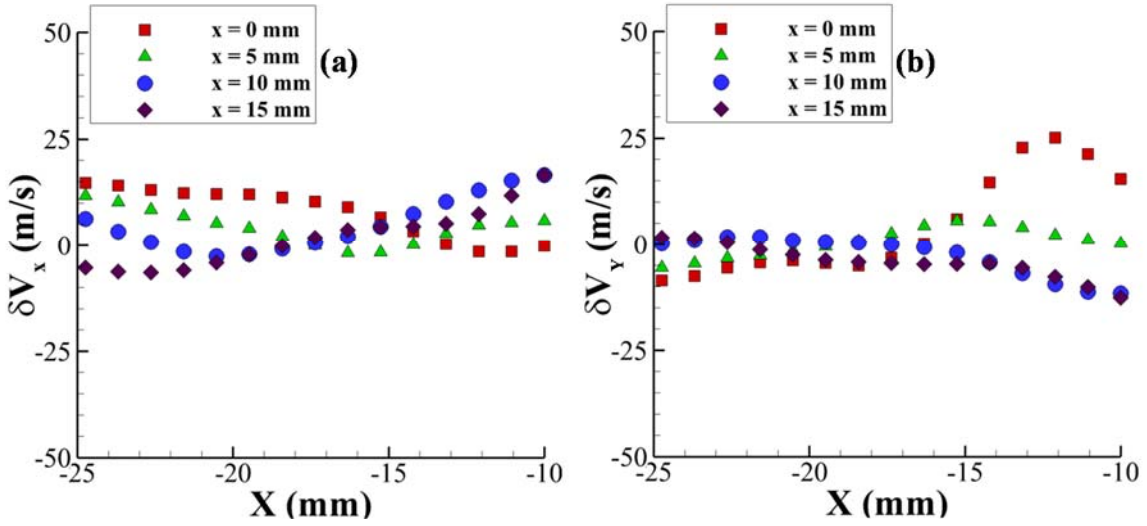

Figure 3.18. Streamwise variation of the velocity difference of the x-component of velocity (a) and y-component of velocity (b) obtained by subtracting the velocity field obtained by seeding the jet from the velocity field obtained by seeding the crossflow for reacting jet case of J = 3 and ϕ_{jet} = 0.9 at Z = 5 mm.

3.5 Instantaneous Velocity Field

In this section instantaneous velocity field of the non-reacting JICF and the reacting JICF has been discussed. Velocity data were collected for duration of 0.5 s at a repetition rate of 10 kHz, providing enough sampling time to extract accurate time-averaged fields and flow statistics. The velocity measurements at 10 kHz discussed in this section provided time-resolved information on the transient wake structure of the reacting jet.

3.5.1 Non-Reacting Flow Field of RJICF

A sequence of instantaneous velocity vectors overlaid on velocity magnitude, the ω_z magnitude and corresponding instantaneous flow streaklines of the non-reacting jet J = 8 at Z = 5 mm measurement plane, is shown in Figure 3.19. The velocity magnitude shows that the flow field comprises of three main regions, the upper and lower shear layer with high velocity fluid and the inner recirculation region. At time = 0.1 ms, a vortex structure

with counter-clockwise rotation (red color) at LSL, X = 0 mm, Y = -17.5 mm and a vortex structure with clockwise rotation (blue color) at USL, X = 10 mm, Y = 0 mm is seen. The time evolution of the flow structures can be seen from time = 0.1 ms – 0.4 ms. The detected flow structure exhibits strong vorticity. The two main sources of vorticity for this flow field are the mixing layer between the jet and crossflow fluid, and from within the nozzle inner wall boundary layer. The sequence of velocity vectors shows that the vorticity originates near the nozzle and eventually sheds off in the inner wake region further downstream of the nozzle. Thus, the non-reacting jet case provides important insight into the dynamics of the dominant wake structure showing the presence of periodic asymmetric vortex structures. The instantaneous flow streaklines show the formation and convection of the wake structures.

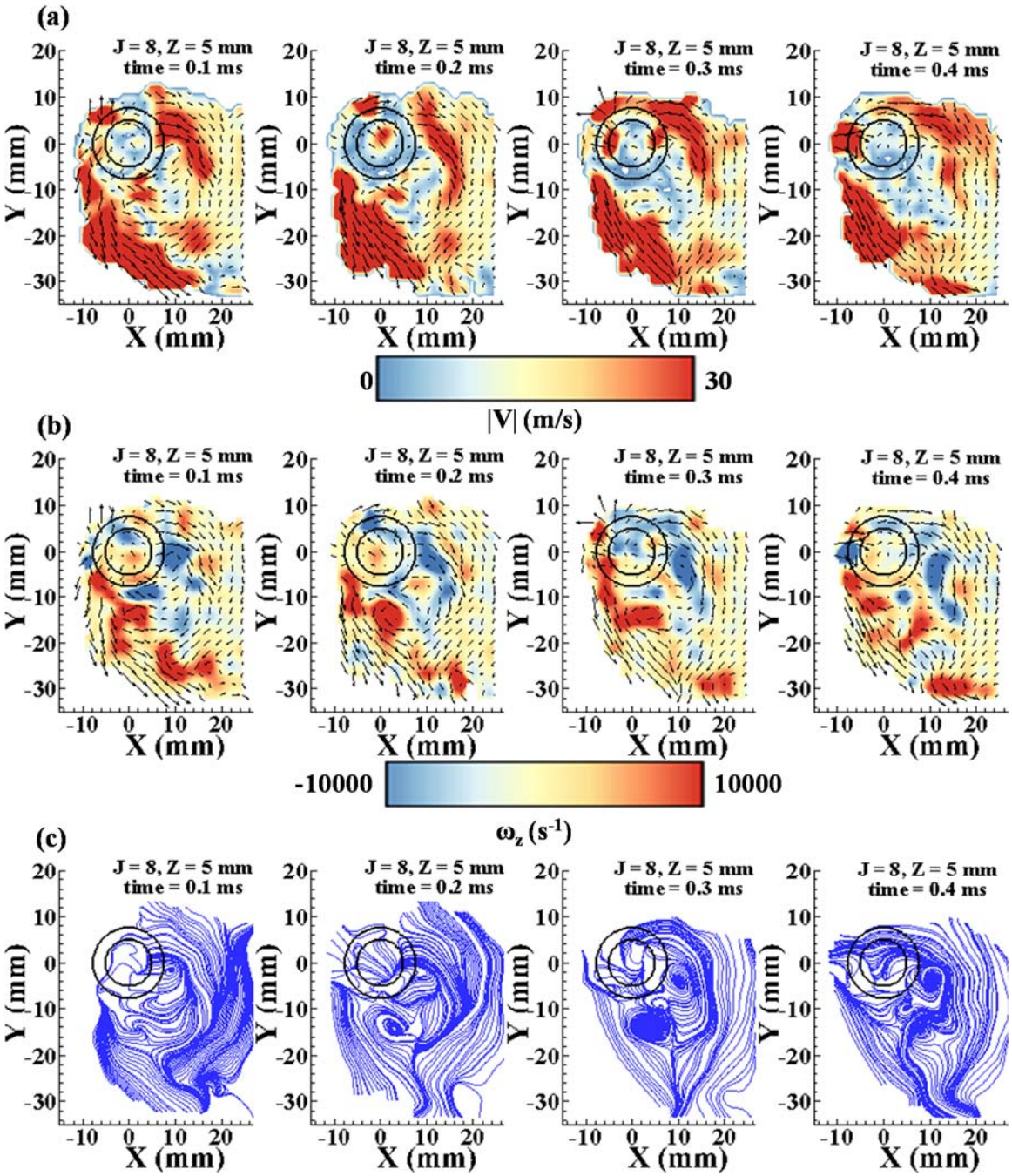

Figure 3.19. Instantaneous vector field of the non-reacting jet case, J =8, measured at Z = 5 mm showing the a) velocity magnitude, b) vorticity magnitude and c) flow streaklines indicating the temporal evolution of the wake structure.

3.5.2 Reacting Flow Field of RJICF

A sequence of instantaneous velocity vectors of reacting jet, J = 3, ϕ_{jet} = 0.9, at Z = 5 mm, overlaid on top of x-velocity, y-velocity and z-vorticity magnitude color map is shown in Figure 3.20. The x-velocity magnitude ranges from -30 – 60 m/s, here the red color represents maximum positive x-velocity and blue color represents minimum negative x-velocity. The flow field comprises of three main regions, the upper and lower high speed regions and the recirculation region, as discussed previously. The inner wake region of the jet is surrounded between USL and LSL with a recirculation region with negative x-velocity. Figure 3.20b shows the same sequence of velocity vectors overlaid on y-velocity. The jet fluid provides a blockage to the incoming crossflow fluid as a result the fluid elements at the interface of crossflow and jet tend to accelerate around core of the jet leading to a positive y-velocity above the injector and a negative y-velocity below the injector. The recirculating region of the flow field has a positive y-velocity. Figure 3.20c shows the vorticity magnitude overlaid on the instantaneous velocity vector. At time = 0.1 ms, a vortex structure with counter-clockwise rotation (red color) at LSL, X = 0 mm, Y = -17.5 mm and a vortex structure with clockwise rotation (blue color) at USL, X = 10 mm, Y = 0 mm is seen. The vortex structure at LSL convects along the mean flow direction and the vortex structure at USL is entrained in the recirculation region. The detected flow structure exhibits strong vorticity magnitudes with $\pm 20{,}000\ s^{-1}$. The most noticeable observation is that the vorticity magnitude for the reacting jet case is found to be twice as much as observed for the non-reacting jet, which suggests that local heat release and density gradient add to the vorticity strength and create a stronger recirculation region. Similar to the non-reacting flow cases, the vorticity originates near the nozzle and convects

downstream along the direction of the mean flow. The dynamics of the wake of the jet is similar to the wake of a bluff body. The velocity vectors show that the upright wake vortices do not necessarily appear in counter-rotating pairs. Unlike the Karman vortex street, the instantaneous flow structures are quite disordered in appearance. A sequence of instantaneous flow streaklines shown in Figure 3.21, shows the appearance and evolution of the flow structures. At time = 0.1 ms a flow structure in the LSL is seen at X = 5 mm, Y = -15 mm. At time = 0.2 ms another flow structure at USL appears at X = -2.5 mm, Y = -10 mm. The flow structure in LSL convects downstream and is no longer seen at time = 0.6 ms. Similarly, the flow structure in USL convects downstream and moves from X = -2.5 mm at time = 0.1 ms to X = 20 mm at time = 0.8 ms, during which another flow structure appears in the LSL at time = 0.8 ms. The sequence of instantaneous streaklines captures the time evolution of the flow structures, the flow structures appear alternately in the LSL and USL and convect away with the mean flow or dissipate in the recirculation region.

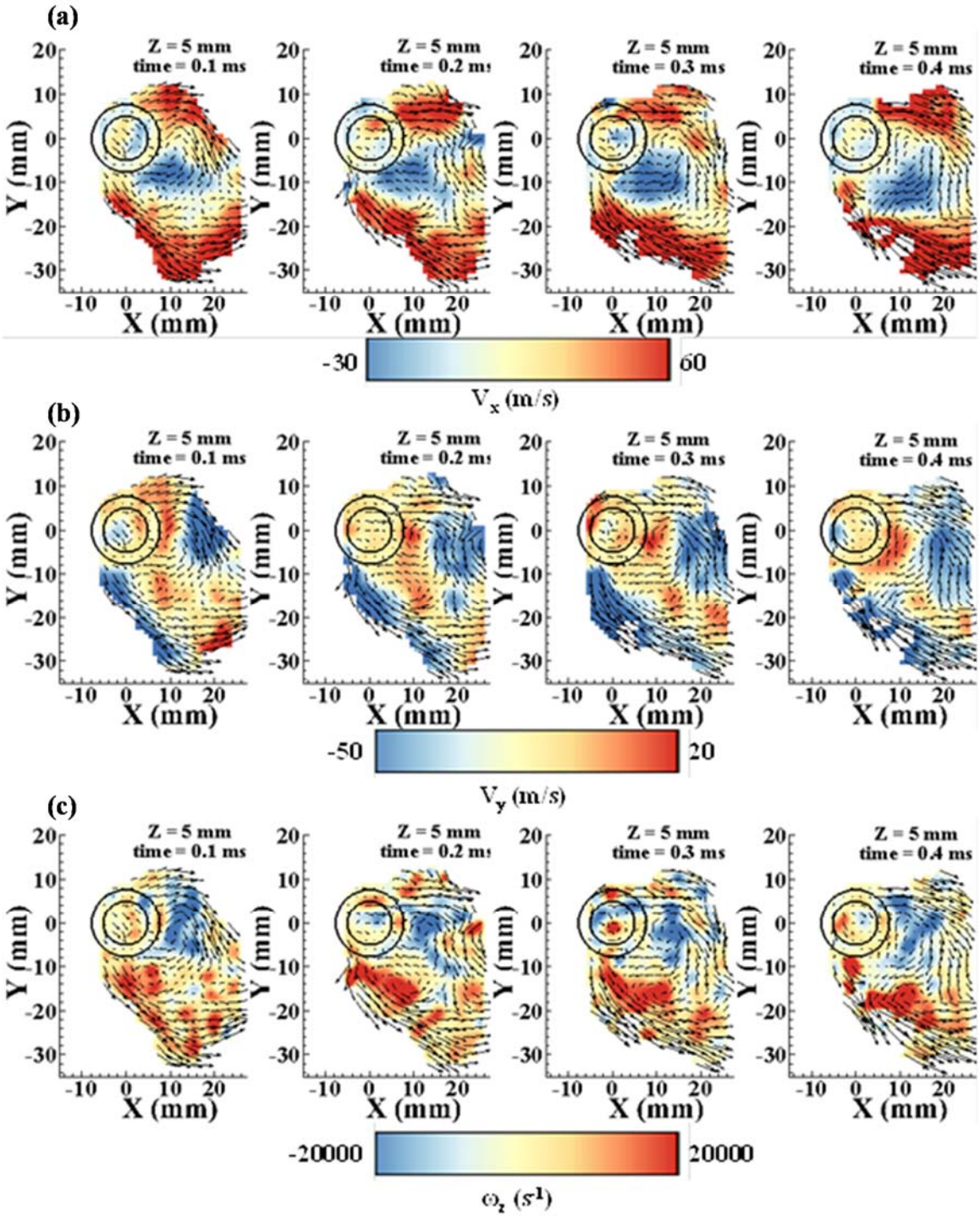

Figure 3.20. Instantaneous vector field of the non-reacting jet case, J =8 ϕ_{jet} = 0.9 at Z = 5mm showing the a) x-velocity magnitude, b) y-velocity magnitude and c) vorticity magnitude indicating the temporal evolution of the wake structure.

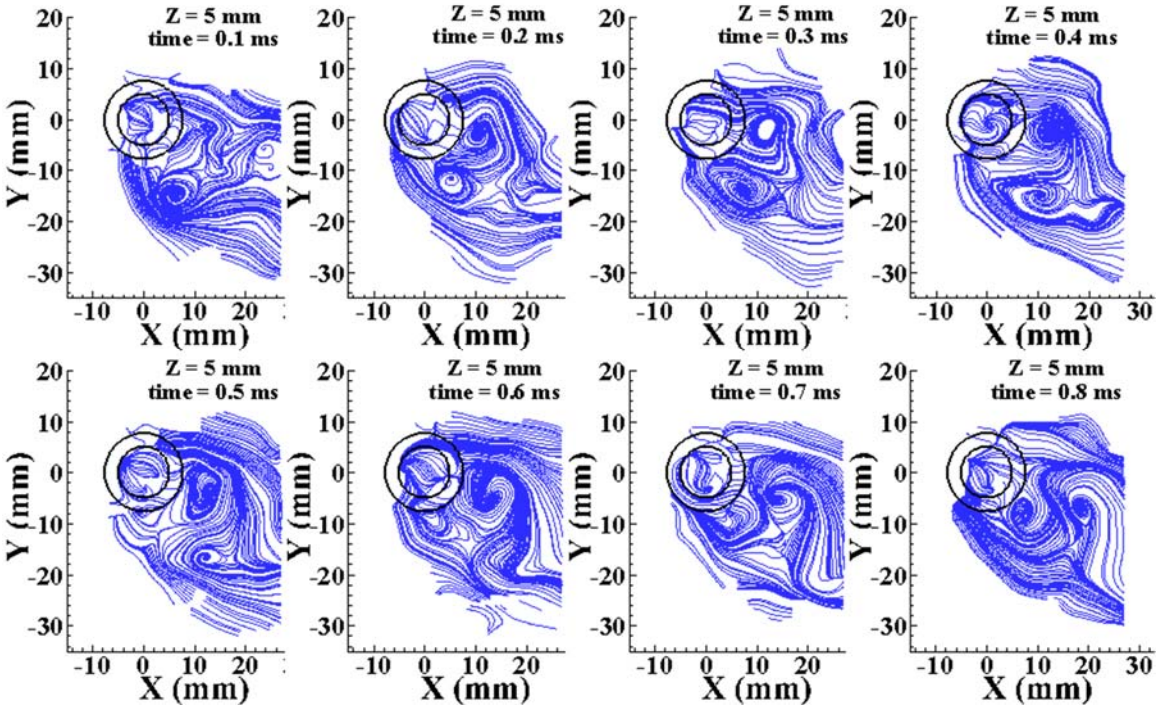

Figure 3.21. Instantaneous flow streaklines of the non-reacting jet case, J =8 ϕjet = 0.9 at Z = 5mm showing the temporal evolution of the wake structure.

3.6 Particle Mie Scattering

3.6.1 Non-Reacting JICF

The size and structure of the shear layer flow structures can be determined from the instantaneous Mie scattering images. A sequence of instantaneous Mie scattering images of non-reacting JICF, J = 8, measured at Z = 5 mm, is shown in Figure 3.22. At any time instance within the span of the laser sheet a train of maximum two structures can be seen on either side of the jet. In this section the instantaneous Mie scattering images are used to analyze the frequency of the flow structures in the near wake region of the flow-field. A 10 mm by 10 mm window is chosen between spatial locations, X = 10 mm – 20 mm, Y = -10 mm – 0 mm, and a spatially averaged intensity is calculated at every time instances. A power spectral density is computed from the time variation of the spatially averaged

intensity field computed at the windowed region. Two distinct peaks in the frequency spectrum is evident in Figure 3.23, corresponding to 170 Hz and 340 Hz. A Strouhal number (*St*) is computed based on the peak frequency (*f*), jet exit diameter (d_{JET}) and mean crossflow velocity (U_{CF}), as defined as in Equation (3.2),

$$St = \frac{f d_{JET}}{U_{CF}} \tag{3.2}$$

Based on the spectral analysis of the spatially averaged Mie scattering intensity field it is seen that the frequency of the flow structures in the near wake region is 170 Hz, which corresponds to a St = 0.188 based on the jet exit diameter (d_{JET} = 10 mm) and mean crossflow velocity (U_{CF} = 9 m/s).

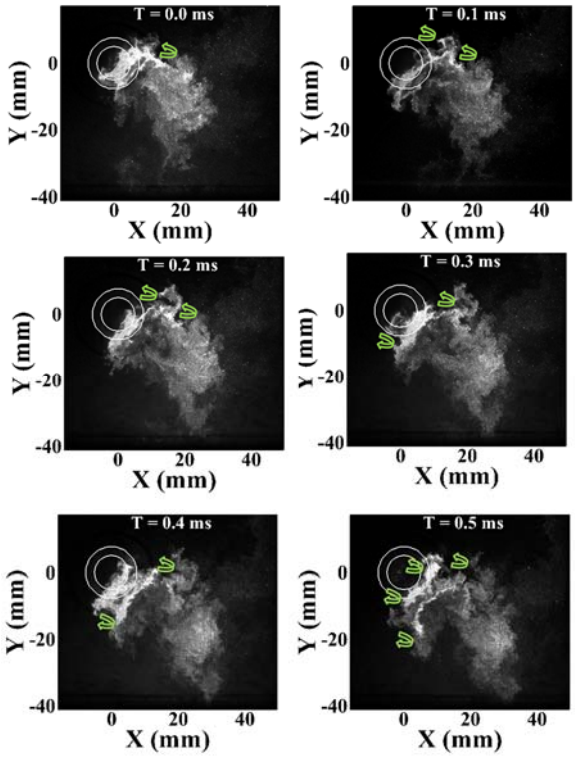

Figure 3.22. A sequence of background subtracted PIV images for the non-reacting jet case of J =8, at Z = 5 mm from the nozzle exit plane. The images reveal that the swirling crossflow has a strong influence on the trajectory of the transverse jet forcing it diagonally (of the image) downwards.

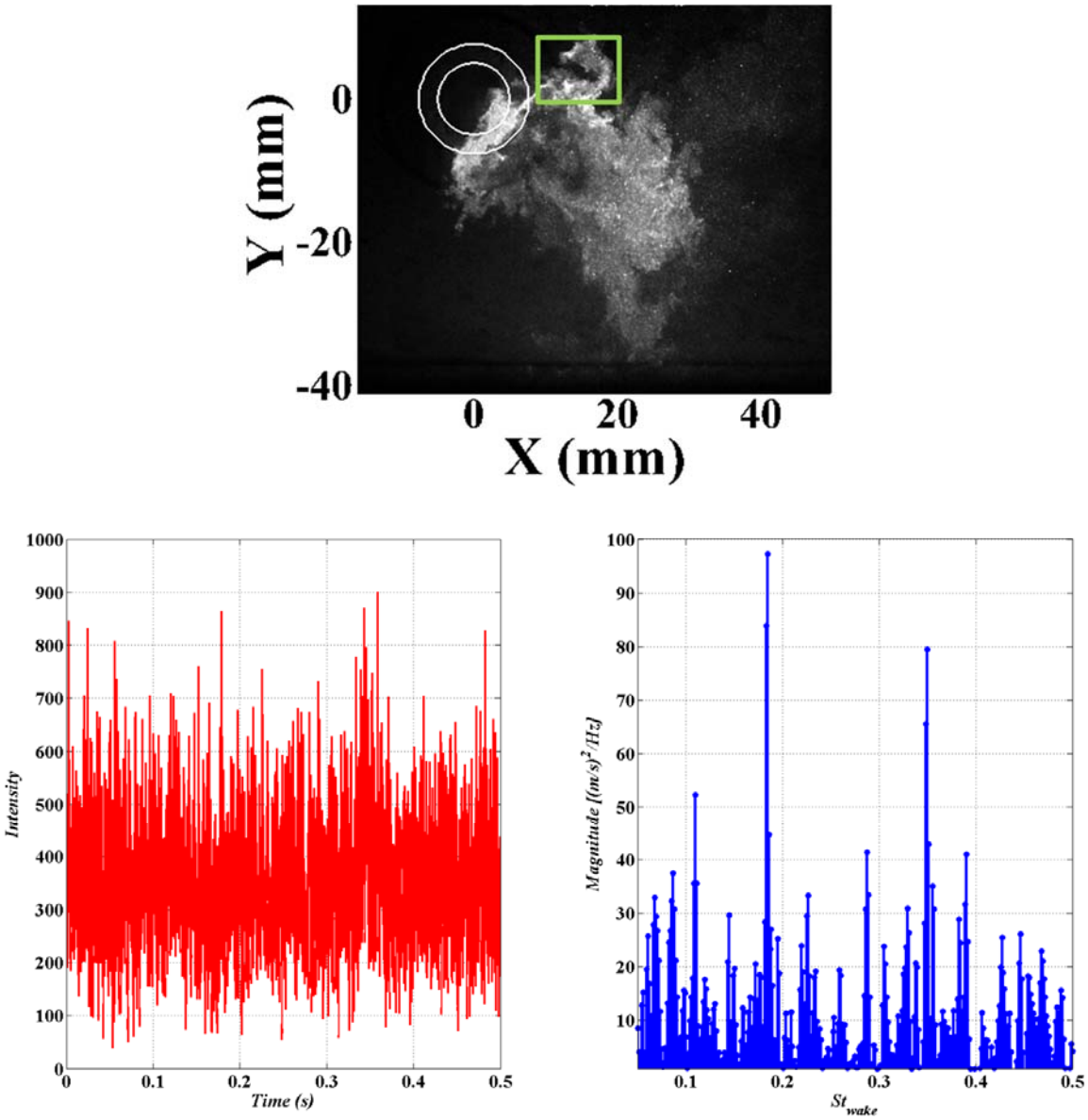

Figure 3.23. Instantaneous variation of intensity within the windowed region of the flow field and the corresponding spectral content showing two peaks at f_{wake} = 166 Hz and 320 Hz, for non-reacting jet J = 8, measured at Z = 5 mm.

3.6.2 Reacting JICF

The size and structure of the shear layer flow structures can be determined from the instantaneous Mie scattering images. A sequence of instantaneous Mie scattering images of reacting JICF, J = 8, ϕ_{JET} = 0.9, measured at Z = -5 mm, is shown in Figure 3.24. It is

clear from the Mie scattering images that there is a continuous entrainment of particle seed in this plane. The instantaneous Mie scattering images are used to analyze the frequency of the flow structures in the wake of the injector. A 10 mm by 10 mm window is chosen between spatial locations, X = 10 mm – 20 mm, Y = -5 mm – 5 mm, and a spatially averaged intensity is calculated at every time instances. A power spectral density is computed from the time variation of the spatially averaged intensity field computed at the windowed region. A peak in the frequency spectrum is evident in Figure 3.25, corresponding to 685 Hz, which corresponds to a St = 0.288 based on the outer wall diameter (D = 15 mm) of the injector and mean crossflow velocity (U_{CF} = 36 m/s).

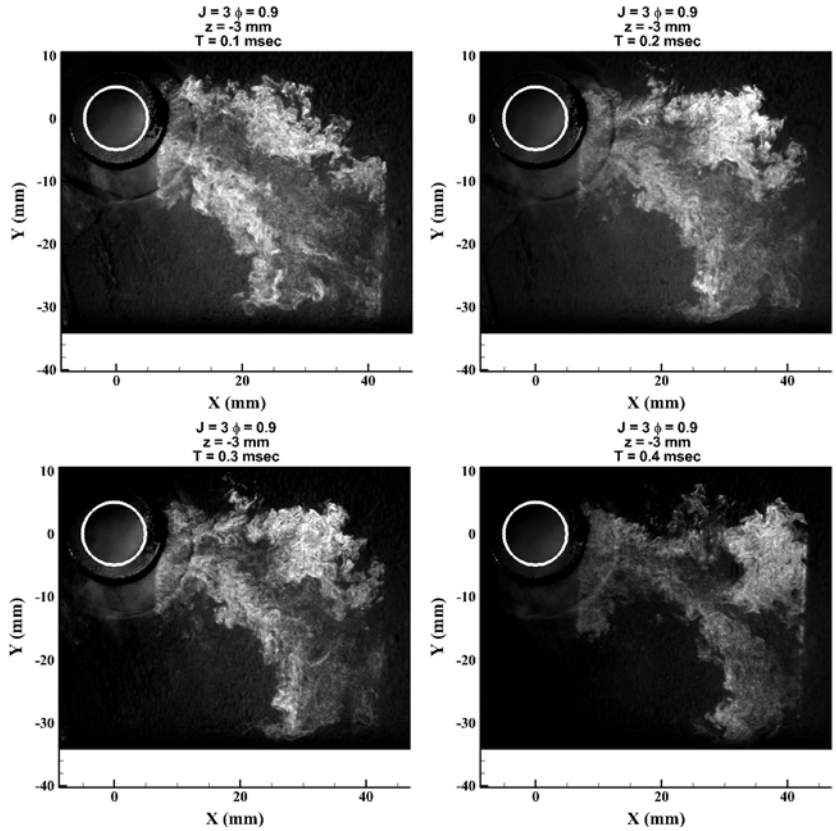

Figure 3.24. A sequence of background subtracted PIV images for the reacting jet case of J =8, ϕ_{jet} = 0.9 at z = -5 mm from the nozzle exit plane. The images reveal that the swirling crossflow has a strong influence on the trajectory of the transverse jet forcing it diagonally (of the image) downwards.

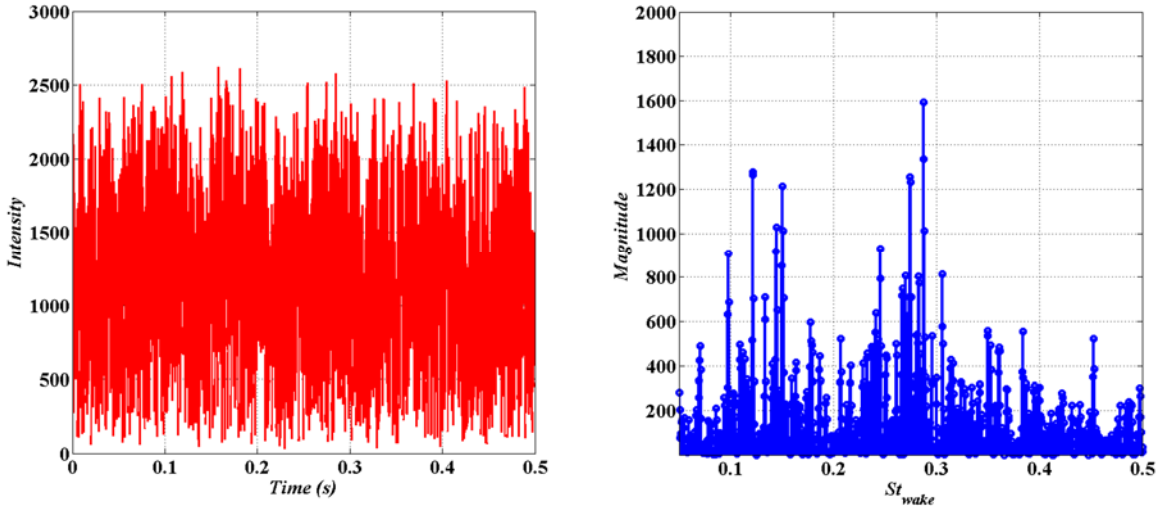

Figure 3.25. Instantaneous variation of intensity within the windowed region of the flow field and the corresponding spectral content showing peak at f_{wake} = 675 Hz, for reacting jet case of J = 8, ϕ_{jet} = 0.9 at z = -5 mm.

3.7 Turbulent Length Scale and Flow Field Dynamics

3.7.1 Integral Length Scales

The two-point correlation function has been used in highly turbulent and non-homogenous flow fields, such as, swirling flow, free shear jet flows, temporally evolving wakes etc., to compute the integral length scales[66][90][91]. A self-similar two-point correlation profile implies that the turbulent processes producing and dissipating energy at different length scales are in equilibrium as the flow evolves downstream. However, in a highly three dimensional reacting flow field a self-similar two-point correlation profile may not be observed. Here, the non-reacting velocity field is considered for the computation of the two-point correlation. A coordinate transformation was performed on the velocity field by rotating it by 45 degrees in a counterclockwise direction (this corresponds to the mean velocity angle calculated from the mean crossflow velocity field at the planes Z = 5, 10 and 15 mm), with the new coordinates X' and Y'. The coordinate transformation allows

computing the two-point correlation function along the streamwise and spanwise direction of the mean velocity vectors in the planes of measurement. Figure 3.26, shows the coordinate transformed time averaged velocity field overlaid on the vorticity magnitude of the non-reacting jet case of J = 8 measured at Z = 5 mm. The fluctuating component of the velocity field was sampled from a windowed region, shown in green rectangular box that includes the upper and lower shear layer region of the flow field. The region of interest was from X' = -2.5 – 27.5 mm and Y' = -15 – 15 mm.

The two-point correlation function is defined as shown in Equation (3.3),

$$\rho_{ij}(r) = \frac{<u_i'(x_o)u_j'(x_o+r)>}{<u_i'(x_o)u_j'(x_o)>} \tag{3.3}$$

The correlation function computed in the streamwise direction consists of combined characteristics of longitudinal and transverse two-point correlation function. However, the correlation function computed in the spanwise direction consists of the characteristics of the transverse two-point correlation function only. The streamwise (ρ_{ii}) and spanwise (ρ_{ij}) two-point correlation coefficients plotted as a function of normalized separation distance, r/d_{JET}, are shown in Figure 3.27a and b. Figure 3.27a shows that the streamwise two-point correlation coefficient for the lower shear layer region, $y'/d_{JET} < 0$, decays to zero within one jet diameter. However, for the upper shear layer region, $y'/d_{JET} > 0$, the correlation approaches to zero within two jet diameter. This implies the streamwise integral length scales are larger for the upper shear layer region of the flow field. Figure 3.27b, shows the variation of the transverse two-point correlation function. The trend indicates that closer to the nozzle exit, $x'/d_{JET} < 0.75$ the correlation value decays faster as compared to further downstream regions. The streamwise (Λ_{11}) and spanwise (Λ_{22}) integral length scales at a

given point, x_o, can be calculated by computing the area under the two-point correlation curve, as shown in Equation (3.4) [92],

$$\Lambda_{ij} = \int_0^\infty u_i'(x_o)u_j'(x_o + r)\ dr \tag{3.4}$$

Figure 3.28, shows the integral length scales computed in the streamwise and spanwise direction at measurement planes Z = 5, 10 and 15 mm. The integral length scales computed in the streamwise direction in all the three measurement planes show two peaks at y'/d_{JET} = -0.75 and 0.5 that corresponds to LSL and USL region of the flow field, respectively. The integral length scales computed in the spanwise direction increases monotonically along the streamwise direction, with length scales as large as the jet exit diameter being observed. This suggests a spatially evolving wake flow field. Across all the three measurement planes Z = 15 mm has smallest integral length scales. In the current experiment, the final interrogation window size provides a vector resolution of 0.83 mm, which extends to 4 and 12 grid points over the span of the smallest and largest computed integral length scales, respectively. With this resolution, the computation of spatial gradients, vorticity and strain rate could be performed with greater accuracy; however, analysis of flow properties based on spatial gradients needs to be carefully assessed due to the risk of aliasing and bias uncertainties.

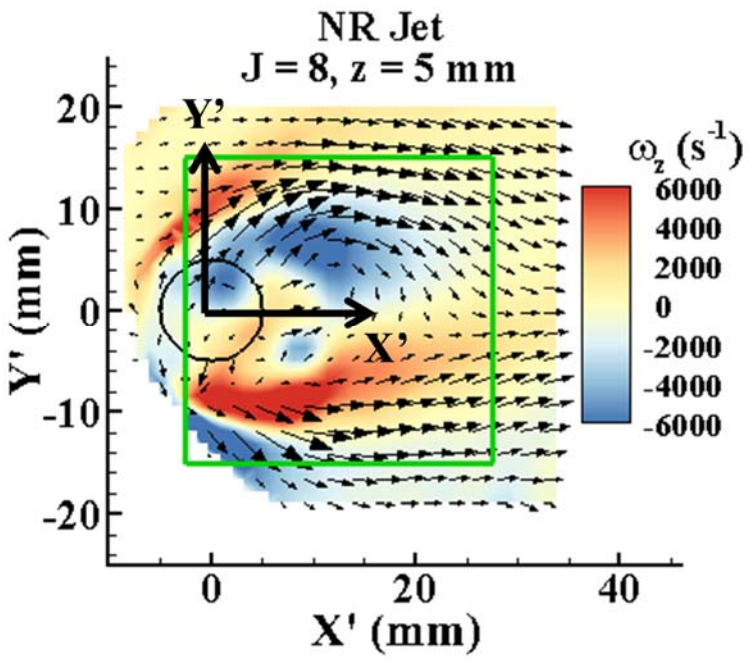

Figure 3.26. Coordinate transformed time averaged velocity vectors overlaid on top of z-vorticity contour map for non-reacting jet of J =8 measured at Z = 5 mm.

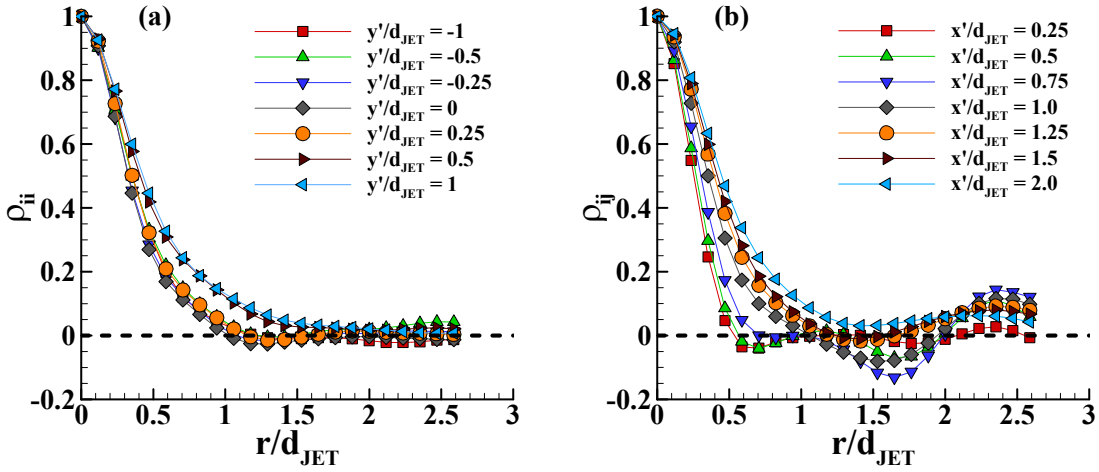

Figure 3.27. Spatial variation of (a) streamwise and (b) spanwise two-point velocity correlation coefficient for non-reacting jet, J = 8 measured at Z = 5 mm.

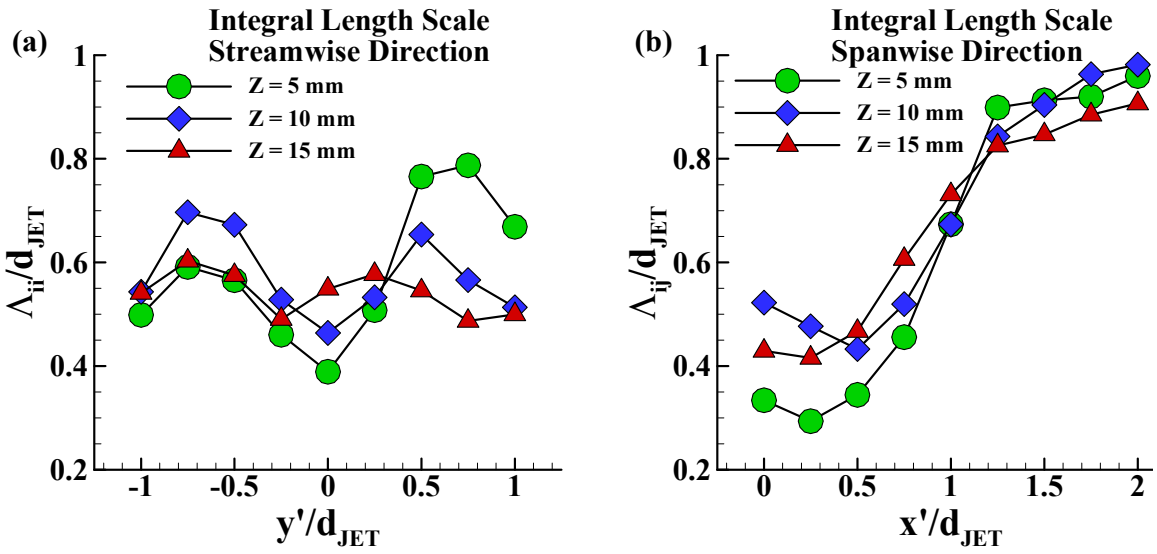

Figure 3.28. Spatial variation of (a) streamwise and (b) spanwise integral length scale for non-reacting jet, J = 8 measured at Z = 5, 10 and 15 mm.

3.7.2 Turbulent Kinetic Energy Spectra

The nature of turbulence in a reacting flow field is highly anisotropic. The energy-cascade hypothesis typically holds in a statistically averaged sense, but it does not does not describe the local instantaneous behavior of turbulence. In turbulent reacting flows, thermal energy is deposited at the smaller scales. In these scales, molecular diffusion dominates and fuel and oxidizer react, resulting in heat release. In fact, combustion represents a source of flow dilatation driven by thermal expansion or variable-density effects, which can deploy extra kinetic energy into the flow field through pressure-dilatation work [93]. This leads to a spatially non-homogenous flow field where the rate of production of turbulent kinetic energy and dissipation varies with time.

Figure 3.29 shows the longitudinal and transverse energy spectrum for the non-reacting jet case of J = 8 at z = 5 mm. The range of length scales plotted lies between the vector resolution of the flow field and the maximum size of the measurement plane. At wavenumbers greater than 2000 m^{-1} the energy spectra flattens. The vector resolution in

this experiment does not provide the complete range of scales, and as a result complete dissipation of the turbulent kinetic energy cannot be captured. The PIV measurement technique results in spatial averaging of the true velocity field, which has a broad band of length scales, into regions with discrete velocity vectors. The interrogation window filters out all the smaller length scales resulting in aliasing and bias in the velocity field. As a result the TKE spectra show an accumulation of energy at higher wavenumbers due to the accumulation of noise in the vector generation algorithm and aliasing effects.

One-dimensional streamwise and spanwise energy spectra are computed along the streamwise direction of the measurement plane for a sequence of 1000 vector fields. Figure 3.30, shows the longitudinal and transverse energy spectrum for the reacting jet case of J = 8, $\phi = 0.9$, at Z = 5 mm. The instantaneous nature of turbulent kinetic energy is found to be varying by an order of magnitude at each of the length scales over a period of 100 ms. The range of length scales plotted lies between the vector resolution of the flow field and the maximum size of the measurement plane. At wavenumbers greater than 2000 m^{-1} the energy spectra flattens. The vector resolution in this experiment doesn't provide the complete range of length scales as a result complete dissipation of the turbulent kinetic energy cannot be captured.

Figure 3.31 and Figure 3.32 shows TKE spectra measured at all the three planes, Z = 5 mm, 10 mm and 15 mm, for J =8 case and reacting jet fluids of H_2/N_2 and premixed NG/air. The computed TKE spectra are ensemble averaged over 5000 vector fields. When compared to the velocity field measured at all the three measurement planes, it is observed that the magnitude of TKE at the integral length scale drops with an increase in distance from the nozzle exit plane. This observation can be correlated to the relative size and

vorticity strength of the time-averaged wake structure as a function of z, as discussed in section 3.1. The vorticity strength of the wake structure decreases, and as a result the magnitude of TKE decreases with an increase in Z-plane. Thus, at Z = 5 mm the level of turbulence is highest resulting in highest rate of mixing and a strong entrainment of hot gases and burnt products into the wake of the jet. The magnitude of TKE at Z = 15 mm drops to a value that is approximately by half the magnitude of TKE at Z = 5 mm. It is evident from Figure 3.31a, b, and Figure 3.32a, b that the ensemble-averaged energy spectra of H_2/N_2 jets show higher TKE at the integral length scale than the premixed NG jets across all the measurement planes. This could be attributed to the higher jet Reynolds number and intense heat release at smaller scales for the H_2/N_2 jets that contribute towards the kinetic energy of the large scale structures.

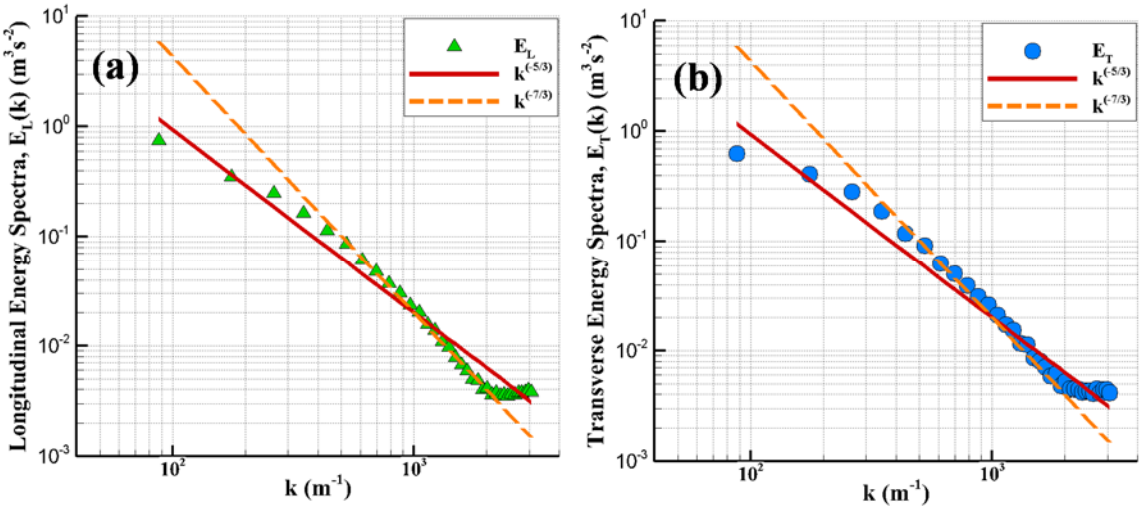

Figure 3.29. One dimensional (a)longitudinal and (b) transverse energy spectra plotted in the wave number space with $k^{-5/3}$ and $k^{-7/3}$ profiles for non-reacting jet case of J = 8 measured at Z = 5 mm.

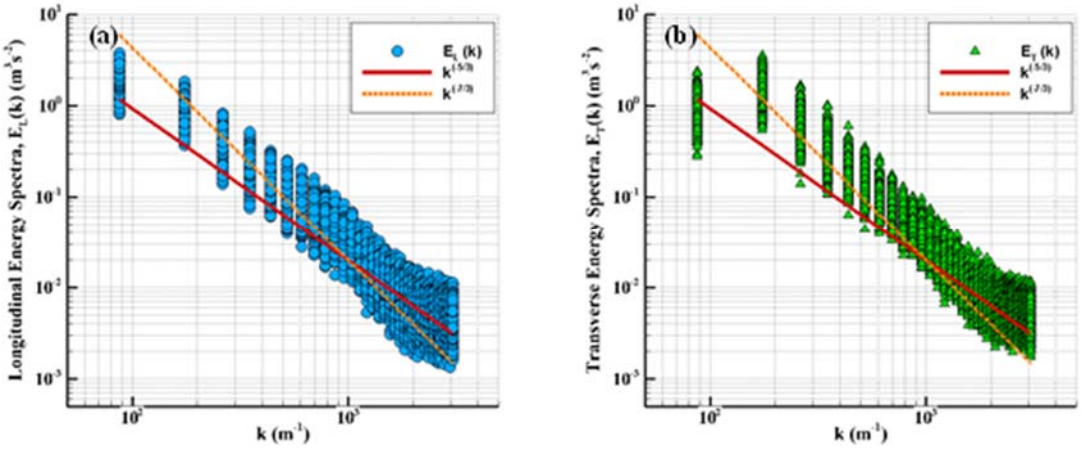

Figure 3.30. One dimensional (a)longitudinal and (b) transverse energy spectra plotted in the wave number space for a sequence of 1000 vector fields with $k^{-5/3}$ and $k^{-7/3}$ profiles for J = 8 premixed NG measured at Z = 5 mm.

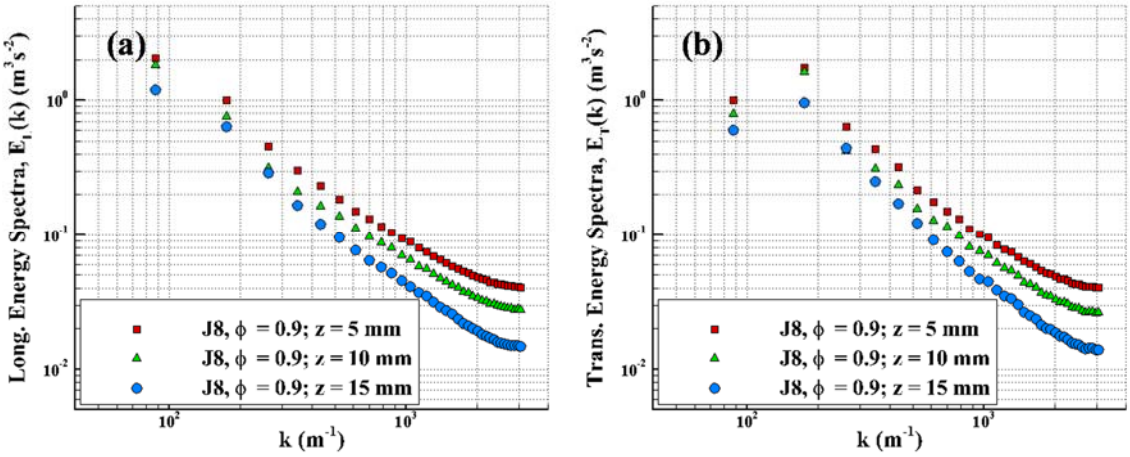

Figure 3.31. Turbulent kinetic energy spectra plotted in wave number space for J = 8 and reacting jet cases of NG-air premixed flame (a) longitudinal spectra, (b) transverse spectra, measured at Z = 5 mm, 10 mm and 15 mm.

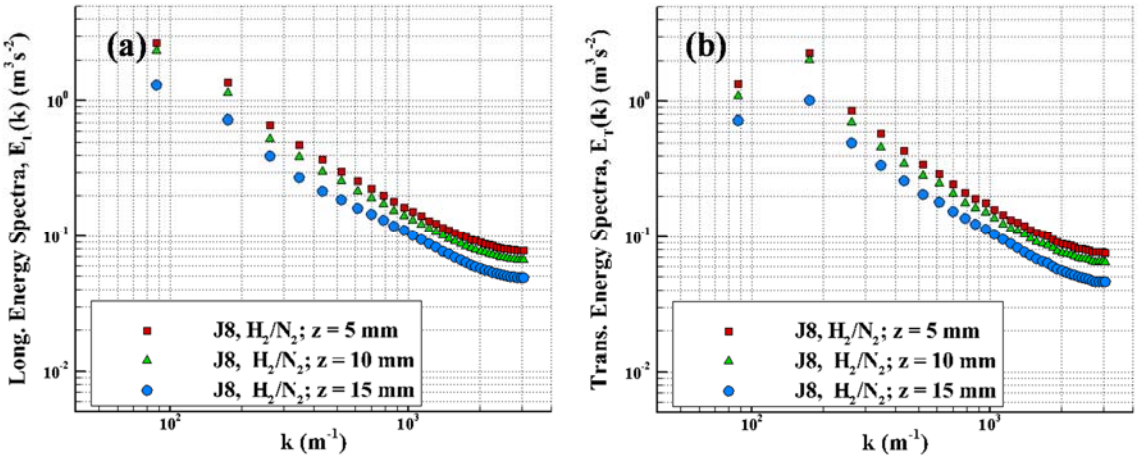

Figure 3.32. Turbulent kinetic energy spectra plotted in wave number space for J = 8 and reacting jet cases of NG-air premixed flame (a) longitudinal spectra, (b) transverse spectra and H_2/N_2 diffusion flame (c) longitudinal spectra, (d) transverse spectra, measured at Z = 5 mm, 10 mm and 15 mm.

3.7.3 Velocity Power Spectra

In a turbulent reacting flow, the velocity field has a broad spectrum of temporal scales, and measurements at 10 kHz can resolve some of these scales. In order to extract the wake dynamics, velocity fluctuation statistics are extracted from three locations in the flow field of J=3 and J=8 reacting jet cases for 40%H_2/60%N_2 jet fluid at Z = 5 mm, as shown in Figure 3.33. These three locations are identified as the lower shear layer (LSL), the upper shear layer (USL) and the recirculation region (RR). To characterize the dynamics of the wake of the jet, it is of interest to examine whether the vortical structures flow past a fixed point with a characteristic frequency. The power spectra of the x component of velocity (V_x), as shown in Figure 3.34 and Figure 3.35, are broad with multiple peaks in the frequency domain. However, the peak frequency is found to be the same for all the three locations in the flow field for reacting jet cases: 552 Hz for the J=3 case and 565 Hz for the J=8 case. A wake Strouhal number (St_{wake}) is computed based on

the peak frequency (f_{wake}), jet exit diameter (d_{JET}) and mean crossflow velocity (U_{CF}), as defined as in Equation (3.5),

$$St_{wake} = \frac{f_{wake}D}{U_{CF}} \tag{3.5}$$

In earlier studies of the wake of an isothermal transverse jet [42][43], the wake vortices were well characterized. The Strouhal number corresponding to the wake vortex shedding in these studies ranged between 0.1 – 0.15. Similarly, based on our analysis, the wake Strouhal number (St_{wake}) corresponding to the velocity fluctuations within the wake of the jet is found to be 0.15, which could imply that this corresponds to the wake vortex shedding. Based on this observation of the characteristic frequency of the wake, it is hypothesized that the associated dynamics are the result of wake vortex shedding around the jet. Thus, with an increase in the momentum flux ratio the change in the frequency of velocity fluctuation is found to be minimal.

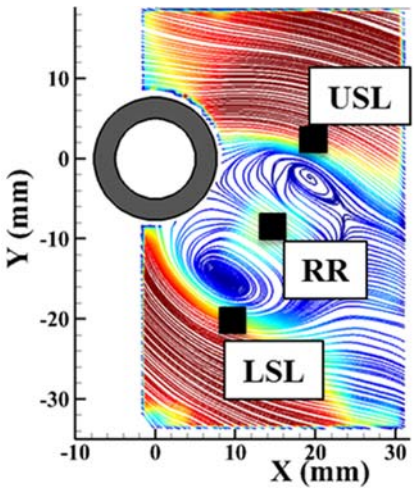

Figure 3.33. Time averaged flow streamlines indicating the three monitor points, viz., upper shear layer (USL), recirculation region (RR) and lower shear layer (LSL)used to extract flow dynamics.

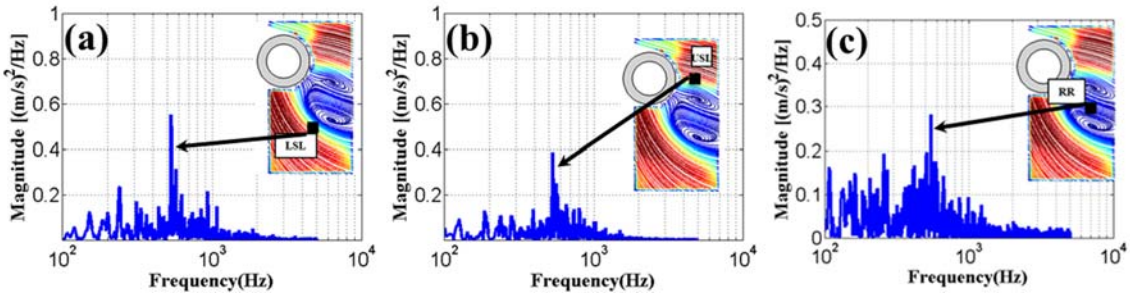

Figure 3.34. Velocity power spectra of the x component of velocity (V_x) extracted from a) upper shear layer (USL), b) lower shear layer (LSL) and recirculation region (RR) for J=3 case at Z = 5 mm. The plot indicates presence of a dominant peak in frequency at f = 552 Hz.

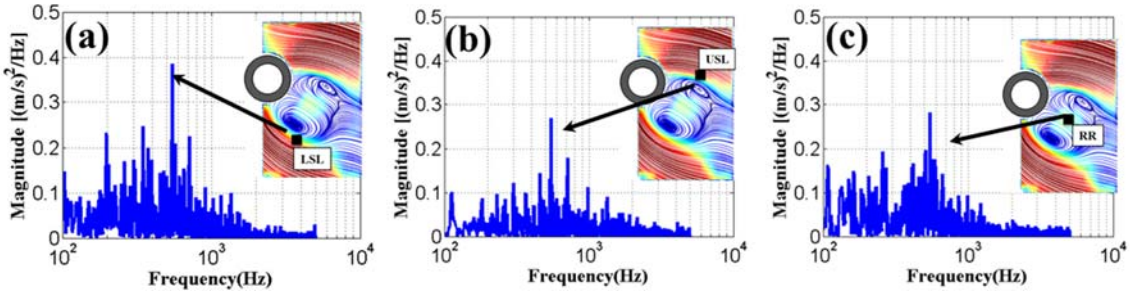

Figure 3.35. Velocity power spectra of the x component of velocity (V_x) extracted from a) upper shear layer (USL), b) lower shear layer (LSL) and recirculation region (RR) for J=8 case at Z = 5 mm. The plot indicates presence of a dominant peak in frequency at f = 565 Hz.

3.7.4 Effect of Jet Velocity Profile

Two types of injectors are used for the PIV measurements discussed in this work. One type of injector was a straight cross-section tube that leads to a parabolic velocity profile to the jet fluid. The second type of injector had a contoured profile which leads to a uniform top-hat velocity profile. The contoured injector has a profile based on a fifth order polynomial [36]. New et al., [45], studied the effect of jet velocity profile on the flow-field of a round jet in crossflow was demonstrated. The authors had considered top-hat and parabolic velocity profiles. It was shown that there is a delay in the formation of

leeward vortices due to a thicker shear layer associated with a parabolic JICF when compared to the top-hat JICF at a similar J. This delay leads to reduction in the rate of entrainment of crossflow fluid by a parabolic JICF. One of the most significant findings of this research is the shift in the wake Strouhal number with change in the jet velocity profile. The values of the wake Strouhal number computed at all the measurement planes for the non-reacting and reacting JICF cases, with parabolic velocity profile, are shown in Table 2. The St_{wake} is found to be between of 0.128 – 0.157 for all the JICF/RJICF cases. The St_{wake} for non-reacting jets are lower than that for the reacting jets. Thus, heat release has a role in increase in the St_{wake}, however, the exact nature of dependence on heat release that leads to an increase in St_{wake} is still unclear. It is also evident that there is a consistent reduction in St_{wake} with an increase in Z separation distance. This is due to the fact with an increase in Z the jet core expands leading to an increase in the effective cross-section of the jet in the Z-plane. As a result the time scale of wake vortex shedding increases leading to a drop in the St_{wake}. The peak frequencies for the non-reacting jet cases are found to be one-third of the peak frequencies for reacting jet cases. The crossflow mean velocities for the non-reacting and reacting cases are 13 m/s and 36 m/s, respectively. Thus, it can be concluded that the dynamics of the wake flow field of the reacting jet are more strongly dependent on the crossflow velocity than on the jet injection parameters. Table 3 shows the wake Strouhal number calculated at all the measurement planes for the reacting and non-reacting jets with a top-hat velocity profile. An increase in the wake shedding frequency and the corresponding St_{wake} is evident for the all the JICF cases with top-hat velocity profile. The St_{wake} is found to be between 0.18 – 0.23, indicating a faster rate of entrainment into the wake of the jet, an observation similar to New and Lim. Thus, there

is a significant increase in the rate of entrainment and mixing of the crossflow and jet fluid with a top-hat jet velocity profile. Again, there is a consistent reduction in the St_{wake} with an increase in nozzle separation distance for all the reacting and non-reacting JICF cases.

The time averaged vorticity field derived from the velocity measurement at plane Z = 5 mm for both non-reacting and reacting jet cases, as shown in Figure 3.36, further indicate the effect of jet velocity profile. The vorticity magnitude as well as the span of the mean vortex structure is larger for top-hat jet velocity profile as compared to parabolic jet velocity profile. Similar comparison has been reported for an iso-thermal jet in crossflow [45]. This suggests the rate of entrainment of crossflow fluid would be faster for a top-hat jet velocity profile.

Another interesting finding was the Strouhal number calculation in the wake of the injector at Z = -5 mm. The flow-field is similar to that of wake of a cylindrical-bluff body and the wake Strouhal number for the reacting jet cases is found to be between St_{wake} = 0.28 -0.295. It is important to note that the Strouhal number at this plane is calculated based on the injector outer wall diameter, D = 15 mm. In a previously reported work on a bluff-body wake stabilized reacting flow the Strouhal number based on the wake vortex shedding frequency was calculated to be approximately 0.28. Thus, the computed value of St_{wake} in this study closely corresponds to a reported value in the literature. Figure 3.37, summarizes the St_{wake} calculated at all the measurement planes for both non-reacting and reacting jet cases.

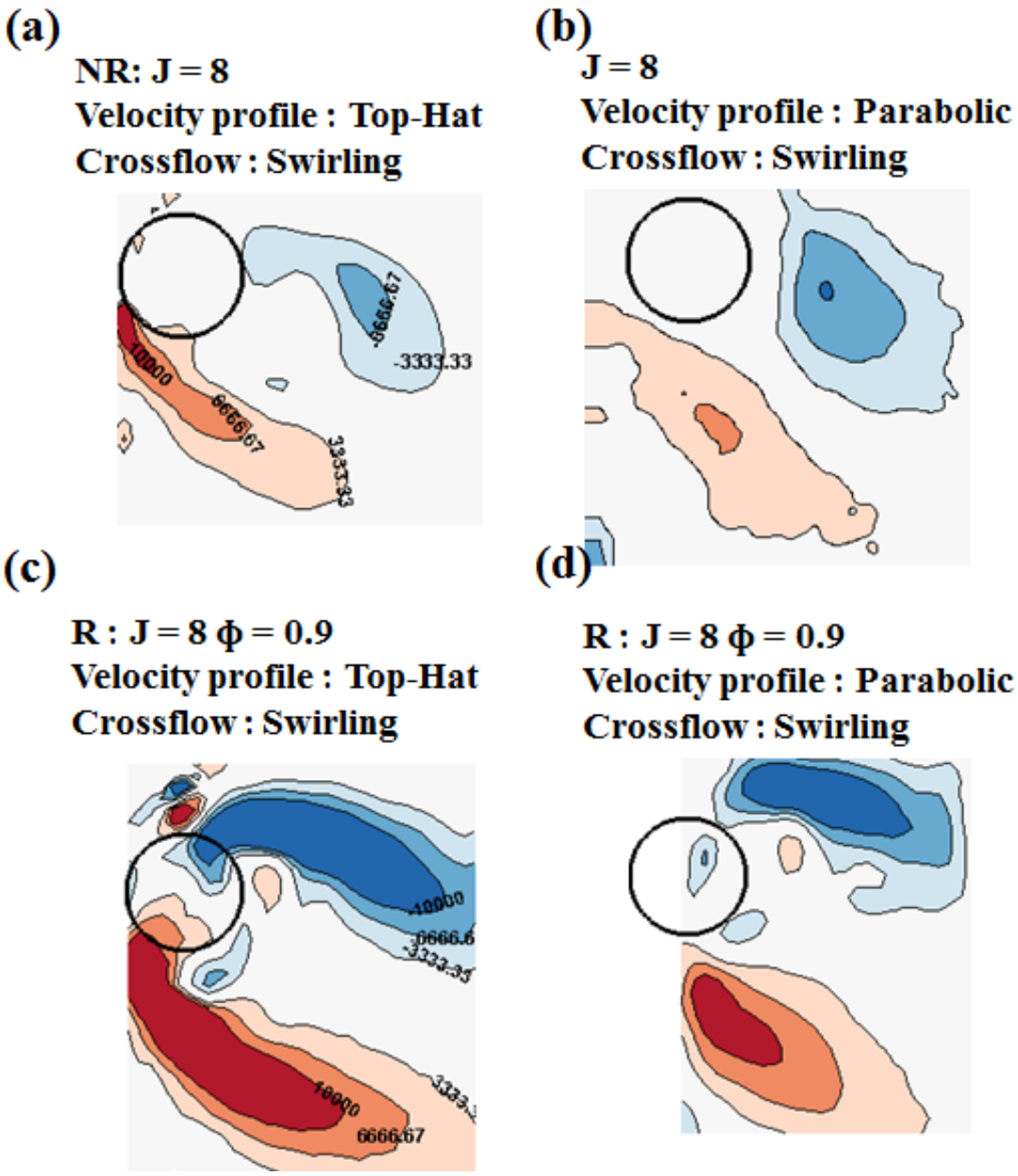

Figure 3.36. Time averaged vorticity field of (a) non-reacting jet with top-hat velocity profile, J = 8, (b) non-reacting jet with parabolic velocity profile, J = 8, (c) reacting jet with top-hat velocity profile, J = 8 ϕ = 0.9 and (d) reacting jet with parabolic velocity profile, J = 8 ϕ = 0.9, showing the effect of jet velocity profile on the vorticity in the wake of the jet.

Table 3.2. The wake Strouhal number, St_{wake} corresponding to the vortex shedding frequency for all the test cases with straight tube injector (parabolic velocity profile).

Case	TYPE	Momentum Flux Ratio, J	Jet	Fuel	Z (mm)	f_{wake} (Hz)	St_{wake}
1	NR	3	Hot Air	NA	5	172	0.132
					10	167	0.128
2	NR	8	Hot Air	NA	5	172	0.132
					10	170	0.131
3	R	3	Premixed NG	$\phi_{JET} = 0.9$	5	540	0.15
					10	512	0.142
4	R	8	Premixed NG	$\phi_{JET} = 0.9$	5	530	0.147
					10	498	0.138
5	R	3	H_2/N_2	40%/60%	5	552	0.153
6	R	8	H_2/N_2	40%/60%	5	565	0.157
					10	532	0.148

Table 3.3. The wake Strouhal number, St_{wake} corresponding to the wake vortices frequency for all the test cases with contoured profile injector (top-hat velocity profile).

Case	TYPE	Momentum Flux Ratio, J	Jet	Fuel	Z (mm)	f_{wake} (Hz)	St_{wake}
1	NR	3	Hot Air	NA	5	168	0.187
					10	167	0.186
					15	162	0.18
2	NR	8	Hot Air	NA	5	170	0.189
					10	166	0.184
					15	162	0.18
3	R	3	Premixed NG	$\phi_{JET} = 0.9$	-5	700	0.292
					5	742	0.206
					10	702	0.195
					15	693	0.193
4	R	8	Premixed NG	$\phi_{JET} = 0.9$	-5	685	0.285
					5	787	0.219
					10	737	0.205
5	R	3	H_2/N_2	40%/60%	5	736	0.204
					10	684	0.19
6	R	8	H_2/N_2	40%/60%	5	827	0.23
					10	748	0.208

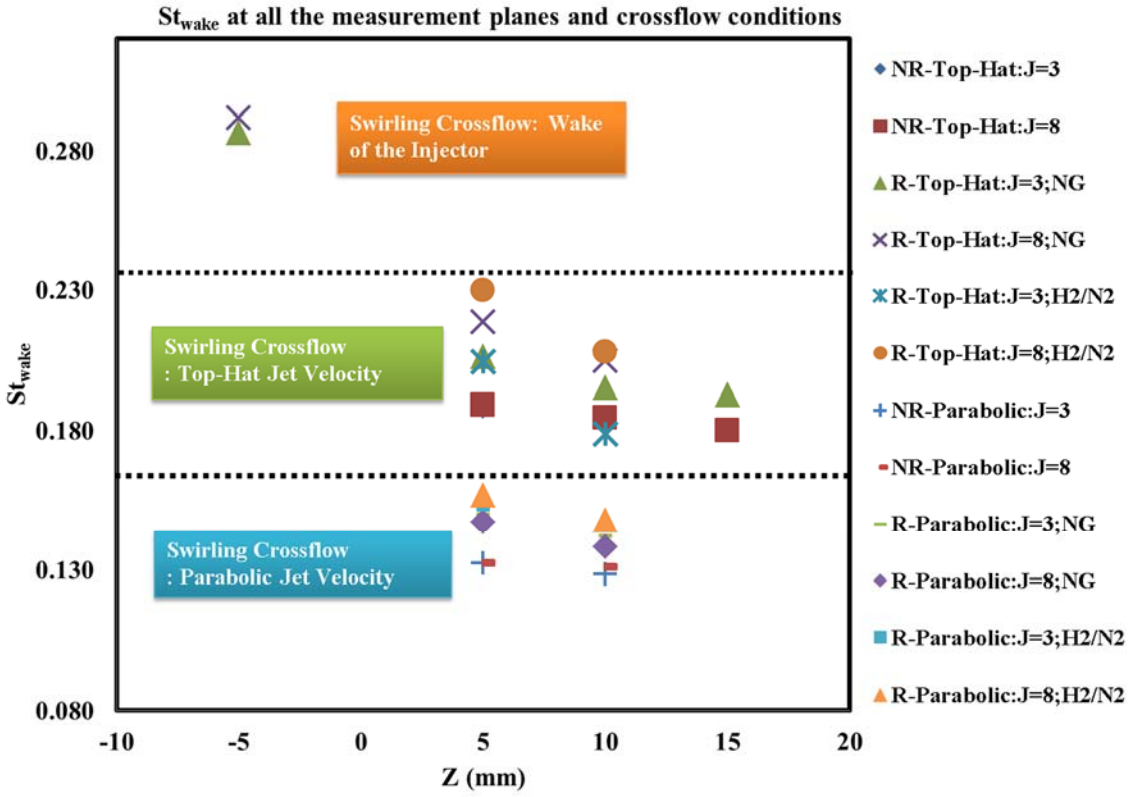

Figure 3.37. Wake Strouhal number calculated at all the measurement planes for both non-reacting and reacting jets comparing the effect of jet velocity profile.

3.8 Proper Orthogonal Decomposition (POD)

Proper orthogonal decomposition (POD) is a powerful mathematical tool used to extract coherent structures present in a flow field. It was introduced by Lumley et al.,[94], to extract coherent structures in turbulent flows. The present analysis uses the method of snapshot POD [95]. In the context of current study each instantaneous PIV measurement is considered to be a snapshot of the flow. Typically all the snapshots (5000 vector fields) collected at a measurement plane are considered for the analysis. The decomposition of the original data sets is based on optimizing the POD modes which form an orthonormal

basis. The objective is to express the data set as a finite series of orthonormal set of vectors as shown in Equation (3.6).

$$U_i'(x,y,t) \approx \sum_{k=1}^{M} a_{i(k)}\varphi_{i(k)}(x,y) \qquad (i = x,y) \tag{3.6}$$

Based on the approximation the series represents the function exactly as M tends to infinity. Here, M represents the number of POD modes. Consider a spatially dependent function $\varphi_{i(k)}$ (x,y), which can be chosen as a Fourier series, Legendre polynomials, Chebyshev polynomials and so on to from an orthonormal set of basis function. For different selections of the space-dependent function, $\varphi_{i(k)}$(x,y), the corresponding time-dependent function, $a_{i(k)}$(t) will be different. In the POD analysis, the spatial functions, $\varphi_{i(k)}$(x,y), are chosen to be orthonormal functions, as shown in Equation (3.7),

$$\int_X \varphi_{k1}(x)\varphi_{k2}(x)dx = \begin{Bmatrix} 1 & k_1 = k_2 \\ 0 & othrwise \end{Bmatrix} \tag{3.7}$$

The first step is to calculate the mean velocity field which is considered at the zeroth POD mode. The fluctuating components of the velocities are calculated by subtracting the mean from the instantaneous velocity field. The instantaneous and mean velocities are defined as shown in Equation (3.8) and Equation (3.9),

$$U_i(x,y,t) = U_{mean} + U_i' \tag{3.8}$$

$$U_{mean}(x,y) = \frac{1}{N}\sum_{N=1}^{N=total} U_i(x,y,t) \tag{3.9}$$

The spatial correlation matrix, C, for the x and y-components of the fluctuating component of velocity are computed as shown in Equation (3.10). The eigenvalue problem given by

Equation (3.11) is solved to extract the eigenvalues (λ) and eigenvectors (A) of the correlation matrix

$$C_i = [U_i'][U_i']^T \tag{3.10}$$

$$CA = \lambda A \tag{3.11}$$

The solutions are ordered in an increasing order of the eigenvalues $\lambda_1 > \lambda_2 > \lambda_3 > \ldots\ldots > \lambda_N$. The orthonormal basis of eigenvectors are computed as per Equation (3.12),

$$\varphi^i = \frac{\sum_{n=1}^{N} A_n^i u^n}{\left\|\sum_{n=1}^{N} A_n^i u^n\right\|} \tag{3.12}$$

Each snapshot is expanded in a series of POD modes and the corresponding temporal modes, a^i as defined in Equation (3.6). The temporal modes are computed by projecting the fluctuating component of velocity onto the vector space of POD modes given by Equation (3.13),

$$a^n = \psi^T u^n \tag{3.13}$$

Where, $\psi^T = [\varphi^1\ \varphi^2\ \varphi^3 \cdots \varphi^N]$. Finally the velocity snapshot is approximated based in Equation (3.6). It has been shown that the total kinetic energy in each of the modes is proportional to the corresponding eigenvalue, thus by sorting the modes and eigenvalues the most energetic POD modes correspond to the first few modes. If the relevant flow structures are seen in the first few POD modes then the entire flow field can be constructed using just the first few POD modes.

The POD analysis on the flow-field of non-reacting jet J = 8 at measurement plane Z = 5 mm is discussed here. Figure 3.38 shows the first six POD modes that contribute

42% of total kinetic energy of the flow field. POD mode structures are shown as velocity vectors overlaid on vorticity magnitude. The first POD mode represents the shear layer between the jet and the crossflow fluid. This is the most energetic mode and comprises of 22.2% of the total kinetic energy. The mean kinetic energy is also highest along the shear layers. The wake structure is seen in POD mode 2, 3 and 4 show a large single vortex structure aligned in the mean flow direction. The vortex structure in POD mode 2 is centered at approximately X = 6.5 mm and Y = -8.5 mm. POD mode 3 shows the vortex structure centered at X = 14 mm and Y = -14 mm and another structure appears above the injector location. A vortex structure is seen centered at X = 20 mm and Y = -20 mm, which seems to be linked to the same vortex structure seen in POD mode 2 and 3. The three modes together show a convection pattern of the wake structure. POD mode 5 and 6 show a counter-rotating pair of vortex structure at LSL and USL. The temporal information for these spatial eigenmodes is stored in the temporal mode coefficients (a^i). The power spectra obtained from the temporal coefficients of the POD eigenmodes of the velocity vectors can be used to identify the coherent structures have a characteristic frequency of 166 Hz. This corresponds to the same frequency seen in the velocity power spectra of J = 8 at Z = 5 mm, and provides a strong evidence that it is associated with the wake vortex dynamics. The time variation of filtered temporal modes of POD mode 2, 3 and 4 is shown in Figure 3.39. The phase difference between the three POD modes is clearly evident from the plot, which shows that POD mode 2 occurs first at a particular time instance followed by mode 3 and 4. This behavior corresponds to the convection of the detected wake vortex structure. Meyer et al., [96], had shown POD analysis of a non-reacting isothermal JICF

which showed very similar dominant POD modes and the wake vortex structure was found to be the most dominant flow structure.

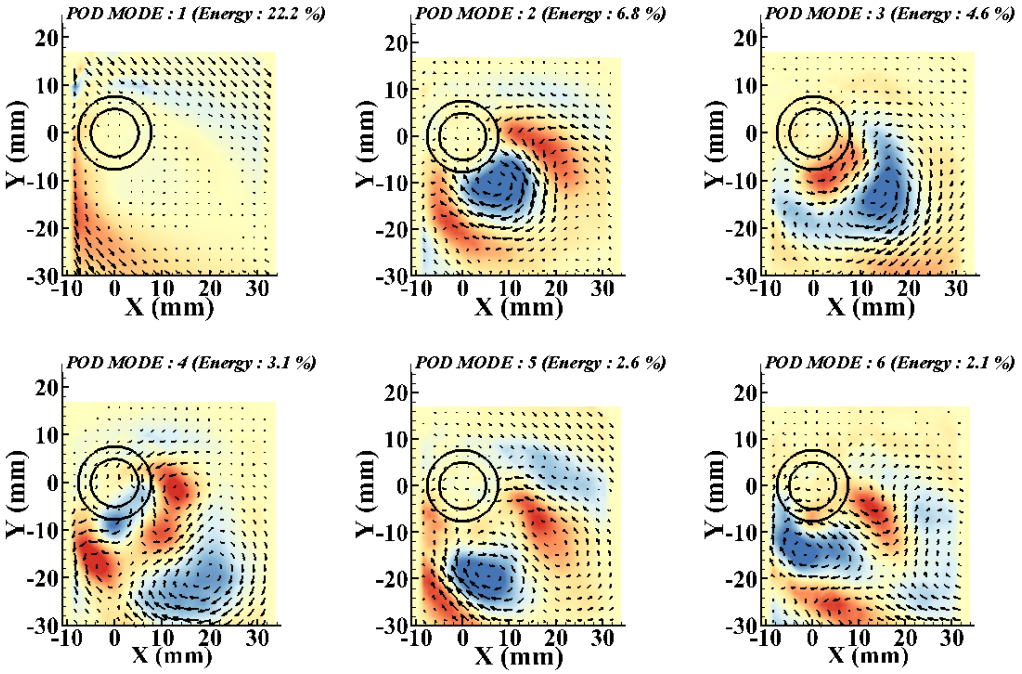

Figure 3.38. POD modes 1 – 6 for the non-reacting jet, J = 8, Z = 5 mm.

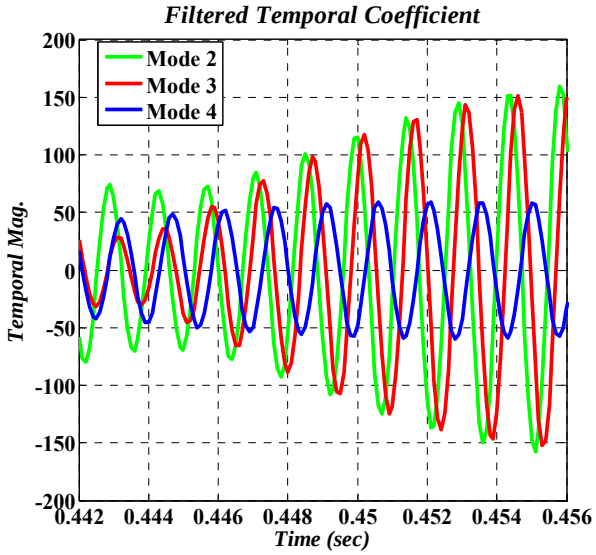

Figure 3.39. The time variation of the filtered temporal coefficient of POD modes 2, 3 and 4 computed from the velocity field J = 8, Z = 5 mm, showing the phase lag between the three modes.

Similarly POD analysis on the flow-field of reacting jet J = 8, ϕ_{JET} = 0.9 at measurement plane Z = 5 mm shows very similar coherent structures as seen in the non-reacting jet case. Figure 3.40, shows the first six POD modes that contribute 55.5% of total kinetic energy of the flow field. The first POD mode, which is also the most energetic mode, comprises of 39.4% of the total kinetic energy. Thus, compared to the non-reacting jet case for the same J, POD mode 1 is much more energetic for the reacting jet case. Figure 3.41, compares the kinetic energy distribution in the first five POD modes across all the measurement planes (Z = 5 mm, 10 mm and 15 mm). The bar graph shows that with an increase in nozzle separation distance the kinetic energy in the shear layer gets redistributed in the wake structures. The energy contribution of POD mode 2 – 5 increases with an increase in nozzle separation distance. This can be related to the drop in the time average vorticity magnitude, along the jet shear layers, with an increase in nozzle separation distance.

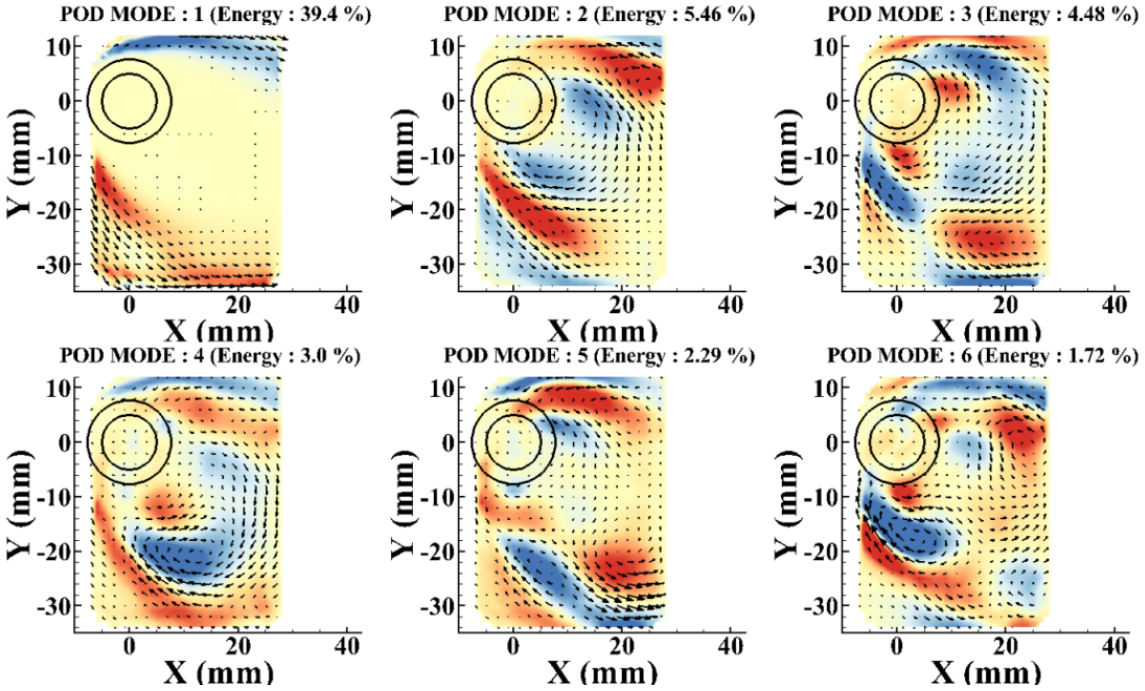

Figure 3.40. POD modes 1 – 6 for the non-reacting jet, J = 8, ϕ_{JET} = 0.9, Z = 5 mm.

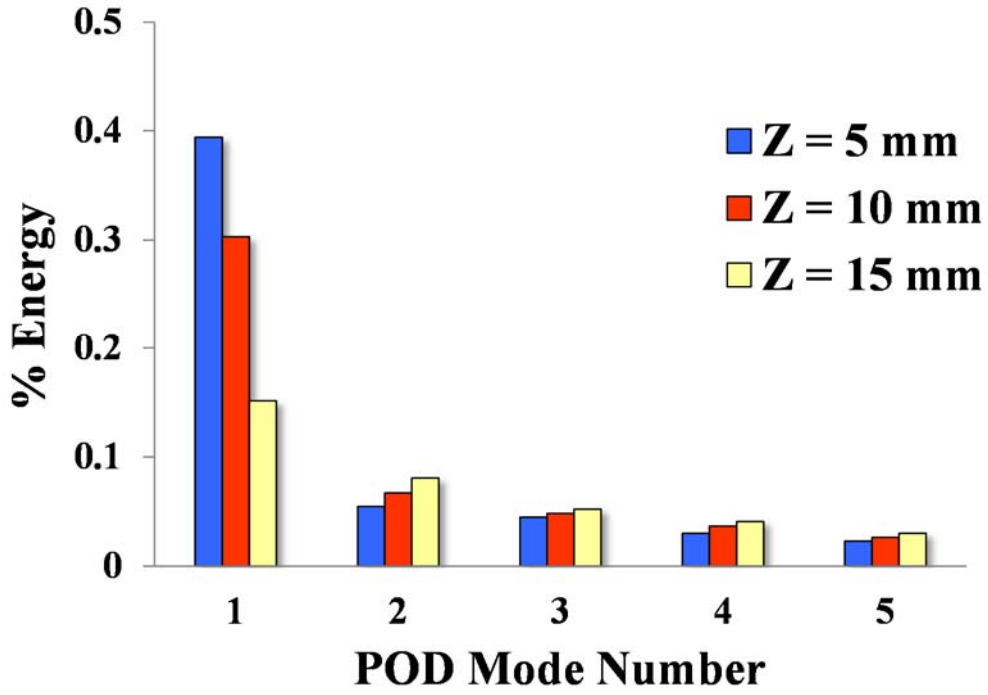

Figure 3.41. Kinetic energy distribution between the first five POD modes across the three measurement planes, Z = 5 mm, 10 mm and 15 mm, for J=8 and ϕ_{jet} = 0.9.

The velocity field of reacting jet case of J = 8 and ϕ_{jet} = 0.9 at Z = 5 mm is reconstructed from the computed POD modes. Figure 3.42, compares the raw instantaneous velocity field with the POD mode reconstructed velocity field with 50 modes, 100 modes and 200 modes. The corresponding difference velocity field calculated by subtracting each of the reconstructed velocity fields from the raw velocity field is also shows below. It takes more than 200 POD modes to accurately reconstruct the velocity field. The main difference in the flow field is in the region with the vortex structures with high vorticity magnitude.

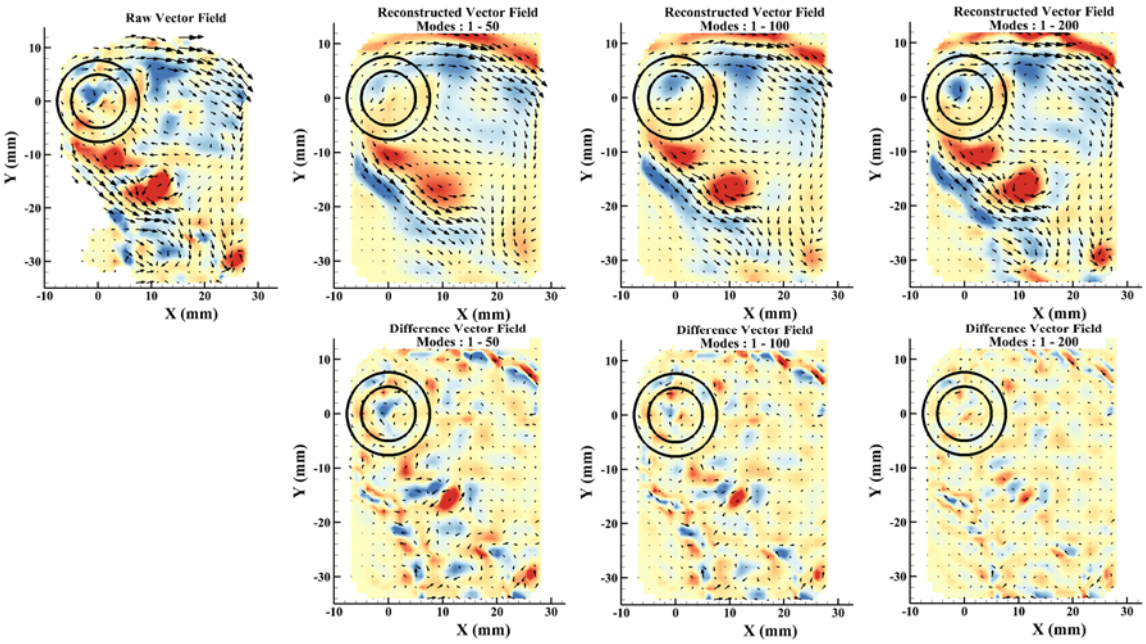

Figure 3.42. Reconstruction of velocity field using a) 50 modes, b) 100 modes and c) 200 modes.

3.9 Conclusions

In this chapter the results of a time resolved PIV measurements in an optically accessible high pressure distributed combustion system are discussed. The secondary combustion zone features transverse injections of premixed natural gas/heated air jets into

a swirling vitiated crossflow. Two component PIV measurements were acquired at a repetition rate of 10 kHz, which enabled tracking of the complex flow structures of the RJICF. The PIV measurements were performed at 5 different planes along the cross-section of the jet in order to understand the three dimensional flow-field associated with RJICF. There have been several studies involving flow velocity measurements of a reacting jet in crossflow reported in literature but the unique aspect of this work is a detailed study on the flow structure and dynamics of wake of the jet and its influence on stabilizing a reaction zone. The PIV measurements clearly indicate the influence of the swirl component in the crossflow on the jet. The time resolved velocity field measurements successfully captured the wake structure. The wake vortices were observed clearly at the Z = 5 mm and 10 mm planes for the J =3 cases and at Z = 5 mm, 10 mm and 15 mm planes for the J = 8 cases, indicating a larger wake and longer upright wake vortices for the higher momentum flux ratio. It was also found that the PIV particles get entrained into a plane 5 mm below the jet injection plane (Z = -5 mm). The mean flow field at this plane had similarities with that of a wake of cylindrical bluff-body.

PIV measurements for both the non-reacting and reacting jets were useful for understanding the overall nature of the associated flow field under the influence of swirling crossflow. The effect of the momentum flux ratio is distinguishable both for the non-reacting and the reacting flow cases. Both cases show an increase in the magnitude of the out of plane vorticity (ω_z) with an increase in momentum flux ratio. This implies that the higher values of jet momentum flux leads to stronger crossflow entrainment and mixing within the wake of the jet.

In a turbulent reacting flow, the velocity field has a broad spectrum of temporal and

length scales, and measurements at 10 kHz can resolve some of these scales. The velocity field of the non-reacting jet cases was analyzed to extract the variation of integral length scale across the measurement planes. The two-point correlation function was computed along the streamwise and spanwise direction of the mean flow field and it was found that the correlation curve gets broader with increasing in streamwise direction. The integral length scale is found to be non-uniform along the measurement plane; however, the spatial variation trend was consistent across all the three measurement planes. The velocity power spectra showed a broad spectrum of temporal scales present in the flow field of the RJICF. The peak frequency of velocity fluctuation ranges between 460 – 570 Hz for all the RJICF cases. The analysis led to an interesting finding that shows that the wake Strouhal number—which is based on the peak frequency, the jet exit diameter and the mean crossflow velocity—lies within a range of 0.13 – 0.15 for all the JICF/RJICF cases studied for jets with parabolic velocity profile. The St_{wake} is for jets with top-hat velocity profiles lie in the range of 0.18 – 0.23, indicating a faster rate of entrainment into the wake of the jet. This shift in St_{wake} can be explained by the fact that there is delay in the formation of leeward wake vortices in case of a jet with parabolic velocity profile. The crossflow mean velocities for the non-reacting and reacting cases are 13 m/s and 36 m/s, respectively, and the corresponding vortex shedding frequency for the RJICF is approximately 550 Hz and that for the JICF is 172 Hz. This suggests that the vortex shedding frequency scales with the mean crossflow velocity magnitude, but further analysis may be needed to support this statement. The OH-PLIF based flame front imaging discussed in Chapter 5 will provide strong evidence of a stabilized reaction zone within the wake field. Thus, the wake Strouhal numbers are useful in understanding the rate of mixing of the fuel jet with the

high temperature vitiated crossflow within the wake of the jet. However, we need to understand the impact of the third component of velocity in this analysis before deriving to any further conclusions. Due to limited optical access to the windowed combustor stereo-PIV based measurement to obtain all three components of velocity could not be applied.

CHAPTER 4. STRUCTURE AND DYNAMICS OF THE WAKE OF A REACTING JET INJECTED INTO A UNIFORM VITIATED CROSSFLOW

4.1 Introduction

A reacting jet in cross-flow (RJICF) configuration features transverse injection of reactive jet fluid into a vitiated cross-flow leading to mixing and chemical reactions. The jet in crossflow (JICF) is a canonical flow-field that features a uniform crossflow and a jet injected into the crossflow in a transverse direction. Current, research is focused on the influence of the crossflow fluid on a reacting jet. In Chapter 4 the influence of a swirling crossflow on the reacting jets was discussed in detail. The reacting jet is found to orient its trajectory along the mean crossflow direction. The reacting jet response to a uniform crossflow has a rich literature [53][52][71][75]. The main contribution of this research is flow field characterization of the wake of the jet to understand the flame stabilization mechanism. In the previous studies it has been identified that a vitiated crossflow helps in flame stabilization within the vicinity of the jet injection. Even higher momentum flux ratio where the local strain rates are extremely high, the leeward side of the jet still provides region with favorable flow conditions for flame stabilization. The most dominant flow structures seen in a JICF with uniform crossflow conditions is shown in Figure 4.1.

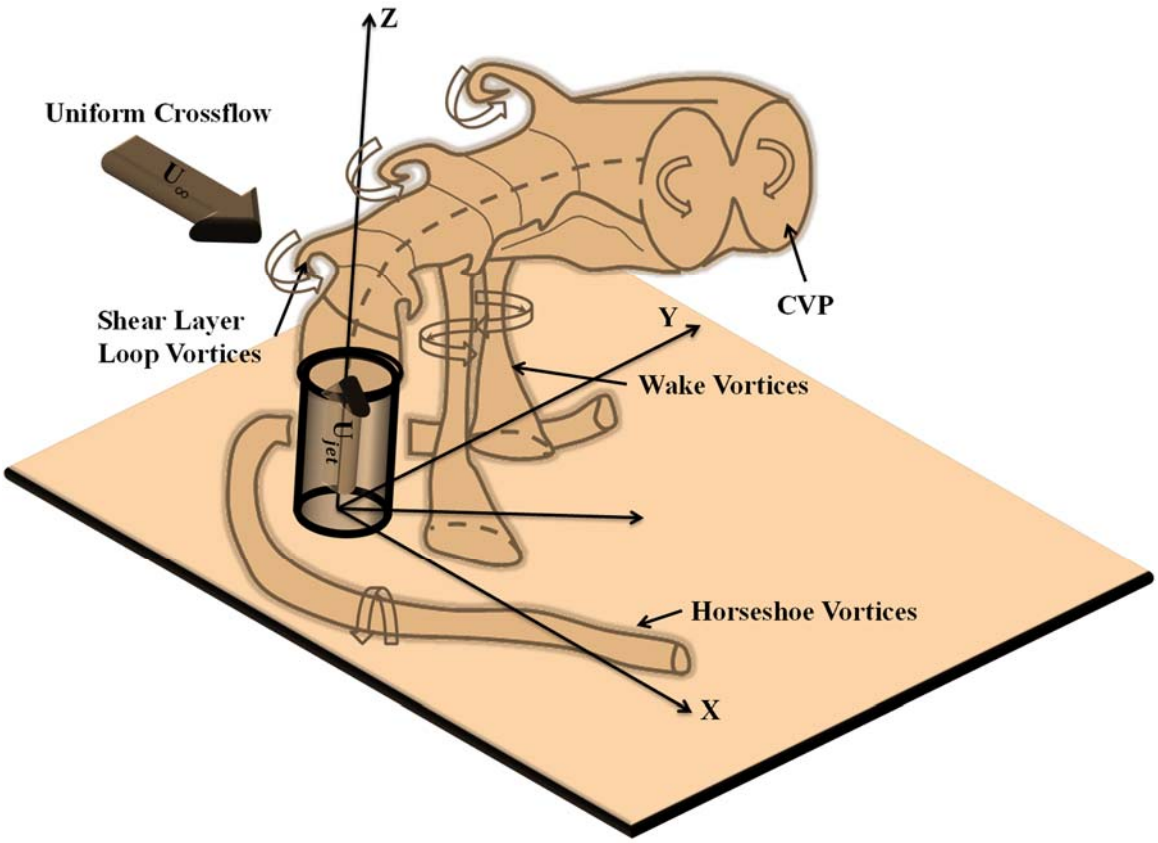

Figure 4.1. The schematic of a transverse jet injected into a uniform crossflow through an extended injector. Crossflow velocity, U_{CF} is in the positive x-direction, the swirling motion is in the Y-Z plane and the jet velocity, U_{JET} is in positive Z-direction.

In this chapter high repetition rate (HRR) two-component PIV measurements along the near wake field of a reacting jet in a uniform crossflow are discussed. The flow dynamics of the wake of the jet is found to be different for a uniform crossflow as compared to a swirling crossflow fluid. A bluff-body-burner was designed to generate a uniform vitiated crossflow. The geometrical details of the bluff-body-burner have been discussed in Chapter 3.

4.2 Experimental Test Matrix

The experimental operating conditions are same as the swirling crossflow cases. The jet fluid comprised of either premixed natural gas or hydrogen diluted with nitrogen. The fuel jets provide a net rise in temperature, ΔT across the SCZ. In the present study HRR two component PIV is used to characterize the structure and dynamics of the transverse jet interacting with a uniform vitiated crossflow. A detailed test matrix is shown in Table 3.1 for the PIV study discussed here.

Table 4.1. Uniform crossflow and jet conditions.

Cross Flow Operating Condition					
Operating Pressure (atm)			**5.5**		
Operating Temperature (K)			**723**		
MCZ Air Flow Rate (kg/s)			**0.39**		
MCZ Equivalence Ratio, ϕ_{main}			**0.5**		
Main Flow Reynolds Number(NR), Re_{main}			**105000**		
Main Flow Reynolds Number(R), Re_{main}			**61000**		
Non-Reacting Jet in Cross Flow					
High Temperature Air Jet	**Momentum Flux Ratio, J**	**Density Ratio, S**	**Jet Reynolds Number, Re_{jet}**		
	3	1	16900		
	8	1	27600		
RJICF Conditions					
FUEL JET	**Momentum Flux Ratio, J**	**Density Ratio, S**	**Jet Reynolds Number, Re_{jet}**	ϕ_{jet} =0.9	ϕ_{jet} = 3.0
Premixed Natural Gas	3	2.5	27500	**ΔT = 36 K**	**ΔT = 145 K**
	8	2.5	45000	**ΔT = 52 K**	**ΔT = 212 K**

Similar to the swirling crossflow cases this study focuses on two momentum flux ratios, J=3 and J=8. For the premixed natural gas jets the jet equivalence ratio is, ϕ_{jet} = 0.9, and for the H_2/N_2 jets the jet comprised of 40% H_2 and 60% N_2. For the non-reacting cases

the crossflow and jet fluid both comprised of high temperature air and temperature of both the fluid streams were matched to provide isothermal conditions. Velocity measurements were performed at 5 planes along the cross-section of the jet, as shown in Figure 4.2a, Z = -5 mm (1), 2 mm (2), 5 mm (3), 10 mm (4) and 15 mm (5) away from nozzle exit plane. Here z represents the distance from the nozzle exit plane. The nozzle exit plane is considered as the origin for this geometry as shown by the coordinate axes in Figure 4.2a and b. The horizontal green lines indicate the locations of laser sheet and the view shown in the schematic is defined as the side view of the jet in the x-z plane. The schematic of the near wake region of the jet is shown in Figure 4.2b. The shear layer between the crossflow and the jet is represented by the black dotted lines and the region outside the shear layer is termed as outer wake region. The PIV measurements were performed along X-Y plane which is perpendicular to the jet axis. The injector protrudes 15 mm into the crossflow and the jet exit diameter is 10 mm. The injector has a contoured profile which provides a uniform velocity profile at the exit of the injector.

4.3 Time Averaged Velocity Field

Velocity data were collected for duration of 0.5 sec at a repetition rate of 10 kHz. A total of 5000 particle image pairs were collected, providing enough sampling time to extract reasonable time-averaged fields. We performed (i) PIV measurements of the vitiated crossflow to quantify the uniform velocity field of the crossflow fluid stream, (ii) PIV measurements for non-reacting jets, and (iii) for the reacting jet cases. For all the three tests the locations of the measurement planes were the same. The time averaged velocity fields obtained from these studies are discussed here.

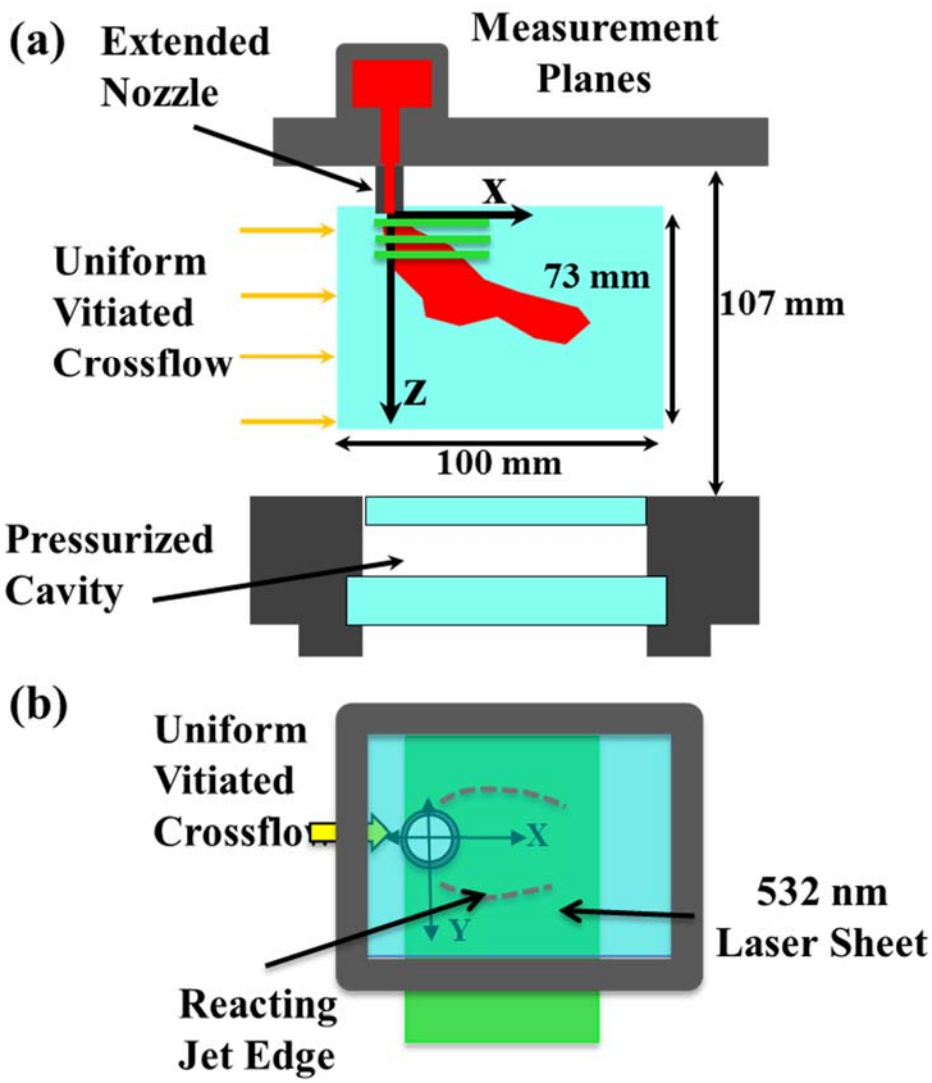

Figure 4.2. (a) Schematic diagram of the window assembly portion of the test rig with the extended nozzle showing the side view of the RJICF. The green horizontal lines indicate the PIV measurement planes. (b) The flow streamlines indicating the near field wake region of the RJICF along one of the X-Y measurement planes.

4.3.1 PIV Measurements of the Crossflow

Two component PIV measurements were performed for characterizing the velocity field of the incoming vitiated crossflow. These measurements will provide valuable information

on the boundary conditions for numerical simulation of the JICF and RJICF experiments. For these experiments, the jet injector face was removed and replaced with a planar metallic blank. The PIV measurements were performed at measurement planes Z = 5, 10, 15 and 20 mm away from the physical location of the jet exit plane. Figure 4.3, shows the velocity vectors are overlaid on top of a false color map of velocity magnitude. The velocity magnitude is found to be constant across all the measurement planes except at the Z = 5 mm. The velocity vectors are parallel to the x-direction, but the velocity magnitude above the Y = 0 mm is smaller than the mean crossflow velocity, U_{CF} = 36 m/s. The directions of the velocity vectors in the planes Z = 10, 15 and 20 mm have a velocity angle of approximately 10 degrees above the Y = 0 mm. The spanwise variation of the mean of x- and y-components of the velocity field at X/d_{JET} = 1.5 and 2.0, is shown in Figure 4.4. The x-component of velocity varies between 35 – 40 m/s at Z = 10, 15 and 20 mm, but at Z = 5 mm it varies as high as 10 m/s between – 25 mm and 25 mm. Figure 4.4b shows the variation of y-component of velocity across all the measurement planes. It is observed that velocity field at Z = 10, 15 and 20 mm consists of a negative y-component of velocity. The minimum y-velocity observed is -17 m/s at Z = 10 mm. Interestingly, at plane Z = 5 mm there is minimal contribution of y-velocity and the minimum velocity observed is -2 m/s. The y-velocity trend indicates that the incoming vitiated crossflow is not completely uniform.

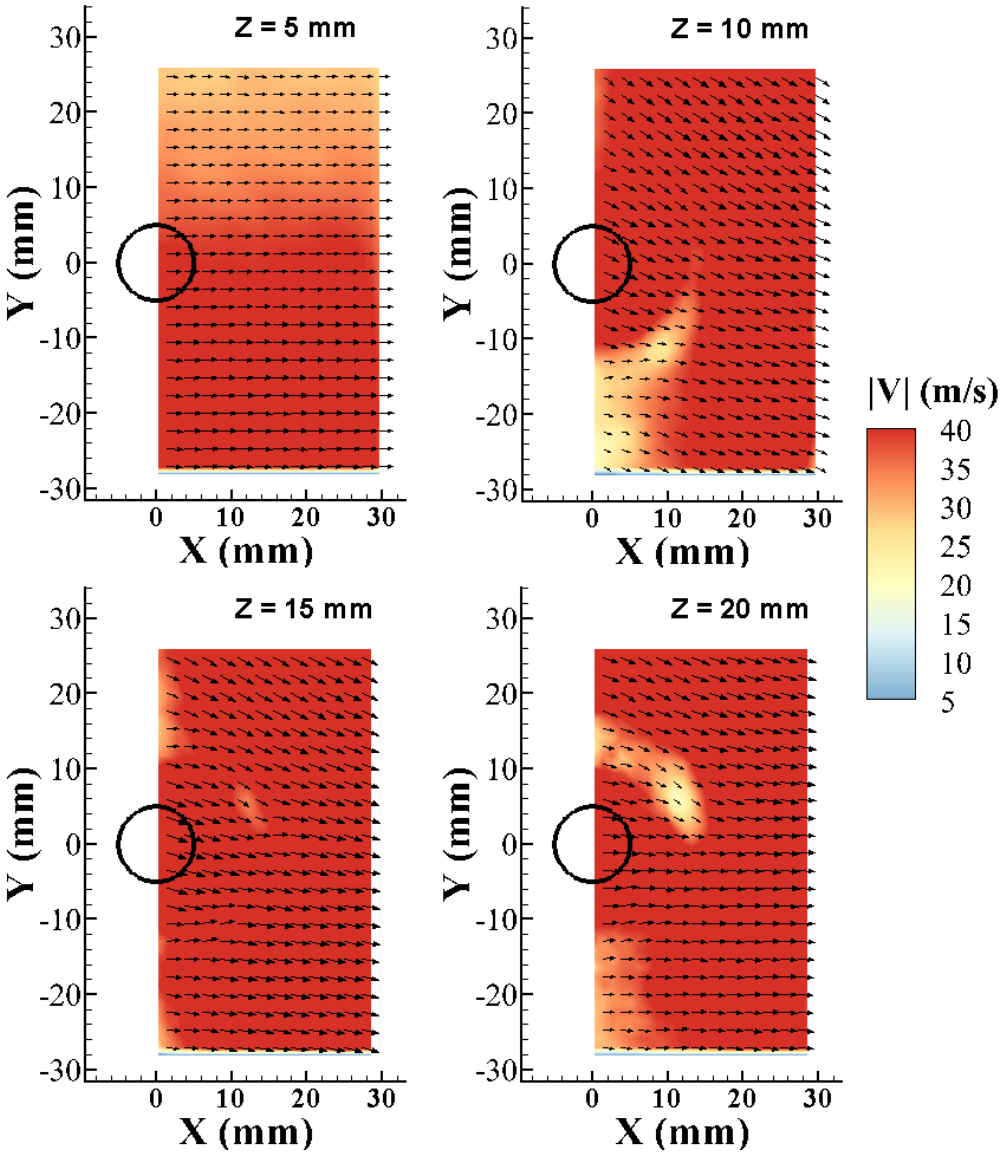

Figure 4.3. Comparing the crossflow velocity field measured at planes Z = 5 mm, 10 mm, 15 mm, 35 mm, 45 mm and 50 mm. The velocity vectors are overlaid on top of velocity magnitude |V| (0 – 40 m/s). The direction of the velocity vectors observed the measurement planes shown confirms the strong swirling motion present in the crossflow.

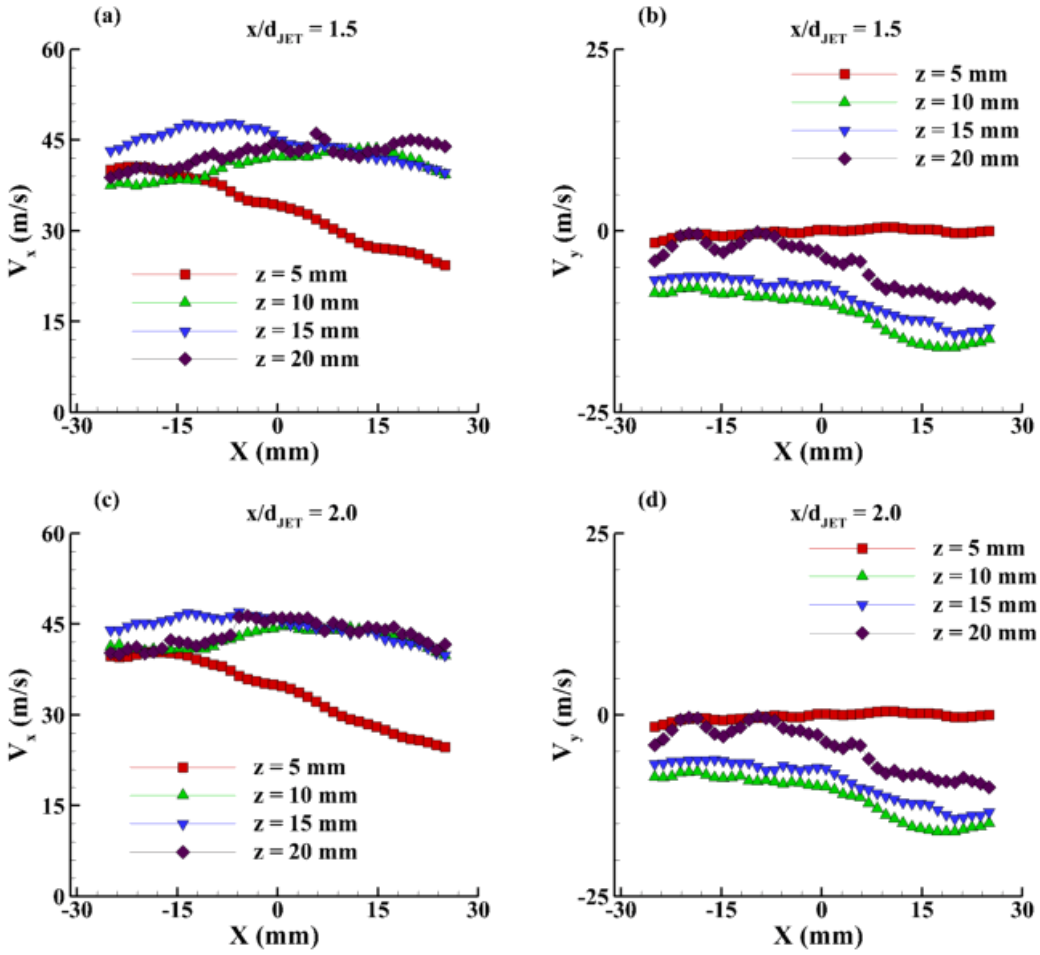

Figure 4.4. Variation of the x- and y- components of velocity of the crossflow measured at planes Z = 5 mm, 10 mm, 15 mm and 20 mm, plotted at X/d_{JET} = 1.5 and 2.0 from the physical location of the center of the injector.(a) time averaged x-component of velocity plotted at X/d_{JET} = 1.5, (b) time averaged y-component of velocity plotted at X/d_{JET} = 1.5, (a) time averaged x-component of velocity plotted at X/d_{JET} = 2.0, (b) time averaged y-component of velocity plotted at X/d_{JET} = 2.0.

4.3.2 Non-Reacting Flow Field of JICF

The time-averaged velocity and vorticity profiles for the non-reacting jet case of J= 8 are shown in Figure 4.5, Figure 4.6 and Figure 4.7. The profiles are extracted from five streamwise locations (X/d_{JET} = 1.0, 1.5, 2.0, 2.5, 3.0). The streamwise variation of x-component of velocity shows a dip in the velocity magnitude within the near wake region of the jet, between X = -10 mm – 10 mm. The velocity deficit is highest at Z = 2 mm. It

is noticeable that the velocity gradient across all the streamwise location reduces with increase in nozzle separation distance. The velocity profile do not show any negative velocity field within the near wake region unlike the swirling crossflow cases. This indicates absence of a recirculation region in the non-reacting jet cases. At Z = 2 mm it is evident that the y-component of velocity is within 5 m/s and it drops down to zero at X/d_{JET} = 3.0, as shown in Figure 4.7. The magnitude of y-component of velocity is found to be as high as 10 m/s at planes Z = 10 and 15 mm. Figure 4.8 shows a decrease in the magnitude of the out of plane vorticity along the streamwise direction.

4.3.3 Reacting Flow Field of RJICF

The time averaged velocity field for the reacting jet case of J = 3, ϕ_{jet}= 0.9 and J = 8, ϕ_{jet}= 0.9 at planes Z = 2mm, 5 mm, 10 mm and 15 mm are shown in Figure 4.8 and Figure 4.9, respectively. Unlike the swirling crossflow conditions for the reacting jets injected into uniform vitiated crossflow the PIV particles were absent, in the measurement plane Z = -5 mm, for all the reacting jet cases. Thus, velocity vectors could

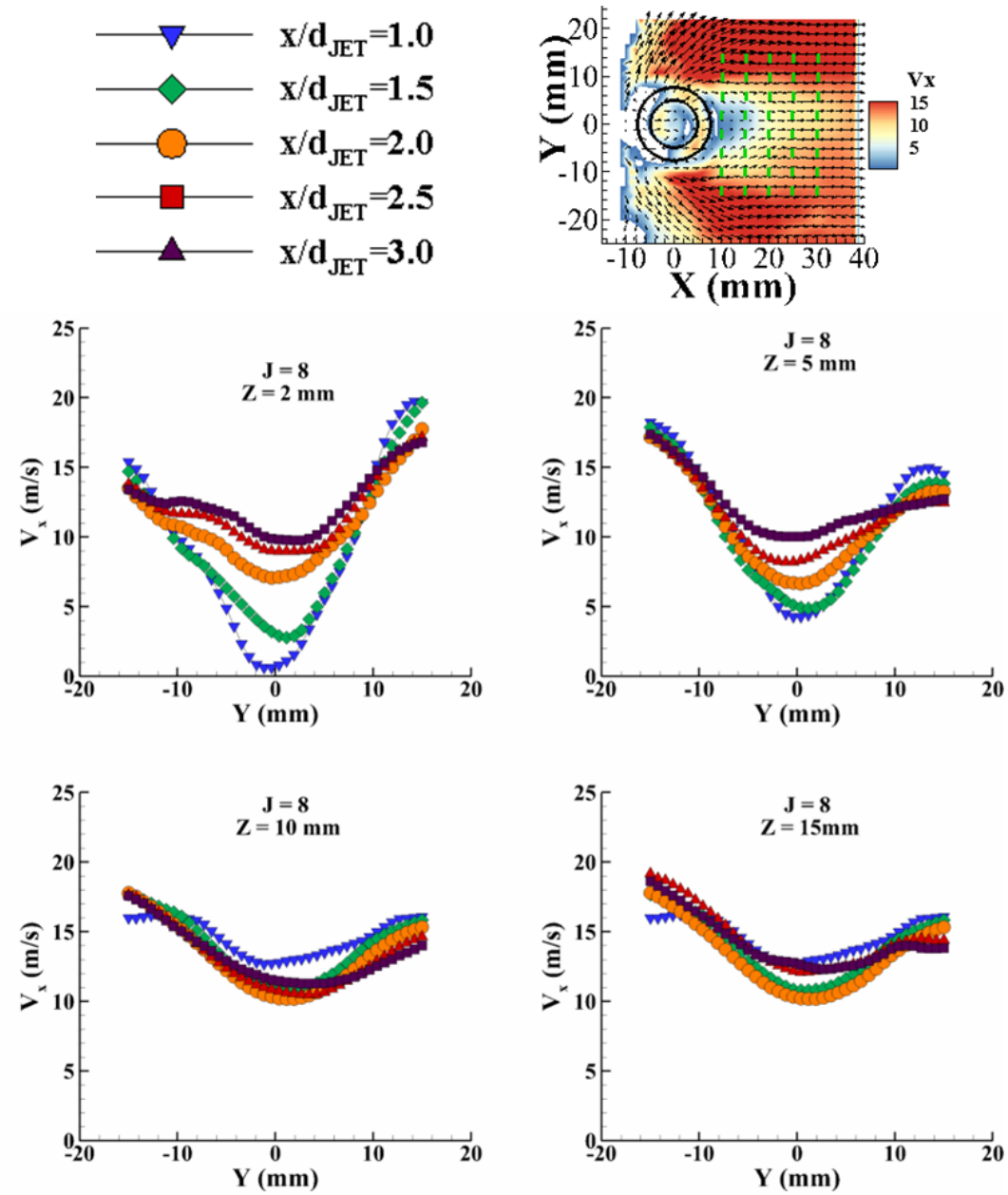

Figure 4.5. Variation of V_x along the streamwise direction indicating the variation in the flow field across different measurement planes of non-reacting jet J = 8. The velocity profiles are extracted from the green dotted lines shown on the time-averaged x-component of velocity field.

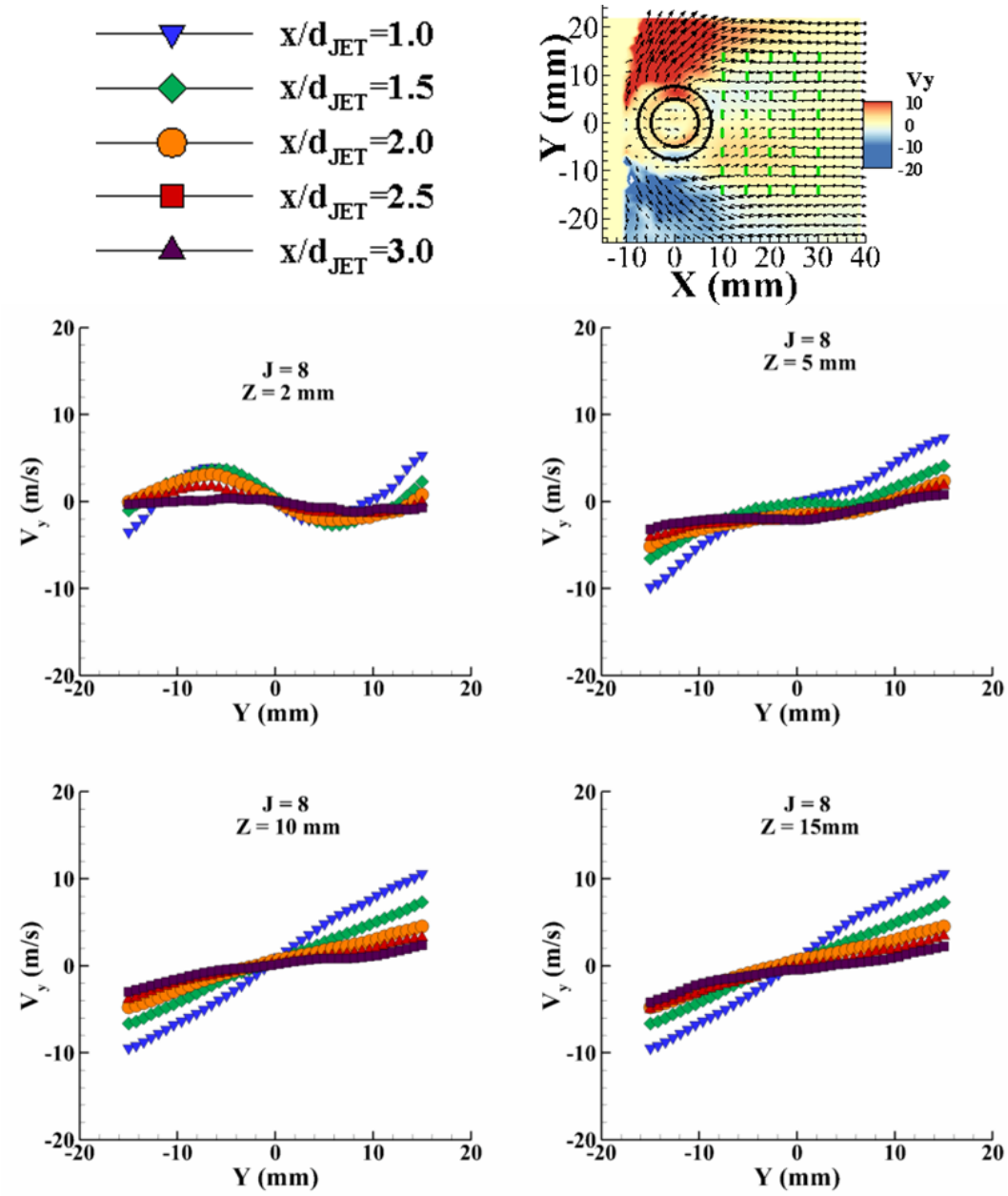

Figure 4.6. Variation of V_y along the streamwise direction indicating the variation in the flow field across different measurement planes of non-reacting jet J = 8. The velocity profiles are extracted from the green dotted lines shown on the time-averaged y-component of velocity field.

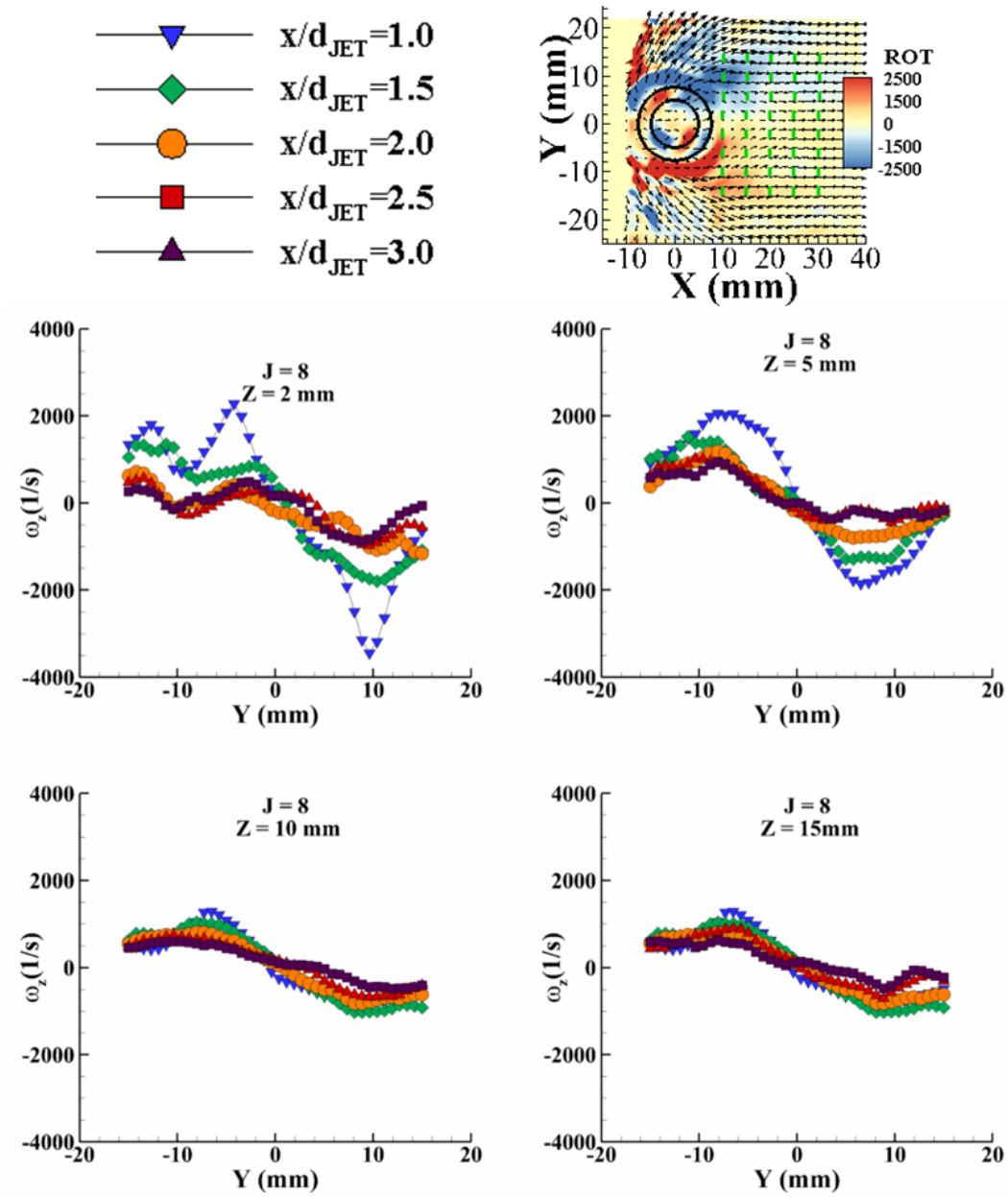

Figure 4.7. Variation of ω_z along the streamwise direction indicating the variation in the flow field across different measurement planes of non-reacting jet J = 8. The vorticity profiles are extracted from the green dotted lines shown on the time-averaged z-component of vorticity field.

not be computed at this plane. The time averaged velocity vectors are overlaid on a false color map of the x-component of velocity contour as shown in Figure 4.8a. The mean flow

is parallel to the x-direction and the flow-field is found to be symmetric about the x-axis. The jet fluid interacts with the incoming crossflow by forming the shear layer that surrounds the wake of the jet. The two shear layers consist of high speed fluids. A strong recirculation region is evident between the two high speed flow regions at Z = 10 mm and 15 mm. The wake entrains the jet fluid and the crossflow fluid leading to mixing and eventually stabilization of a reaction zone. Figure 4.8b shows the same vector field overlaid on a false color map of the y-component of velocity. The jet provides a blockage to the incoming crossflow as a result the crossflow fluid accelerates around the jet. The high magnitude of y-velocity is seen between X = 0 - 10 mm in the region of interaction of the crossflow fluid and jet fluid. The fluid stream for J = 8 case wraps around the jet and comes down towards the wake due to low pressure created within the recirculation region of the jet wake after X = 20 mm. This is evident from the negative y-velocity region above Y = 0 mm and positive y-velocity region below Y = 0 mm. Figure 4.8c shows the velocity vectors overlaid on a false color map of the z-component of vorticity (ω_z). A steady counter-rotating wake structure aligned in the direction of the mean velocity vectors is clearly evident at all the measurement planes in both the reacting jet cases. These wake structures are steady and well defined and are similar to the wake structure behind a cylindrical bluff body, however, in this case the blockage to the incoming crossflow is provided by a deforming column of jet fluid. A detailed analysis involving time resolved dynamics of the wake of the jet is discussed in a section 4.7.3.

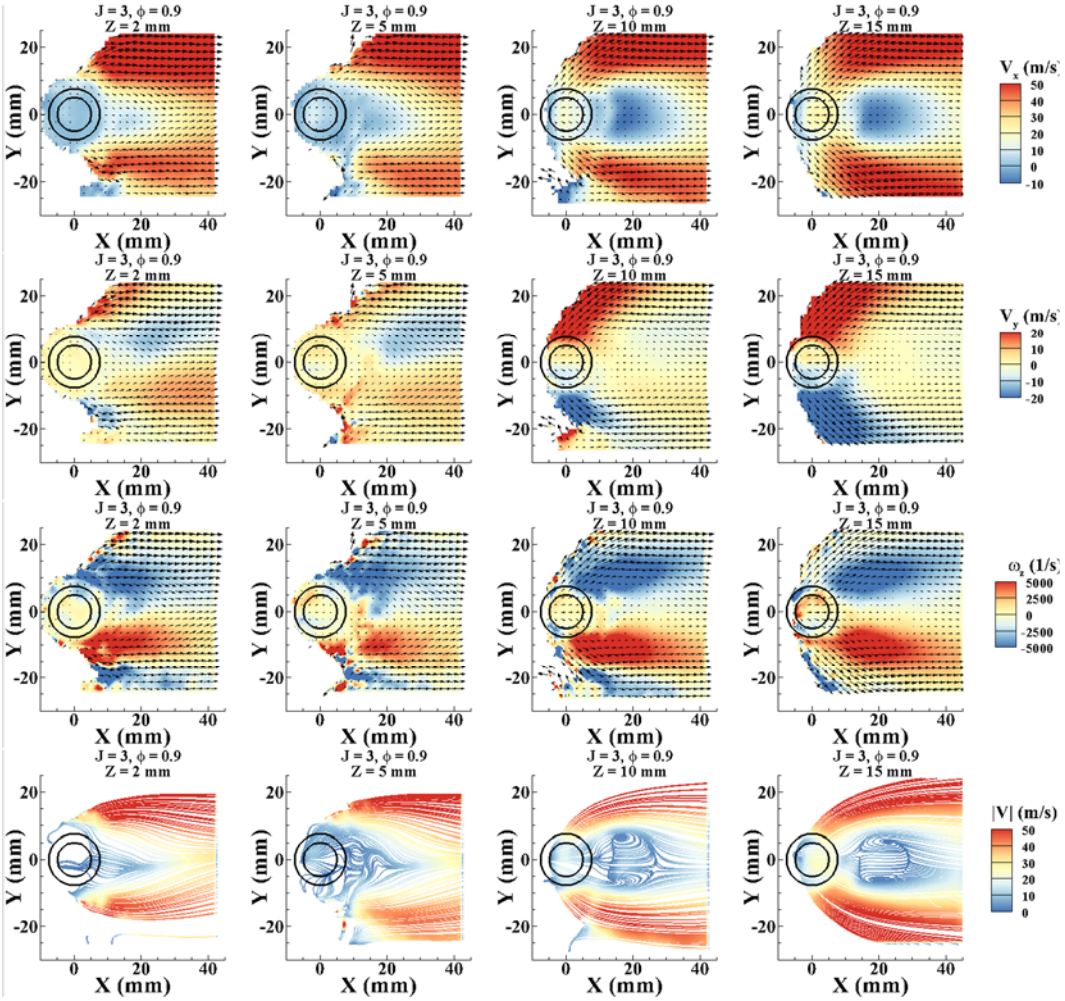

Figure 4.8. Computed velocity vectors overlaid on top of x- velocity (row 1), V_x (-10 – 50 m/s),y- velocity (row 2), V_y (-10 – 10 m/s), z-vorticity (row 3), ω_z (-5000 – 5000 s^{-1}) and flow streamlines (row 4) colored by the velocity magnitude, |V| (0 – 50 m/s) for J = 3 and ϕ_{jet} = 0.9, measured at Z = -5 mm, 5 mm, 10 mm and 15 mm.

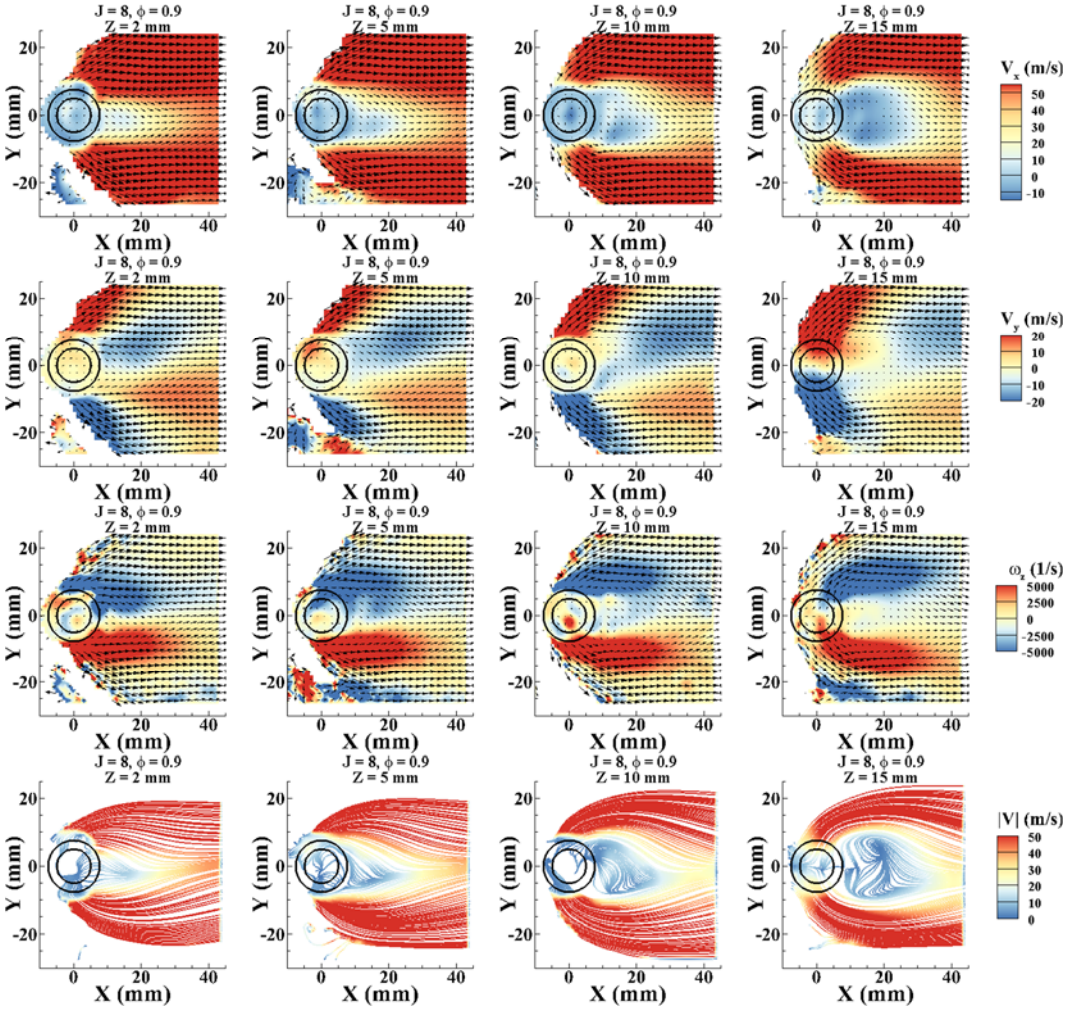

Figure 4.9. Computed velocity vectors overlaid on top of x- velocity (row 1), V_x (-10 – 50 m/s),y- velocity (row 2), V_y (-10 – 10 m/s), z-vorticity (row 3), ω_z (-5000 – 5000 s^{-1}) and flow streamlines (row 4) colored by the velocity magnitude, |V| (0 – 50 m/s) for J = 8 and ϕ_{jet} = 0.9, measured at Z = -5 mm, 5 mm, 10 mm and 15 mm.

4.3.4 Velocity Field Characteristics: Swirling / Uniform Crossflow

For the reacting jets in swirling crossflow steady wake structures are evident within half a jet diameter away from the jet injection plane (Z = 0 mm). However, there is a delay in the formation of these structures for the reacting jets in uniform vitiated crossflow. The non-reacting flow fields for both the crossflow cases show a difference in the flow structure,

as well. It is observed that the wake of the non-reacting jet in uniform crossflow doesn't have a well-defined recirculation region, as the x-component of velocity at every streamwise location is above zero. In order to understand this difference in the measured velocity field between the swirling crossflow and uniform crossflow cases velocity field of the non-reacting jet cases are further analyzed. A coordinate transformation was performed on the velocity field of the non-reacting jets with swirling crossflow by rotating it by 45 degrees in a counterclockwise direction (this corresponds to the mean velocity angle calculated from the mean crossflow velocity field at the planes Z = 5, 10 and 15 mm [97]). The coordinate transformation ensured that the mean flow direction for the swirling crossflow is not parallel to the new x-axis. Velocity profiles are extracted along the streamwise direction for the non-reacting jet cases. Figure 4.10a, shows the coordinate transformed time averaged velocity field of J=8 at Z = 5 mm with swirling crossflow. A corresponding velocity profile extracted from the streamwise location (X/d_{JET} = 2.0). Similarly, the time averaged velocity field of J=8 at Z = 5 mm with uniform crossflow and the corresponding representative velocity profile extracted from the streamwise location (X/d_{JET} = 2.0) is shown in Figure 4.10b. The two velocity profiles are plotted together and shown in Figure 4.11. A curve-fitting function is used to fit a fifth-order polynomial to the velocity profiles. A unique polynomial function is generated for each of the velocity profiles and it is integrated to determine the flow rate at every streamwise locations. Table zz, summarizes the flow rates calculated at X/d_{JET} = 1.0, 1.5 and 2.0 and at measurement planes Z = 10 mm and 15 mm. It is important to note that the computed flow rate is completely based on the in-plane velocity field and it will vary at different measurement planes. A maximum difference of 0.03 m^3/s is seen in the flow rate between the uniform

and swirling crossflow cases at any streamwise location. This could be attributed to i) minor variations in the operating temperature of the fluid stream, ii) the accuracy of the curve-fitting function (computes coefficients within 95% of confidence interval), iii) difference in the out of plane velocity component due to the swirling motion. The variation in the velocity magnitude for a comparable flow rate between a swirling crossflow (q = 0.399 m^3/s)and a uniform crossflow (q = 0.381 m^3/s) at a streamwise location two jet diameters away from the jet injection plane is evident in Fig zz. It shown that, the non-reacting jet with swirling crossflow experiences a significantly higher velocity gradient as compared to the uniform crossflow case. In addition to that the swirling crossflow inherently has a strong velocity gradient along the z-direction as discussed previously in chapter 4. The higher velocity gradient could be responsible for higher out of plane vorticity magnitude and strain rates. It has been already discussed that the time averaged vorticity magnitude for the swirling crossflow case is twice as high as compared to uniform crossflow. Thus, higher vorticity magnitude could trigger early formation of the wake structures in case of swirling crossflow cases.

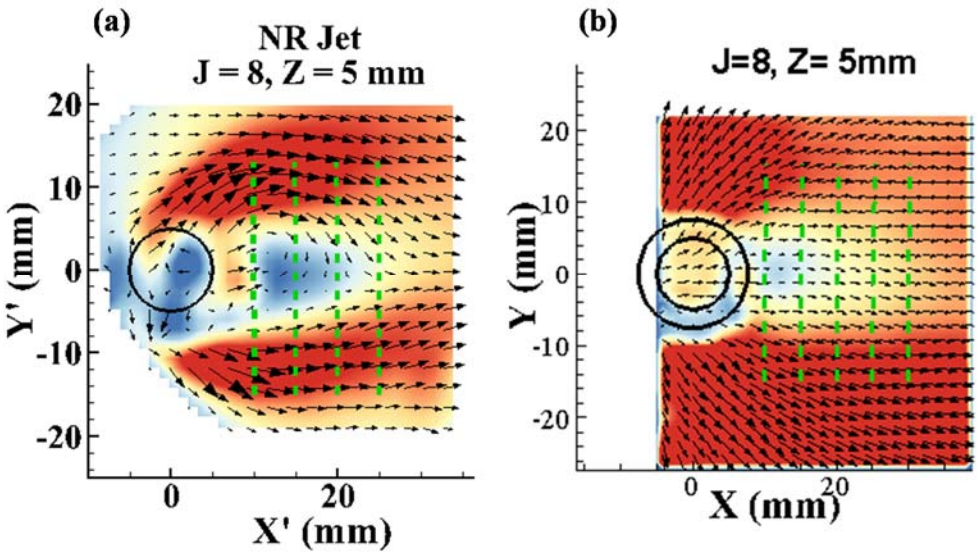

Figure 4.10. Velocity field comparison between a) non-reacting jet in swirling crossflow and b) non-reacting jet in uniform crossflow, for J = 8, Z = 5 mm. Velocity profiles at two jet diameters from the nozzle in the streamwise direction indicate higher velocity gradient for the jet in swirling crossflow.

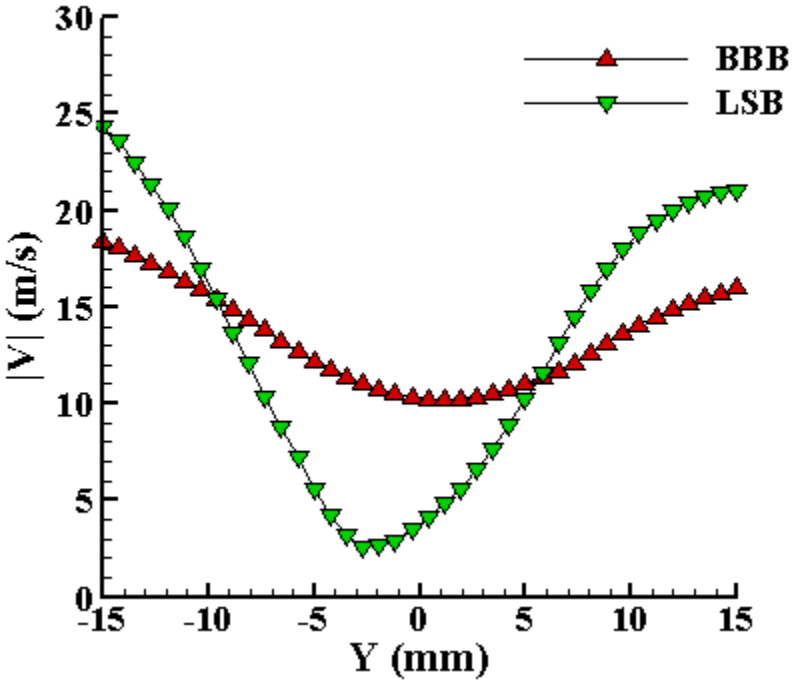

Figure 4.11. Velocity profile comparison between a) non-reacting jet in swirling crossflow and b) non-reacting jet in uniform crossflow, for J = 8, Z = 5 mm. Velocity profiles at two jet diameters from the nozzle in the streamwise direction indicate higher velocity gradient for the jet in swirling crossflow.

Table 4.2. Flow rate computed at various streamwise locations at Z = 5 mm.

X/d_{JET}	Q ($m^3/s\text{-}m^2$)(Uniform)	Q ($m^3/s\text{-}m^2$)(Swirl)
1	0.473	0.478
1.5	0.427	0.392
2	0.399	0.381

4.4 Instantaneous Flow Field

The recirculation region within the near wake region of the jet is a suitable site for flame stabilization. The wake vorticity entrains fuel-air mixtures and reaction products within the wake of the jet which would sustain a reaction zone. It is therefore important to understand the dynamics of the wake structure. The velocity measurements at 10 kHz discussed in this section provide time-resolved information on the transient wake structure of the non-reacting and reacting jets injected into a uniform hot air/vitiated crossflow.

4.4.1 Non-Reacting Flow Field

A sequence of instantaneous velocity vectors of non-reacting jet case of J = 8, measured at Z =10 mm, overlaid on the contour map of velocity magnitude and vorticity magnitude, are shown in Figure 4.12 and Figure 4.13, respectively. The sequence of velocity vector field shows convection of the fluid stream from X = 20 mm to 40 mm. As the fluid stream in the lower shear layer (LSL) convects downstream, it is evident that at time = 0.2 ms the leading edge of LSL (X = 20 mm and Y = -20 mm) turns in a clockwise direction and forms a vortex structure with clockwise rotation.

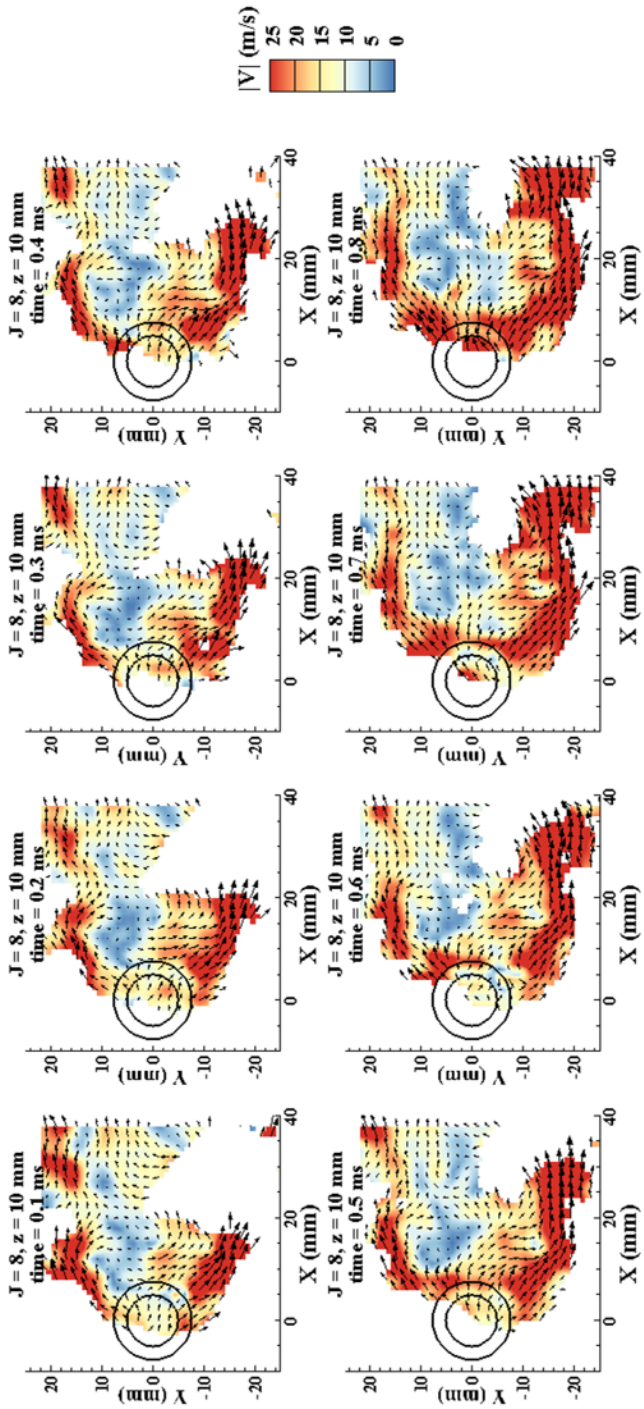

Figure 4.12. Instantaneous velocity vector overlaid on velocity magnitude computed for the non-reacting jet case, J =8, measured at Z = 5 mm.

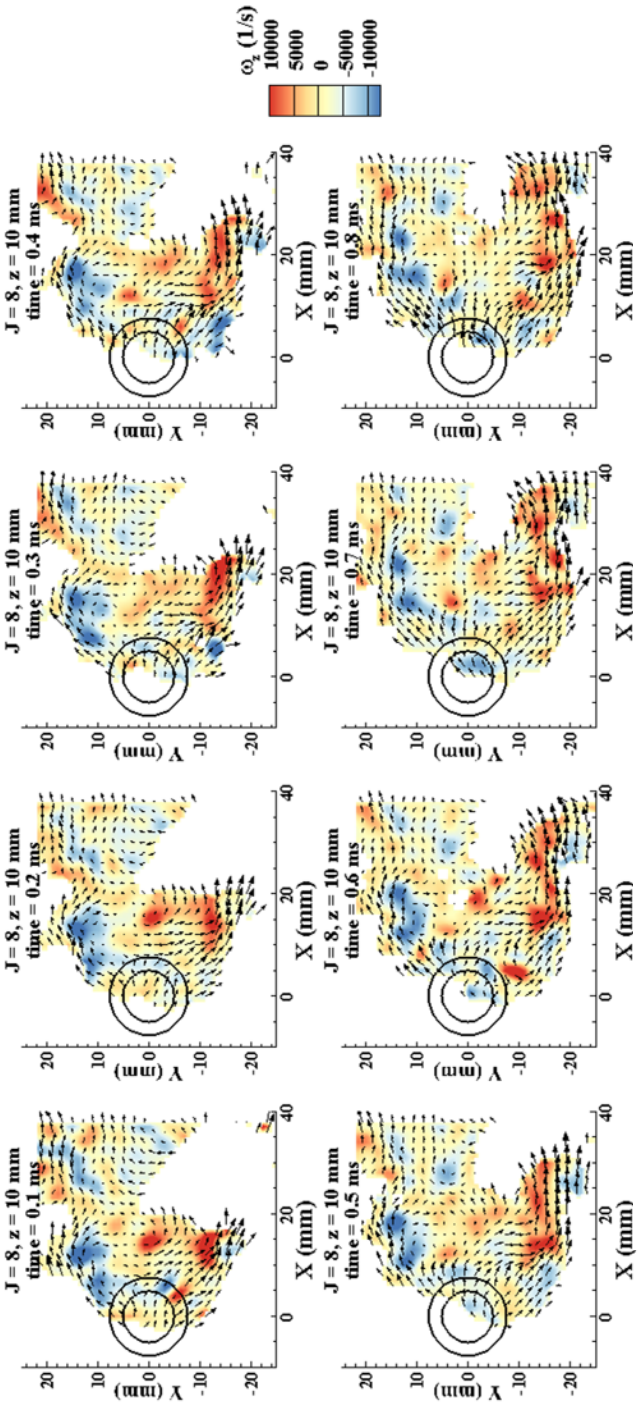

Figure 4.13. Instantaneous velocity vector overlaid on vorticity magnitude computed for the non-reacting jet case, J =8, measured at Z = 5 mm.

It takes approximately 0.7 ms to convect from X = 20 mm to 40 mm, which is approximately convecting with a velocity magnitude of 28 m/s. As the length of the LSL and USL increases the size of the recirculation region grows. The clockwise vorticity in the USL and anti-clockwise vorticity in the LSL is entraining the jet and crossflow fluid into the recirculation region. The detected flow structures exhibit strong vorticity as high as $\pm 10000\, s^{-1}$. Thus, the non-reacting jet case provides important insight into the dynamics of the dominant wake structure showing the presence of periodic asymmetric vortex structures similar to those observed behind a cylindrical bluff body in a crossflow.

4.4.2 Reacting Flow Field

A sequence of instantaneous velocity vectors overlaid on top of a false color map of the velocity magnitude for the J = 8, ϕ_{jet} = 0.9 reacting jet case for the Z = 10 mm plane is shown in Figure 4.14. The instantaneous velocity vectors within the USL and LSL are parallel to the X-axis, unlike the swirling crossflow cases. The recirculation region extends upto three jet diameter downstream of the jet injection location. There is a sharp velocity gradient within the interface of shear layer and recirculation region which is responsible for high magnitude vorticity in these regions. Figure 4.15, shows the same sequence of velocity vectors overlaid on top of vorticity contour map. A series of counter-rotating vortex structures are observed at time = 0.1 ms in the LSL. The vortex structures either convect out of the span of measurement plane or combine with another structure and dissipate within the recirculation region. The instantaneous flow field resembles the wake of a cylinder in crossflow.

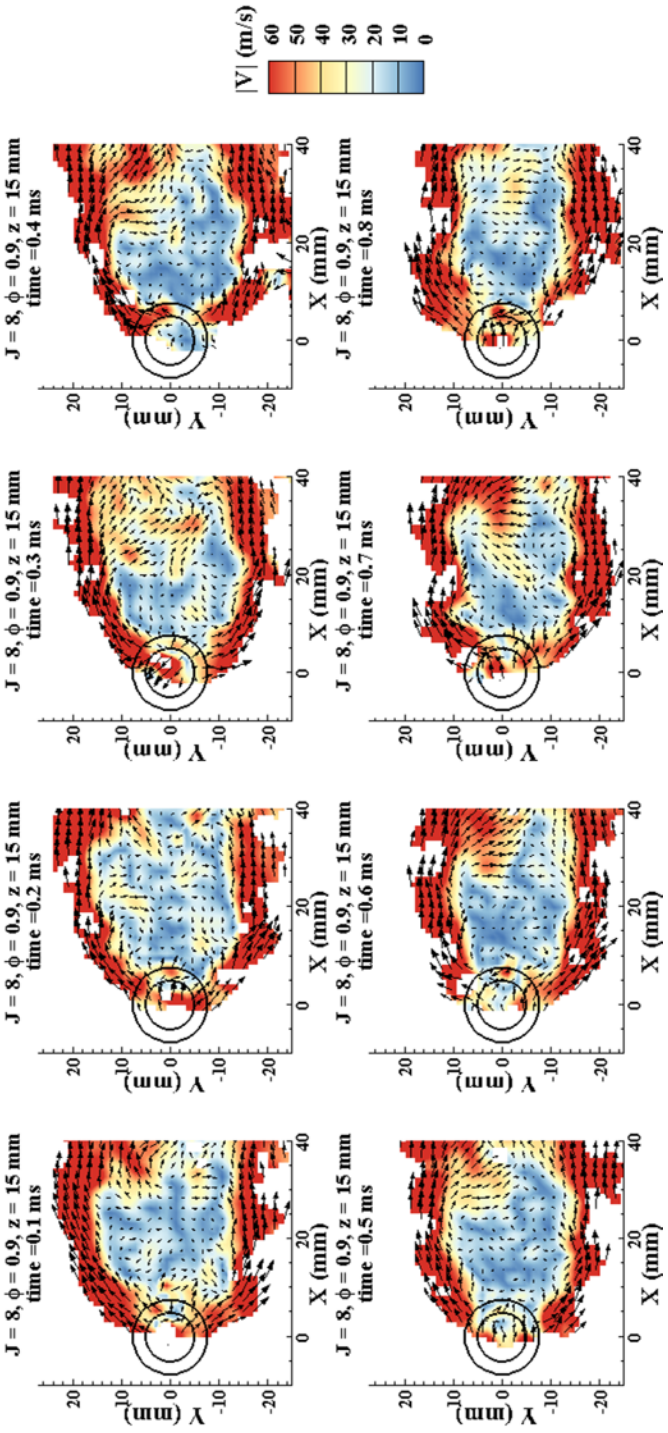

Figure 4.14. Instantaneous flow velocity vectors with background false colored by velocity magnitude of J=8 ϕ_{jet} = 0.9 at Z = 5 mm, showing the temporal evolution of the most dominant flow

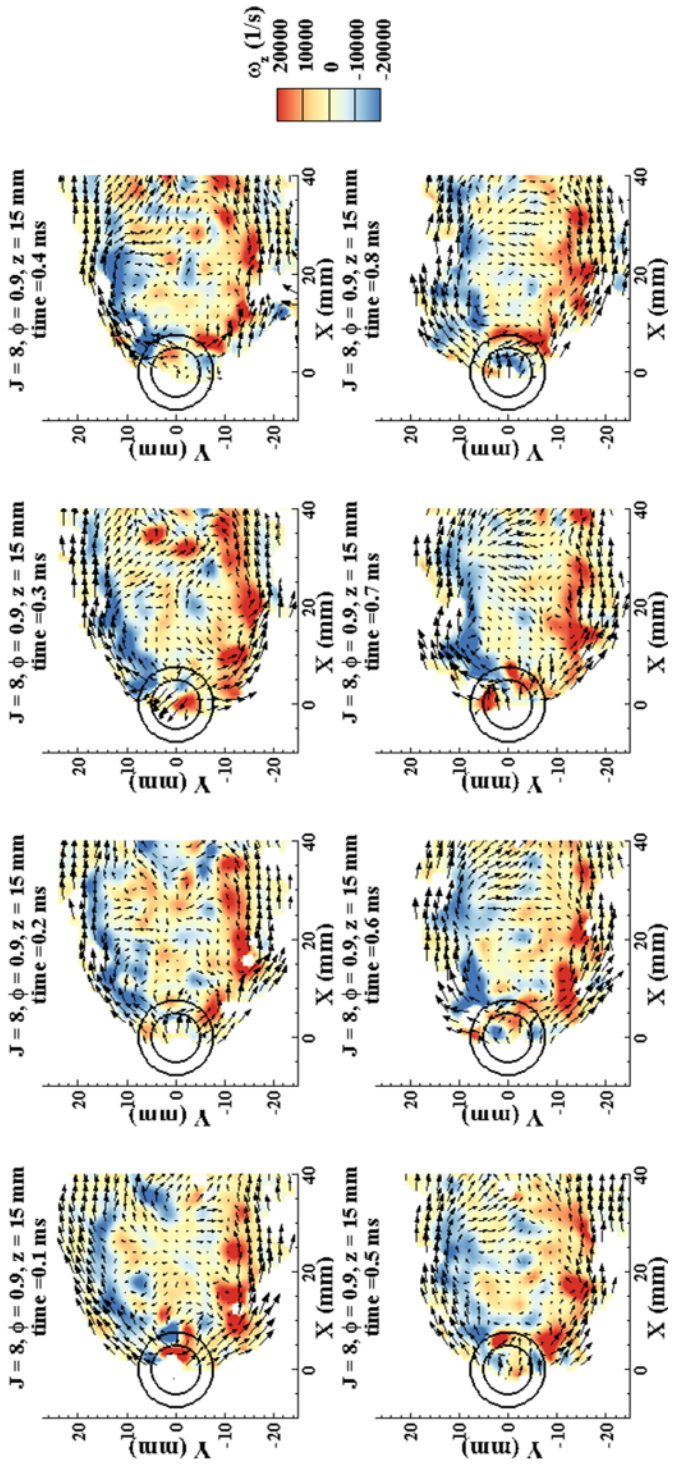

Figure 4.15. Instantaneous vector field with background false colored by Z-vorticity (ω_z) of J=8 ϕ_{jet} = 0.9 at Z = 5 mm, to show the dynamics of the flow field.

4.5 Particle Mie Scattering

4.5.1 Non-Reacting JICF

2D PIV measurements are performed along the jet cross-section to extract the flow structures dynamics and to understand their influence on the jet flame. The size and structure of the shear layer flow structures can be determined from the instantaneous Mie scattering images. A 10 mm by 10 mm window is chosen from USL and LSL and a spatially averaged intensity is calculated at every time instances. A power spectral density is computed from the time variation of the spatially averaged intensity field computed at the windowed region. An instantaneous snapshot of Mie scattering image of non-reacting JICF, J = 8, measured at Z = 5 mm and corresponding spectral plot is shown in Figure 4.16. The peak in the frequency spectrum is seen at 116 Hz at both USL and LSL. A Strouhal number (*St*) is computed based on the peak frequency (*f*), jet exit diameter (d_{JET}) and mean crossflow velocity (U_∞). Based on the spectral analysis of the spatially averaged Mie scattering intensity field it is seen that the frequency of the flow structures in the near wake region is 116 Hz, which corresponds to a St = 0.09 based on the jet exit diameter (d_{JET} = 10 mm) and mean crossflow velocity (U_{CF} = 13 m/s). The St computed from the Mie scattering images of non-reacting jet in uniform crossflow is lower than the St calculated for non-reacting jets in swirling crossflow.

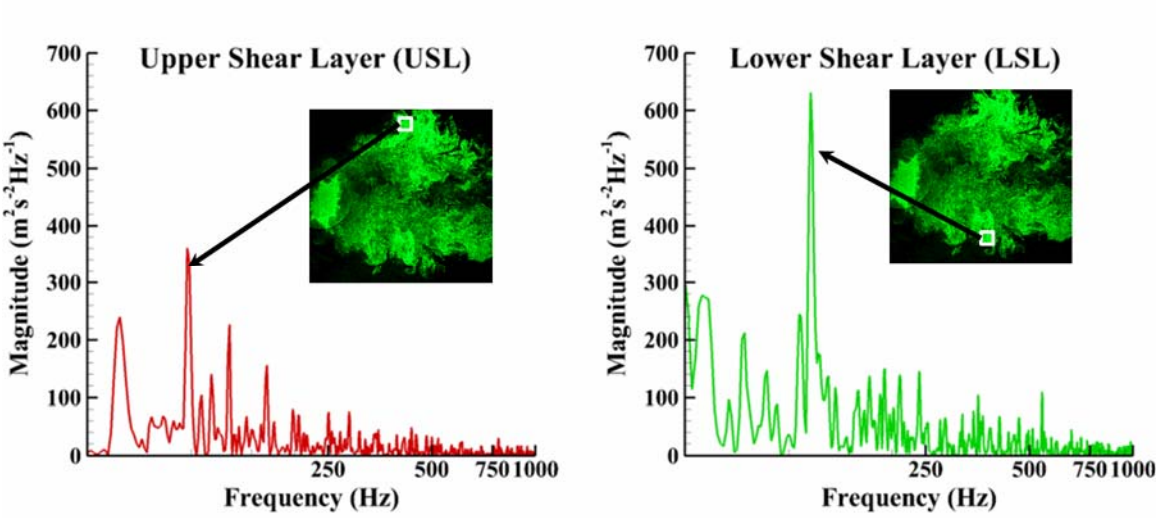

Figure 4.16. An instantaneous Mie scattering image and corresponding PSD plot extracted from a) USL and b) LSL of the intensity field of the non-reacting jet case of J =8, at Z = 5 mm from the nozzle exit plane.

4.5.2 Reacting JICF

A 10 mm by 10 mm window is chosen from USL and LSL and a spatially averaged intensity is calculated at every time instances. A power spectral density is computed from the time variation of the spatially averaged intensity field computed at the windowed region. An instantaneous snapshot of Mie scattering image of reacting JICF, J = 3 ϕ = 0.9, measured at Z = 15 mm and corresponding spectral plot is shown in Figure 4.17. The peak in the frequency spectrum is seen at 440 Hz at both USL and LSL. Based on the spectral analysis of the spatially averaged Mie scattering intensity field it is seen that the frequency of the flow structures in the near wake region is 440 Hz, which corresponds to a St = 0.122 based on the jet exit diameter (d_{JET} = 10 mm) and mean crossflow velocity (U_{CF} = 13 m/s). A second peak in the frequency spectrum seen at USL f = 248 Hz. The St computed from the Mie scattering images of non-reacting jet in uniform crossflow is lower than the St calculated for non-reacting jets in swirling crossflow.

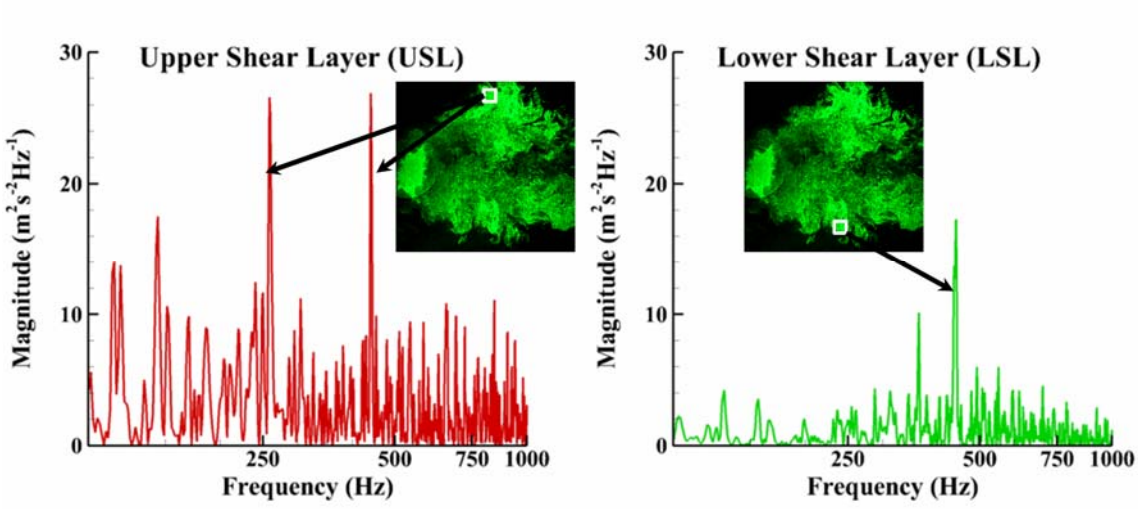

Figure 4.17. An instantaneous Mie scattering image and corresponding PSD plot extracted from a) USL and b) LSL of the intensity field of the reacting jet case of J = 3 and ϕ = 0.9, at Z = 15 mm from the nozzle exit plane.

4.6 Turbulent Length Scale and Flow Field Dynamics

4.6.1 Integral Length Scales

The two-point correlation function has been used in highly turbulent and non-homogenous flow fields, such as, swirling flow, free shear jet flows, temporally evolving wakes etc., to compute the integral length scales. A self-similar two-point correlation profile implies that the turbulent processes producing and dissipating energy at different length scales are in equilibrium as the flow evolves downstream. However, in a highly three dimensional reacting flow field a self-similar two-point correlation profile may not be observed. Here, the non-reacting velocity field is considered for the computation of the two-point correlation. For the uniform crossflow cases the velocity vectors are parallel to the x-direction, thus, a coordinate transformation was not necessary for this analysis. Figure 4.18, shows the time averaged velocity field overlaid on the vorticity magnitude of the non-reacting jet case of J = 8 measured at Z = 5 mm. The fluctuating component of the

velocity field was sampled from a windowed region, shown in green rectangular box that includes the upper and lower shear layer region of the flow field. The region of interest was from X = 0 – 55 mm and Y = -25 – 25 mm. The correlation function computed in the streamwise direction consists of combined characteristics of longitudinal and transverse two-point correlation function. However, the correlation function computed in the spanwise direction consists of the characteristics of the transverse two-point correlation function only. The streamwise (ρ_{ii}) and spanwise (ρ_{ij}) two-point correlation coefficients plotted as a function of normalized separation distance, r/d_{JET}, are shown in Figure 4.19a and b. Figure 4.19a shows that the streamwise two-point correlation coefficient for the LSL region, $Y'/d_{JET} < 0$, and the USL region $Y'/d_{JET} > 0$, decays to zero within 1.25 and 1.5 jet diameter, respectively. This implies that with a uniform crossflow the streamwise integral length scales are of comparable size for both the shear layer region. In case of a swirling crossflow it was observed that the USL length scale was larger than the LSL and hence, it had asymmetric flow structures. Figure 4.19b, shows the variation of the transverse two-point correlation function. The trend indicates that closer to the nozzle exit, $X'/d_{JET} < 1.0$ the correlation value decays to zero as compared to further downstream regions where the correlation value asymptotically converges towards zero. This indicates that the zone of influence of the flow structures only upto one jet diameter downstream of the jet injection location. The streamwise (Λ_{11}) and spanwise (Λ_{22}) integral length scales at a given point, x_o, is calculated by computing the area under the two-point correlation curve. Figure 4.20, shows the integral length scales computed in the streamwise and spanwise direction at measurement planes Z = 5, 10 and 15 mm. The length scales have comparable sizes at Z = 5 mm and 10 mm. The integral length scales are largest at Z = 15 mm, with as

large as 1.3 jet diameters. The integral length scales computed in the spanwise direction shows a more interesting behavior. It is observed that the length scales increase with increase in nozzle separation distance with the largest length scales are calculated at Z = 15 mm. This trend of the integral length scales is aligned with the findings from time averaged flow field, it was observed that the wake recirculation region was largest at Z = 15 mm. This further supports the argument that there is a delay in the formation of the wake structures.

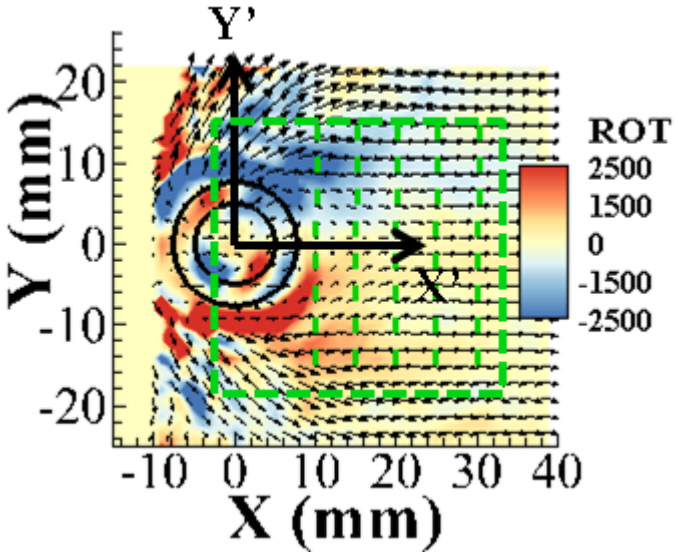

Figure 4.18. Time averaged velocity vectors overlaid on top of Z-vorticity contour map for non-reacting jet of J =8 measured at Z = 5 mm.

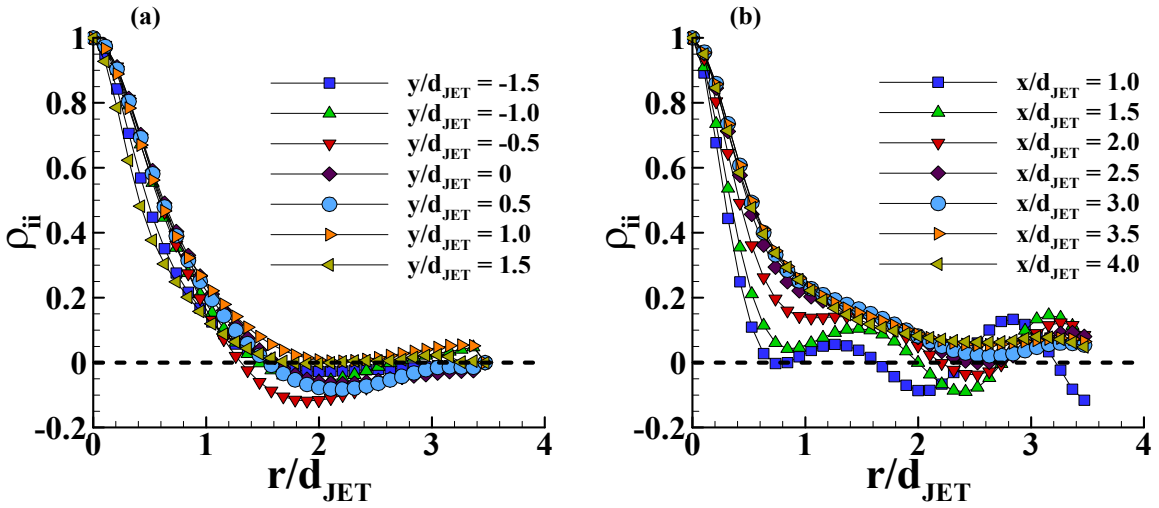

Figure 4.19. Spatial variation of (a) streamwise and (b) spanwise two-point velocity correlation coefficient for non-reacting jet, J = 8 measured at Z = 5 mm.

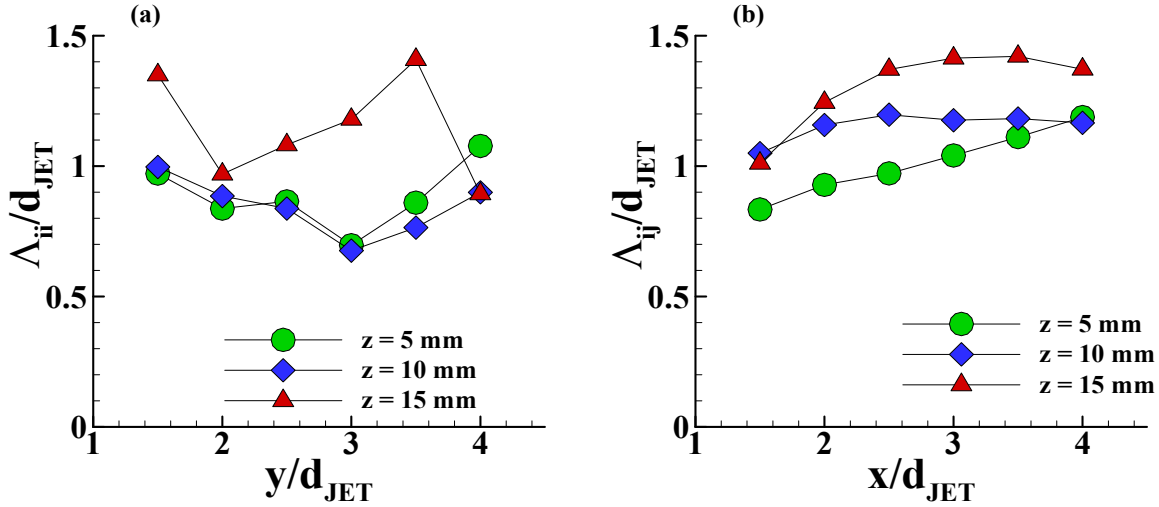

Figure 4.20. Spatial variation of (a) streamwise and (b) spanwise integral length scale for non-reacting jet, J = 8 measured at Z = 5, 10 and 15 mm.

4.6.2 Turbulent Kinetic Energy Spectra

The turbulent kinetic energy (TKE) spectra computed in the streamwise and spanwise direction of the flow-field is plotted in the wavenumber space for the reacting across two measurement planes. Here the turbulent kinetic energy is computed from the contributions of fluctuating component of x and y components of velocity. Figure 4.21

compares the streamwise and spanwise TKE spectra for the reacting jet cases of J = 3 ϕ_{jet} = 0.9 and J = 8 ϕ_{jet} = 0.9, at Z = 10 mm and 15 mm. The TKE at the largest length scale (k~0.1) for J = 8 is found to be higher as compared to J = 3 case. This can be attributed to the fact that the jet Reynolds number for J = 8, Re_{jet} = 45000, is higher than that for J = 3, Re_{jet} = 27500, and the higher Reynolds number results in a higher turbulence kinetic energy. Thus, a higher momentum flux ratio induces higher levels of turbulence intensity into the flow field which implies a higher degree of mixing. It is also seen that the TKE at the largest length scale is highest at J = 8 and Z = 15 mm. Similarly, for J = 3 highest magnitude of TKE is seen at Z = 15 mm. In the previous section it was shown that largest length scales are formed at Z = 15 mm and since the turbulent kinetic energy is introduced into the flow at the integral length scales, the TKE is highest for planes with largest integral length scales.

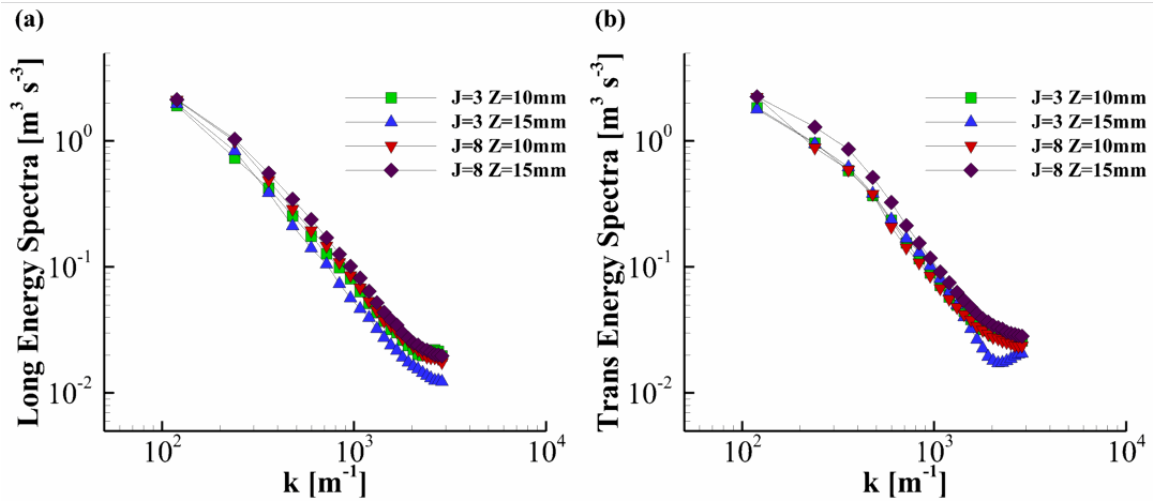

Figure 4.21. Turbulent kinetic energy spectra plotted in wave number space for the reacting jet cases J = 3, ϕ_{jet} = 0.9 and J = 8, ϕ_{jet} = 0.9.

4.6.3 Velocity Temporal Spectrum

In a turbulent reacting flow, the velocity field has a broad spectrum of temporal scales, and measurements at 10 kHz can resolve some of these scales. In order to extract the wake dynamics, velocity fluctuation statistics are extracted from the USL and LSL of J = 3, ϕ_{jet} = 0.9 case at Z = 15 mm measurement plane. To characterize the dynamics of the wake of the jet it is of interest to examine whether the vortical structures flow past a fixed point with a characteristic frequency. The power spectra of the x component of velocity (V_x) extracted from a location within the USL shows two peaks in the frequency at one at 362 Hz and the other at 441 Hz, as shown in Figure 4.22. The peak at 362 Hz is found to be dominant both at USL and LSL. Based on this observation of the characteristic frequency of the wake and the instantaneous velocity magnitude and ω_z magnitude, it is hypothesized that the associated dynamics are the result of wake vortex shedding around the jet. The Strouhal number based on the wake vortex shedding frequency, jet exit diameter and incoming mean crossflow velocity is calculated to be 0.1. Thus, compared to the reacting jets in swirling crossflow where the St_{wake} was as high as 0.18, the vortex shedding dynamics is slower for the reacting jets in uniform crossflow. The effect of a swirling or uniform crossflow on wake vortex shedding dynamics of a reacting jet has not been reported earlier in the literature.

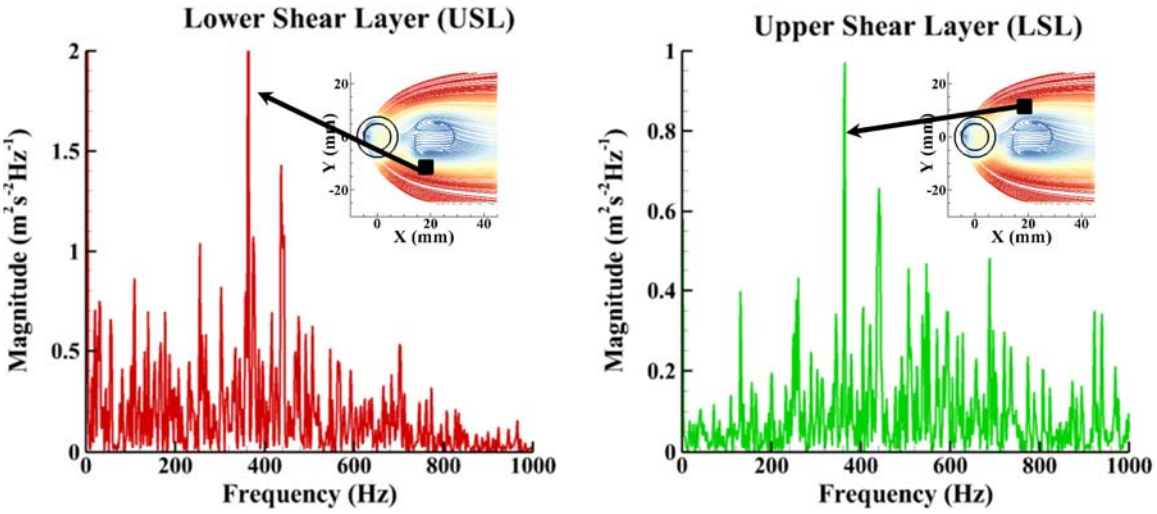

Figure 4.22. The power spectral density (PSD) of the fluctuating part of the x-component of velocity (V_x) extracted from (a) upper shear layer and (b) lower shear layer (LSL) for the reacting jet case J = 3, ϕ = 0.9, Z = 15 mm. The plots indicates presence of a single peak frequency at f = 362 Hz.

The values of the wake Strouhal number computed for all of the RJICF cases are shown in Table 4.3. It is interesting to see that St_{wake} is found to be within a narrow range of 0.09 – 0.12 for all the JICF/RJICF cases, irrespective of the momentum flux ratio or fuel reactivity. The peak frequencies for the non-reacting jet cases are found to be one-third of the peak frequencies for reacting jet cases. The crossflow mean velocities for the non-reacting and reacting cases are 13 m/s and 36 m/s, respectively. Thus, it can be concluded that the dynamics of the wake flow field of the reacting jet are more strongly dependent on the crossflow velocity than on the jet injection parameters.

Table 4.3. Wake Strouhal number (St_{wake}) for all the test cases.

Case	TYPE	Momentum Flux Ratio, J	Jet Type	Fuel	f_{wake} (Hz)	St_{wake}
1	NR	3	Air	NA	116	0.09
2	NR	8	Air	NA	122	0.092
3	R	3	Premixed NG	Φ = 0.9	362	0.105
4	R	8	Premixed NG	Φ = 0.9	411	0.114

4.7 Proper Orthogonal Decomposition (POD)

Proper orthogonal decomposition (POD) is a powerful mathematical tool used to extract coherent structures present in a flow field. The decomposition technique is used to analyze an ensemble of data or instantaneous velocity vectors. In this section a brief discussion on the POD analysis on the flow-field of non-reacting jet case of J = 8 at Z = 5 mm and reacting jet case of J = 3 ϕ_{jet} = 0.9 at Z = 15 mm is presented.

Figure 4.23 shows the most dominant POD modes computed from the velocity field of the non-reacting jet J = 8, that contribute 50% of total kinetic energy of the flow field. POD mode structures are shown as velocity vectors overlaid on vorticity magnitude. POD mode 1 shows the mean structure of the shear layer which is the most energetic feature of the flow field. POD modes 2 to 6 together represent the wake structures within the near wake region. These modes contain the dynamics of the wake structures. The first POD mode represents the shear layer between the jet and the crossflow fluid. This is the most energetic mode and comprises of 26.7% of the total kinetic energy. The mean kinetic energy is also highest along the shear layers. A wake structure is seen in POD mode 2, 3 and 4 show a large single vortex structure aligned in the mean flow direction. The vortex

structure in POD mode 2 is centered at approximately X = 7.5 mm and Y = 0 mm. POD mode 3 shows the vortex structure centered at X = 20 mm and Y = 7.5 mm and another structure appears above the injector location. A vortex structure is seen centered at X = 27 mm and Y = 0 mm, which seems to be linked to the same vortex structure seen in POD mode 2 and 3. The three modes together show a convection pattern of the wake structure. POD mode 5 show a counter-rotating pair of vortex structure at LSL and USL.

Figure 4.24 shows the POD modes computed from the velocity field of the reacting jet J = 3, ϕ = 0.9, Z = 15 mm and the corresponding power spectra of the temporal modes in the frequency domain. It is evident that the dominant frequency in the temporal modes of mode 2, 6 and 7 is 362 Hz with a second peak at 441 Hz. The flow structure that represents the dynamics at 441 Hz is captured by mode 5. The dominant frequency of 362 Hz was captured in the velocity power spectra analysis and its appearance in the POD mode dynamics indicates that it is related to the wake vortex structure. Figure 4.25 shows the trend of percentage energy in each of the first seven modes at measurement planes of Z = 5, 10 and 15 mm. It is clear for the bar chart that there is an increase in the energy content of modes 2 to 7 with an increase in nozzle separation distance. The contribution of POD mode 1 reduces from 67.5% at Z = 5 mm to 50.5% at Z = 15 mm, which results in corresponding increase in the energy of other POD modes. These calculations are again analogous to the trend observed in streamwise and spanwise turbulent kinetic energy. The wake structures are more developed and their contribution to the turbulent kinetic energy increases with increase in nozzle separation distance.

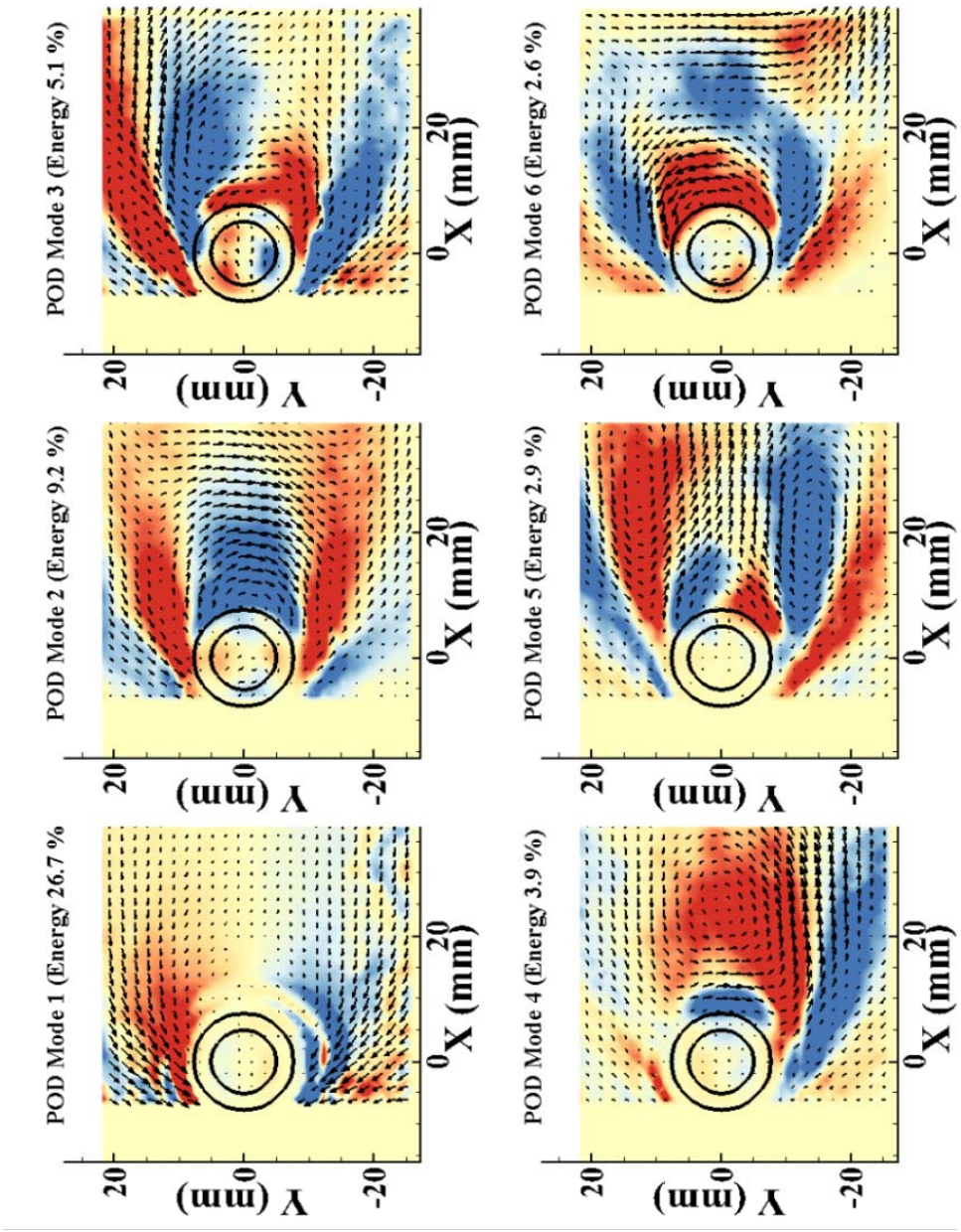

Figure 4.23. POD modes 1 – 6 for the non-reacting jet, J = 8, Z = 5 mm.

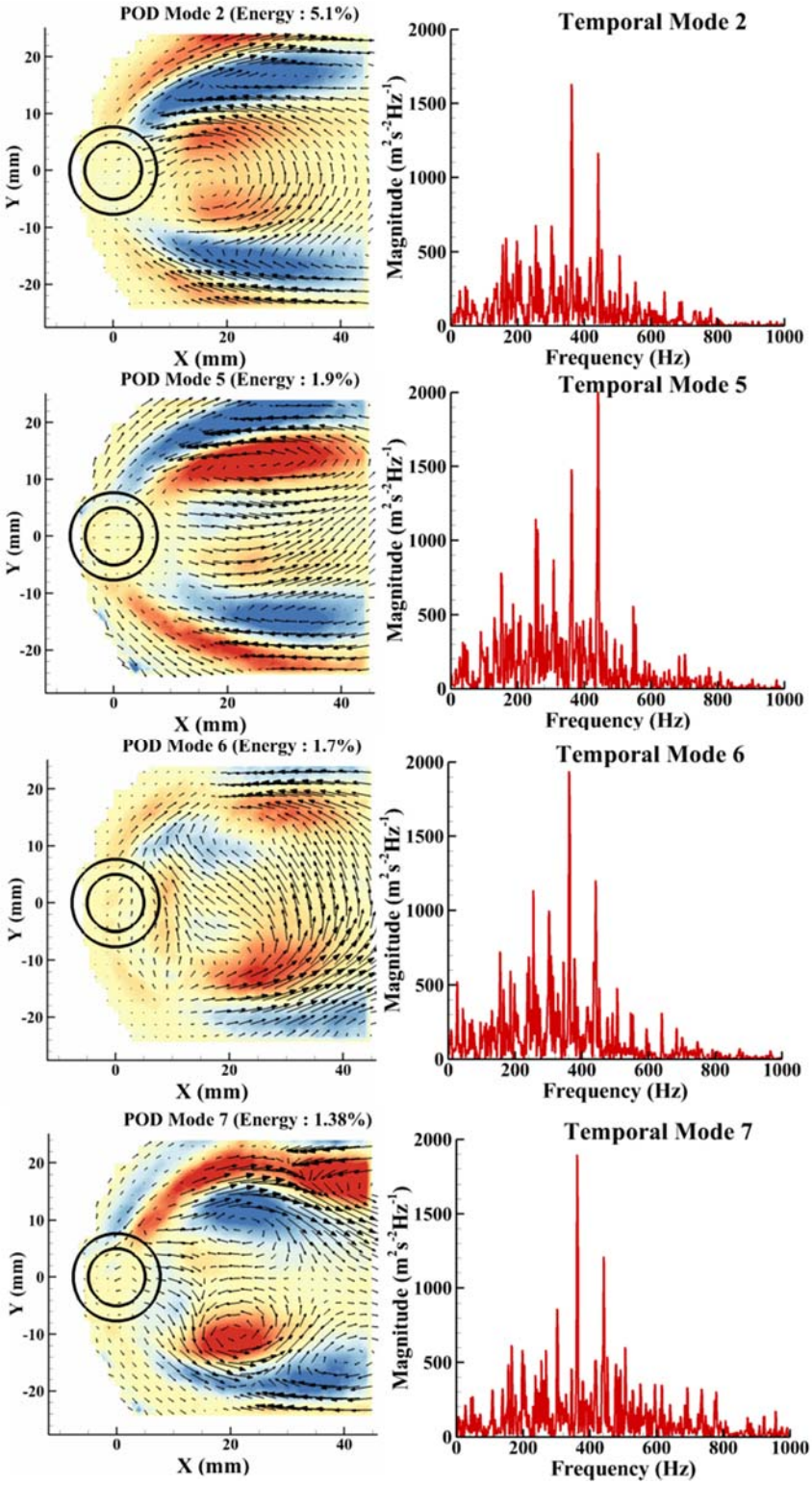

Figure 4.24. POD modes 2, 5, 6 and 7 and the corresponding frequency spectra of the temporal modes, for the reacting jet, J = 8, ϕ_{JET} = 0.9, Z = 5 mm.

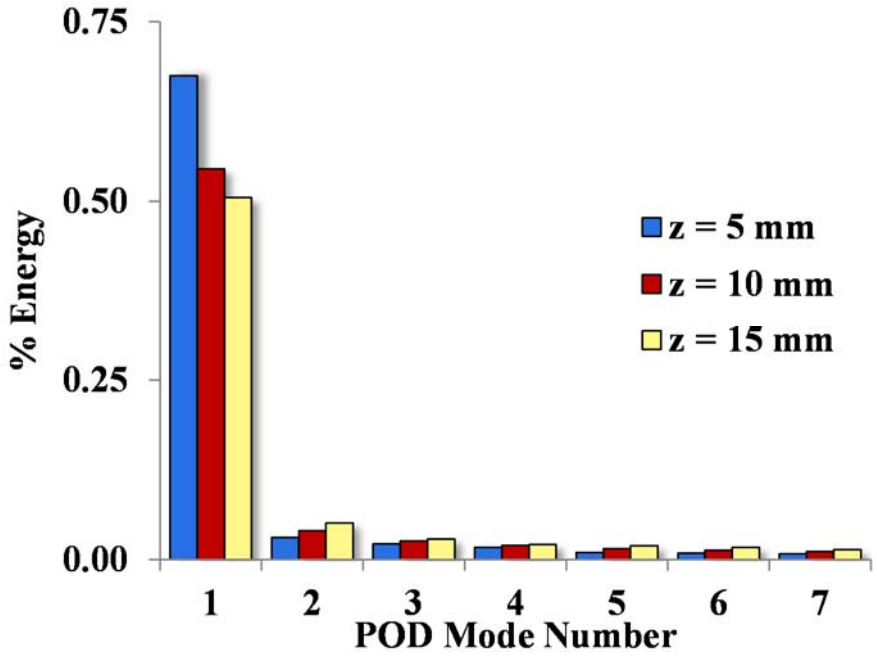

Figure 4.25. Kinetic energy distribution between the first five POD modes across the three measurement planes, Z = 5 mm, 10 mm and 15 mm, for J = 3 and ϕ_{jet} = 0.9.

4.8 Conclusions

In this chapter the results of a time resolved PIV measurements in an optically accessible high pressure distributed combustion system are discussed. The secondary combustion zone features transverse injections of premixed natural gas/heated air jets into a unifor vitiated crossflow. Two component PIV measurements were acquired at a repetition rate of 10 kHz, which enabled tracking of the complex flow structures of the RJICF. The PIV measurements were performed at 5 different planes along the cross-section of the jet in order to understand the three dimensional flow-field associated with RJICF.

The main contribution to the literature of RJICF was the quantitative comparison of the structure and dynamics of the flow-field of a RJICF under the influence of a uniform vitiated crossflow and a swirling vitiated crossflow. The uniform vitiated crossflow was

produced by a bluff-body-burner. The jet is aligned with the mean direction of the crossflow which is in the X-direction unlike the swirling crossflow cases where the jet was inclined at 45 degrees to the X-direction. PIV measurements of reacting and non-reacting jet cases show an interesting trend in the formation of wake vortex structures. It is discovered that there is a delay in the formation of wake vortex structure and unlike the swirling crossflow cases the wake structure appears after one jet diameter form the jet injection plane. Also unlike the swirling crossflow cases there is no entrainment of PIV seed particles in planes below the jet injection location. Furthermore, it is found that the velocity gradient in the wake of the jet in a uniform crossflow is half the velocity gradient seen in case of a swirling crossflow. As a result, the vorticity magnitude computed at all the measurement planes for uniform crossflow cases are approximately half the vorticity magnitudes computes for reacting jets in swirling crossflow. It is also seen that there is a faster recovery of velocity in the wake of the jet in a uniform crossflow. These variations in the flow-field of the jet would appropriately answer the initial observation of delay in the formation of a recirculation region in uniform crossflow cases. The weaker vorticity field also suggests that there will be reduction in the rate of entrainment of combustible mixtures in the near wake region of the jet. Additionally, there is a shift towards lower St_{wake} of the non-reacting and reacting jets in uniform crossflow. The St_{wake} is found to be varying in the range of 0.09 – 0.12 for all the JICF/RJICF cases. This analysis complements to the earlier conclusion that there is drop in the rate of jet-crossflow entrainment into the wake of the jet.

CHAPTER 5. HIGH-REPETITION-RATE SIMULTANEOUS PIV/OH-PLIF MEASUREMENTS IN THE WAKE OF A REACTING JET INTO A SWIRLING VITIATED CROSSFLOW

5.1 Introduction

The search for clean energy sources has motivated the design and development of advanced energy conversion systems that can meet the current and future energy needs with minimal impact on the environment. Emissions from natural-gas-fueled power generation gas turbines are regulated by environmental legislation, which places increasingly stringent limits on the emission of nitrogen oxides (NO_x) [12]. One means to achieve low NO_x emissions is to reduce peak flame temperatures, which can be attained by the premixed, lean burn approach: premixing the air and the fuel prior to combustion and burning the globally lean mixture, downstream, in the combustor [17]. However, lean combustion is often accompanied by instability, wherein, resulting pressure pulsations can lead to catastrophic mechanical damage. Secondary injection of the fuel, also referred to as staged combustion, has been identified as a means of increasing the power output of the gas turbine systems with minimal contribution to NO_x emission and also as a means of controlling combustion instabilities. Recent progress in the field of turbine blade materials has enabled gas turbine manufacturers to raise the turbine inlet temperatures leading to an increase in thermal efficiency of the engine [17].

In previous chapters (Chapter 4 and 5) the flow field of the reacting jet was investigated using high-repetition-rate (HRR) (5 kHz/10 kHz), two-component particle imaging velocimetry (PIV). The swirling nature of the crossflow was characterized in detail [40]. Premixed jets composed of natural gas and air were injected through an extended nozzle into the vitiated flow downstream of a low swirl burner (LSB) that produced the vitiated, swirled flow. The jet-to-crossflow momentum flux ratio was varied to study the corresponding effect on the flow field. The results indicate that the shear layer and wake field vortices play a significant role in stabilizing a steady reaction front within the near wake region of the jet. In this study we describe an investigation of flame structure and fluid dynamics for a reacting jet in a vitiated crossflow at elevated pressure. Simultaneous two-component PIV and OH-PLIF measurements were performed at a repetition rate of 10 kHz in a gas turbine combustor operating at 5.5 bars. The flow-flame interaction within the wake of an auto-igniting jet carrying fuel issuing into a swirling, vitiated crossflow is investigated. Interesting phenomena such as flame detachment and re-attachment, local extinction, and vortex-flame interactions are observed. These measurements, acquired at relevant engine conditions, are a natural utilization of high-speed diagnostic systems and provide crucial insight to the complex processes of flow-flame interaction.

5.2 Experimental Test Matrix

The reacting jet fluid in our study was composed of two types of fuel, i) H_2 diluted with N_2 (40%/60%) and ii) premixed natural gas (ϕ_{jet} = 0.9). The experimental data discussed here are based on simultaneous two components PIV and OH-PLIF at 10 kHz. A detailed test matrix is shown in Table 5.1for the simultaneous PIV/OH-PLIF study

discussed in this chapter. The swirling crossflow and the jet fluid comprised of hot air only for the non-reacting cases, the crossflow and jet temperatures are maintained to ensure a density ratio, S = 1. The simultaneous PIV/OH-PLIF measurements were performed at the z = 5 mm, 10 mm and 15 mm planes.

Table 5.1. Test matrix for the simultaneous PIV/OH-PLIF study.

Cross Flow Operating Condition					
Operating Pressure (atm)			5.5		
Operating Temperature (K)			723		
MCZ Air Flow Rate (kg/s)			0.39		
MCZ Equivalence Ratio, ϕ_{main}			0.5		
Main Flow Reynolds Number(NR), Re_{main}			105000		
Main Flow Reynolds Number(R), Re_{main}			61000		
Non-Reacting JICF Conditions					
High Temperature Air Jet	Momentum Flux Ratio, J	Density Ratio, S	Jet Reynolds Number, Re_{jet}		
	3	1	16900		
	6	1	24200		
	8	1	27600		
Reacting JICF Conditions					
FUEL JET	Momentum Flux Ratio, J	Density Ratio, S	Jet Reynolds Number, Re_{jet}	ϕ_{jet} =0.9	ϕ_{jet} = 3.0
Premixed Natural Gas	3	2.5	27500	ΔT = 36 K	ΔT = 145 K
	8	2.5	45000	ΔT = 52 K	ΔT = 212 K
				40%/60%	50%/50%
H2/N2	3	4.25	72,000	ΔT = 28 K	ΔT = 96 K
	8	4.25	118,000	ΔT = 44 K	ΔT = 147 K

5.3 OH-PLIF Image Processing

The raw OH-PLIF images collected required image corrections to remove the noise and to account for the non-uniformity in the laser sheet intensity profiles and the CMOS detector of the camera. In order to correct the OH-PLIF images, three steps were followed. First, the images were calibrated and scaled to physical space. Next, background subtraction was performed using the time-averaged background signal acquired after each measurement (representative of the measurement plane) with the laser sheet blocked. Then the non-linearity in the CMOS detector was corrected by white noise correction. A diffused light source was used in front of the intensified camera and the images were normalized by the white noise of the CMOS detector. Then, the background-corrected images were divided by an ensemble-averaged flat-field image, which was derived from PLIF images of OH within the vitiated crossflow. The OH distribution was judged to be uniform, and thus any non-uniformity in the OH-PLIF images results from laser sheet non-uniformity and imaging artefacts such as intensifier fixed-pattern noise. A MATLAB image processing algorithm was developed for flame front/edge detection. A two-dimensional median filter and an adaptive noise removal filter (Wiener2) were used to remove the high-frequency noise in the images. A Gaussian filter with a kernel size of 3 by 3 pixels was used to further smooth the OH-PLIF images. The OH-PLIF gradient field was binarized, and a morphological operation was applied onto the binarized images that thin objects to a single pixel lines. The output of the flame-front detection algorithm was stored as the flame-front edge. The time averaged OH-PLIF image of the vitiated crossflow is shown in Figure 5.1a, which is used to divide the raw PLIF images (shown in Figure 5.1b), of the reacting jet case of J = 3, 40%H_2/60%N_2, Z = -5 mm, to correct the non-uniformity in the

laser sheet intensity. The post-processed corrected PLIF image is shown in Figure 5.1c. A flame front edge detection algorithm is used to extract iso-lines of maximum gradient of the OH-signal. Figure 5.1d shows the flame front edges overlaid on top of the corrected OH-PLIF images. Figure 5.2 highlights the same procedure correcting the OH-PLIF image and extracting the flame-front edges of the reacting jet case of J = 3, 40%H_2/60%N_2, Z = 5 mm.

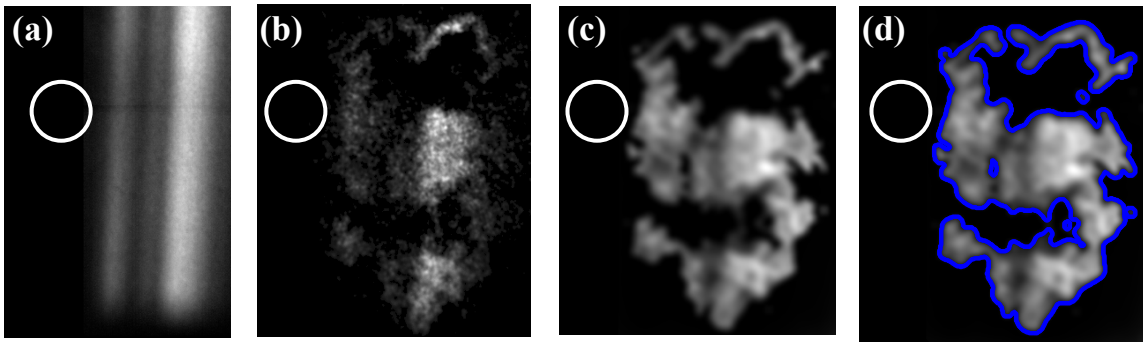

Figure 5.1. OH-PLIF image correction procedure (a) time average OH-PLIF image of the vitiated crossflow, (b) raw OH-PLIF image of the reacting jet, (c) intensity corrected OH-PLIF image and (d) flame front edge for reacting jet J = 3, 40%H_2/60%N_2 measured at Z = -5 mm.

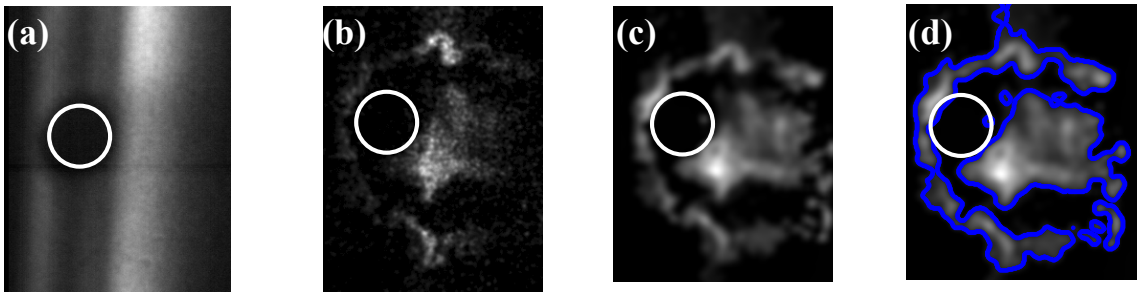

Figure 5.2. OH-PLIF image correction procedure (a) time average OH-PLIF image of the vitiated crossflow, (b) raw OH-PLIF image of the reacting jet, (c) intensity corrected OH-PLIF image and (d) flame front edge for reacting jet J = 3, 40%H_2/60%N_2 measured at Z = 5 mm.

5.4 Time Averaged OH-PLIF Intensity Field

5.4.1 Time Averaged OH-PLIF Intensity Field in the X-Z Plane

A time averaged OH-PLIF intensity field is shown in Figure 5.3, highlighting the jet flame trajectory and the extent of penetration of the jet flame into the crossflow. These measurements were performed along the X-Z plane which is normal to the PIV measurement planes. The injector is shown in a grey box protruding into the flow field. The crossflow moves from left to right in the figure. The time averaged images show that there is no reaction in the windward side of the jet and the jet flame is anchored along the leeward side of the jet. The unreacted part of the jet core for the J = 8 case, as highlighted in Figure 5.3, is longer than the reacting jet case of J = 3, indicating deeper penetration of the reacting jet for higher momentum flux ratio. For both the reacting jet case, J=3 ϕ_{jet} = 3 and J=8 ϕ_{jet} = 3, it can be clearly seen that the wake of the jet exhibits a strong OH-PLIF intensity field, hence, justifying the focus of current paper on understanding the flow-field within the wake of the jet.

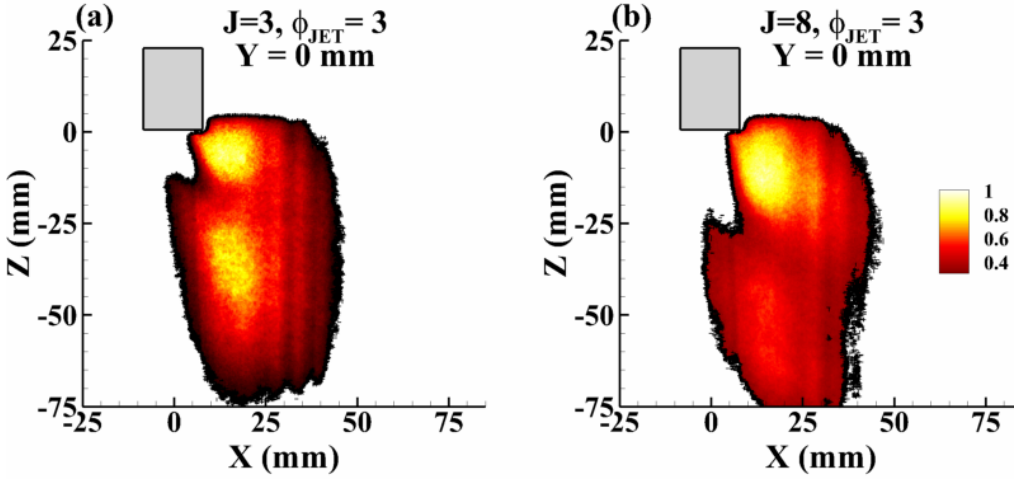

Figure 5.3. Time averaged normalized OH-PLIF intensity field for reacting jet cases of J=3 ϕ_{jet} = 3 and J=8 ϕ_{jet} = 3 measured at Y = 0 mm, indicating the jet flame trajectory under the influence of swirling crossflow.

A time averaged OH-PLIF intensity field of H_2/N_2 non-premixed jet, is shown in Figure 5.4, highlighting the jet flame trajectory and the extent of penetration of the jet flame into the crossflow. These measurements were performed along the X-Z plane which is normal to the PIV measurement planes. The time averaged images show that both the reacting jet cases, J=3 40%H_2/60%N_2 and J=8 40%H_2/60%N_2, are attached to the injector. The jet core with zero PLIF intensity is seen for both the reacting jet cases. It is evident that the wake of the jet exhibits a strong OH-PLIF intensity field and the intensity field is still seen in a small region below the jet injection location in the immediate vicinity of the injector.

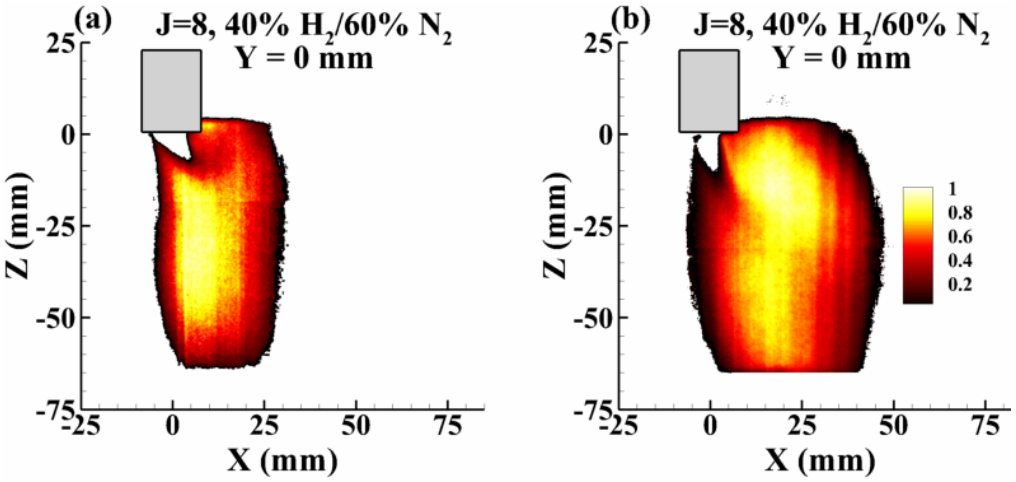

Figure 5.4. Time averaged normalized OH-PLIF intensity field for reacting jet cases of J=3 40% H_2/60% N_2 and J=8 40% H_2/60% N_2 measured at Y = 0 mm, indicating the jet flame trajectory under the influence of swirling crossflow.

5.4.2 Time Averaged OH-PLIF Intensity Field in the X-Y Plane

A time averaged OH-PLIF intensity field is shown in Figure 5.5, highlighting the mean structure of the jet flame and its variation across z = 5, 10 and 15 mm. The mean OH-PLIF intensity shows the presence of flame front along the windward side of the jet,

however, OH-PLIF intensity is relatively lower than rest of the flame body. The core of the jet, with zero intensity, enveloped between the flame front along the windward side of the jet and the wake region reaction zone is evident at Z = 5 and 10 mm measurement planes. The recirculation region that entrains burnt products as well as unburnt reactants shows a broad region of OH-PLIF intensity.

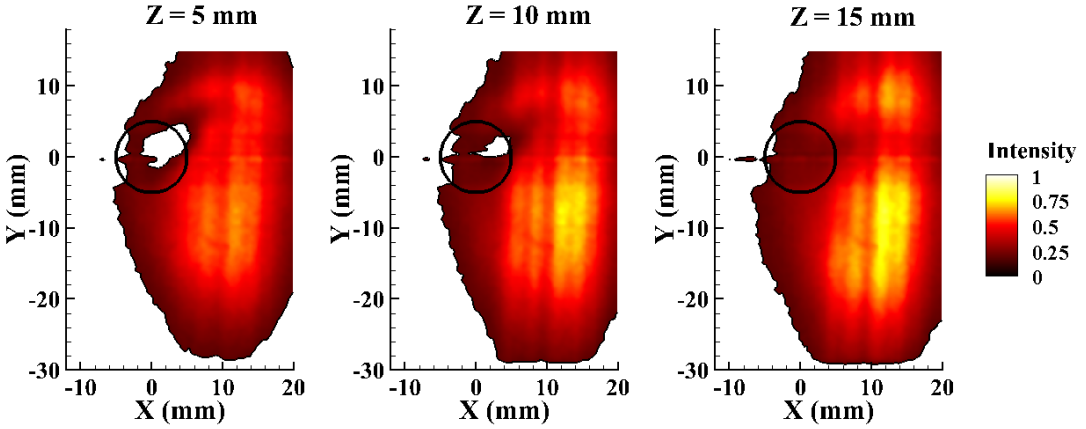

Figure 5.5. The time averaged OH-PLIF intensity field for J = 8; 40%H_2/60%N_2 case measured at a) Z = 5 mm, b) Z = 10 mm and c) Z = 15 mm away from the nozzle exit.

5.5 Instantaneous OH-PLIF Intensity Field

5.5.1 Auto-Ignition Study of H_2/N_2 Reacting Jets

In order to capture the sequence of auto-igniting H_2 jet, the camera and laser system are synchronized with the secondary fuel valve actuation. This is performed only at the center plane (Y = 0 mm) of the jet flame trajectory. A series of instantaneous processed OH-PLIF images showing the temporal evolution of the auto-igniting jet is shown in Figure 5.6, for the reacting jet case of J = 8 and fuel 40%H_2/60%N_2. Every fourth image in the sequence of the OH-PLIF images are shown here. The yellow rectangle represents the physical location of the injector. There is a lag between the valve actuation and the trigger

of the camera as a result initial 400 – 500 images do not show any OH. Thus, it is difficult to exactly synchronize the systems to measure the ignition delay in these systems. In this section the OH-PLIF images discussed show the propagation of flame front from the time instance when the first flame kernel appears. The first flame kernel appears along the leeward side of the jet. The recirculation region in the leeward side of the jet promotes fuel-air mixing and provides conditions favorable to sustain a reaction. Consider, at time = 0.0 ms the first flame kernel appears in the leeward side of the jet attached to the nozzle exit. This flame kernel propagates 40 mm into the crossflow within 1.2 ms when a thin reaction front appears along the windward side of the jet. It takes approximately 3.6 ms to establish a fully connected jet flame that penetrates 50 – 60 mm into the crossflow. The OH-PLIF intensity shows a sharp gradient in the intensity field across the windward side shear layer, indicating a thin reaction front. The reaction occurs mainly within the jet and crossflow shear layer and it takes about 1.2 – 2.0 ms to attain a chemically reactive mixture in the windward side. The thin reaction front in the windward side is mainly due to high levels of compressive strain rates leading to high scalar dissipation rate. On the other hand, in the leeward side of the jet there is wide region of OH-PLIF intensity field. The recirculation region in the wake of the jet entrains hot products and unburnt fuel-air mixture leading to super-equilibrium concentrations of OH radical owing to high fluorescence intensity in these regions. Thus, the sequence of OH-PLIF images capturing the auto-ignition dynamics of the H_2 jet flame show that there is a finite delay in the formation of flame kernel and it takes approximately 2 ms to form chemically reactive mixture in the windward side of the jet leading to combustion.

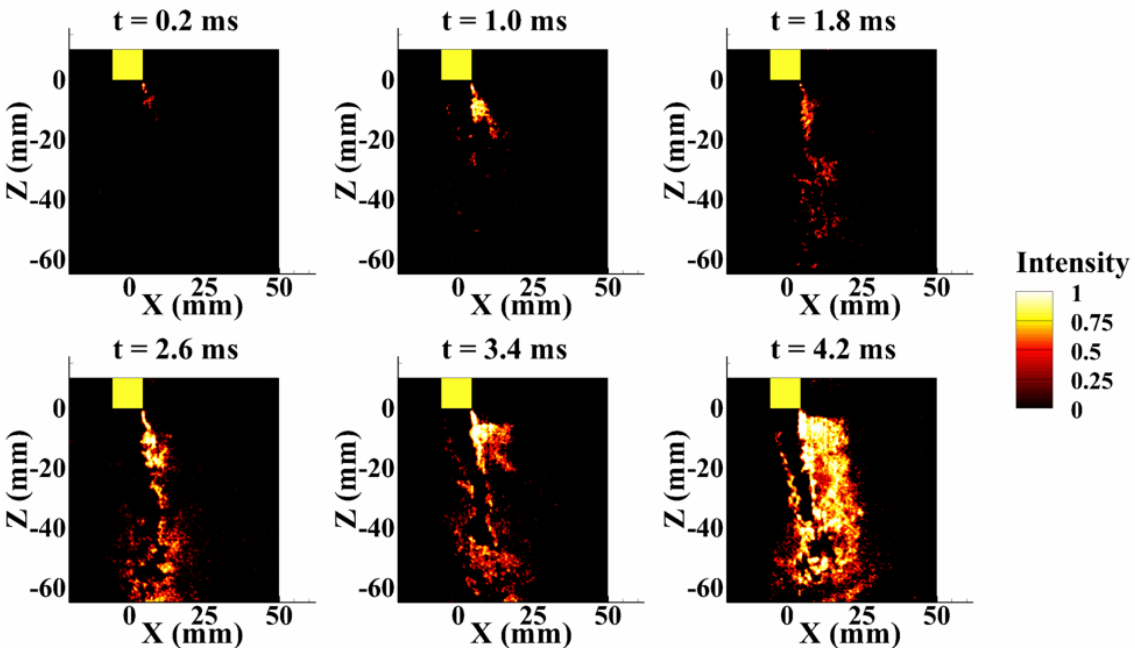

Figure 5.6. OH PLIF single-shot images for the reacting jet case of 40% H_2/60% N_2, J=8 acquired at the jet center plane (y = 0 mm). The sequence of images indicates the initiation of auto-ignition and temporal evolution of the flame front.

5.5.2 Instantaneous OH-PLIF Intensity Field in the X-Y Plane

A sequence of processed OH-PLIF images corresponding to the reacting jet case for J = 3 and ϕ_{jet} = 3.0 is shown in Figure 5.7. This sequence of images is based on measurement along the cross-section of the jet, lying in the X-Y plane. The measurement plane shown here corresponds to Z = 5 mm. The grey concentric circles represent the physical location of the nozzle, centered at X = 0 mm and Y = 0 mm, with the smaller circle corresponds to the jet exit diameter (d_{JET} = 10 mm). The natural gas jets do not show any OH-PLIF intensity on the windward side of the jet. This could be due to large compressive strain rates prevalent on the windward side of the jet making it difficult to sustain a stable reaction front. However, the leeward side and wake region of the jet seem to be favorable in sustaining a stable reaction zone. This sequence of images is an

illustrative of the complexity of the flame structure prevalent in an RJICF. An interesting transient behavior is observed between time t = 0.1 ms to 0.4 ms. The flame front is being pushed downstream at locations X = 15 – 20 mm and y- locations corresponding to Y = -5 mm and -20 mm. Eventually, part of the flame front breaks-off from the main body of the reaction zone. This observation highlights the importance of obtaining velocity, vorticity and strain rate field simultaneously at these locations in order to identify the role of fluid dynamics in local extinction leading to flame break-up.

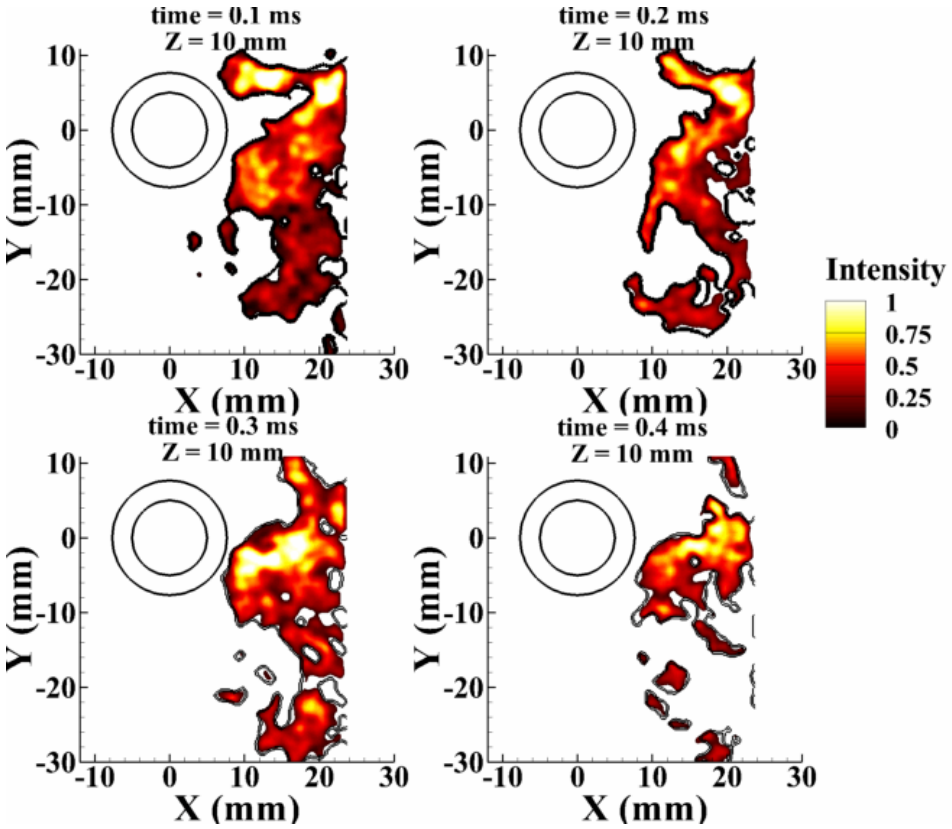

Figure 5.7. Instantaneous OH-PLIF intensity field overlaid on top of the flame front edge for the reacting jet case of J = 3, ϕ_{jet} = 3.0 at plane Z = 5 mm.

A sequence of instantaneous OH-PLIF images of the jet flame cross-section is shown in Figure 5.8 for the reacting jet case of J=8 and 40%H_2/60% N_2 at the measurement

plane Z = 10 mm, where Z indicates the distance from the nozzle exit plane. The jet flame reaction front is observed to have a highly distorted flame structure. The direction of the mean crossflow is shown by the white arrow in the first image, which is based upon the PIV measurements discussed in the subsequent section. Under the influence of swirling crossflow the jet flame is anchored at an angle to the nozzle exit plane. The white concentric circles represent the inner and outer diameter of the injector. It is observed that the flame front tries to wrap around the core of the jet entraining hot products and unburnt fuel air mixture into the wake of the jet. The flame structure can be described as two arm like structure the envelopes a region with a broad OH-PLIF intensity field of the jet flame. Between time = 0.2 ms – 1.2 ms the OH-PLIF intensity field within the recirculation region moves towards the nozzle in a direction opposite to the mean flow field, indicating the local velocity field is pushing the products and fuel-air mixture towards the nozzle. The flame is always anchored on both the windward and leeward side of the jet. The OH PLIF signal in the windward region is much weaker than the OH PLIF signal on the leeward side, which could be attributed to the local compressive strain rates leading to high rates of scalar dissipation. The momentum-flux ratio is seen to play a key role in flame structure of the RJICF. For J=3 it is characterized by attached flames as seen in the OH-PLIF measurements along the flame trajectory. OH PLIF images in the cross-section of the jet indicate that the windward side of the jet is characterized by a thin, non-premixed flame located in the windward shear layer. The leeward side flame structure is significantly different and is characterized by a broad, diffuse reaction zone in the recirculation region. The wake vortex structure is mainly responsible for the characteristic kidney-shaped flame structure in the lee-ward side of the jet.

These OH-PLIF measurements thus, show that the flame structure and flame stabilization mechanism is significantly different for a reacting jet in vitiated crossflow as compared to reacting jets in non-vitiated high temperature crossflow [72] and low temperature crossflow [53].

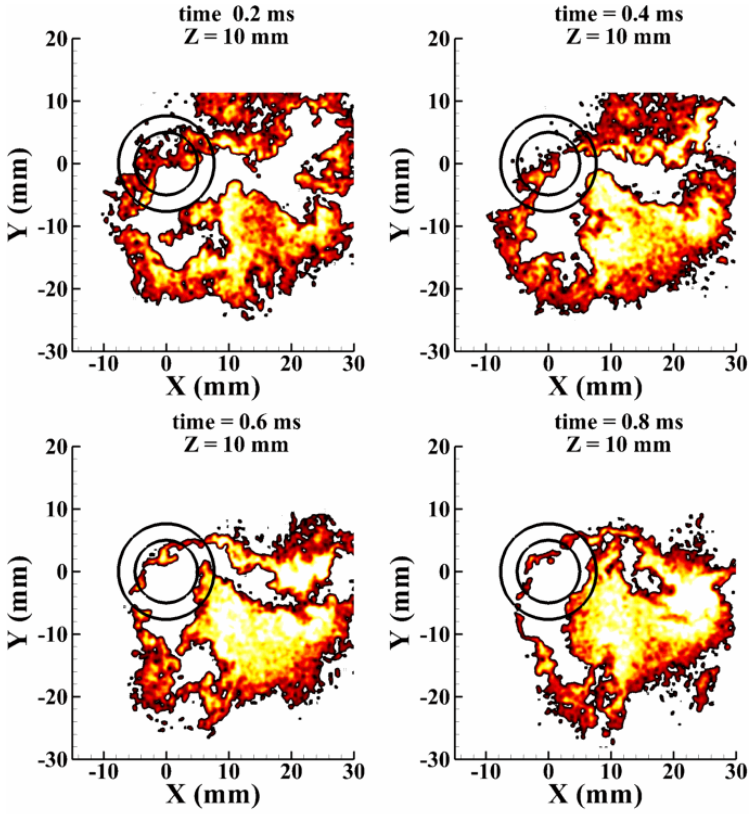

Figure 5.8. Instantaneous OH PLIF images for the reacting jet case of 40% H_2 60% N_2 J = 8 along the cross-section of the jet flame visualized at Z = 10mm. The consecutive sequence of OH-PLIF images are 0.2 ms apart.

5.6 Flame Length and Stretch Rate

In turbulent flames vortex-flame interactions in a wide range of length scales causes flame front to wrinkle and consequently an increase in flame surface area. In a premixed flame this is attributed to local velocity gradients and flame curvature [98][99][100]. An increase in flame surface area then leads to increase in the turbulent flame speed and a

faster rate of consumption of fuel-air mixtures. In computational studies in a flamelet based assumption flame surface area is calculated to estimate the reaction rate. It has been demonstrated earlier that turbulent flame properties such as flame surface area, Σ, stretch rate, **κ,** etc., could be calculated experimental by performing simultaneous OH-PLIF and PIV diagnostics [100]. In this study simultaneous PIV/OH-PLIF diagnostics are used to differentiate the flame structures of a premixed natural gas flame and a non-premixed H_2 flame in a reacting jet in crossflow configuration. The flame stretch rate, κ, as defined in Equations (5.1) and (5.2)**,** is the sum of the flow velocity strain rates, K_s (Equation (5.3)) and the flame curvature, K_c (Equation (5.4)) that are defined as

$$\kappa = \frac{1}{A}\frac{dA}{dt} \tag{5.1}$$

$$\kappa = K_s + K_c \tag{5.2}$$

$$K_s = -n.(n.\nabla)V + \nabla.V \tag{5.3}$$

$$K_C = S_L/R_C \tag{5.4}$$

A planar analog can be computed from experimental data using the flame front edges extracted from the OH-PLIF images. In this work, the reaction layer length was computed by dividing the OH-PLIF measurement domain into 0.8 mm by 0.8 mm cells (same as the vector resolution), then summing the total reaction layer length within each cell. In order to calculate the flame stretch rate, here, we have defined the mean flame stretch rate as a function of reaction layer length in Equation (5.5),

$$\kappa = \frac{1}{L_{flame}}\frac{dL_{flame}}{dt} \tag{5.5}$$

This gives us an estimate of the mean flame stretch rate within the measurement plane. The mean flame length, L_{flame}, and mean flame stretch rate, κ, of the reacting jet case of J = 3, 40%H_2/60%N_2 measured at Z = 5 mm is shown in Figure 5.9a and b. It is evident that a flame front with a convex curvature is present in the cells above the injector. The red color in the contour map shows the cells with consistent presence of a reaction front or the location of flame brush. The mean flame stretch rate computed from the flame length shows that the region with largest reaction layer length has smallest stretch rate. The blue color in the contour map of mean flame stretch rate overlaps with the red color contour map of the mean flame length. Thus, based on this analysis it is further confirmed that the H_2 jet flame is stable along the windward side of the jet where the stretch rate is favorable to sustain a stable reaction front. Figure 5.10a and b shows the mean flame length and mean flame stretch rate of the reacting jet case of J =3, ϕ = 3 measured at Z = 5 mm. Unlike the H_2 jet flame the premixed NG flame has a concave curvature and is half a jet diameter away from the center of the injector. It is also seen that the region with stable flamelets overlaps with the region with minimum flame stretch rate. It is known that the flame stretch rate is a function of velocity strain rates and the flame curvature. Figure 5.11 shows the flamelets overlaid on top of time averaged vorticity field for H_2 flame (Figure 5.11a) and premixed NG flame (Figure 5.11b). It is evident that the H_2 flame is primarily stabilized at the stagnation plane between the crossflow and the windward shear layer of the jet. This imparts a convex curvature to the flame structure. On the other hand NG flame is recirculation region stabilized and the mean flamelet is located at the stagnation plane between the leeward shear layer and the recirculation region. This leads to the concave curvature of the flamelet. Thus, there is a difference in the flame stabilization mechanism

between the two reactant fluids. Thus, with the help of simultaneous OH-PLIF and PIV diagnostics it was possible to identify both qualitatively and quantitatively the regions with favorable flame stretch rate and flow strain rates that helps stabilizing a reaction front.

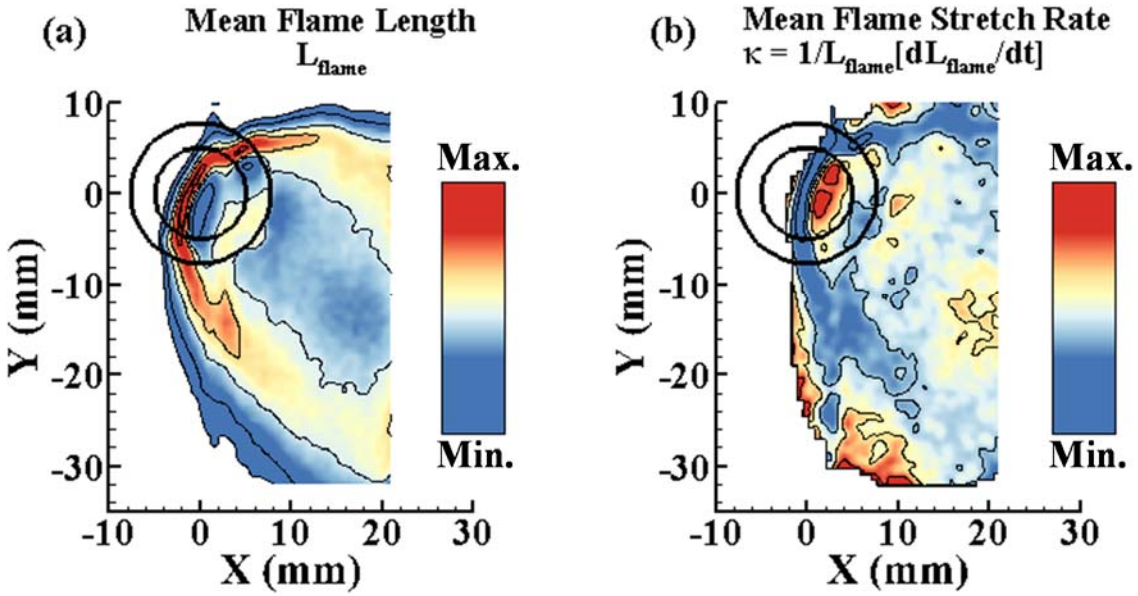

Figure 5.9. Time average (a) flame length and (b) flame stretch rate for the reacting jet case of 40% H_2 60% N_2 J =3, measured at Z = 5 mm.

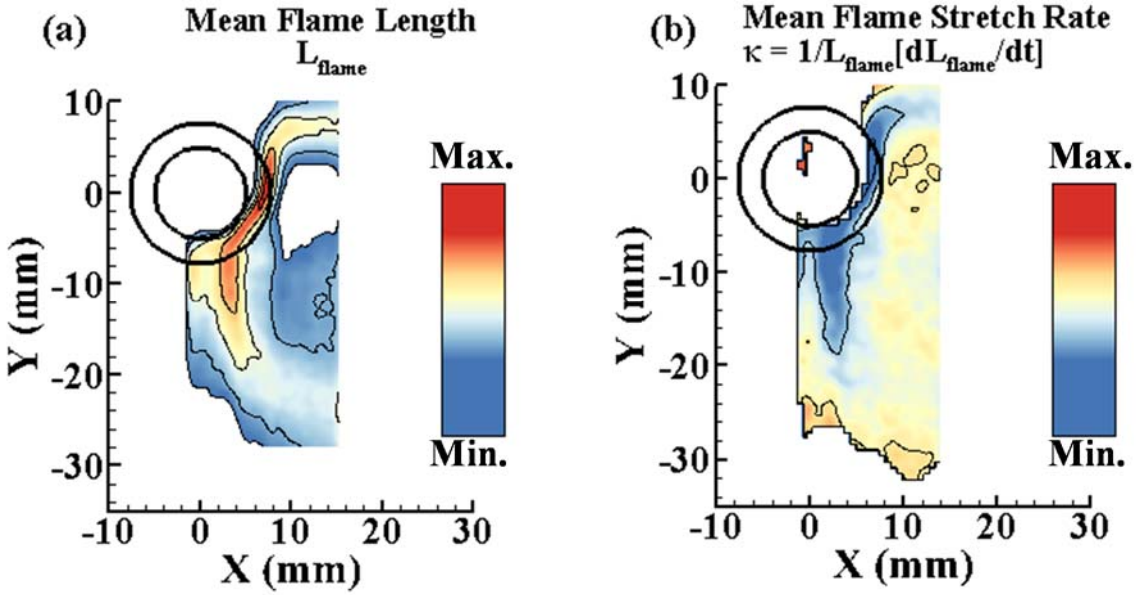

Figure 5.10. Time average (a) flame length and (b) flame stretch rate for the reacting jet case of J =3, ϕ = 3.0, measured at Z = 5 mm.

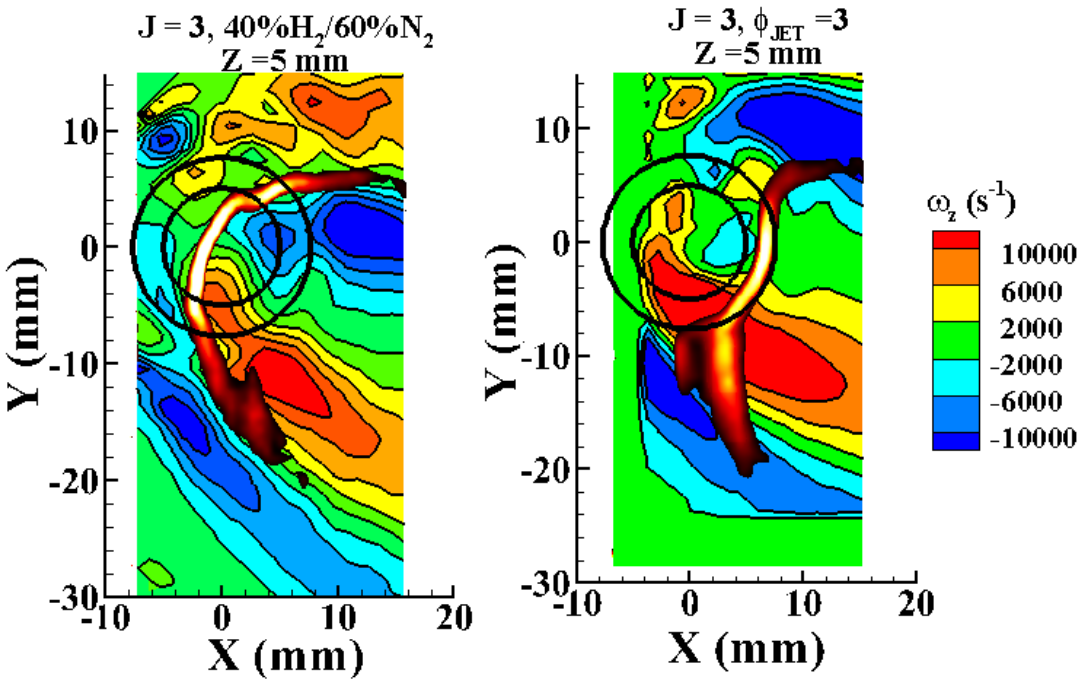

Figure 5.11. Mean OH-PLIF iso-surface overlaid on top of time averaged vorticity field for reacting jet case of a) 40% H_2 60% N_2 J =3 and b) J =3, ϕ = 3.0.

5.7 Flow-Flame Interaction

The time-averaged data provided insight into the steady features of the flow field. A close inspection of a sequence of instantaneous measurements discussed in this section will reveal new insights into the flow-flame interaction of the reacting jet. A sequence of 10 instantaneous velocity field and OH-PLIF images for the J = 8 reacting jet case (40%H_2/60%N_2) are shown in Figure 5.12. This sequence captures some of the unsteady features and transient events such as vortex-flame interactions, flame shedding, or flame detachment due to local extinction.

5.7.1 Instantaneous OH-PLIF Intensity

A 1-ms sequence of images of flame front edges is shown in Figure 5.12. A thin reaction front above the location of the injector, corresponding to the windward side of the

jet, is evident in all the OH-PLIF images. The sharp intensity gradient indicates that H_2 burns like a diffusion flame within the windward side of the jet. However, the wake of the jet promotes mixing of H_2 with the entrained hot products and vitiated crossflow. The wake of the jet provides favorable flow conditions to sustain a stable reaction zone. The sequence of images shown in Figure 5.12, is illustrative of the complex flame structure in the wake of the reacting jet. The reaction front has a characteristic kidney shaped structure, which can be attributed to the interaction of the wake vortices with the flame front. The image sequence also shows regions with local extinction and re-ignition in the upper and lower shear layer, which could be attributed to localized high compressive strain rates. However, it has been reported that the presence of flame holes and apparent extinction/ re-ignition is sometimes attributed to through plane motion of the flame front [101], [102]. Between time = 0.1 ms – 0.3 ms, at the location X = 10 mm, Y = 10 mm, flame re-ignition may be occurring, but this behavior, alternatively, might be due to through-plane flame propagation. An interesting behavior is seen between time = 0.6 ms – 1.0 ms, within the region X = 15 and 20 mm and Y = -20 and -25 mm. It is seen that the flow field is pushing the reaction front downstream, simultaneously; it appears that the flame front is being wrapped around a vortex structure. This event continues and results in thinning of the flame front until time = 1.0 ms, eventually leading to a local extinction at X = 20 mm and Y = -24 mm. This transient event will be further discussed quantitatively in Section 3.2.2. The image sequence captures another interesting transient event observed between time = 0.3 ms – 0.6 ms, where the flame front stretches, elongates and forms a neck at X = 15 mm and Y = 10 mm seen at time = 0.5 ms. The necked region eventually separates from the main body of the reaction zone and is convected downstream. This behavior can be related

to a sudden acceleration in the flow field that causes localized high compressive strain rates, leading to flame separation from the main reaction zone. Thus, in order to extract quantitative information concerning these transient behaviors, it is also important to obtain velocity, vorticity and strain rates.

5.7.2 Vortex-Flame Interaction

Figure 5.13, shows the flame edges, extracted from the OH-PLIF intensity field, and velocity vectors overlaid on the velocity magnitude contour map. The contour map scale ranges between 0 to 75 m/s. The red contours represent high velocity magnitude and blue contours represent low velocity. The interface between the inner and outer wake regions of the jet exhibits highest magnitudes for velocity, and the recirculation region features a strong negative velocity region, with velocity vectors pointing against the direction of swirl. For the better clarity of the vector field every second vector is shown in both x and y direction. The high speed fluid pushes the reaction zone downstream, and the the recirculation region pushes the reaction zone towards the nozzle exit. The image sequence between time = 0.1 ms – 0.5 ms shows high velocity within the upper shear layer, which correlates well with the transient event of necking of the reaction front followed by separation from the main flame body. Between time = 0.5 ms – 1.0 ms, it is observed that an increase in the magnitude of the velocity within the recirculation region pushes the reaction front closer to the nozzle.

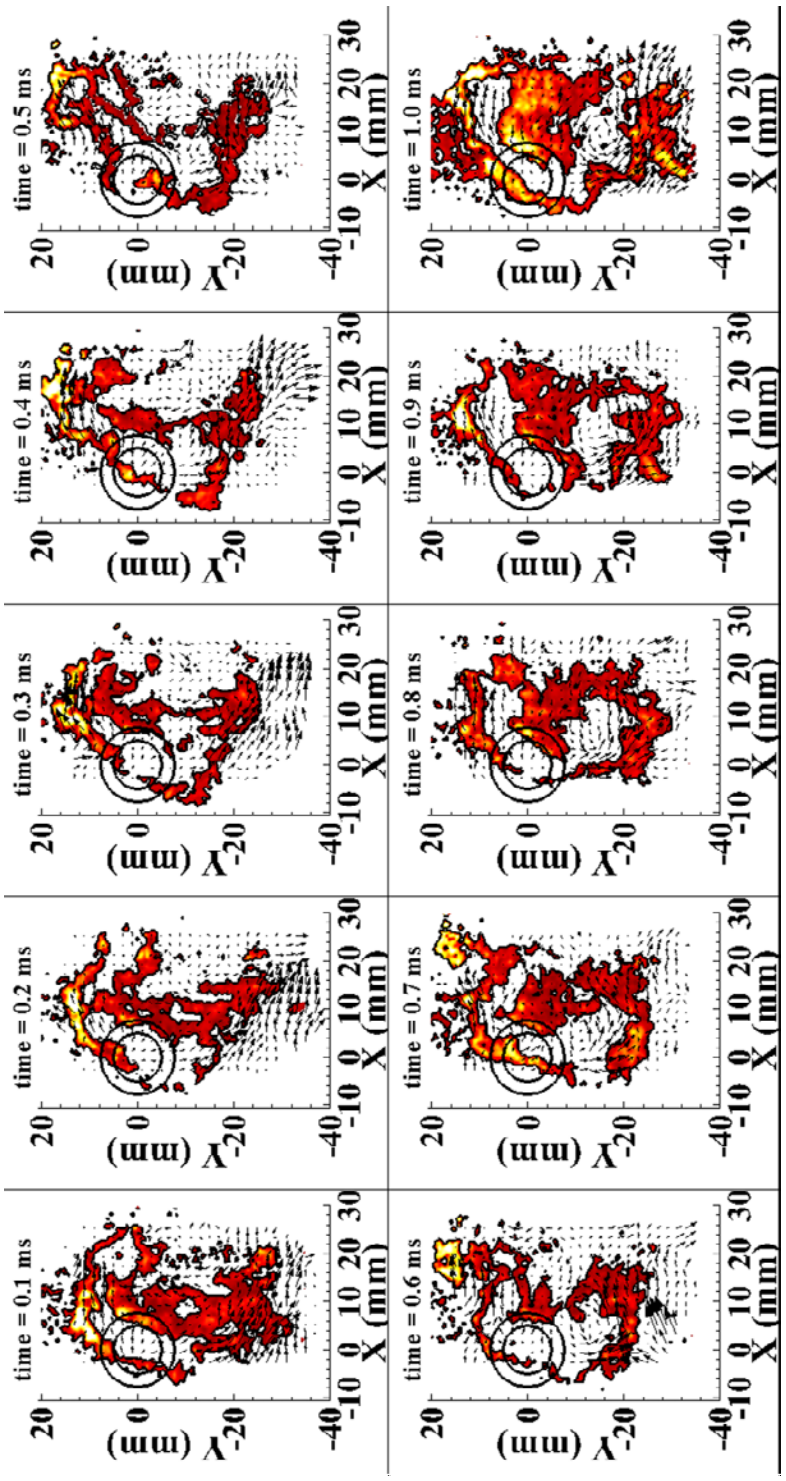

Figure 5.12. Sequence (Δt = 0.1 ms) of images in RJICF flame front edge overlaid on top of OH-PLIF images– time separation = 0.1 ms, for reacting jet case of J=8, 40%H_2/60%N_2 at Z = 10 mm.

Figure 5.14, shows the sequence of out-of-plane vorticity magnitude (-20000 s^{-1} to 20000 s^{-1}), which provides additional insight into the vortex - flame interaction. The red in the contour map represents counter clockwise rotation and blue represents clockwise rotation. A vortex structure, at time = 0.5 ms (with a counter-clockwise rotation represented by red contour), located at X = 5 mm and Y = -15 mm, appears to push the flame front downstream. It is also evident that the flame front wraps around this flow structure, thus, increasing the flame surface area and simultaneously thinning the reaction front. At time = 1.0 ms a local extinction is evident at the location X = 16 mm and Y = -24 mm, which could be due to the combined effect of higher instantaneous value of vorticity coupled high compressive strain rates. Thus, it is clear that the wake vortices have a strong influence on the flame front, causing thinning of the flame front leading to local extinction. It is also evident that the wake structures entrain the surrounding hot products and unburnt fuel-air mixture into the recirculation region, which promotes mixing and helps stabilizing a reaction zone.

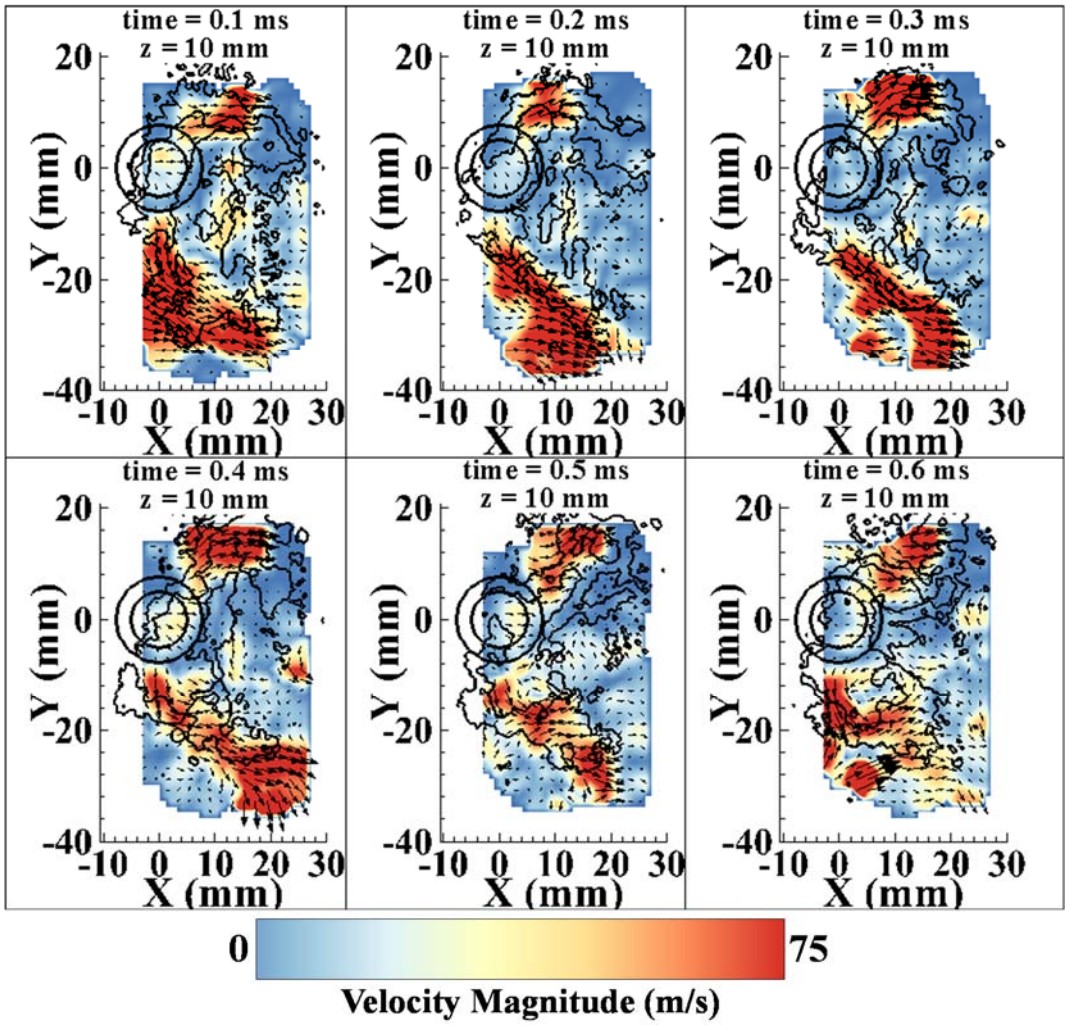

Figure 5.13. Sequence (Δt = 0.1 ms) of images in RJICF flame fronts overlaid against contours of velocity magnitude and velocity vectors, for reacting jet case of J=8, 40%H_2/60%N_2 at Z = 10 mm.

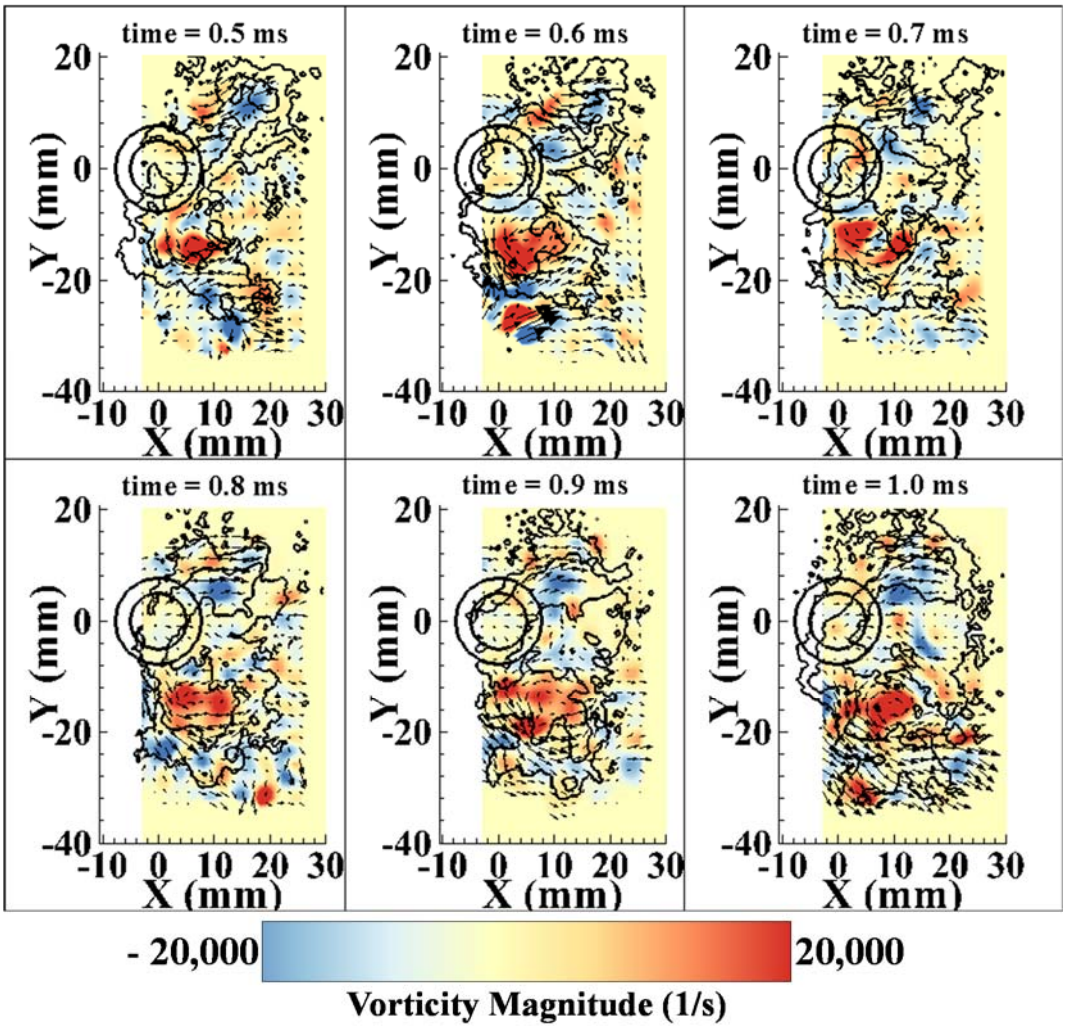

Figure 5.14. Sequence (Δt = 0.1 ms) of images in RJICF flame fronts overlaid against contours of vorticity, for reacting jet case of J=8, 40%H_2/60%N_2 at Z = 10 mm.

5.7.3 Local Flame Extinction

The flame edges and velocity vector overlaid on top of compressive strain (derived for the velocity field) is shown in Figure 5.15. This sequence of images features an instance of flame detachment from the main reaction zone due to adverse flow conditions. It is evident that the flame front, between time = 0.3 ms – 0.6 ms, stretches, elongates and forms a neck. As discussed previously in section 5.7.2, the high-speed fluid in the upper shear

layer pushes the flame front further downstream which also increases magnitudes of local compressive strain rates. At time = 0.4 ms and location X = 10 mm and Y = 10 mm the reaction front starts to wrinkle and distort. This region of high compressive strain (greater than -30000 s^{-1}) acts on the flame front for a duration of 0.4 ms, which eventually leads to detachment of a small pocket of reacting fluid from the main flame body, as seen at time = 0.7 ms. The relationship between the principal compressive strain rate and the scalar dissipation rate has been investigated extensively in a laboratory scale burner [103]. The highly three-dimensional nature of the flow field requires measurement of all three-components at two parallel planes for accurate computation of strain rate and vorticity. It has been postulated that if the z-axis is the principal axis, two-dimensional flow information is sufficient to compute in-plane principal strain rate [104]. Hence, the PIV data which provides only four out of the nine strain rate tensor components would be sufficient for computing in-plane strain rate. Previous experimental and numerical studies have indicated that the maximum scalar gradient tends to align with the axis of the principal compressive strain and the strongest dissipation layers form orthogonal to this axis. The thinnest reaction fronts are also found to be normal to the axis of principal compressive strain. The total duration for which the critical value of compressive strain acts on the reaction zone, also dictates if local extinction will occur.

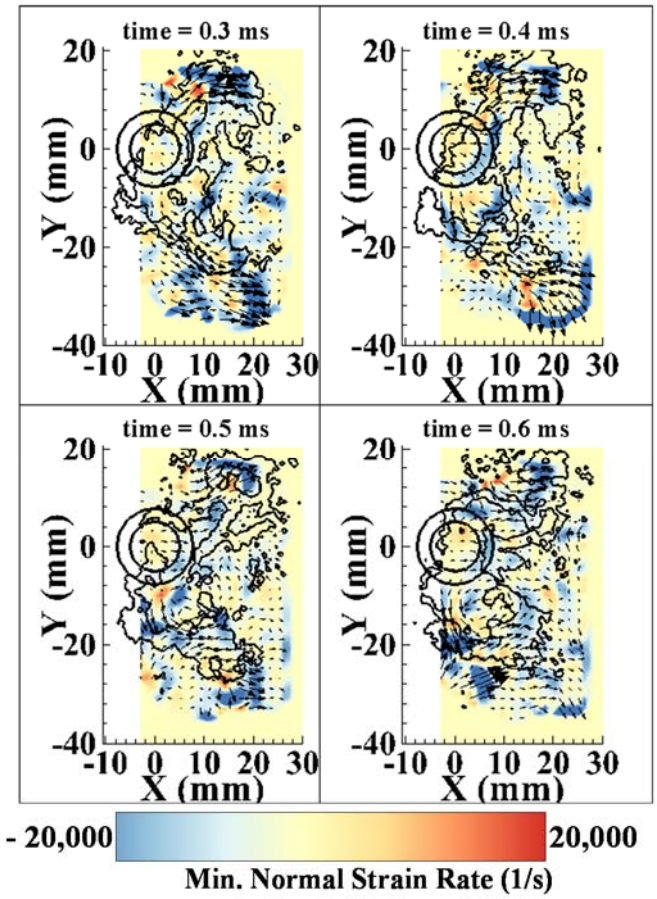

Figure 5.15. Sequence (Δt = 0.1 ms) of images in RJICF flame fronts overlaid against contours of minimum principal normal strain, for reacting jet case of J=8, 40%H_2/60%N_2 at Z = 10 mm.

5.7.4 Flame Structure Variation due to Fuel Reactivity

Figure 5.16, compares the flame structure for reacting jet cases of H_2/N_2 and premixed natural gas with a momentum flux ratio of J = 8, measured at Z = 10 mm. The wake structure interacts with the flame front in a similar manner, as the flame structure for both the cases has the characteristic kidney shape. The main difference between the flame structures for the two fuels is the presence of a thin flame front on the windward side of the H_2/N_2 jet flame. For a fixed momentum flux ratio, the in-plane strain rates are approximately same for both H_2/N_2 jets and premixed NG jets. However, the reaction zone

in case of a premixed NG jet starts downstream of the jet injection point unlike with H_2/N_2 jets. This difference in the flame structure is mainly due to lower flame speed and higher propensity for strain-induced extinction in case of a premixed NG flame.

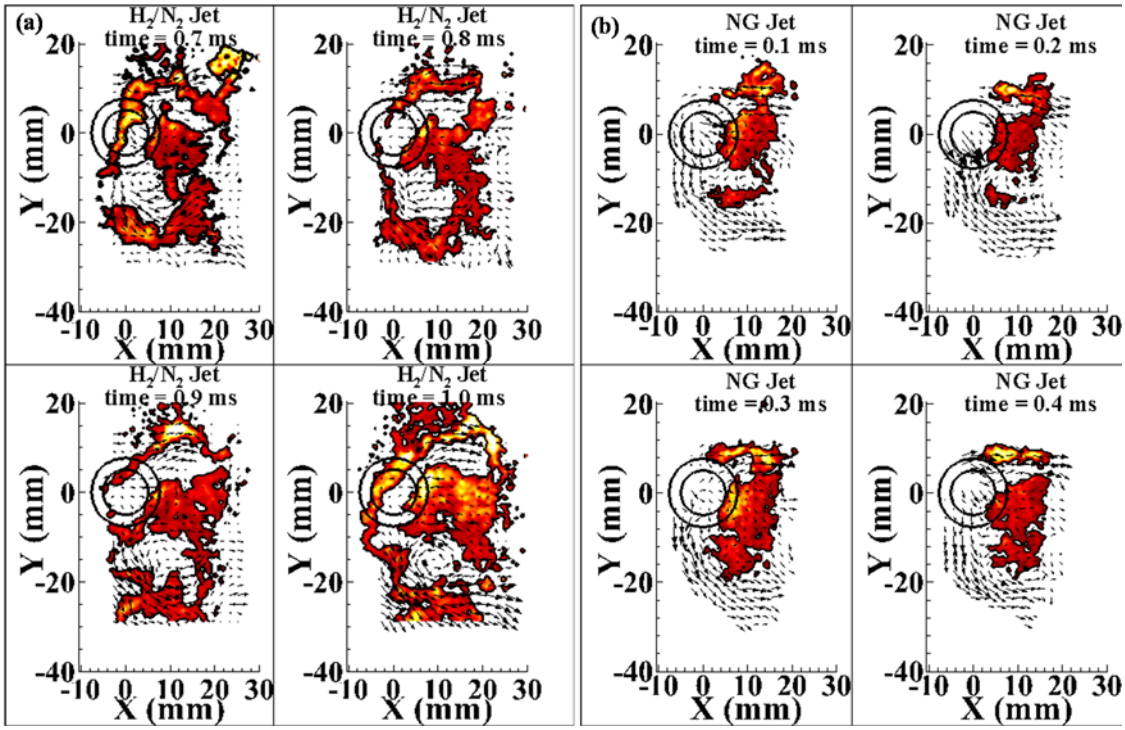

Figure 5.16. Flame front edge overlaid on top of OH-PLIF image for reacting jet case of (a) J=8;H_2/N_2 and (b) J=8; premixed NG.

5.8 Flow-Flame Interaction Below the Jet Injection Plane (Z = -5 mm)

The instantaneous as well as time-averaged OH-PLIF measurements along jet flame trajectory (X-Z plane) indicate a region with high OH-PLIF intensity within the immediate vicinity of the injector. The OH-PLIF images also showed entrainment of reaction products below the jet injection plane. To further understand the flow-flame interaction in a plane below the jet injection plane simultaneous PIV and OH-PLIF measurements were performed. It was discussed in Chapter 4 that PIV measurements of reacting jets injected

into swirling crossflow indicate entrainment of TiO_2 below the jet injection plane. The flow-field is similar to a cylindrical bluff-body in a crossflow. Due to the swirling nature of the crossflow the mean flow field is oriented at approximately 45 degrees with respect of the x-axis. Based on the time-averaged flow-field discussed in Chapter 4 the velocity field has two high speed regions along the shear layers and a low velocity wake region enveloped between the two shear layers. A sequence of instantaneous velocity vectors overlaid on top of OH-PLIF intensity field of a reacting jet case of J= 3 and ϕ_{JET} = 3 measured at Z = -5 mm (5 mm below the jet injection plane) is shown in Figure 5.17. The sequence shows entrainment of the reaction products as well as unburnt fuel-air mixture entrained in the plane Z = -5 mm. The upper shear layer region shows a continuous OH-PLIF field oriented in the direction of the upper shear layer. The OH-PLIF field is more distributed in the form of small island like structures within the lower shear layer region. The reaction zone here is also oriented in the direction of lower shear layer velocity vectors. It is evident that the wake of the injector does not show any OH-PLIF intensity field. This could imply that there is no further reaction occurring at Z = -5 mm and the OH-PLIF intensity is only due to the entrainment of reaction products. Figure 5.18, shows the velocity vectors and the flame-front edges overlaid on velocity magnitude contour map. The velocity field shows that the lower shear layer has an in-plane motion. From time = 0.1 ms – 0.4 ms the lower shear layer is oriented in an upward direction against the swirling motion. At time = 0.6 ms the mean flow direction changes and gets aligned in the direction of the swirling crossflow. Figure 5.19, shows the velocity vectors and the flame-front edges overlaid on top of out of plane vorticity contour map. The source of vorticity in this measurement plane is completely different than in planes above the jet injection plane. The

vorticity is generated by fluid and injector wall interaction at Z = -5mm. The seeded and unseeded regions are clearly demarcated by the high vorticity magnitude forming a boundary to the velocity field. It is difficult to clearly identify the jet fluid and the crossflow fluid at this location.

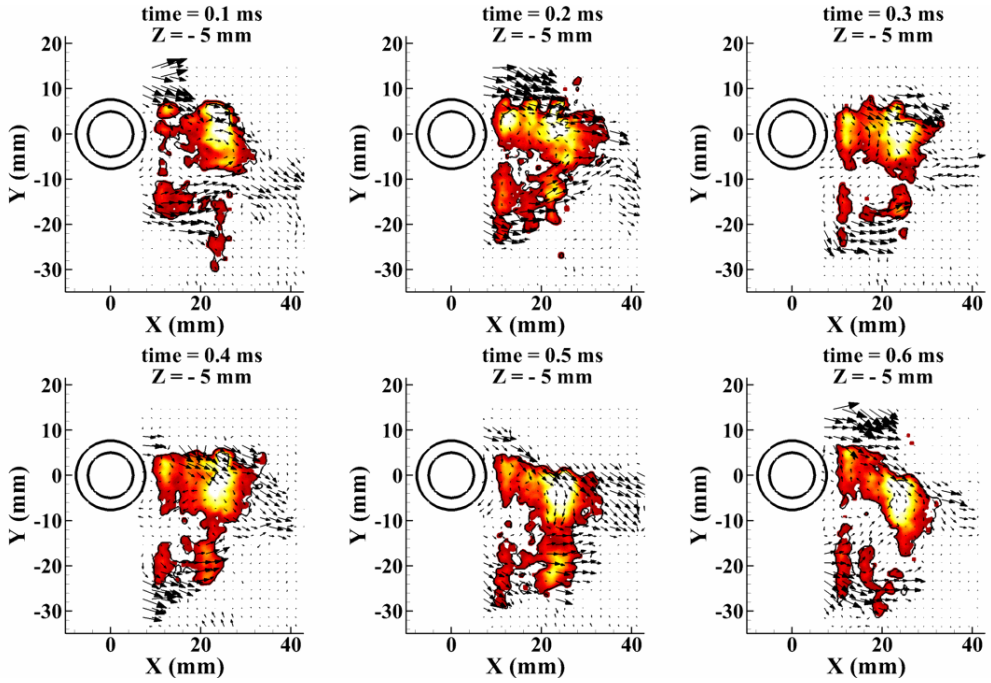

Figure 5.17. Instantaneous velocity vectors for the reacting jet case of, J= 3 and ϕ_{JET} = 3 measured at Z = -5 mm, velocity vectors are overlaid on top of OH-PLIF intensity field.

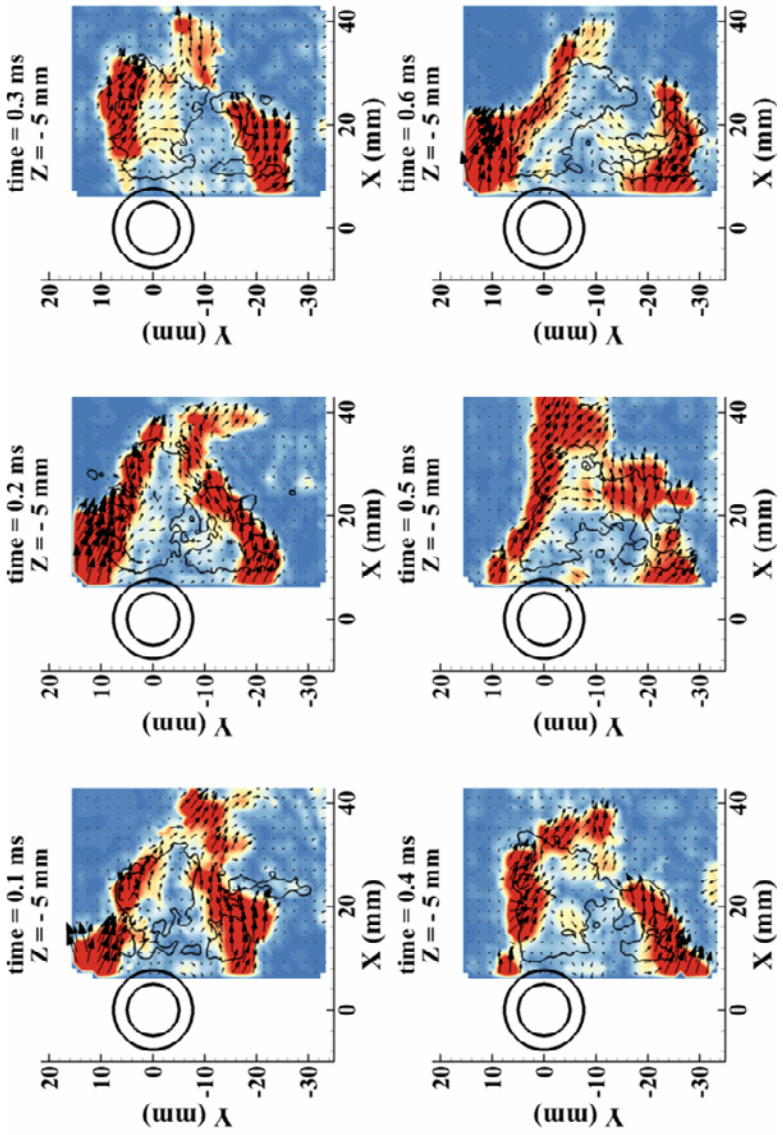

Figure 5.18. Instantaneous velocity vectors for the reacting jet case of, J= 3 and $\phi_{JET} = 3$ measured at Z = -5 mm, velocity vectors are overlaid on top of velocity magnitude (V).

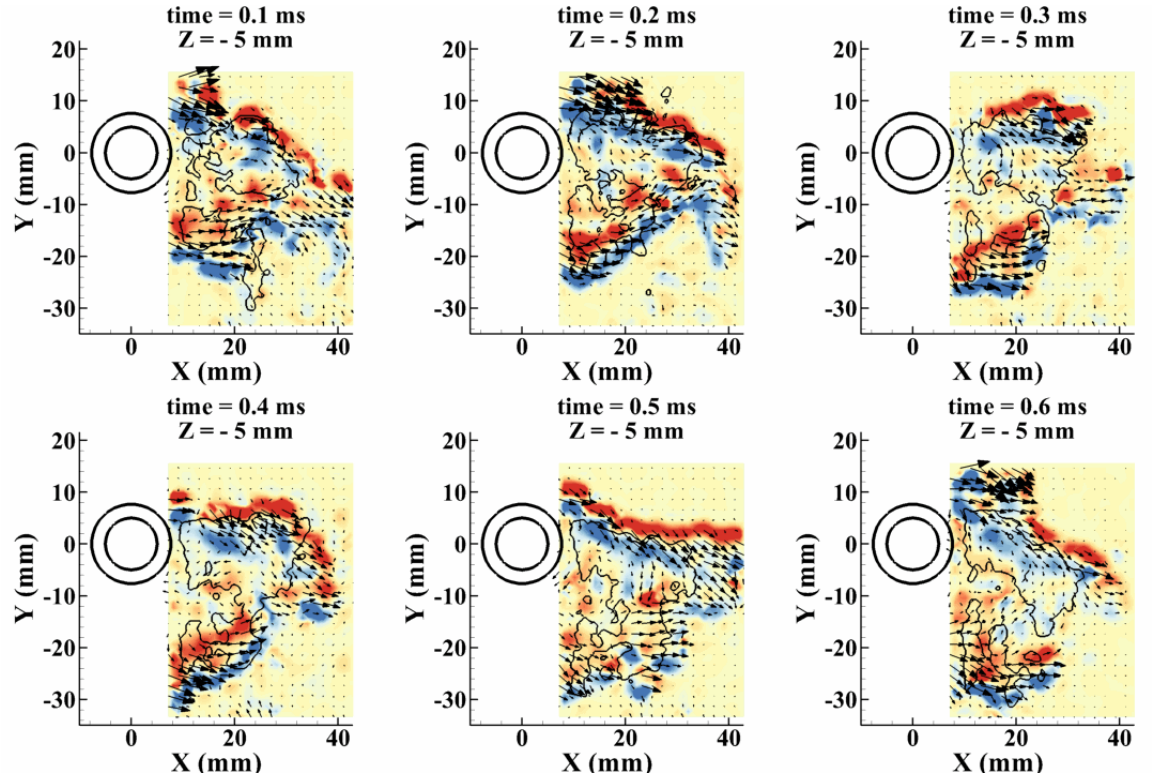

Figure 5.19. Instantaneous velocity vectors for the reacting jet case of, J= 3 and ϕ_{JET} = 3 measured at Z = -5 mm, the velocity vectors are overlaid on top of Z-component of vorticity (ω_z).

5.9 Conclusions

In this chapter the results of high resolution temporal and spatial measurements in an optically accessible, high-pressure staged combustion system are discussed. Simultaneous two-component particle image velocimetry (PIV) and planar laser-induced fluorescence of the OH radical (OH-PLIF) were performed at a repetition rate of 10 kHz. The test rig features a main combustion zone (MCZ) and a secondary combustion zone (SCZ). The secondary combustion zone (SCZ) features a transverse reactive jet injected into a swirling vitiated crossflow, which was optically accessible.

The measurements were performed at 3 different planes along the cross-section of the jet at planes Z = 5, 10 and 15 mm away from the nozzle exit. Two jet momentum flux ratios, J=3 and J=8, were studied for reacting jet cases with jet fluids consisting of either 40% H_2/60% N_2 or premixed natural gas and air (NG/air, ϕ_{jet} = 0.9). The PIV measurements clearly show the influence of swirling crossflow on the reacting jet. Multi-plane velocity measurements give insight into the extent of penetration of the jet, based on the size and vorticity magnitude of the wake structure. As expected, the J=8 case had a deeper penetration into the flow field as compared to J = 3 case. A three-dimensional wake vortex structure was generated using the time averaged velocity data at the three different interrogation planes for J = 8 case. This analysis gives an approximate size of the upright wake vortices.

The instantaneous PLIF images were processed to generate flame front edges using a MATLAB-based edge detection algorithm. The instantaneous sequences of velocity vectors (and the derived quantities) overlaid on the reaction zone and various other flow variables provided significant insight into the flow-flame interactions and local-extinctions associated with the RJICF. The wake structure distorted and elongated the flame fronts, eventually puncturing the reaction zone and causing local extinction due to extremely high rates of scalar dissipation. A combined influence of high vorticity magnitude and the planar compressive strain rate were identified to be critical in causing flame detachment events. The flame structure for H_2 diffusion flames and the premixed NG flames were found to be similar within the wake of the jet. The reaction zones (in both diffusion and premixed flames) had a characteristic kidney shape, due to the interaction of the jet fluid with the wake vortex structure. However, the most interesting finding was the ability of

H_2/N_2 diffusion flame to sustain a thin reaction front even on the windward side of the jet. This difference is attributed to the lower flame speed and higher propensity for strain-induced extinction in case of a premixed NG flame.

The RJICF also serves as an important test case for the development of numerical models for turbulent reacting flow fields typical of gas turbine combustors. High data rate measurements similar to those discussed in this paper will provide significantly improved understanding of the complex processes of fuel/air mixing and validation data for critical development of high fidelity turbulence-chemistry interaction models.

CHAPTER 6. CONCLUSIONS

Recent progress in the field of turbine blade materials has enabled gas turbine manufacturers to raise the turbine inlet temperatures leading to an increase in thermal efficiency of the engine [8]. Staged combustion has been explored for power generation gas turbine engines to increase engine efficiency with minimal contribution to pollutant formation. Fuel staging in these low emission combustion technologies also serves a means of controlling combustion instabilities. Secondary fuel injection into the vitiated flow from the primary combustion process is one approach. In this work, advanced diagnostic measurements were performed on an experimental representation of such a system, with a transverse jet injection into a vitiated crossflow. The primary objective of this research was to understand the response of a reacting jet to different crossflow conditions relevant to a turbine engine combustor. The structure and dynamics associated with secondary injection of fuel into a swirling vitiated crossflow and a uniform vitiated crossflow was studied in detail. The reacting jets were composed of air assisted natural gas and high-hydrogen-content (HHC) fuels such as H_2 diluted with N_2. High-repetition-rate particle image velocimetry (PIV) and OH planar laser-induced fluorescence (PLIF) were used individually and simultaneously to visualize fuel/air mixing and combustion at data rates of 5-10 kHz.

The measurements provided qualitative as well as quantitative information on the evolution of complex flow structures and transient events such as re-ignition, local extinction and vortex-flame interactions in the turbulent reacting flow.

6.1 Summary and Research Contribution

In this work spatio-temporally resolved advanced laser diagnostic in an optically accessible high pressure staged combustion system is presented. The secondary combustion zone features transverse injections of premixed natural gas or HHC fuel jets into a vitiated crossflow. The first major contribution of this research is a detailed characterization of the velocity field of the wake of the jet and its role in leeward side flame stabilization in a reacting jet in vitiated crossflow configuration. This also involves the nature of crossflow and its corresponding influence on the near wake region flow-field of the reacting jet. High resolution PIV measurements show the influence of the nature of crossflow (swirling or uniform) on the flow-field of the reacting jet. This is the first contribution to the literature of reacting jets in crossflow where the influence of a swirling crossflow on the structure and dynamics of a RJICF is investigated. In order to, produce a swirling crossflow a low-swirl-burner was used as the vitiator. Two component PIV measurements were acquired at a repetition rate of 10 kHz, which enabled tracking of the flow structures in the wake of the RJICF. Velocity data was collected for a duration of 0.5 s at a repetition rate of 10 kHz, providing enough sampling time to extract accurate time-averaged fields and flow statistics. We performed PIV measurements (i) to characterize the velocity of the vitiated crossflow fluid stream without the jet, (ii) characterize the velocity field of the non-reacting jets, and (iii) the reacting jets. Multi plane measurements along the X-Y planes were made to fully characterize the three dimensional nature of the

complex flow-field of JICF. The swirling nature of the crossflow was completely characterized; the mean velocity angle was approximately at 45 degrees with respect to the X-direction. There is a velocity gradient established along the Z-direction of the flow field which is the nature of flow-field of a LSB. The experimental investigation involves the study of effects of two J values, 3 and 8, on the structure and dynamics of the reacting (R) jet flame. With J = 3 it was observed that the fuel reacts closer to the nozzle exit with the reaction zone stabilized within the wake of the jet, while with J=8 the jet carrying fuel penetrates deeper into the crossflow and has a higher degree of mixing, resulting in a distributed reaction zones. The influence of the swirling crossflow is evident; the jet is aligned with the mean direction of the swirling crossflow. The flow field of the reacting jet shows the presence of a counter-rotating wake vortex structure. The wake vortices were evident at the measurement planes of Z = 5 mm (0.5 d_{JET}) and 10 mm (1.0 d_{JET}) for J = 3 cases and for J = 8 cases they were seen even at Z = 15 mm (1.5 d_{JET}). The effect of momentum flux ratio is apparent both in non-reacting and the reacting flow cases. Both cases show an increase in the magnitude of the out of plane vorticity (ω_z) with an increase in momentum flux ratio. This implies that the higher values of jet momentum flux leads to stronger crossflow entrainment and mixing within the wake of the jet. The velocity field of the non-reacting jet cases was analyzed to extract the variation of integral length scale across the measurement planes. The two-point correlation function was computed along the streamwise and spanwise direction of the mean flow field and it was found that the correlation curve gets broader with increase in streamwise direction. The integral length scale is found to be non-uniform along the measurement plane, however, the spatial variation trend was consistent across all the three measurement planes and it was also seen

the integral scale is found to be largest at Z = 5 mm. The velocity power spectra showed a broad spectrum of temporal scales present in the flow field of the RJICF. The analysis shows that the peak frequency in the velocity spectra corresponds to St_{wake} varying between 0.13 – 0.15 for all the JICF/RJICF cases studied. The crossflow mean velocities for the non-reacting and reacting cases are 13 m/s and 36 m/s, respectively and the corresponding vortex shedding frequency for the RJICF is approximately 550 Hz and that for JICF is 172 Hz. This suggests that the vortex shedding frequency scales with the mean crossflow velocity magnitude, however, further analysis may be needed to needed to support this statement. These frequencies were also identified from the instantaneous Mie scattering analysis of the raw PIV images and from the temporal coefficients of the POD modes corresponding to the wake structures.

The second significant contribution of this study is the shift in the wake Strouhal number calculated at all the measurement planes for the reacting and non-reacting jets with a top-hat jet velocity profile. It has been reported in the literature that there is a delay in the formation of leeward vortices due to a thicker shear layer associated with a parabolic JICF when compared to the top-hat JICF at a similar J. This delay leads to reduction in the rate of entrainment of crossflow fluid by a parabolic JICF. Based on similar observations in this study an increase in the wake shedding frequency and corresponding increase in St_{wake} is evident for the all the JICF cases with top-hat velocity profile. The St_{wake} is found to be between 0.18 – 0.23, indicating a faster rate of entrainment into the wake of the jet. Another interesting finding was the Strouhal number calculation in the wake of the injector at a measurement plane 5 mm below the jet injection location. The flow-field is similar to

that of wake of a cylindrical-bluff body and the wake Strouhal number for the reacting jet cases is found to be between St_{wake} = 0.28 -0.295.

The third significant contribution to the literature of RJICF was the quantitative comparison of the structure and dynamics of the flow-field of a RJICF under the influence of a uniform vitiated crossflow and a swirling vitiated crossflow. The uniform vitiated crossflow was produced by a bluff-body-burner. The jet is aligned with the mean direction of the crossflow which is in the X-direction unlike the swirling crossflow cases where the jet was inclined at 45 degrees to the X-direction. PIV measurements of reacting and non-reacting jet cases show an interesting trend in the formation of wake vortex structures. It is discovered that there is a delay in the formation of wake vortex structure and unlike the swirling crossflow cases the wake structure appears after one jet diameter form the jet injection plane. Also unlike the swirling crossflow cases there is no entrainment of PIV seed particles in planes below the jet injection location. Furthermore, it is found that the velocity gradient in the wake of the jet in a uniform crossflow is half the velocity gradient seen in case of a swirling crossflow. As a result, the vorticity magnitude computed at all the measurement planes for uniform crossflow cases are approximately half the vorticity magnitudes computes for reacting jets in swirling crossflow. It is also seen that there is a faster recovery of velocity in the wake of the jet in a uniform crossflow. These variations in the flow-field of the jet would appropriately answer the initial observation of delay in the formation of a recirculation region in uniform crossflow cases. The weaker vorticity field also suggests that there will be reduction in the rate of entrainment of combustible mixtures in the near wake region of the jet. Additionally, there is a shift towards lower St_{wake} of the non-reacting and reacting jets in uniform crossflow. The St_{wake} is found to be

varying in the range of 0.09 – 0.12 for all the JICF/RJICF cases. This analysis complements to the earlier conclusion that there is drop in the rate of jet-crossflow entrainment into the wake of the jet.

The final major contribution of this work is characterization of flow-flame interaction in the wake of the reacting jets in swirling vitiated crossflow. Simultaneous two-component particle image velocimetry (PIV) and planar laser-induced fluorescence of the OH radical (OH-PLIF) were performed at a repetition rate of 10 kHz. The measurements were performed at 4 Z-planes which are along the cross-section of the jet, Z = -5 mm, 5 mm, 10 mm and 15 mm away from the nozzle exit. Two jet momentum flux ratios, J=3 and J=8, were studied for reacting jet cases with jet fluids consisting of either 40% H_2/60% N_2 or premixed natural gas and air. The PIV measurements have already demonstrated the influence of swirling crossflow on the reacting jet. The instantaneous sequences of velocity vectors (and the derived quantities) overlaid on the reaction zone and various other flow variables provided significant insight into the flow-flame interactions and local-extinctions associated with the RJICF. The wake structure distorted and elongated the flame fronts, eventually puncturing the reaction zone and causing local extinction due to extremely high rates of scalar dissipation. A combined influence of high vorticity magnitude and the planar compressive strain rate were identified to be critical in causing flame detachment events. The flame structure for H_2 diffusion flames and the premixed NG flames were found to be similar within the wake of the jet. The reaction zones (in both diffusion and premixed flames) had a characteristic kidney shape, due to the interaction of the jet fluid with the wake vortex structure. However, the most interesting finding was the ability of H_2/N_2 diffusion flame to sustain a thin reaction front even on the

windward side of the jet. This difference is attributed to the lower flame speed and higher propensity for strain-induced extinction in case of a premixed NG flame. OH-PLIF measurements along the jet flame trajectory (Y-planes) also show this difference in the flame structure of a H_2 diffusion flame and a premixed NG flame. The instantaneous OH-PLIF images of H_2/N_2 jets indicate a thin non-premixed flame along the windward side of the jet which is not seen in case of premixed NG flames. The leeward side of the jet shows distributed regions of OH-PLIF intensity which could suggest a distributed mode of combustion due to enhanced mixing and entrainment of crossflow-jet fluid into the near wake region of the jet. The instantaneous sequence of velocity vectors and OH-PLIF images measured at Z = -5 mm shows entrainment of the reaction products as well as unburnt fuel-air mixture. The upper shear layer region shows a continuous OH-PLIF field oriented in the direction of the upper shear layer. The OH-PLIF field was seen to be more distributed in the form of island like structures within the lower shear layer region. The reaction zone was seen to be oriented in the direction of lower shear layer velocity vectors. The wake of the injector did not show any OH-PLIF intensity field. This could imply that there was no further reaction occurring at Z = -5 mm and the OH-PLIF intensity is only due to the entrainment of reaction products.

In addition to practical applications, RJICF also serves as an important test case for the development of numerical models for turbulent reacting flow fields typical of gas turbine combustors. High data rate measurements discussed in this dissertation provides high quality experimental data set acquired at engine relevant conditions. This provides significantly improved understanding of the complex processes of fuel/air mixing and validation data for critical development of high fidelity computational models.

6.2 Proposed Future Work

6.2.1 Simultaneous OH-PLIF/PIV Measurements in Bluff-Body-Burner

The PIV measurements in the reacting jets in uniform crossflow showed interesting variations in the flow structures and dynamics. The delay in the formation of the wake vortex structure and absence of PIV seed particles in planes below the jet injection location indicate a weaker recirculation region behind the jet. This could lead to reduced rate of entrainment of fuel-air mixtures or burnt productions into the wake of the jet, which could further lead to a lee side lifted jet flame in case of premixed natural gas jets. Thus, it is proposed to perform high-repetition-rate simultaneous PIV/OH-PLIF measurements along the reacting jet cross-sections to further understand the flow-flame interactions.

6.2.2 Experimental Study on Accelerating-Crossflow Staged Combustion System (ACSCS)

The next phase of research in the current work is to study the reacting jet response to an accelerating vitiated crossflow. This is the last variable in this detailed experimental study of response of a reacting jet to various crossflow conditions. In terms of a staged combustion system this configuration is practically most relevant. Thus, the knowledge gained from the current research on the flow-flame behavior of a reacting jet in a high pressure vitiated crossflow opened a new avenue of research in the form of an Accelerating-Crossflow Staged Combustion System (ACSCS) test rig.

The design and fabrication of the ACSCS test rig was involved as a part of the current research and brief description of the design and proposed test conditions is discussed in this section. An accelerating crossflow has a potential advantage, particularly, in terms of NO_x emissions. Rate of NO_x formation is a strong function of flame temperature

and the flow residence time. With an accelerating crossflow the residence time in the SCZ will be significantly lower as compared to a uniform crossflow. Also with an increase in Ma number there is a corresponding drop in the static temperature of the crossflow. Thus, both these parameters are being altered in such a way that there will be negligible contribution of SCZ towards overall NO_x formation. The current staged combustion test rig has a constant cross-section of 4.2 in X 4.2 in, and based on the operating conditions the vitiated crossflow Ma number is calculated to be 0.05. The objective behind designing the ACSCS test rig is to inject secondary fuel (premixed NG or syngas)) in the form of transverse jets at higher Ma number and to study the response of the reacting jet. It is intended to determine the range of Ma number at which the reacting jet would ignite and attain complete combustion. With an accelerating crossflow the reacting jet will experience significantly higher rates of strain, thus, advanced laser diagnostics will be implemented to measure the velocity field and the flame front location to gain more information of the flow-field.

The details of the design considerations have been included in an earlier unpublished work. In this section the key design parameters and operating conditions are included. Figure 6.1, shows the cross-section of the ACSCS test rig with critical dimensions highlighted. The ACSCS rig consists of the main combustion zone (MCZ). The MCZ of the ACSCS test rig has a modular design which facilitates the installation of the bluff-body-burner (BBB) or the low-swirl burner (LSB) with a ceramic flow straightener interchangeably.

Figure 6.2 shows, the converging section of the test is optically accessible and it is intended to inject the secondary fuel within the converging section where the crossflow

will be accelerating. The converging section has a cross-sectional area of 4.2 in X 4.2 in at the inlet and 4.2 in X 0.88 in at the outlet that leads to an inlet to outlet area ratio of 4.77:1. Thus, the walls converge in only one direction at an angle of 18.9 degrees, as shown in Figure 6.3. The distance between the injector plug and the wall opposite to it kept constant (4.2 in) in order to avoid the reacting jet hitting the inner window. The length of the converging section is 12 in with 10 in of convergence and 2 in of straight section at the throat of the device. Two thermocouples will be located within the straight section that will be inserted into a hole drilled through the downstream flanges. The blind end of the hole ends 0.25 in away from the inner wall. These thermocouples are facilitated for health monitoring purpose of the rig. The throat of the ACS rig is where the heat transfer rate will be highest thus cooling holes are strategically located near the throat for the survivability of the rig. The diverging section is 12.5 in long and it expands to an exit area of 4.2 in X 4.2 in. The film cooling manifold is shown in Figure 6.4, unlike the constant area windowed combustor the film cooling manifold has outlets on all four sides of the combustor. This change is to make sure the inner TBC wall temperature is below the maximum operable limit.

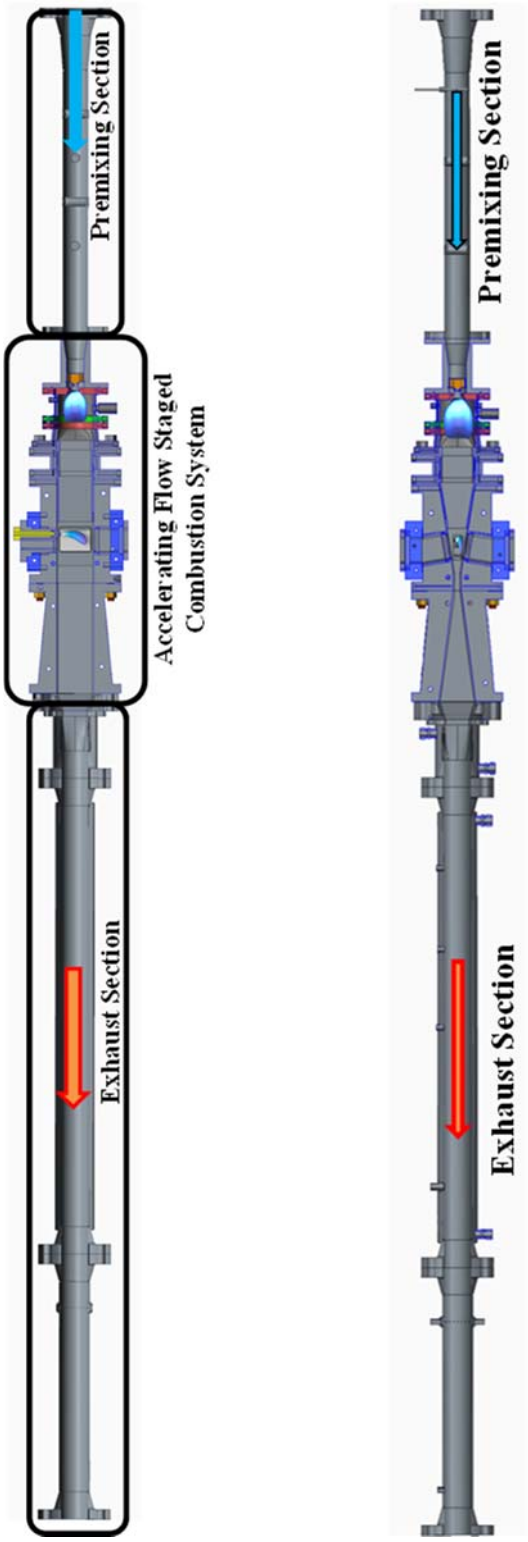

Figure 6.1. Schematic showing the new accelerating crossflow staged combustion system.

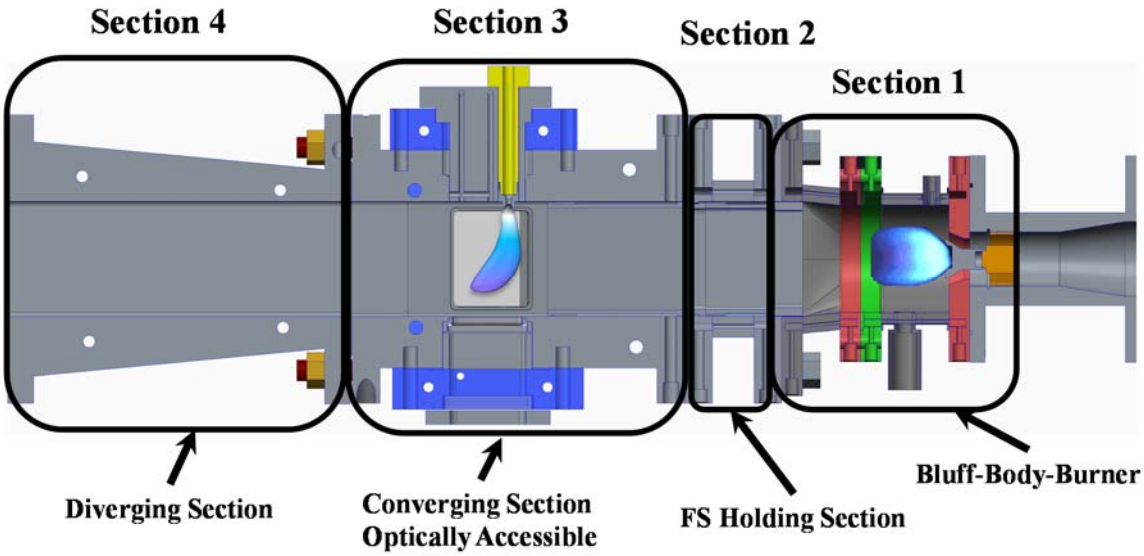

Figure 6.2. Schematic showing key sections of the accelerating crossflow staged combustion system.

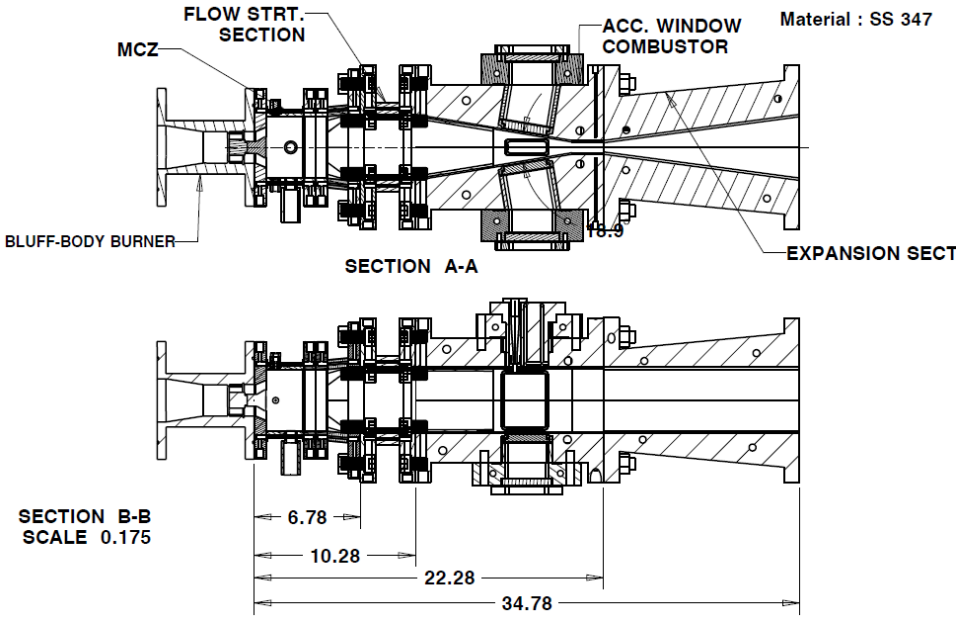

Figure 6.3. Schematic showing key dimensions of the accelerating crossflow staged combustion system.

The converging part of the rig is fabricated out of stainless steel (SS 347) and the diverging section is constructed out of SS 316. All the parts that will be exposed to combustion gas are water cooled and the inner surfaces are thermal barrier coated (TBC). The TBC is 500 μm thick and is Yttria-stabilized zirconia (Metal Coating Technology Inc.). The water cooled sections are designed to withstand a maximum overall equivalence ratio (ϕ) of 0.6 which produces an adiabatic flame temperature of 1963 K. However, the LBO limit for the bluff body burner is in the range of ϕ = 0.5 -0.51 and thus, it is proposed to operate the MCZ at ϕ = 0.53 to ensure a stable operation of the rig. The adiabatic flame temperature corresponding to ϕ = 0.53 is 1843 K. The details of the heat transfer analysis used to design the water cooled combustion hardware and the window film cooling have been discussed previously [73]. A brief summary of the heat transfer analysis is discussed in this section. The schematic of the one-dimensional heat transfer model is shown in Figure 6.5. It is assumed that the heat transfer occurs through convection and radiation from the exhaust gases. The excellent resistivity of the TBC liner ensures that the maximum temperature of SS 347 metal never exceeds the allowable temperature range ($\approx$1100 K or 1500 F). One of the main concerns for this device is operating close to the maximum operable temperature limit of the TBC liner. The vendor specific maximum operable temperature of the TBC liner is 1590 K (2400 F). The heat transfer model used a 1-D, periodic model in which the properties vary only in the axial direction. Under steady-state assumption, the heat transfer into the combustor wall must equal the heat transfer in to the water channels. For the purpose of heat transfer analysis the ACSCS test rig was divided into three parts, i) The main combustion zone (MCZ) and the transition section, ii) the flow straightener holder section and iii) The converging and diverging section. The

analysis assumes that the cooling water out of the MCZ and transition section is reused in the flow-straightener holder section. Similarly, the cooling water coming out of the converging section is used for cooling the diverging section. Also the diabatic inlet temperatures for section 2.0 and 3.0 are based on the temperature of the flow at the exit of section 1.0 and 2.0 respectively.

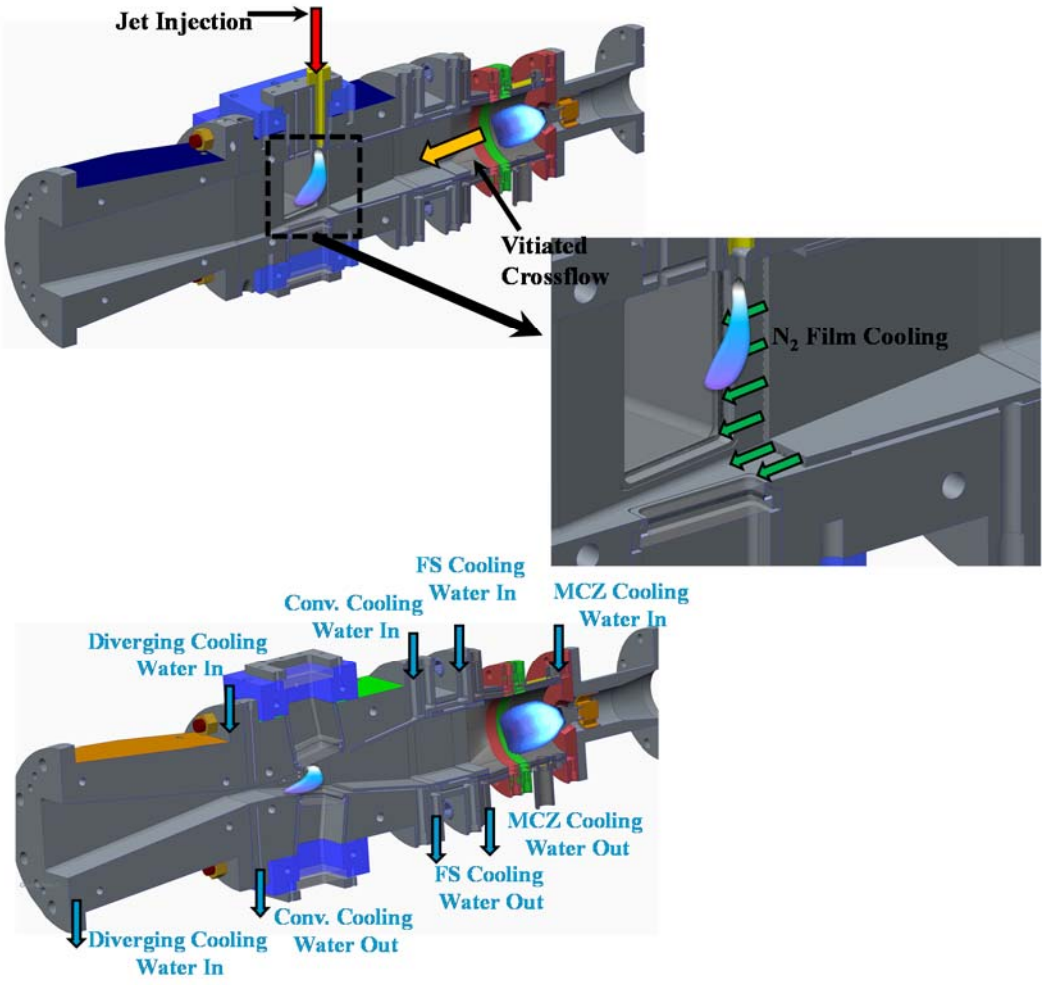

Figure 6.4. Details showing the cooling scheme for the accelerating crossflow staged combustion system test rig.

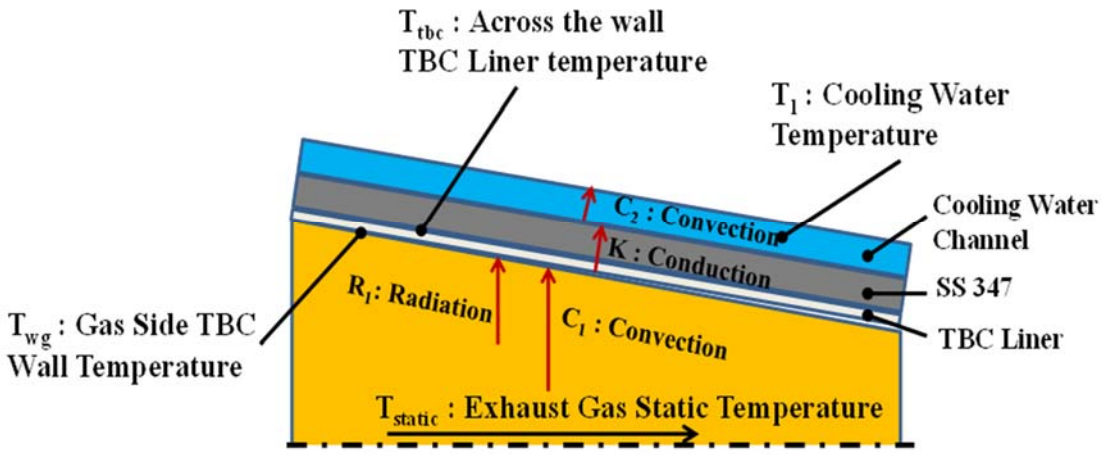

Figure 6.5. Schematic showing the one-dimensional heat transfer model used for the heat transfer analysis.

The results from the heat transfer analysis are shown in Figure 6.6. The plots show the variation of TBC inner surface temperature and the cooling water temperature along the streamwise direction for the converging diverging section. Four different conditions are analysed, i) crossflow mass flow rate that corresponds to a throat Ma = 0.2 at $\phi = 0.6$, ii) crossflow mass flow rate that corresponds to a throat Ma = 0.8 at $\phi = 0.6$, iii) crossflow mass flow rate that corresponds to a throat Ma = 0.8 at $\phi = 0.53$ and iv) crossflow mass flow rate that corresponds to a throat Ma = 0.8 at $\phi = 0.53$ with additional N_2 cooling. The first three conditions show that without any additional N_2 cooling the TBC liner temperature, particularly at the throat region, would exceed the maximum rated temperature for the TBC material. However, with 0.15 kg/s (15% of total flow rate) of N_2 added to the vitiated gas through the film cooling manifolds the TBC liner temperature stays 50 K below the maximum operable limit. The film cooling fluid stream is introduced at 0.28 m downstream from the dump plane of MCZ or 0.14 m downstream from the inlet of the converging section. For this condition the cooling water temperature also remains

15 K below the boiling point. The cooling water required for cooling the MCZ and the flow-straightener holder section is 0.4 kg/s (6.3 gpm) and that for cooling the converging diverging section is 0.7 kg/s (11 gpm).

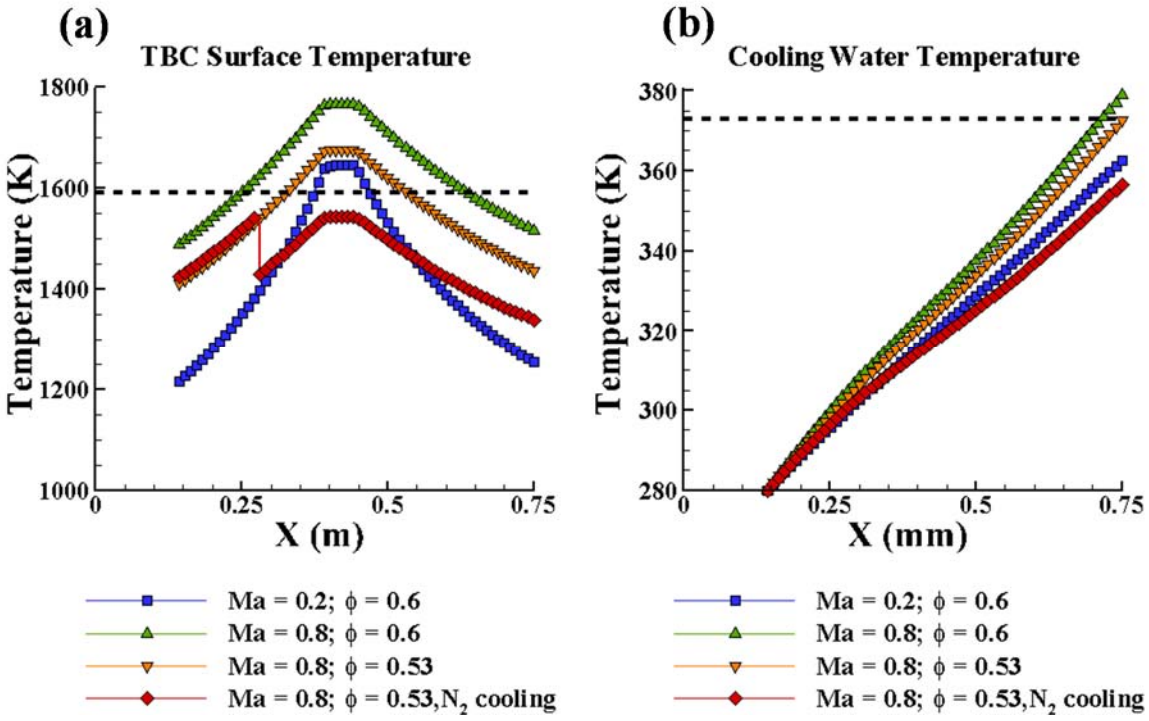

Figure 6.6. Variation of (a) TBC inner wall temperature and (b) cooling water temperature along the converging-diverging section, for various crossflow mass flow rates.

It is proposed to perform PIV measurements to characterize the accelerating crossflow velocity field and the velocity field of corresponding reacting jets. OH-PLIF measurements along the jet trajectory would provide qualitative information on the influence of the accelerating crossflow on flame structure in the windward and leeward side of the jet. These measurements would also help in identifying the range of Ma number at which a stable reacting jet could be established. Furthermore, simultaneous PIV/OH-PLIF measurements at multiple measurement planes would aid to the understanding of

flow-flame interaction in these operating conditions. Finally, a detailed emissions map (NO_x, CO, UHC etc.) needs to be developed for a range of Ma number conditions to identify the conditions with desirable emission characteristics.

LIST OF REFERENCES

LIST OF REFERENCES

1. Stocker, T. F., Qin, D., Plattner, G. K., Tignor, M., Allen, S. K., Boschung, J., & Midgley, B. M. (2013). IPCC, 2013: Climate Change 2013: The Physical Science Basis. Contribution of Working Group I to the Fifth Assessment Report of the Intergovernmental Panel on Climate Change.

2. Forster, P., Ramaswamy, V., Artaxo, P., Berntsen, T., Betts, R., Fahey, D. W., & Van Dorland, R. (2007). Changes in atmospheric constituents and in radiative forcing. Chapter 2. In Climate Change 2007. The Physical Science Basis.

3. Denman, K. L., Brasseur, G., Chidthaisong, A., Ciais, P., Cox, P. M., Dickinson, R. E., & Zhang, X. (2007). Couplings between changes in the climate system and biogeochemistry. Climate change, 2007, 541-584.

4. IPCC, 1990: Climate Change: The IPCC Scientific Assessment. Cambridge University Press, Cambridge, United Kingdom and New York, NY, USA, 212 pp

5. Paltsev, S., Jacoby, H. D., Reilly, J. M., Ejaz, Q. J., Morris, J., O'Sullivan, F., and Kragha, O. (2011). The future of US natural gas production, use, and trade. Energy Policy, 39(9), 5309-5321.

6. Wu, J., Brown, P., Diakunchak, I., Gulati, A., Lenze, M., & Koestlin, B. (2007, January). Advanced gas turbine combustion system development for high hydrogen fuels. ASME Turbo Expo 2007: Power for Land, Sea, and Air (pp. 1085-1091). American Society of Mechanical Engineers.

7. Tester, J. W., Drake, E. M., Driscoll, M. J., Golay, M. W., & Peters, W. A. (2005). Sustainable Energy: Choosing Among Options. 1st.

8. Correa, S. M. (1993). A review of NOx formation under gas-turbine combustion conditions. Combustion science and technology, 87(1-6), 329-362.

9. Fischer, W. (2012). SGT-8000H Product Line: Actual Update.*PowerGen Europe, Cologne*.

10. Ma, M., Yu, X., & Chen, T. (2015). New progress of high-efficiency and low-emission 9HA combine cycle gas turbine power generation demonstration project. Journal of Renewable and Sustainable Energy, 7(4), 041514.

11. Ratliff, P., Garbett, P., & Fischer, W. (2007). The new Siemens gas turbine SGT5-8000H for more customer benefit. Reprint from VGB Power Tech.

12. Lieuwen, T. C., & Yang, V. (Eds.). (2013). *Gas turbine emissions* (Vol. 38). Cambridge University Press.

13. Saravanamuttoo, H. I. H., Rogers, G. F. C., Cohen, H & Straznicky, P. V. (2009). Gas turbine theory. Pearson Education.

14. Jones, R. E. (1974). Advanced technology for reducing aircraft engine pollution. Journal of Manufacturing Science and Engineering, 96(4), 1354-1360.

15. Tacina, R. R. (1990, July). Combustor technology for future aircraft. In Proc. 26th AIAA/SAE/ASME/ASEE Joint Propulsion Conference, Orlando, Florida, USA (pp. 16-18).

16. Segalman, I., McKinney, R. G., Sturgess, G. J., & Huang, L. M. (1993). Reduction of NOx by fuel-staging in gas turbine engines-A commitment to the future. In AGARD CONFERENCE PROCEEDINGS AGARD CP (pp. 29-29). AGARD.

17. Lefebvre, A. H., Gas Turbine Combustion. Taylor & Francis, 2nd edition, 1999.

18. Jones, R., Goldmeer, J., & Monetti, B. (2011). Addressing Gas Turbine Fuel Flexibility. GE Energy Report GER4601 rev. B, October, 29, 2012.

19. Ford, T. (1998). V2500 technology. Aircraft Engineering and Aerospace Technology, 70(4), 289-290.

20. Eckardt, D., & Rufli, P. (2001, June). Advanced Gas Turbine Technology: ABB/BBC Historical Firsts. ASME Turbo Expo 2001: Power for Land, Sea, and Air (pp. V003T02A010-V003T02A010). American Society of Mechanical Engineers.

21. Joshi, N. D., Mongia, H. C., Leonard, G., Stegmaier, J. W., & Vickers, E. C. (1998, June). Dry low emissions combustor development. ASME 1998 International Gas Turbine and Aeroengine Congress and Exhibition (pp. V003T06A027-V003T06A027). American Society of Mechanical Engineers.

22. Leonard, G., & Stegmaier, J. (1994). Development of an aeroderivative gas turbine dry low emissions combustion system. Journal of Engineering for Gas Turbines and Power, 116(3), 542-546.

23. Held, T. J., Mueller, M. A., Li, S. C., & Mongia, H. (2001). A data-driven model for NO_x, CO and UHC emissions for a dry low emissions gas turbine combustor. AIAA paper, 3425, 2001.

24. Huang, Y., & Yang, V. (2009). Dynamics and stability of lean-premixed swirl-stabilized combustion. Progress in Energy and Combustion Science, 35(4), 293-364.

25. Wooler, P. T. (1969). Flow of a circular jet into a cross flow. Journal of Aircraft, 6(3), 283-284.

26. Margason, R. J. (1993, November). Fifty years of jet in cross flow research. In In AGARD, Computational and Experimental Assessment of Jets in Cross Flow 41 p (SEE N94-28003 07-34) (Vol. 1).

27. Karagozian, A. R. (2010). Transverse jets and their control. Progress in Energy and Combustion Science, 36(5), 531-553.

28. Kamotani, Y., & Greber, I. (1972). Experiments on a turbulent jet in a cross flow. AIAA journal, 10(11), 1425-1429.

29. Smith, S. H., & Mungal, M. G. (1998). Mixing, structure and scaling of the jet in crossflow. Journal of fluid mechanics, 357, 83-122.

30. Keffer, J., & Baines, W. D. (1963). The round turbulent jet in a cross-wind. Journal of Fluid Mechanics, 15(04), 481-496.

31. Karagozian, A. R. (2003). Background on and Applications of Jets in Crossflow (pp. 3-13). Springer Vienna.

32. Muppidi, S., & Mahesh, K. (2008). Direct numerical simulation of passive scalar transport in transverse jets. Journal of Fluid Mechanics, 598, 335-360.

33. Muppidi, S., & Mahesh, K. (2006). Two-dimensional model problem to explain counter-rotating vortex pair formation in a transverse jet. Physics of Fluids (1994-present), 18(8), 085103.

34. Yuan, L. L., Street, R. L., & Ferziger, J. H. (1999). Large-eddy simulations of a round jet in crossflow. Journal of Fluid Mechanics, 379, 71-104.

35. Bagheri, S., Schlatter, P., Schmid, P. J., & Henningson, D. S. (2009). Global stability of a jet in crossflow. Journal of Fluid Mechanics, 624, 33-44.

36. Cortelezzi, L., & Karagozian, A. R. (2001). On the formation of the counter-rotating vortex pair in transverse jets. Journal of Fluid Mechanics, 446, 347-373.

37. Kelso, R. M., Lim, T. T., & Perry, A. E. (1996). An experimental study of round jets in cross-flow. Journal of fluid mechanics, 306, 111-144.

38. Muppidi, S., & Mahesh, K. (2007). Direct numerical simulation of round turbulent jets in crossflow. Journal of Fluid Mechanics, 574, 59-84.

39. Muppidi, S., & Mahesh, K. (2005). Study of trajectories of jets in crossflow using direct numerical simulations. Journal of Fluid Mechanics, 530, 81-100.

40. Panda, P. P., Roa, M., Szedlacsek, P., Laster, W. R., & Lucht, R. P. (2015). Structure and dynamics of the wake of a reacting jet injected into a swirling, vitiated crossflow in a staged combustion system. Experiments in Fluids, 56(1), 1-20.

41. Fric, T. F., & Roshko, A. (1994). Vortical structure in the wake of a transverse jet. Journal of Fluid Mechanics, 279, 1-47.

42. Fric, T. F., & Roshko, A. (1991). Structure in the near field of the transverse jet. In Turbulent Shear Flows 7 (pp. 225-237). Springer Berlin Heidelberg.

43. Moussa, Z. M., Trischka, J. W., & Eskinazi, S. (1977). The near field in the mixing of a round jet with a cross-stream. Journal of Fluid Mechanics, 80(01), 49-80.

44. Grout, R. W., Gruber, A., Yoo, C. S., & Chen, J. H. (2011). Direct numerical simulation of flame stabilization downstream of a transverse fuel jet in cross-flow. Proceedings of the Combustion Institute, 33(1), 1629-1637.

45. New, T. H., Lim, T. T., & Luo, S. C. (2006). Effects of jet velocity profiles on a round jet in cross-flow. Experiments in Fluids, 40(6), 859-875.

46. Gollahalli, S. R., & Nanjundappa, B. (1995). Burner wake stabilized gas jet flames in cross-flow. Combustion science and technology, 109(1-6), 327-346.

47. Choudhuri, A. R., & Gollahalli, S. R. (2000). Effects of ambient pressure and burner scaling on the flame geometry and structure of hydrogen jet flames in cross-flow. International journal of hydrogen energy, 25(11), 1107-1118.

48. Johnson, M. R., & Kostiuk, L. W. (2000). Efficiencies of low-momentum jet diffusion flames in crosswinds. Combustion and Flame, 123(1), 189-200.

49. Huang, R. F., & Chang, J. M. (1994). Coherent structure in a combusting jet in crossflow. AIAA journal, 32(6), 1120-1125.

50. Bandaru, R. V., & Turns, S. R. (2000). Turbulent jet flames in a crossflow: effects of some jet, crossflow, and pilot-flame parameters on emissions. Combustion and flame, 121(1), 137-151.

51. Su, L. K., & Mungal, M. G. (2004). Simultaneous measurements of scalar and velocity field evolution in turbulent crossflowing jets. Journal of fluid mechanics, 513, 1-45.

52. Hasselbrink, E. F., & Mungal, M. G. (2001). Transverse jets and jet flames. Part 1. Scaling laws for strong transverse jets. Journal of Fluid Mechanics, 443, 1-25.

53. Hasselbrink, E. F., & Mungal, M. G. (2001). Transverse jets and jet flames. Part 2. Velocity and OH field imaging. Journal of Fluid Mechanics, 443, 27-68.

54. Chan, W. L., Kolla, H., Chen, J. H., & Ihme, M. (2014). Assessment of model assumptions and budget terms of the unsteady flamelet equations for a turbulent reacting jet-in-cross-flow. Combustion and Flame, 161(10), 2601-2613.

55. Kolla, H., Grout, R. W., Gruber, A., & Chen, J. H. (2012). Mechanisms of flame stabilization and blowout in a reacting turbulent hydrogen jet in cross-flow. Combustion and Flame, 159(8), 2755-2766.

56. Denev, J. A., Fröhlich, J., & Bockhorn, H. (2009). Large eddy simulation of a swirling transverse jet into a crossflow with investigation of scalar transport. Physics of Fluids, 21(1), 015101.

57. Abdilghanie, A., Frouzakis, C. E., & Fischer, P. F. (2013). Direct Numerical Simulation of Autoignition in a Jet in a Cross-Flow Configuration: ALCF-2 Early Science Program Technical Report (No. ANL/ALCF/ESP-13/3). Argonne National Laboratory (ANL).

58. Westerweel, J. (1997). Fundamentals of digital particle image velocimetry. Measurement science and technology, 8(12), 1379.

59. Adrian, R. J. (2005). Twenty years of particle image velocimetry. Experiments in fluids, 39(2), 159-169.

60. Westerweel, J., Elsinga, G. E., & Adrian, R. J. (2013). Particle image velocimetry for complex and turbulent flows. Annual Review of Fluid Mechanics, 45, 409-436.

61. Boxx, I., Carter, C. D., Stöhr, M., & Meier, W. (2013). Study of the mechanisms for flame stabilization in gas turbine model combustors using kHz laser diagnostics. Experiments in fluids, 54(5), 1-17.

62. Boxx, I., Arndt, C.M., Carter, C., & Meier, W. (2012) High-speed laser diagnostics for the study of flame dynamics in a lean premixed gas turbine model combustor. Exp Fluids 52(3):555-567.

63. Stöhr, M., Sadanandan, R., & Meier, W. (2011). Phase-resolved characterization of vortex–flame interaction in a turbulent swirl flame. Experiments in Fluids, 51(4), 1153-1167.

64. Steinberg, A.M., Sadanandan, R., Dem, C., Kutne, P., & Meier, W. (2013) Structure and stabilization of hydrogen jet flames in cross-flows. Proc. Combust. Inst.34(1):1499–1507.

65. Boxx, I., Slabaugh, C., Kutne, P., Lucht, R. P., & Meier, W. (2015). 3kHz PIV/OH-PLIF measurements in a gas turbine combustor at elevated pressure. Proceedings of the Combustion Institute, 35(3), 3793-3802.

66. Slabaugh, C. D., Pratt, A. C., & Lucht, R. P. (2015). Simultaneous 5 kHz OH-PLIF/PIV for the study of turbulent combustion at engine conditions. Applied Physics B, 118(1), 109-130.

67. Böhm, B., Heeger, C., Boxx, I., Meier, W., & Dreizler, A. (2009). Time-resolved conditional flow field statistics in extinguishing turbulent opposed jet flames using simultaneous highspeed PIV/OH-PLIF. Proceedings of the Combustion Institute, 32(2), 1647-1654.

68. Lamont, W. G., Roa, M., Meyer, S. E., & Lucht, R. P. (2012). Emission Measurements and CH* Chemiluminescence of a Staged Combustion Rig for Stationary Gas Turbine Applications. Journal of Engineering for Gas Turbines and Power, 134(8), 081502.

69. Roa, M., Lamont, W. G., Meyer, S. E., Szedlacsek, P., & Lucht, R. P. (2012, June). Emission measurements and OH-PlIF of reacting hydrogen jets in vitiated crossflow for stationary gas turbines. In ASME Turbo Expo 2012: Turbine Technical Conference and Exposition (pp. 491-498). American Society of Mechanical Engineers.

70. Sullivan, R., Wilde, B., Noble, D. R., Periagaram, K., Seitzman, J. M., & Lieuwen, T. C. (2013). Unsteady flame-wall interactions in a reacting jet injected into a vitiated cross-flow. Proceedings of the Combustion Institute, 34(2), 3203-3210.

71. Sullivan, R., Wilde, B., Noble, D. R., Seitzman, J. M., & Lieuwen, T. C. (2014). Time-averaged characteristics of a reacting fuel jet in vitiated cross-flow. Combustion and Flame, 161(7), 1792-1803.

72. Micka, D. J., & Driscoll, J. F. (2012). Stratified jet flames in a heated (1390K) air cross-flow with autoignition. Combustion and Flame, 159(3), 1205-1214.

73. Lamont, W. G. (2012). Experimental study of a staged combustion system for stationary gas turbine applications. PhD Dissertation, Purdue University.

74. Roa, M. (2014). Investigation of a Reacting Jet Injected into a Vitiated Crossflow using CARS, High-Repetition-Rate OH-PLIF, and High-Repetition-Rate PIV. PhD Dissertation, Purdue University.

75. Wilde, B. (2014). Dynamics of Variable Density Ratio Reacting Jets in Unsteady, Vitiated Crossflow. PhD Dissertation, Georgia Institute of Technology.

76. Fugger, C., A. (2015). Experimental investigation of a transverse reacting jet in a high pressure oscillating vitiated crossflow. PhD Dissertation, Purdue University.

77. Cheng, R., Yegian, D., Miyasato, M., Samuelsen, G., Benson, C.E., Pellizzari, R., & Loftus, P. (2000) Scaling and development of low-swirl burners for low-emission furnaces and boilers. Proc. of Combust. Inst. 28:1305-1313.

78. Kline, S. J., & McClintock, F. A. (1953). Describing uncertainties in single-sample experiments. Mechanical engineering, 75(1), 3-8.

79. Figliola, R. S., & Beasley, D. (2015). Theory and design for mechanical measurements. John Wiley & Sons.

80. Stopper, U., Meier, W., Sadanandan, R., Stöhr, M., Aigner, M., & Bulat, G. (2013). Experimental study of industrial gas turbine flames including quantification of pressure influence on flow field, fuel/air premixing and flame shape. Combustion and Flame, 160(10), 2103-2118.

81. Anderson, R. C., Hicks, Y. R., & Locke, R. J. (2011). Excitation/Detection Strategies for OH Planar Laser-Induced Fluorescence Measurements in the Presence of Interfering Fuel Signal and Absorption Effects. National Aeronautics and Space Administration, Glenn Research Center.

82. Janus, B., Dreizler, A., & Janicka, J. (2005). Experimental study on stabilization of lifted swirl flames in a model GT combustor. Flow, Turbulence and Combustion, 75(1-4), 293-315.

83. Beerer, D. J., & McDonell, V. G. (2011). An experimental and kinetic study of alkane autoignition at high pressures and intermediate temperatures. Proceedings of the Combustion Institute, 33(1), 301-307.

84. Beerer, D. J., & McDonell, V. G. (2011). An experimental and kinetic study of alkane autoignition at high pressures and intermediate temperatures. Proceedings of the Combustion Institute, 33(1), 301-307.

85. Picano, F., Battista, F., Troiani, G., & Casciola, C. M. (2011). Dynamics of PIV seeding particles in turbulent premixed flames. Experiments in Fluids, 50(1), 75-88.

86. Lucht, R. P., Sweeney, D. W., & Laurendeau, N. M. (1983). Laser-saturated fluorescence measurements of OH concentration in flames. Combustion and Flame, 50, 189-205.

87. Eckbreth, A. C. (1996). Laser diagnostics for combustion temperature and species (Vol. 3). CRC Press.

88. Frank, J. H., Miller, M. F., & Allen, M. G. (1999). Imaging of laser-induced fluorescence in a high-pressure combustor. AIAA Paper, (99-0773).

89. Sadanandan, R., Meier, W., & Heinze, J. (2012). Experimental study of signal trapping of OH laser induced fluorescence and chemiluminescence in flames. Applied Physics B, 106(3), 717-724.

90. Uzun, A., & Hussaini, M. Y. (2007). Investigation of high frequency noise generation in the near-nozzle region of a jet using large eddy simulation. Theoretical and Computational Fluid Dynamics, 21(4), 291-321.

91. Ewing, D., George, W. K., Rogers, M. M., & Moser, R. D. (2007). Two-point similarity in temporally evolving plane wakes. Journal of Fluid Mechanics, 577, 287-307.

92. Pope, S. B. (2000). Turbulent flows. Cambridge university press.

93. Luo, K. H. (1999). Combustion effects on turbulence in a partially premixed supersonic diffusion flame. Combustion and Flame, 119(4), 417-435.

94. Berkooz, G., Holmes, P., & Lumley, J. L. (1993). The proper orthogonal decomposition in the analysis of turbulent flows. Annual review of fluid mechanics, 25(1), 539-575.

95. Hilberg, D., Lazik, W., & Fiedler, H. E. (1993). The application of classical POD and snapshot POD in a turbulent shear layer with periodic structures. In Eddy Structure Identification in Free Turbulent Shear Flows (pp. 251-259). Springer Netherlands.

96. Meyer, K. E., Pedersen, J. M., & Özcan, O. (2007). A turbulent jet in crossflow analysed with proper orthogonal decomposition. Journal of Fluid Mechanics, 583, 199-227.

97. Candel, S. M., & Poinsot, T. J. (1990). Flame stretch and the balance equation for the flame area. Combustion Science and Technology, 70(1-3), 1-15.

98. Filatyev, S. A., Driscoll, J. F., Carter, C. D., & Donbar, J. M. (2005). Measured properties of turbulent premixed flames for model assessment, including burning velocities, stretch rates, and surface densities. Combustion and Flame, 141(1), 1-21.

99. Poinsot, T., Veynante, D., & Candel, S. (1991). Quenching processes and premixed turbulent combustion diagrams. Journal of Fluid Mechanics, 228, 561-606.

100. Boxx, I., Carter, C. D., & Meier, W. (2014). On the feasibility of tomographic-PIV with low pulse energy illumination in a lifted turbulent jet flame. Experiments in Fluids, 55(8), 1-17.

101. Chakraborty, N., Kolla, H., Sankaran, R., Hawkes, E. R., Chen, J. H., & Swaminathan, N. (2013). Determination of three-dimensional quantities related to scalar dissipation rate and its transport from two-dimensional measurements: Direct Numerical Simulation based validation. Proceedings of the Combustion Institute, 34(1), 1151-1162.

102. Kothnur, P. S., & Clemens, N. T. (2005). Effects of unsteady strain rate on scalar dissipation structures in turbulent planar jets. Physics of Fluids (1994-present), 17(12), 125104.

103. Rehm, J. E., & Clemens, N. T. (1998, December). The relationship between vorticity/strain and reaction zone structure in turbulent non-premixed jet flames. In Symposium (International) on Combustion (Vol. 27, No. 1, pp. 1113-1120). Elsevier.

104. Boxx, I., Stöhr, M., Carter, C., & Meier, W. (2010). Temporally resolved planar measurements of transient phenomena in a partially pre-mixed swirl flame in a gas turbine model combustor. Combustion and Flame, 157(8), 1510-1525.

APPENDICES

APPENDIX A. ACSCS RIG DRAWINGS

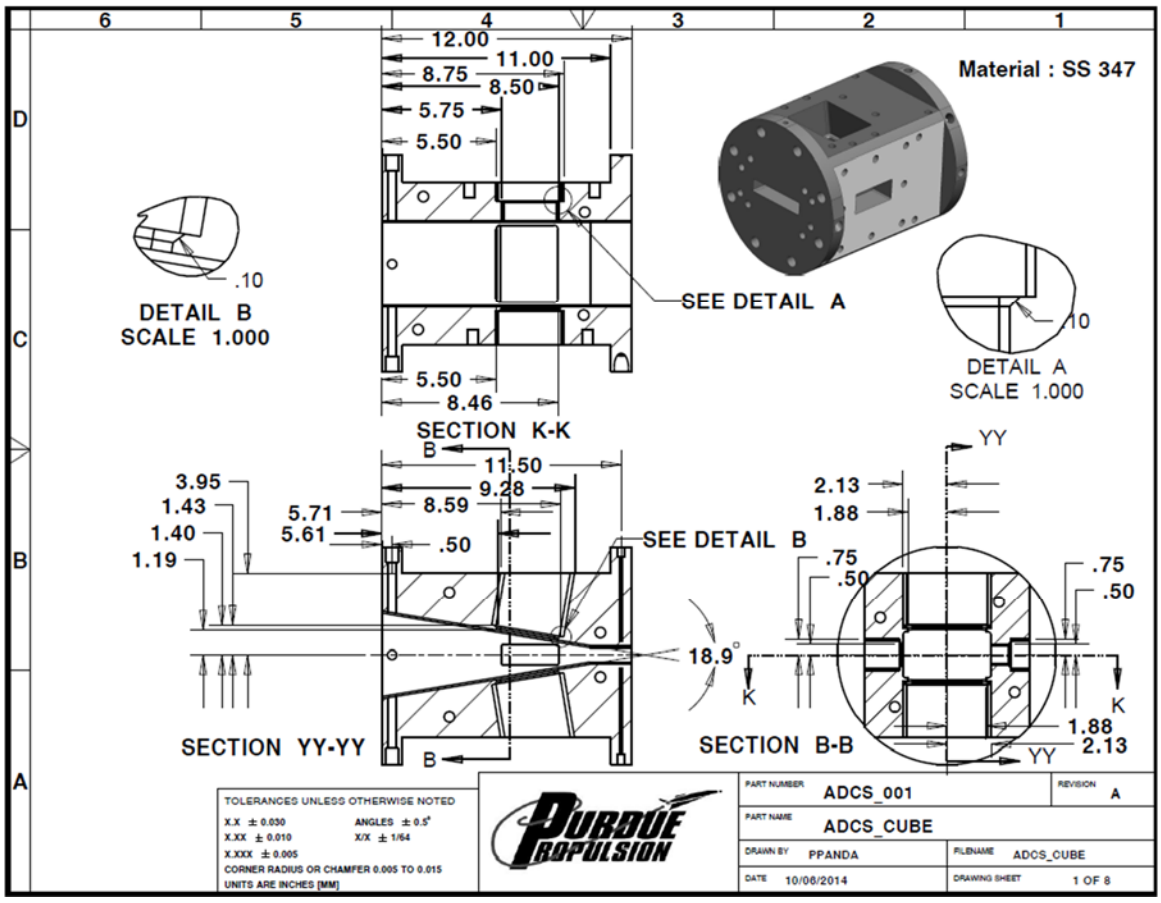

Figure A.1. Optically accessible converging section.

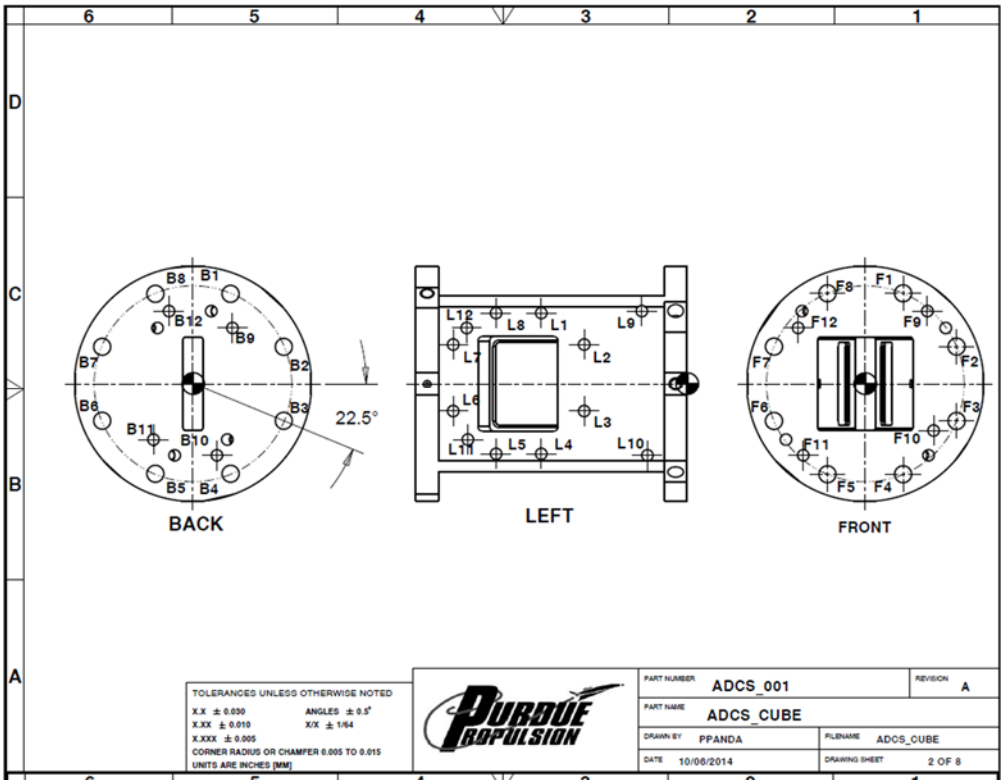

HOLES	XDIM	YDIM	DESC.
F1	1.674	4.042	1/2-20 UNF - 2B TAP 0.750 29/64 DRILL (0.453)
F2	4.042	1.674	
F3	4.042	-1.674	
F4	1.674	-4.042	
F5	-1.674	-4.042	
F6	-4.042	-1.674	
F7	-4.042	1.674	
F8	-1.674	4.042	
F9	2.750	3.250	∅ 0.500 2.00 DEEP
F10	3.025	-2.100	∅ 0.500 3.250 DEEP
F11	-2.750	-3.200	∅ 0.500 1.750 DEEP
F12	-2.973	-2.505	∅ 0.500 3.250 DEEP

HOLES	XDIM	YDIM	DESC.
B1	1.674	4.042	1/2-20 UNF - 2B TAP 0.750 29/64 DRILL (0.453)
B2	4.042	1.674	
B3	4.042	-1.674	
B4	1.674	-4.042	
B5	-1.674	-4.042	
B6	-4.042	-1.674	
B7	-4.042	1.674	
B8	-1.674	4.042	
B9	1.750	2.500	∅ 0.500 2.250 DEEP
B10	1.060	-3.200	∅ 0.500 1.500 DEEP
B11	-1.750	-2.500	∅ 0.500 2.250 DEEP
B12	-3.250	-1.060	∅ 0.500 1.500 DEEP

HOLES	XDIM	YDIM	DESCRIPTION
L1	-6.450	3.165	1/2-20 UNF - 2B TAP 0.750 29/64 DRILL (0.453)
L2	-4.550	1.765	
L3	-4.550	-1.235	
L4	-6.450	-3.135	
L5	-8.450	-3.135	
L6	-10.350	-1.235	
L7	-10.350	1.765	
L8	-8.450	3.165	

HOLES	XDIM	YDIM	DESCRIPTION
L9	-2.000	3.250	∅ 0.500 THRU HOLE
L10	-1.750	-3.200	
L11	-9.700	-2.500	
L12	-9.750	2.500	

Figure A.2. Locations of water cooling holes and bolts on front, back and left face of the converging section.

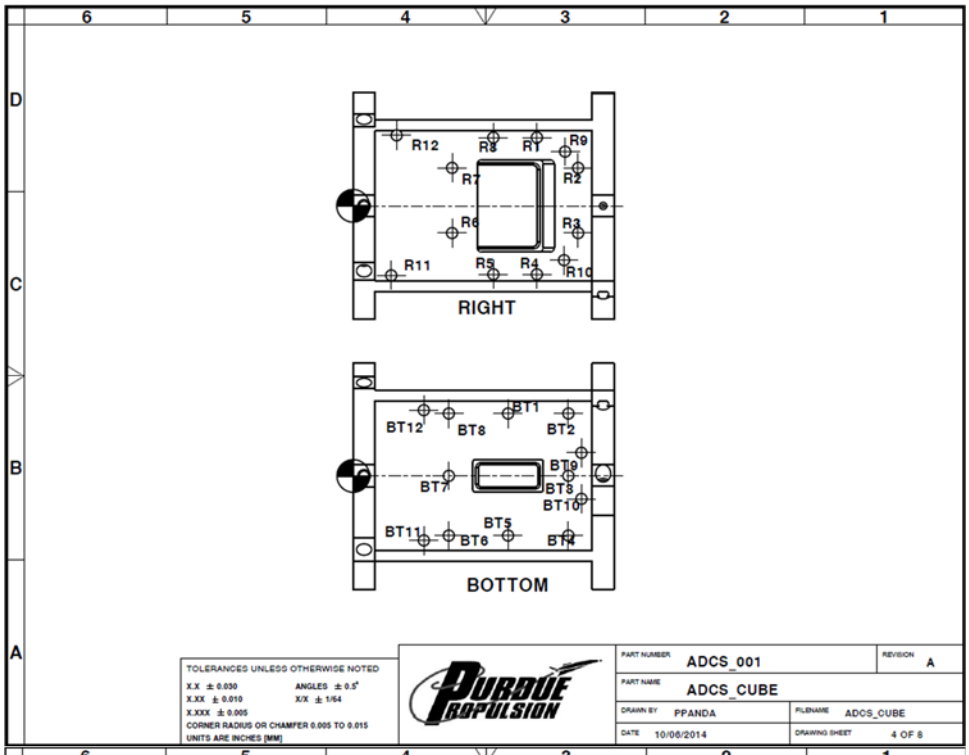

HOLES	XDIM	YDIM	DESC.
R1	8.450	3.150	1/2-20 UNF - 2B TAP 0.750 29/64 DRILL (0.453)
R2	10.350	1.750	
R3	10.350	-1.250	
R4	8.450	-3.150	
R5	6.450	-3.150	
R6	4.550	-1.250	
R7	4.550	1.750	
R8	6.450	3.150	
R9	9.750	2.500	∅ 0.500 THRU HOLE TO BE PLUG WELDED ON BOTH ENDS
R10	9.700	-2.500	
R11	1.750	-3.200	
R12	2.500	3.250	

HOLES	XDIM	YDIM	DESC.
BT1	7.125	2.870	1/2-20 UNF - 2B TAP 0.750 29/64 DRILL (0.453)
BT2	9.900	2.870	
BT3	9.900	0.000	
BT4	9.900	-2.750	
BT5	7.125	-2.750	
BT6	4.400	-2.750	
BT7	4.400	0	
BT8	4.400	2.870	
BT9	1.750	1.060	∅ 0.500 2.250 DEEP
BT10	0.883	-3.023	∅ 0.500 1.500 DEEP
BT11	-1.500	-2.970	∅ 0.500 2.250 DEEP
BT12	-3.250	-1.060	∅ 0.500 1.500 DEEP

TOLERANCES UNLESS OTHERWISE NOTED
X.X ± 0.030 ANGLES ± 0.5°
X.XX ± 0.010 X/X ± 1/64
X.XXX ± 0.005
CORNER RADIUS OR CHAMFER 0.005 TO 0.015
UNITS ARE INCHES [MM]
PURDUE PROPULSION
PART NUMBER ADCS_001
REVISION A
PART NAME ADCS_CUBE
DRAWN BY PPANDA
FILENAME ADCS_CUBE
DATE 10/06/2014
DRAWING SHEET 5 OF 8

Figure A.3. Bolt locations on right and bottom face of the converging section.

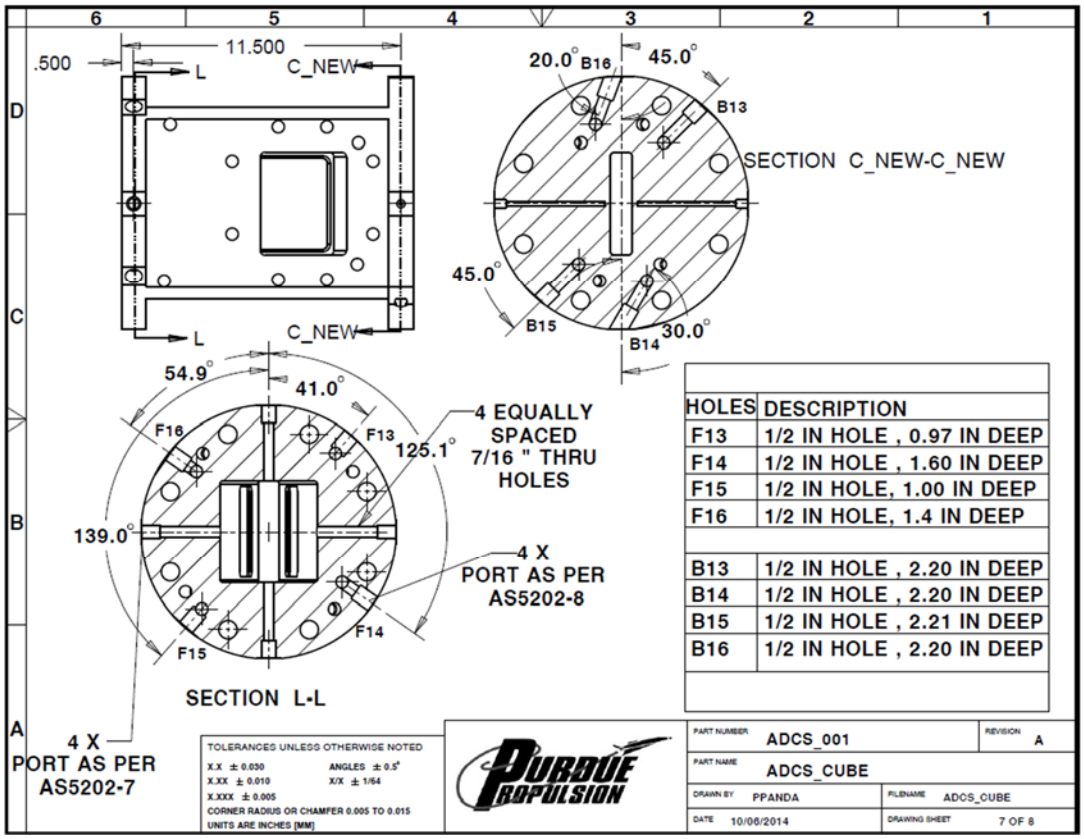

Figure A.4. Cooling water N_2 film cooling inlet ports.

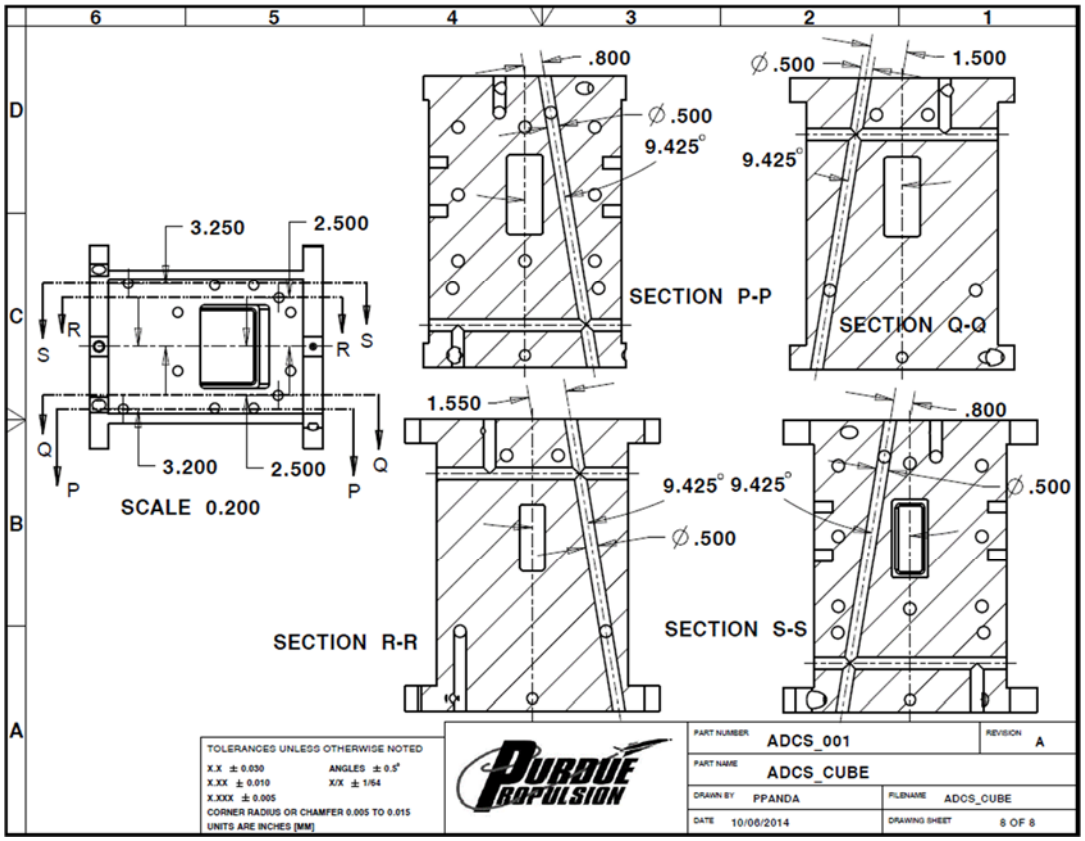

Figure A.5. Water cooling channels location.

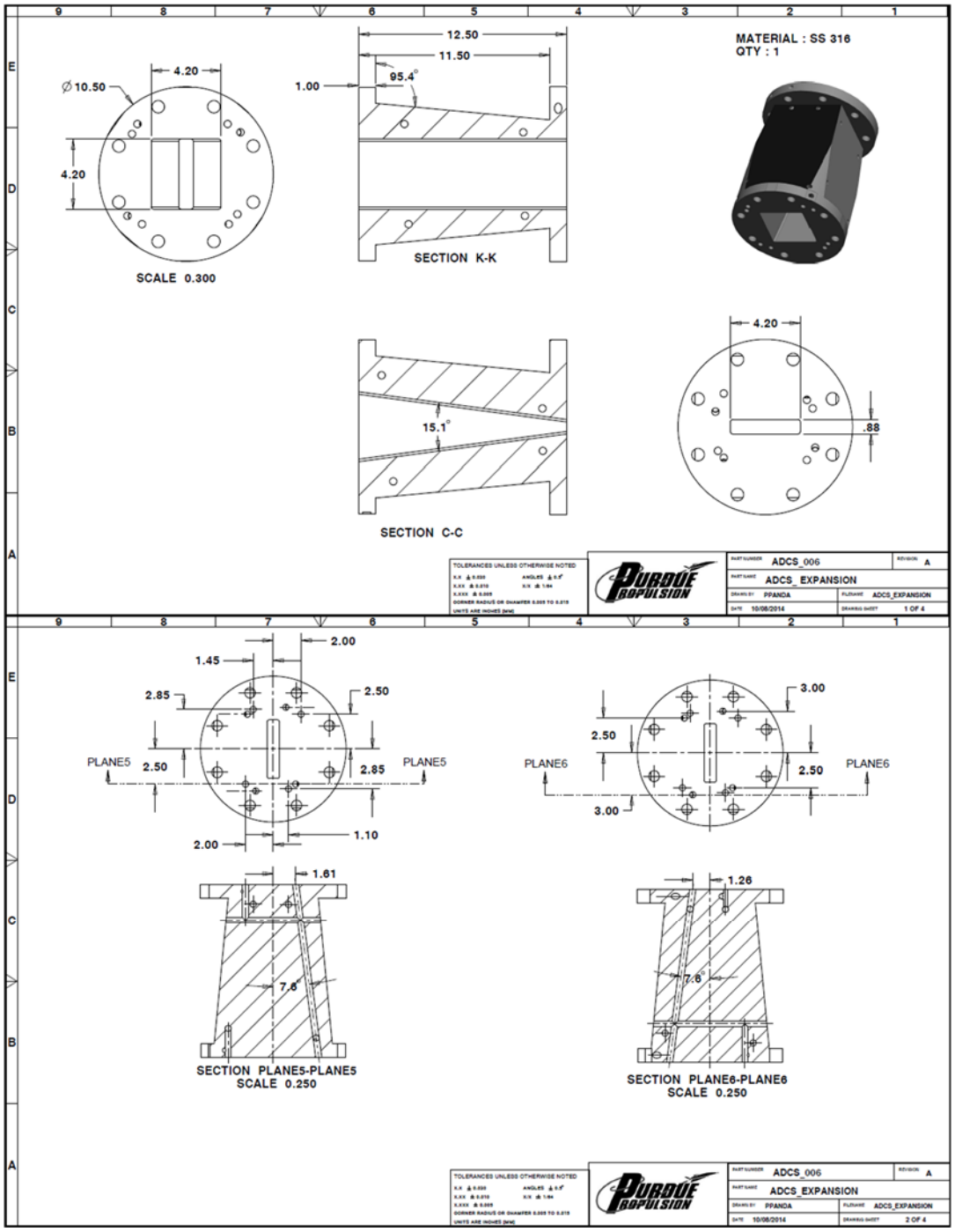

Figure A.6. Diverging section details.

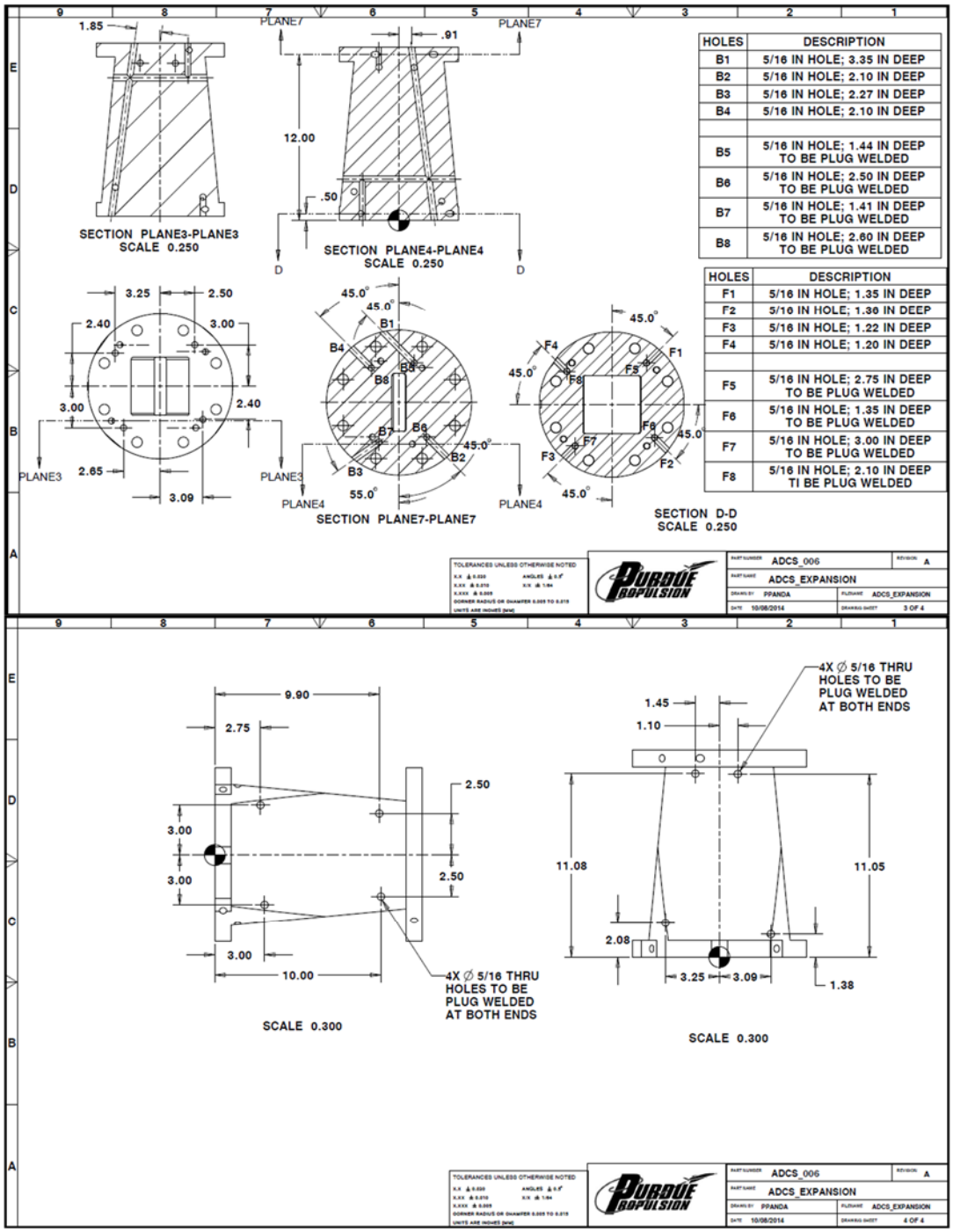

Figure A.7. Cooling water ports and channels in the diverging section.

APPENDIX B. MATLAB CODE FOR PROPER ORTHOGONAL DECOMPOSITION (POD) ANALYSIS

```
%% MATLAB Code for Proper Orthogonal Decomposition on Velocity Vectors
%%Written by Pratikash Panda,Dt: 02/24/2015
%%reference : Identify Flow Structure with POD by Knu Erik Meyer

%% Reading LaVision processed vectors
clear all;
clc;
% Number of Vectors imported
numberofvec = 5000;
% Number of POD modes to compute
nMode = 50;

for  i=1:numberofvec

   if i < 10
      currentvec = loadvec(['B0000' num2str(i) '.vc7']);
   end
   if i < 100 && i >= 10
      currentvec = loadvec(['B000' num2str(i) '.vc7']);
   end
   if i < 1000 && i >= 100
      currentvec = loadvec(['B00' num2str(i) '.vc7']);
   end
   if i < 10000 && i >= 1000
      currentvec = loadvec(['B0' num2str(i) '.vc7']);
   end

 C=repmat(currentvec,[1 1 i]);

 Vec(:,:,i) = C(:,:,i);

  if i == round(numberofvec*.2)
     fprintf('\n20%% completed')
  end
  if i == round(numberofvec*.4)
     fprintf('\n40%% completed')
  end
  if i == round(numberofvec*.6)
     fprintf('\n60%% completed')
```

```
  end
  if i == round(numberofvec*.8)
     fprintf('\n80%% completed')
  end
  if i == numberofvec
     fprintf('\n100%% completed\n')
  end
end

% Plot average and one velocity snapshot
AF = averf(Vec);

figure(1)
showf(Vec(:,:,3),'Vx','Contourf',20,'Spacing',2,'ScaleArrow',0.04,'CLim',[-75 75]);

figure(2)
showf(AF,'rot','Contourf',20,'Spacing',2,'ScaleArrow',0.04,'CLim',[-15000 15000]);



xx = Vec.x;
yy = Vec.y;

%% Section 1 Constructing Fluctuation Component Matrix
for i=1:numberofvec
%
   U(:,:,i) = Vec(:,:,i).vx -AF.vx;
   V(:,:,i) = Vec(:,:,i).vy -AF.vy;
end

for i=1:numberofvec
   Vec_fluc(:,:,i) = Vec(:,:,i);
end

for i=1:numberofvec

   Vec_fluc(:,:,i).vx =U(:,:,i);
   Vec_fluc(:,:,i).vy =V(:,:,i);
end

% Plot average and one fluctuating velocity snapshot
figure(1)
showf(Vec_fluc(:,:,3));
```

```
figure(2)
AF_fluc = averf(Vec_fluc);
showf(AF_fluc);

%% Section 2 Decomposition Algorithm
% create matrix will all fluctuating velocity components for each snapshot in a column
ni=50;% Number of rows
nj=56;% Number of columns
ns=numberofvec;% Number of snapshots
nMode = 10;
Uall=[reshape(U,ni*nj,ns);reshape(V,ni*nj,ns)]; % Uall is a 2*ni*nj,ns matrix

% Do POD analysis
R=Uall'*Uall; % Autocovariance matrix
[eV,D]=eig(R); % solve: eV is eigenvectors, D is eigenvalues in diagonal matrix
[L,I]=sort(diag(D)); % sort eigenvalues in ascending order - I is sorted index vector
for i=1:length(D)
   eValue(length(D)+1-i)=L(i); % Eigenvalues sorted in descending order
   eVec(:,length(D)+1-i)=eV(:,I(i)); % Eigenvectors sorted in the same order
end;
   eValue(length(eValue))=0; % last eigenvalue should be zero
   menergy=eValue/sum(eValue); % relative energy associated with mode m

% calculate the first Nmodes
for i=1:nMode
   tmp=Uall*eVec(:,i); % find mode
   phi(:,i)=tmp/norm(tmp); % normalize mode
end

% calculate the first n temporal modes (ai)
for i=1:numberofvec
   a_mode(:,i)=phi'*Uall(:,i); % find temporal mode
end

%Storing SPATIAL Modes

for j=1:nMode
    ntot = ni*nj;
   for i=1:ntot
        phiPODx(i,j)=phi(i,j);
      phiPODy(i,j)=phi(i+ntot,j);
   end
end
```

```
 nx=50;
ny=56;
for i = 1:nMode
   phix_seg = phiPODx(:,i);
   phiy_seg = phiPODy(:,i);
%     VxPOD(:,:,i) = ones(nx,ny,numberofvec);
%     VyPOD(:,:,i) = ones(nx,ny,numberofvec);
   for j = 1:nx
      phixPOD(:,j,i) = phix_seg(1+(j-1)*ny:ny+(j-1)*ny);
      phiyPOD(:,j,i) = phiy_seg(1+(j-1)*ny:ny+(j-1)*ny);
   end
end


for i=1:nMode
   phi_POD(:,:,i) = Vec(:,:,i);
end


for i=1:nMode


   phi_POD(:,:,i).vx =1*phixPOD(:,:,i);
   phi_POD(:,:,i).vy =1*phiyPOD(:,:,i);
end


figure(10)
showf(phi_POD(:,:,7),'rot',2,'CMap','jet','Contourf',50,'Spacing',2,'ScaleArrow',100,'CLim
',[]);
%
showf(phi_POD(:,:,3),'Streamline',2,'CMap','gray','Contourf',50,'Spacing',64,'ScaleArrow'
,0.1,'CLim',[-500 -400]);

% calculate the snapshot un
for i=1:numberofvec
   UPOD(:,i)=phi*a_mode(:,i); % find un snapshot
end

%% Reconstruct the Velocity Field
for j=1:numberofvec
   ntot = ni*nj;
   for i=1:ntot
      VPODx(i,j)=UPOD(i,j); %First nx*ny rows contain Ux
      VPODy(i,j)=UPOD(i+ntot,j);% Next nx*ny rows contain Uy
   end
end
```

```
% Reconstructing the fluctuating velocity snapshot
nx=50;
ny=56;
for i = 1:numberofvec
   vx_seg = VPODx(:,i);
   vy_seg = VPODy(:,i);
%     VxPOD(:,:,i) = ones(nx,ny,numberofvec);
%     VyPOD(:,:,i) = ones(nx,ny,numberofvec);
    for j = 1:nx
       VxPOD(:,j,i) = vx_seg(1+(j-1)*ny:ny+(j-1)*ny);
       VyPOD(:,j,i) = vy_seg(1+(j-1)*ny:ny+(j-1)*ny);
    end
    if i == round(numberofvec*.2)
      fprintf('\n20%% completed')
   end
   if i == round(numberofvec*.4)
      fprintf('\n40%% completed')
   end
   if i == round(numberofvec*.6)
      fprintf('\n60%% completed')
   end
   if i == round(numberofvec*.8)
      fprintf('\n80%% completed')
   end
   if i == numberofvec
      fprintf('\n100%% completed\n')
   end

end

% Initializing Vec_POD
for i=1:numberofvec
   Vec_POD(:,:,i) =Vec(:,:,i);
end
%Creating the velocity field computed form POD Modes
for i=1:numberofvec

   Vec_POD(:,:,i).vx =VxPOD(:,:,i);
   Vec_POD(:,:,i).vy =VyPOD(:,:,i);
end
 figure(3)
showf(Vec_POD(:,:,3));

figure(4)
```

```
AF_POD = averf(Vec_POD);
showf(AF_POD);

%% Adding Mean to Reconstruct the Velocity Field
for i=1:numberofvec
%
   Urec(:,:,i) = Vec_POD(:,:,i).vx + AF.vx;
   Vrec(:,:,i) = Vec_POD(:,:,i).vy + AF.vy;
end

for i=1:numberofvec
   Vec_rec(:,:,i) = Vec(:,:,i);
end

%Creating the velocity field computed form POD Modes+MEAN
for i=1:numberofvec

   Vec_rec(:,:,i).vx =Urec(:,:,i);
   Vec_rec(:,:,i).vy =Vrec(:,:,i);
end

  figure(5)

showf(Vec_rec(:,:,235),'div','CMap','jet','Contourf',20,'Spacing',2,'ScaleArrow',0.04,'CLi
m',[-10000 10000]);
  figure (6)

showf(Vec(:,:,233),'rot','CMap','jet','Contourf',20,'Spacing',2,'ScaleArrow',0.04,'CLim',[-
30000 30000]);

  Vec_err = Vec;
  for i=1:5000
    Vec_err(:,:,i).vx = Vec(:,:,i).vx - Vec_rec(:,:,i).vx;
    Vec_err(:,:,i).vy = Vec(:,:,i).vy - Vec_rec(:,:,i).vy;
  end

  figure (7)

showf(Vec_err(:,:,233),'div','CMap','jet','Contourf',20,'Spacing',2,'ScaleArrow',0.04,'CLi
m',[-30000 30000]);

figure(6)
```

```
AF_rec = averf(Vec_rec);
showf(AF_rec,'rot','CMap','jet','Contourf',20,'Spacing',2,'ScaleArrow',0.04,'CLim',[-5000
5000]);

%% Plotting the POD Mode energy distribution
figure(7)
loglog(menergy);
% loglog(eValue);
%Plotting one temporal coefficient as a function of time
figure(8)
plot(time,a_mode(2,:),'-g',time,a_mode(3,:),'-r');
plot(a_mode(2,:),a_mode(3,:),'*');

%% Computing the spectral content of the POD Mode
Mode1 = a_mode(2,:)+a_mode(3,:);

time(1) = 0;
delta_t = 0.0001;
for i=1:numberofvec-1
      time(i+1)=time(i)+delta_t;
end



       framerate =10000;
       m=length(time);
       nfft = pow2(nextpow2(m));
       wx = window(@hann,length(Mode1));
       [Pwrx Fbx] = periodogram(Mode1,wx,nfft,framerate);
        figure(11)
       set(gca,'FontSize',20)
       set(gcf, 'Color', [1,1,1]);
       stem(Fbx,Pwrx,'-r','Linewidth',2);
       axis([100 1000 0.10 2000]);
       grid on;
       xlabel('Frequency(Hz)','FontWeight','bold','FontSize',20,'FontName','Times');
       ylabel('Magnitude
[(m/s)^{2}/Hz]','FontWeight','bold','FontSize',20,'FontName','Times');
```

VITA

VITA

Pratikash Prakash Panda
Graduate School, Purdue University

Pratikash Panda received a Bachelor of Technology in Mechanical Engineering from National Institute of Technology, Rourkela, India in 2008. Following his graduation, he worked for a year at Schlumberger, India as a Mechanical Engineer. He graduated with a Master's degree from School of Mechanical Engineering under the supervision of Prof. Hukam C. Mongia and Prof. Charles Merkle. The area of research during his Master's was hybrid RANS/LES based numerical modelling of turbulent reacting flows. He continued for a Ph.D. in the School of Mechanical Engineering at Purdue University under the supervision of Prof. Robert P. Lucht. The primary area of his doctoral research involves experimental investigation of turbulent flames using advanced laser diagnostics techniques at engine relevant conditions.

He is a recipient of the John Zink Graduate Fellowship, 2013 – 2014, at Purdue University. He received the 2013 ASME IGTI Student Scholarship.

.

LIST OF PUBLICATIONS

LIST OF PUBLICATIONS

Journal

1. Panda P, Roa M, Lucht R.P, Szedlacsek P, Laster,W. “Structure and dynamics of the wake of a reacting jet injected into a swirling vitiated crossflow,” Experiments in Fluid(2015), DOI: 10.1007/s00348-014-1885-3.

2. Panda P, Roa M, Slabaugh, C.D., Peltier,S, Carter,C, Lucht R.P, Laster,W “High-Repetition-Rate planar measurement in the wake of a reacting jet injected into a swirling vitiated crossflow,” Combustion and Flame (*In Review*).

3. Satija, A., Huang, X., Panda, P. P., & Lucht, R. P. (2015). Vibrational CARS thermometry and one-dimensional simulations in laminar H 2/air counter-flow diffusion flames. International Journal of Hydrogen Energy, 40(33), 10662-10672.

4. Roa M, Lamont,W, Panda,P, Lucht R.P, Szedlacsek P, Laster,W. “High repetition rate OH-PLIF and DP-CARS measurements to investigate a reacting jet injected into a swirling vitiated crossflow,” Combustion and Flame (*In Review*).